

High Reynolds Number Flow Past Configurations of Multiple Blades

A thesis submitted to the School of Mathematics of the University
of East Anglia in partial fulfilment of the requirements for the
degree of Doctor of Philosophy

By Simon Kirby

September 2010

© This copy of the thesis has been supplied on condition that anyone who consults it is understood to recognise that its copyright rests with the author and that no quotation from the thesis, nor any information derived therefrom, may be published without the author's prior, written consent.

© Copyright 2010

by

Simon Kirby

Abstract

This thesis uses asymptotic and numerical techniques to examine high Reynolds flow past an array of many blades in various configurations. Two-dimensional flows are considered in this thesis which we treat as a limiting case of three-dimensional rotor blade flow as one passes far away from the centre of blade rotation. Chapter 2 considers the flow past a horizontally aligned array of flat blades with a very small ground clearance, and analyses effects associated with slip-streaming. Chapter 3 investigates the flow past many blades with a global angle of attack. Viscous-inviscid coupling is essential in the model derived in this chapter, with the solutions of the viscous and inviscid problems requiring simultaneous treatment. The coupling is observed through unknown pressure differences and wake-shapes. Chapter 4 extends the analysis of Chapter 3 to include a many-blade limit, where the boundary-layer is modelled as a periodic sublayer embedded within a growing bulk-layer.

In Chapter 5, we examine a pressure interactive many-blade limit as an extension to the work in Chapter 4. In our analysis, the boundary-layer generates a pressure-displacement interaction. In Chapter 6, a global angle of attack is reintroduced into the interactive many-blade limit of Chapter 5 so that the sublayer is affected to leading order and the flow response is described. Chapter 7 considers larger global angles of attack that still preserve the interactive structure but cause different interactions between the flow and the blades. In both chapters, the adaptations of the interactive limit are made clear for each case considered. Finally, Chapter 8 considers flow past an array of vertically aligned blades in a channel. The analysis describes the flow upstream of the blades, between the blades and the wake flow. Analytical solutions for the primarily inviscid leading order flow at the leading edge are derived for given downstream pressures and a discussion of the flow development there in relation to the downstream channel geometry is given. Numerical solutions of the full problem are given for the flow past 1, 2 and 9 blades and the relevant flow features in each case are analysed.

Acknowledgements

I would like to express my sincere thanks to my primary adviser, Dr. Richard Purvis, whose expertise in the subject area, patience and advice have guided me through this thesis. I would like to thank my second supervisor, Dr. Paul Hammerton, for some constructive comments on my thesis. A personal thank you goes to Dr. Mark Cooker, for help in producing and presenting different outreach activities as a distraction from the project and to Professor Frank Smith for assistance with a particular numerical issue. Financial support from the Engineering and Physical Sciences Research Council is greatly appreciated.

I would like to thank my family for their support and interest in my work over the duration of my time at university, from undergraduate to postgraduate, to which I hope my achievements give you much happiness. Finally, I would like to thank Elizabeth Eves, whose love, support and care when the going has been tough has been paramount to the completion of my studies.

Contents

Abstract	v
Acknowledgements	vii
1 Introduction	1
1.1 Physical background	1
1.2 Thesis outline	8
2 Flow past many blades in extreme ground effect	13
2.1 Formulation	15
2.1.1 Velocity expansions	16
2.2 Discontinuity region	18
2.2.1 Non-uniform oncoming velocity	21
2.2.2 Uniform oncoming flow	22
2.3 Summary of the full problem	25
2.4 Numerical methods	26
2.4.1 Leading edge solution	26
2.4.2 Blade-ground gap solution	27
2.4.3 Over blade and wake solution	28
2.4.4 Solution algorithm	28
2.5 Results	30
2.5.1 Flow characteristics	30
2.5.2 Small H	34
2.5.3 Large H	39
2.6 Summary	43

3	Flow past many blades at a global angle of attack	45
3.1	Introduction	45
3.2	Formulation	47
3.2.1	The viscous boundary-layer	48
3.2.2	The inviscid free-stream	51
3.3	Solution of the inviscid problem	53
3.3.1	Finding the complex function w	53
3.3.2	Summary of the full problem	57
3.4	Numerical methods	58
3.4.1	Boundary-layer	58
3.4.2	Inviscid Solution	59
3.4.3	Solution algorithm	60
3.5	Results	61
3.5.1	Method validation	62
3.5.2	Solutions for $N = 5$ flat blades	62
3.5.3	Short, thick and many blades	69
3.6	Summary	79
4	Many-blade limit with a global angle of attack	83
4.1	Introduction	83
4.2	Structure	84
4.2.1	Region II: bulk viscous flow	86
4.2.2	Region I: viscous sublayer	89
4.2.3	Region III: free-stream	90
4.3	Numerical Solution	93
4.4	Results	95
4.4.1	Comparisons	95
4.5	Summary	100
5	The pressure interactive many-blade limit	101
5.1	Introduction	101
5.2	The boundary-layer structure	103
5.2.1	The bulk-layer	105
5.2.2	Interactive sublayer	107

5.2.3	Leading-edge discontinuity	108
5.2.4	Inviscid free-stream region	110
5.2.5	Comparisons with the non-interactive limit	113
5.2.6	The condensed limit	114
5.3	Numerical formulation	115
5.3.1	Finite-difference discretisation	116
5.3.2	Solution over the blade	117
5.3.3	Solution in the wake	120
5.3.4	The leading edge solution	121
5.3.5	The streamwise sweep	122
5.3.6	Flow reversal	123
5.4	Results	124
5.4.1	Symmetric flow problems	124
5.4.2	Non-symmetric flow problems	126
6	The pressure interactive many-blade limit with a global angle of attack	139
6.1	Structure with a global angle of attack	139
6.2	The leading order response for $\alpha = Re^{-1}\bar{\alpha}$	141
6.3	Results	143
6.3.1	Flat blade	144
6.3.2	Angled and thick blades	152
7	The pressure interactive many-blade limit with larger global angles of attack	159
7.1	Analysis for larger global angles of attack	159
7.2	Formulation for $\alpha = O(Re^{-4/5})$	160
7.3	Formulation for $\alpha = O(Re^{-3/5})$	162
7.4	Short scale balance in the sublayer	165
7.5	Results	168
7.6	Summary	179
8	Flow past vertically aligned blades within a channel	183
8.1	Introduction	183

8.2	Formulation	186
8.2.1	Expansions within the main pipe	187
8.3	Flow discontinuity region	188
8.3.1	Expansions and formulation	188
8.3.2	Derivation for the case $N = 2$	191
8.3.3	The special case $\bar{h}_1 = \bar{h}_2 = \bar{h}_3 = \bar{h}$	193
8.3.4	Generalisation for N dividing blades	194
8.3.5	The solution for Ψ	196
8.4	Leading edge results	197
8.4.1	The case $N = 1$	197
8.4.2	The case $N = 2$	198
8.4.3	Cases of $N > 2$	199
8.5	Numerical Solution	200
8.5.1	Transformation for each daughter channel	201
8.5.2	Discretisation in the daughters	203
8.5.3	Discretisation in the wake	204
8.5.4	Solution algorithm	205
8.6	Results	206
8.6.1	The case $N = 1$	206
8.6.2	The case $N = 2$	212
8.6.3	A case of large N	217
8.7	Summary	222
9	Conclusions	227
9.1	Summary	227
9.2	Further work	230
	Bibliography	233

List of tables

5.1	Summary of the values used and calculated in the presented figures (to 3 s.f.).	130
6.1	The calculated values of the leading edge pressure jumps, c_+ , the Y -shift and lift L (all to 3 s.f.) for the case of a flat blade with a global angle of attack $\bar{\alpha}$	148
6.2	The calculated values of the leading edge pressure jumps, c_+ , the Y -shift and lift L (all to 3 sf) for the case of an angled flat plate with a global angle of attack $\bar{\alpha}$	152
6.3	The calculated values of the leading edge pressure jumps, c_+ , the Y -shift and lift L for the case of a thick blade with a global angle of attack $\bar{\alpha}$ (all to 3 s.f.).	153
6.4	Separation and reattachment positions x_S^+ and x_R^+ on the upper blade surface and x_S^- and x_R^- on the lower blade surface for the thick blade case.	157
7.1	The calculated values (to 3 sf) of the leading edge pressure jumps, c_+ , the Y -shift and lift for a flat blade with a global angle of attack $\bar{\alpha}$	169
7.2	The calculated values of the leading edge pressure jumps, c_+ , the Y -shift and lift (to 3 s.f.) for an angled blade $f_{\pm}(x_s) = -0.2x_s$ with a global angle of attack $\bar{\alpha}$	178
7.3	The calculated values of the leading edge pressure jumps, c_+ , the Y -shift and lift (to 3 s.f.) for a thick blade with $f_{\max} = 1.4$ with a global angle of attack $\bar{\alpha}$	179
7.4	The calculated values of the leading edge pressure jumps, c_+ , the Y -shift and lift (to 3 s.f.) for a thick blade with $f_{\max} = 1.8$ with a global angle of attack $\bar{\alpha}$	179

8.1	The positive values (to 4 s.f.) of all downstream end positions δ_m and leading edge positions λ_n in the χ -plane for the case $\bar{h}_m = \bar{h}, \forall m$. The negative values of δ_m and λ_n are given by $-\delta_m$ and $-\lambda_n$ in each case.	199
8.2	The blade shape functions f_n applied to the constriction and dilation cases of $N = 9$ blades in figure 8.18.	219

List of figures

2.1	The flow problem under consideration. The total normal distance $y = O(Re^{-1/2})$ and the streamwise distance $x = O(1)$. The coordinate of the first leading edge is taken as $(0, H)$. The blade length l is taken to be an $O(1)$ non-dimensional length.	16
2.2	Streamfunction solution for the leading edge region when $p_0 = 0.3621, u_0 = 0.5252$. The blade lies at $H = 1$. In (a), streamlines are plotted in increments of 0.025. In (b), various streamlines showing the behaviour close to the leading edge of the blade are plotted.	24
2.3	Velocity solutions u (solid line) and v (dotted line) at the leading edge of blade 2 for a wake of length 3.	31
2.4	Viscid-inviscid interaction in the u velocity profiles at small streamwise distances $x = 0.001, 0.005, 0.01, 0.02, 0.03, 0.05, 0.1, 0.2$ beneath the blade leading edge. In (a) flow profiles are taken from beneath the first blade with $H = 1$, (b) from under the second blade with $H = 1$ and (c) from beneath the second blade with $H = 4$	32
2.5	Pressure solutions between the blade and ground for each of the $N = 6$ blades for different values of H	33
2.6	Calculated values of lift, L , friction drag, τ , and p_0 for every blade with values of $H = 32, 16, 8, 4, 2, 1, 1/2, 1/4, 1/8, 1/16$	35
2.7	Calculated u velocity profiles between the blade and the ground. The profiles are taken from the mid-blade positions of each of the $N = 6$ blades.	36

2.8	The pressure solutions $p(x)$ under each blade in the six-blade case for small x . Solutions plotted are for $H = 1/16$ (dotted line) and $H = 1/8$ (solid line).	36
2.9	Streamwise u -velocity profiles taken at the midpoint of each wake ($N = 6$) for various ground clearances H	39
2.10	Streamwise velocity profiles taken from the mid-blade positions beneath each blade. The uppermost profile corresponds to the solution taken from the first blade.	40
2.11	Streamwise velocity profiles at distances $x = 0.5, 1, 1.5$ downstream of the trailing edge in the third, fourth, fifth and sixth wakes. In figures (c) and (d), matching to $u = 1$ in the far-field is not shown for clarity.	43
3.1	The flow configuration close to $N = 3$ thick blades considered in this analysis.	48
3.2	The contours γ_+ and γ_- used with Cauchy's integral formula for (x_0, y_0) lying strictly inside either γ_+ or γ_- with $y_0 \neq 0$	54
3.3	The deformed contours γ_+ and γ_- used for Cauchy's integral formula at the point $(x_0, 0)$	55
3.4	Computed results for the test cases taken from (a) Smith & Timoshin (1996b), (b) Purvis & Smith (2004) and (c) Bhattacharyya & Smith (2004).	63
3.5	Displacement thickness, pressure sums $\langle p \rangle(x)$ and velocity differences $[v](x)$ calculated for the symmetric problem with $N = 5$ flat blades and wakes of length unity. The flat blades lie at x values satisfying $0 \leq x \leq 1, 2 \leq x \leq 3, \dots$	64
3.6	Pressures $p_{\pm}(x)$ and velocities $v_{\pm}(x)$ calculated for the symmetric problem with $N = 5$ flat blades and wakes of length unity.	65
3.7	Computed pressure differences and sums, $[p]$ and $\langle p \rangle$ and velocity differences and sums for $[v]$ and $\langle v \rangle$ with $\bar{\alpha} = 1, N = 5$	66
3.8	Pressures and velocities $p_{\pm}(x)$ and $v_{\pm}(x)$ for $N = 5$ flat blades at a global angle of attack $\bar{\alpha} = 1$	67

3.9	Boundary-layer displacement thicknesses δ_+ , δ_- and computed wake-shapes $s(x)$ for values of small $\bar{\alpha}$ for $N = 5$ flat blades and wakes of length unity.	70
3.10	Corresponding pressures p_+ (solid line) and p_- (dashed line) for the cases in figure 3.9 at $y = 0^\pm$	71
3.11	Boundary-layer displacement thicknesses δ_+ , δ_- and computed wake-shapes $s(x)$ for larger values of $\bar{\alpha}$ for $N = 5$ flat blades and wakes of length unity.	72
3.12	Corresponding pressures p_+ (solid line) and p_- (dashed line) for the cases in figure 3.11 at $y = 0^\pm$	73
3.13	Computed values of the scaled lift, L , friction drag, τ and Y -shifts on each blade, Y_s , for the results presented in figures 3.9 - 3.12.	74
3.14	Displacement thicknesses and pressures for five flat blades of length $l_j = 0.25$, for the cases of (a) $\bar{\alpha} = 0.5$ and (b) $\bar{\alpha} = 2.0$	75
3.15	Displacement thicknesses and pressures with $\bar{\alpha} = 0.5, 2.0$ and blade thicknesses given by $f_+(x) = 2(x - x^2)$, $f_-(x) = x^2 - x$	77
3.16	Displacement thicknesses for five aerofoils with $\bar{\alpha} = 0.5, 2.0$ and blade thicknesses given by $f_+(x) = 4(x - x^2)$, $f_-(x) = 2(x - x^2)$	78
3.17	Displacement thicknesses and wake-shapes with corresponding pressure solutions p_+ and p_- (solid and dashed lines respectively) for 10 flat blades, $\bar{\alpha} = 2.0$	79
4.1	Scaled \bar{u} velocities from the previous chapter suggesting the periodic nature of the viscous sub-layer. Profiles are taken from the mid-blade (top figure) and mid-wake (bottom figure) positions taken from the 10 blade computation performed in figure 3.17, where $\bar{\alpha} = 1$	85
4.2	The proposed structure of the current many-blade limit showing the three regions of flow over one blade-wake period.	86

4.3	Comparisons of (a) $p_+(x_s)$, (b) $p_-(x_s)$ and (c) $s(x_s)$, the wake-shape between the solutions for the many-blade analysis of this chapter (solid line) and the full problem (dashed line) for the sixth blade of a 12 flat blade array. Here, $\bar{\alpha} = 0.1$	96
4.4	As figure 4.3 but $\bar{\alpha} = 1$	97
4.5	As figure 4.3 but $\bar{\alpha} = 4$	98
4.6	Comparisons between the wake-shapes computed using the many-blade limit of this chapter (solid line) and those in wakes 5, 10 and 15 in a 20 blade array using the code from the previous chapter. Here, a flat blade occupies the region $0 \leq x_s \leq 1$ and $\bar{\alpha} = 1$	99
5.1	Boundary-layer structure over one period ($0 \leq x_s \leq L$) past a thick, non-symmetric blade showing the sublayer, bulk-layer and free-stream. Also shown is a small, leading edge region which is discussed in section 5.2.3.	104
5.2	Velocity, pressure and skin friction solutions for the case of $f_{\max} = 0$. In (a), the velocity profiles are taken from positions just before the trailing edge (solid line), mid-wake (broken line) and just after the leading edge (dotted line).	125
5.3	Streamfunction, pressure and skin friction solutions for the case of $f_{\max} = 0.5$	127
5.4	Comparison of the computed streamlines for the case of $f_{\max} = 4.9$ for (a) the FLARE approximation and (b) the upwinding scheme.	128
5.5	Corresponding pressure solutions for $f_{\max} = 4.9$ using the upwinding scheme (solid line) and FLARE approximation (dotted line).	129
5.6	Streamfunction, pressure and skin friction solutions for the case of a flat blade tilted at an angle $\beta = 0.258$. The calculated value of $c_+ = -1.21$. The streamlines and pressure are shown over two L -periods.	131

5.7	Calculated periodic velocity profiles for $\hat{u}(6, Y)$ and $\hat{v}(6, Y)$ on successive sublayer sweeps. The solid and dotted lines are the velocity profiles from the final and penultimate sweeps respectively. Figures (b) and (d) are close-ups of the boxed areas in figures (a) and (c).	132
5.8	Streamfunction, pressure and skin friction solutions for the case of a flat blade tilted at an angle $\beta = 0.299$. Here, the value of $c_+ = -1.84$	134
5.9	Streamfunction, pressure and skin friction solutions for the case of a thick blade ($f_{\max} = 0.8$) at local angle of attack $\beta = 0.575$. Here, the calculated value of $c_+ = -2.97$	135
5.10	Streamfunction, pressure and skin friction solutions for the case of a thick blade ($f_{\max} = 1.4$) at local angle of attack $\beta = 0.386$. Here, the calculated value of $c_+ = -1.50$	136
5.11	Streamfunction, pressure and skin friction solutions for the case of a thick blade ($f_{\max} = 1.6$) at local angle of attack $\beta = 0.4$. Here, the calculated value of $c_+ = -1.81$	137
5.12	Streamfunction and pressure solutions for the case of a flat blade at angle of attack $\beta = 0.4$, with $c_- = c_+ - 0.5$	138
5.13	Streamfunction and pressure solutions for the case of a flat blade at angle of attack $\beta = 0.4$, with $c_- = c_+ - 1$	138
6.1	Succession of blades and wakes (given by the dashes and spaces respectively) all tilted at the global angle of attack $\alpha \ll 1$. . .	140
6.2	Influence of the global angle of attack $\alpha = Re^{-1}\bar{\alpha}$ on the vertical position of the blade within the sublayer on entering the interactive multi-blade limit.	142
6.3	Streamline plots with the global angle of attack $\bar{\alpha}$ for the case of a flat blade.	145
6.4	Pressure solutions for the case of a flat blade with the global angles of attack in figure 6.3.	146
6.5	Skin frictions τ_{\pm} for the case of a flat blade with the global angles of attack in figure 6.3.	147

6.6	Streamline plots with the global angle of attack $\bar{\alpha}$ for the case of an angled blade given by $f_{\pm}(x_s) = -0.2x_s$	149
6.7	Pressure solutions for the case of the angled blade and global angles of attack in figure 6.6.	150
6.8	Skin friction solutions for the case of the angled blade and global angles of attack in figure 6.6.	151
6.9	Streamline plots with the global angle of attack $\bar{\alpha}$ for the case of thick blade with $f_{\pm}(x_s) = \pm 1.7\sin^2(\pi x_s)$	154
6.10	Pressure solutions for the thick blade and the global angles of attack $\bar{\alpha}$ in figure 6.9.	155
6.11	Skin friction solutions for the thick blade and the global angles of attack $\bar{\alpha}$ in figure 6.9.	156
7.1	Illustration of the development of the interactive many-blade limit structure with a global angle of attack $\alpha = O(Re^{-4/5})$	161
7.2	The new contour Γ^* used to solve the free-stream problem for a point (x_0, y_0) with $y_0 \neq \bar{\alpha}$	163
7.3	The contour Γ^* used to solve the free-stream problem for the point $(x_0, \bar{\alpha})$, with the inclusion of two other small semi-circles of radius ϵ	164
7.4	Illustration of the development of the interactive many-blade limit structure with a global angle of attack $\alpha = O(Re^{-3/5})$	165
7.5	Illustration of the flow geometry within the sublayer for $\alpha = Re^{-2/5}\bar{\alpha}$	166
7.6	Streamline plots for a flat blade with the global angles of attack $\bar{\alpha} = -0.1, -0.25, -0.5$	170
7.7	Corresponding pressure solutions for flow past a flat blade with the global angles of attack in figure 7.6.	171
7.8	Calculated skin friction for flow past a flat blade with the global angles of attack in figure 7.6.	171
7.9	Streamline plots for an angled blade $f_{\pm}(x_s) = -0.2x_s$ with the global angles of attack $\bar{\alpha} = -0.1, -0.25, -0.5$	172
7.10	Corresponding pressure solutions for flow past an angled blade $f_{\pm}(x_s) = -0.2x_s$ with the global angles of attack in figure 7.9.	173

7.11	Calculated skin friction for flow past an angled blade $f_{\pm}(x_s) = -0.2x_s$ with the global angles of attack in figure 7.9.	173
7.12	Streamline plots for a thick blade with parameter $f_{\max} = 1.4$ and the global angles of attack $\bar{\alpha} = 0, -0.1, -0.25, -0.5$	174
7.13	Corresponding pressures for the solutions in figure 7.12.	175
7.14	Calculated skin friction for the solutions presented in figure 7.12.	175
7.15	Streamline plots for a thick blade with parameter $f_{\max} = 1.8$ and the global angles of attack $\bar{\alpha} = 0, -0.1, -0.25, -0.5$	176
7.16	Corresponding pressures for the solutions in figure 7.15.	177
7.17	Calculated skin friction for the solutions presented in figure 7.15.	177
8.1	Problem illustration with $N = 5$ dividing blades in a non-symmetric configuration. The daughter channels from one to six are labelled. The coordinate of the n^{th} leading edge is taken as $(0, h_n)$	186
8.2	Illustration of $N = 4$ dividing blades in the discontinuity region. The flow speed jumps to u_m^c in the m^{th} channel and will be different in general for each.	189
8.3	Conformal mapping of the χ -plane onto the Z -plane with $N = 2$. The labels A-F are the vertices of the polygon in the Z -plane with corresponding points A'-F' in the χ -plane. The positions λ_1, λ_2 and δ are the two leading edge points and one other downstream end points respectively, whose position in the χ -plane is unknown. The points B'-F' satisfy $-1 < \lambda_1 < \delta < \lambda_2 < 1$	191
8.4	Two leading edge region solutions found for the case $N = 1$. In (a) we choose $\psi_1 = 1.1$ and (b) $\psi_1 = 2$	197
8.5	Leading edge region solutions found for the case $N = 2$. The chosen values of (ψ_1, ψ_2) are in (a) $(0.5, 2.2)$, (b) $(0.3, 0.6)$, (c) $(1, 4)$ and (d) $(8.1, 1)$	198

8.6	Leading edge region solutions found for cases of $N > 2$. In each case, the daughter channel widths are taken as $\bar{h}_j = 1$ and $H = N + 1$. The chosen values of (ψ_1, \dots, ψ_N) are, in (a) (0.5, 1, 3), (b) (1, 3.5, 4, 4.5, 5), (c) (1, 1.5, 2, 5, 6, 6.5, 7) and (d) (1, 1.2, 1.4, 1.6, 6.6, 7.4, 7.9, 8, 9).	200
8.7	Illustration of mapping a regularly spaced grid from (a) the computational space to (b) the actual daughter channel geometry. Here, $g(x) = f(x) = 0$ except for $ x \leq 1$, where $g(x) = 6 - 2.8(1 - x^2)^2$ and $f(x) = 0.8(1 - x^2)^2$	202
8.8	Streamfunction solutions for two symmetric configurations. The total channel width $H = 4$	207
8.9	Corresponding pressure solutions for the streamfunction solutions plotted in (a) figure 8.8(a) and (b) figure 8.8(b). In each figure, the value of p^* , the pressure at the trailing edge is given to four significant figures.	208
8.10	Leading edge and full problem streamfunction solutions for two non-symmetric configurations. The total channel width $H = 4$	210
8.11	Leading edge and full problem streamfunction solutions for two cases of asymmetric blades. The total channel width $H = 4$	211
8.12	Corresponding pressure solutions for the streamfunction solutions plotted in (a) figure 8.10(a), (b) figure 8.10(b), (c) figure 8.11(a) and (d) figure 8.11(b). In each figure, the value of p^* is given to four significant figures.	212
8.13	Streamfunction solutions for three symmetric configurations of $N = 2$ blades. The total channel width $H = 6$. Streamlines are plotted in increments of 0.2.	214
8.14	Corresponding pressure solutions for the streamfunction solutions plotted in (a) figure 8.13(a), (b) figure 8.13(b) and (c) figure 8.13(c). In each figure, the value of p^* is given to four significant figures.	215

8.15	Streamfunction solutions for three other configurations of $N = 2$ blades. The total channel width is chosen as $H = 6$. Streamlines are plotted in equal increments of 0.2	216
8.16	Calculated leading edge streamfunctions for the solutions in (a) figure 8.15(a), (b) figure 8.15(b) and (c) figure 8.15(c). . .	217
8.17	Corresponding pressure solutions for the streamfunction solutions plotted in (a) figure 8.15(a), (b) figure 8.15(b) and (c) figure 8.15(c).	218
8.18	Streamfunction solutions for four configurations of $N = 9$ blades. The total channel width is chosen as $H = 20$, so that the entrance width to each daughter is 2. Streamlines are plotted in increments of 0.5.	220
8.19	The pressure corresponding to the streamfunctions plotted in figures 8.18(a)-(d). The pressures in (d) are, in descending order of $p(0), p_3, p_6, p_{10}, p_7, p_4$ and p_5, p_1, p_9, p_8, p_2	221
8.20	Wake velocity profiles in u of the flat configuration of blades in 8.18a.	222
8.21	Wake velocity profiles in u of the non-symmetric configuration of blades in 8.18d.	223
8.22	Wake velocity profiles with $H = 80$. Figures (a) and (b) are velocity profiles for the flat blade case, figures (c) and (d) for the non-symmetric configuration. The entrance widths to daughters two and nine in each of the above figures are fixed as two.	224
8.23	Two examples of the u velocities away at large x for the case of flat blades (solid line) and the non-symmetric configuration (dotted line).	224

Chapter 1

Introduction

1.1 Physical background

The responses of fluid flow past many blades are seen extensively throughout the industrial world. In particular, high-speed flows are seen in various rotorcraft, such as helicopter rotor blades, propellers and turbines. Helicopters have many important roles, for example in reaching off-shore oil rigs, air ambulances and news reporting, as well as military applications, such as air-attack, troop deployment and other supply logistics. In such applications, the helicopter's abilities to perform vertical take-off or landing (VTOL) and hover for long periods of time are exploited. These abilities rely on the continually spinning nature of the helicopter rotor, to provide lift and overcome gravity. Furthermore, each rotor blade passes through the air-flow induced by the blade ahead and generates a new flow for the blade behind to enter. Such flow regimes may be understood by examining the flow around the rotor blade system in each case. If the rotor-flow can be understood, then there are design considerations for the helicopter, for example to improve its efficiency in the generation of thrust in forward flight and VTOL.

Related to the helicopter rotor blade is the propeller, used in shipping and on some aircraft. In this instance, the rotation of the propeller is used to generate forward movement rather than to directly overcome gravity. The importance of understanding high-speed flow induced by the propeller of an aircraft is paramount for safety. For example, the infamous V22 Osprey tilt-rotor aircraft, capable of performing VTOL, has been involved in several

fatal accidents. One such accident occurred in 2004, killing 19 US Marines on board. The report by Gross *et al.* (2004) finds that the accident was caused by the aircraft entering a vortex ring state, causing the engines to stall in landing. The vortex ring state can occur when the aircraft starts to descend vertically, causing the propeller blades to exit a slip-streaming state, form large recirculations of the flow and induce high turbulence (Johnson (1994)). By gaining insight into the flow in this regime, a recovery technique may be developed or design alterations may be found allowing vertical descent to be carried out safely. Further safety considerations for aircraft are the arrival and take-off spacings of aircraft at busy airports. Here, understanding the dispersion of wing-tip vortices and avoiding turbulent wakes is vital to maintain the aerodynamics of each departing or arriving aircraft (see Dougherty *et al.* (2004) and Gerz *et al.* (2005)). One technological advancement to regularise the effects of wing-tip vortices on large aircraft has been the introduction of winglets upon the wing-tips. These winglets can generate vortices that can be useful to the aircraft (Jupp & Rees (1987)) and offer a reduction of 1 – 2% in drag caused by the wing-tips (Kroo (2005)).

Fluid flow in and around aircraft jet engines is also of much importance, not least to reduce annoyance caused by noise levels in take-off and landing. Noise levels around airports are governed internationally by the International Civil Aviation Organisation through noise level certification and in the UK, noise quotas are applied to many airports at night (Girvin (2009)). Polacsek *et al.* (2009) give a discussion into the generation of noise within a jet engine and state that the rotor-stator interaction mechanisms are one of the major contributions of noise from aircraft. Hence, by understanding the nature of the flow past the turbines in the jet engine, future improvements may be found in reducing noise levels by suggesting where to place noise dampening surfaces. Furthermore, improvements in efficiency may be found, such as a reduction in fuel consumption. Papers by, for example, Ovenden (2005) and Richards *et al.* (2007) both stress the difficulty in calculating the sound propagation within jet engines due to the little understood and complicated nature of the fluid flow.

There are many other interesting applications, for example the flow around

wind turbines, in domestic fans, food mixers and blenders, hover lawn-mowers and Formula One cars. In the last application, the design of certain aerodynamic features on the car, such as the front spoiler and undertray, are required to interact with the ground to produce as much downforce as possible and to affect the performance of an approaching car behind through slipstreaming effects. Understanding the flow induced in such configurations may lead to race benefits resulting from the design of these aerodynamic surfaces.

The high-speed flows induced by the rotor or propeller alone in such applications are very complex and thus difficult to measure experimentally or describe theoretically. Even with a single blade in the rotor, to describe the full flow characteristics poses a serious challenge. With the rotor located on an arbitrary body, such as a helicopter or a turbo-propellered aircraft, the added interactions between the rotors and the mainframe or wings represent a serious challenge. Further, to consider interactions with the ground or other nearby objects adds considerable difficulty to an already complicated problem. An account of the isolated rotor is given by Johnson (1994). The rotor was first modelled as an actuator disc in applications to marine propellers by Rankine in 1865 and Froude in 1885. Momentum theory was developed by considering the actuator disc acting upon the air around it, forcing a column of air through the actuator and causing a thrust. By using Newton's laws of motion, an explicit formula was derived for the thrust by considering the mature wake motion away from the disc. The calculated thrust relied upon a conservation of energy argument, due to a velocity increment in the wake. Although this classical momentum theory provides an approximation for the lift provided by one rotor, it does not give explicit details on the flow behaviour around the blades to include interactions between the blades and of vortex shedding, which are important for the design of, for example, helicopter rotors.

More recent attempts to understand basic helicopter aerodynamics are given by Bramwell (1976) and Seddon *et al.* (2001), among a very large array of literature. Bramwell (1976) discusses a varied selection of topics, from the aerodynamics of a helicopter in vertical ascent and forward flight, to

structural and elastic interactions of the blades. Seddon *et al.* (2001) includes discussion on theoretical approaches and focuses more on the control and stability of the helicopter. Efforts to introduce physical concepts and apply mathematical analysis to the propeller setting are given by Bertram (2000) and Hafez & Kwak (2003) in both ship and aircraft contexts. Also of interest is Conlisk (1997), who gives a review into the development and recent trends in both computational and experimental techniques.

Experimental studies have been conducted by, for example, Washizu *et al.* (1966), Caradonna & Tung (1981), Yu (1995), Yu (2000) and Hoffmann *et al.* (2007) for various flight regimes to investigate flow interactions with the main airframe and the ground and noise propagation. The major drawback with experiments is that they are often very expensive to carry out and the data produced can be very difficult to interpret, with the main physical mechanisms involved not being captured particularly clearly. Inevitably, we turn to fluid dynamics to try to gain insight into the flow mechanisms present in such multi-blade flows.

Generally, two main approaches are adopted in tackling such multi-blade problems, the first being an inviscid, potential flow approach. Potential flow calculations, particularly for the helicopter rotor have been carried out by, for example, Caradonna & Isom (1972), Isom (1974), Chaffin & Berry (1990), Strawn (1996) and Brown *et al.* (2002). Isom (1974) considers the role of time dependent flows past a helicopter rotor with transonic blade-tip speeds and Strawn (1996) give calculations into acoustic effects and noise generation from the rotors. However, the major drawback with inviscid flow computations is the neglect of viscosity and the non-application of the no-slip boundary condition. Viscous effects are often estimated in inviscid calculations, whether by approximations or given directly by empirically measured data. The inviscid calculations are therefore not so useful in predicting viscous interactions between the blades.

The second approach is by direct numerical simulation, by numerically solving the Navier-Stokes equations with high Reynolds number. The Reynolds

number is given by the ratio of inertial and viscous forces. Due to the inclusion of viscosity, the no-slip condition may be applied and viscous separation and vortices can occur. Ingham *et al.* (1990) calculate solutions to the Navier-Stokes equations through a row of normally aligned flat blades using finite-difference techniques, whilst Natarajan *et al.* (1993) consider the flow past a row of flat plates using Galerkin finite element methods. Some other examples of direct numerical simulation in various multi-blade contexts are given by Kapadia & Roy (2003), Bhattacharyya & Smith (2004) and Rodi (2006). A downside to using direct numerical simulation is that the codes are often computationally very expensive, especially when compared to inviscid calculations. Furthermore, for increasing Reynolds number the results produced can be less accurate. This is particularly true in vortex and eddy generation; inaccuracies arise due to poorer convergence in the numerical solution and the need for very fine or adaptive discretisation close to the blade surfaces.

The inclusion of other influences into inviscid and direct numerical simulation calculations, such as the mainframe of an aircraft, a wing or ground effect adds considerable difficulty in accurately capturing the flow dynamics. McCroskey (1995) give an overview of the methods used and the complications induced by an aircraft and the ground for both experimental and numerical techniques. For example, the main-frame and tail-rotor of a helicopter cause the rotor wake to roll up into a horseshoe vortex in the proximity of the ground. Another interaction occurs between the mainframe and propeller wake of the V22 Osprey (mentioned earlier), where the wake can be forced back into the propeller by the mainframe when in vertical descent. McCroskey (1995) states that this induces extra noise and a 10% decrease in the thrust produced by the propellers.

Typically, the Reynolds number is large in the physical applications discussed and as yet, relatively little investigation in comparison to experiments and computations has been undertaken in boundary-layer theory past many rotor- or propeller-blades. In purely inviscid models, no boundary-layer exists due to the neglect of viscosity. In direct numerical simulations, the

boundary-layer may not be captured accurately without very fine grid refinement, adding to computing time. Rosenhead (1963) gives a derivation of the boundary-layer problem in the context of three-dimensional rotor blades. In the derivation, the rotor blades are symmetric and a sketch solution is given for the radial and tangential flow components in the boundary-layer on a flat plate. Smith & Timoshin (1996a) consider symmetric, three-dimensional rotary boundary-layer flow. There, the authors give computational solutions for a variety of blade numbers and blade and wake lengths for a cut disc. At large radial distances (that is, away from the centre of rotation) it is shown that an axisymmetric terminal form of the velocity exists, even in the presence of many blades and wakes. Further, a many-blade limit was sought, where the boundary-layer takes on a double viscous structure. Symmetric three-dimensional solutions are found for infinite and finite blade spans and a discussion of the flow beyond the blade-tips in the latter case is given. The blade-tip vortices are captured in the calculations and the behaviour shown agrees well with that observed in experiment.

Smith & Timoshin (1996b) consider the two-dimensional problem resulting from the large radii analysis of Smith & Timoshin (1996a), and includes non-symmetric blade shapes. In this instance, viscous-inviscid interaction occurs between the inner (viscous) boundary-layer and the outer (inviscid) free-stream. The new interaction is seen in the model through a coupling of the boundary-layer and the free-stream, requiring simultaneous solution. The coupling arises due to unknown pressure differences across all the blade surfaces and unknown wake-shapes. Boundary-layer solutions are presented for various symmetric and non-symmetric blade configurations before a many-blade limit is sought. A similar double viscous structure arises, whereby the boundary-layer is composed of a slowly growing bulk-layer and a periodic inner sublayer over one blade and wake. This many-blade limit holds for both the symmetric and non-symmetric blade configurations described and appears in the numerical calculations after only four or five blades are passed.

Pressure interactive flow past many blades is considered by Bowles & Smith (2000a), where a pressure gradient appears at leading order within the boundary-layer, unlike in Smith & Timoshin (1996b). The interactive

flow considered arises in the many-blade limit of Smith & Timoshin (1996b) after sufficiently many blades downstream. They found that a pressure-displacement law covers the entire blade-wake period, a novel result since interactive flows, such as the triple-deck problem at the trailing edge of a flat blade (see Stewartson (1969) and Messiter (1970)), are usually local in nature. Interactive sublayer solutions are given through streamwise velocity, pressure and skin friction for various blade thicknesses and lengths. Analytical descriptions of an interesting short-blade limit, where the length of the blade is much less than that of the wake, is given in relation to helicopter aerodynamics. Bowles & Smith (2000b) consider the influence of non-symmetry in the interactive flow problem. In this instance, a flow discontinuity arises at the leading edge of the blade in order to satisfy the equi-pressure condition at the trailing edge. It is found that the nature of the discontinuity is a pressure jump. The short-blade limit of Bowles & Smith (2000a) is then extended to include non-symmetry of the blade with several analytical results derived, such as an expression for the pressure change from the blade leading edge to the near wake and an approximate equation for lift.

Jones & Smith (2003) consider viscous interactions in ground effect for the case of one blade. In this instance, the flow structure is such that an interactive boundary-layer problem governs the flow beneath the blade. A leading edge region, similar to that in Bowles & Smith (2000b) is encountered. If the ground clearance is small and the blade is cambered enough, numerical solutions show that flow reversal can occur beneath the blade. An asymptotic analysis into the extreme case of small ground clearance is undertaken and a discussion of three-dimensional effects is given. Interactions between an array of multiple blades in ground effect are considered by Purvis & Smith (2004). A coupled viscous-inviscid model is derived with the inclusion of ground effect. Results are given for various blade geometries and ground clearances, with the ground effect seen in the results by comparing the wake-shapes and pressures as the ground clearance becomes small. The cases of very large or very small ground clearances are studied analytically, with the results gained agreeing well with the numerical computations. A many-blade limit is then sought, with the double viscous structure described above. It

is shown that the sublayer becomes periodic after passing many blades and comparisons between wake-shapes obtained from the full, coupled model are compared to the many-blade limit, showing good agreement.

The boundary-layer flow that emerges from a vertically aligned cascade of blades is considered by Smith (2002). For the case of external wakes, where the flow is free to interact with the free-stream, the periodic nature of the flow emerging from between the blades quickly disappears after a short downstream distance and approaches a uniform state. The case of internal wakes, where the blades are contained within a larger channel, is governed by lateral periodicity with a non-zero pressure gradient. In both cases, the flow is investigated just downstream of the aligned trailing edges. For the case of internal wakes, the uniform flow state approached downstream and the pressure rise can be calculated analytically. Wake starting flows that are non-symmetric (but still laterally periodic) are then considered analytically and numerically to demonstrate the turning of the wake and the differences in the development of the velocities downstream.

1.2 Thesis outline

The aim of this thesis is to investigate the flow past many blades by examining different viscous-inviscid interactions as described in the papers above. In this thesis, the flows considered are taken to be steady, laminar and two-dimensional in nature. The flow velocity is non-dimensionalised with respect to U_∞ , taken as the velocity of the free-stream and the streamwise and normal coordinates with respect to L , a typical blade length. The pressure is non-dimensionalised with respect to ρU_∞^2 . The governing equations are thus given by the non-dimensionalised, incompressible fluid form of the Navier-Stokes equations

$$U \frac{\partial U}{\partial x} + V \frac{\partial U}{\partial y} = -\frac{\partial P}{\partial x} + \frac{1}{Re} \left(\frac{\partial^2 U}{\partial x^2} + \frac{\partial^2 U}{\partial y^2} \right), \quad (1.1)$$

$$U \frac{\partial V}{\partial x} + V \frac{\partial V}{\partial y} = -\frac{\partial P}{\partial y} + \frac{1}{Re} \left(\frac{\partial^2 V}{\partial x^2} + \frac{\partial^2 V}{\partial y^2} \right), \quad (1.2)$$

$$\frac{\partial U}{\partial x} + \frac{\partial V}{\partial y} = 0, \quad (1.3)$$

where the non-dimensional streamwise and normal velocities are given by $U = U(x, y)$ and $V = V(x, y)$ respectively, with the pressure $P = P(x, y)$. The non-dimensional streamwise and normal coordinates are given by x and y respectively. The dimensionless parameter Re in the governing equations (1.1) - (1.3) is the Reynolds number, given by

$$Re = \frac{U_\infty L}{\nu}, \quad (1.4)$$

where ν is the constant kinematic viscosity. We will address high Reynolds number flows past many blades with ground effect, a global angle of attack and past an internal array of vertically aligned blades.

In Chapter 2, we begin by considering fluid flow past many blades within a very small distance of the ground. Jones & Smith (2003) considered this problem for one blade in two-dimensions, but not past many blades, whilst Purvis & Smith (2004) considered flow past many blades but at ground clearances much larger than Jones & Smith (2003). A natural extension to these papers is to consider flow interactions past many blades within a very small ground clearance, whilst still being applicable to the physical applications. The model derived is a boundary-layer one, with the pressure being unknown beneath all the blades and a pressure jump at the leading edge of each blade. Numerical results are given for flat blades at various ground clearances before an analysis of the very large and very small cases of ground clearance is given. When the ground clearance becomes very large, we show that the asymptotic limit of our analysis is the ground effect case of Purvis & Smith (2004). For very small clearances, we show that the flow beneath each blade can be modelled by a small viscous region just after the leading edge before the flow is dominated by Couette flow for the remainder of the blade.

Chapter 3 investigates the high Reynolds number flow past an array of blades with a global angle of attack. Smith & Timoshin (1996b) investigates the flow past many blades and this chapter extends the analysis to include a global angle of attack. The global angle of attack is taken to be large enough such that a leading order change occurs within the boundary-layer problem. This flow regime is a new non-symmetry not yet investigated in the context

of flows past many blades. The model is a coupled viscous-inviscid one, with the boundary-layer and free-stream problems requiring simultaneous solution. Solutions are given for flat blades with various global angles of attack and some numerical calculations are conducted for short and thick blades, all revealing similar results. A ten-blade calculation with a global angle of attack is studied and we argue that this case suggests a many-blade limit holds where the boundary-layer can be modelled by a double viscous structure.

In Chapter 4, we derive the many-blade limit with a global angle of attack. The double viscous structure for the boundary-layer structure is adopted, with the inclusion of a global angle of attack of the same size as in Chapter 3. The double viscous structure for the boundary-layer is shown to contain a periodic sublayer and a slowly growing bulk-layer. Numerical results are calculated and compared to solutions gained using the method in Chapter 3, showing good overall agreement. We show that for a larger global angle of attack, the many-blade limit is approached in our calculations after passing more blades than that reported in Smith & Timoshin (1996b) and Purvis & Smith (2004).

Interactive boundary-layer flow is considered in Chapters 5, 6 and 7. In Chapter 5, we outline the complete flow structure as in Bowles & Smith (2000a,b) and develop a new numerical technique to solve the sublayer problem. The numerical technique is based upon Newton linearisation of the interactive boundary-layer equations and the necessary adjustments to the procedure in the advent of flow reversal are discussed. Chapter 5 finds some new solutions to the non-symmetric problem of Bowles & Smith (2000b), using a different method to force periodicity. In Chapter 6, we add the global angle of attack into the interactive boundary-layer structure, by finding a global angle of attack that first causes a leading order change to the sublayer problem. This change is incorporated into the structure through a boundary condition, the numerical code is adapted to include the new boundary condition and solutions are given for different blade geometries and global angles of attack. In Chapter 7, we find larger angles of attack that cause

a leading order change to the interactive many-blade limit within the bulk-layer and the free-stream. A further global angle of attack is found that is large enough to cause a tilt of the sublayer structure. The new interactions in the tilted sublayer case are found numerically and we present solutions for various blade geometries.

In the final chapter, we consider boundary-layer flow past a vertically aligned array of blades within a bounding channel. Smith (2002) considers the wake flow of such an array of blades but not the flow leading up to and within the array of blades and those of Smith & Jones (2000), Smith *et al.* (2003) and Smith & Jones (2003), who consider the flow response upon passing the leading edges of the blades. This chapter takes a different standpoint, by modelling the whole flow upstream of and between each set of blades and in the wake. The boundary layer equations are shown to hold everywhere in our problem, with a discontinuity at the leading edge arising due to the Kutta condition. An analytical solution for the leading order leading edge flow is given and depends on the downstream fluxes within the channels formed by the blades. Results for the leading edge problem are presented for various prescribed fluxes. Solutions to the full boundary-layer problem are given for differing numbers of blades and blade shapes and a numerical investigation is undertaken where the upper and lowermost channels become very large.

Chapter 2

Flow past many blades in extreme ground effect

We begin by analysing high Reynolds number flow past an array of flat blades in extreme ground effect. Our motivation for this problem stems from the design of Formula One cars, specifically the front spoiler or diffuser. The purpose of the front spoiler is to create as much downforce as possible, keeping the car firmly rooted to the track and enabling high-speed cornering. Furthermore, an efficient car will experience as little drag as possible, improving fuel consumption. Within our problem, we are interested in the lift and drag generated on the spoilers present downstream. There are other applications too, for example in hover lawn-mowers and food blenders, where the continual spinning of the rotor blade occurs near a stationary, flat surface.

Previous work by Jones & Smith (2003) considers a one blade problem in extreme ground effect. The ground clearance is taken to be very small, in non-dimensional coordinates of distance $O(Re^{-1/2})$ and the term *extreme ground effect* is defined by taking a ground clearance of this size. Here, we have adopted the non-dimensional coordinates in section 1.2 and from now on in this chapter, and every subsequent one, our analysis will assume those non-dimensional variables. The boundary-layer created on the blade interacts directly with the ground, since the boundary-layer growth is of the same size as the ground clearance. Between the blade and the ground, the problem is governed by the pressure interactive boundary-layer equations. The same equations hold elsewhere, but due to matching with the free-stream, the

pressure is constant. Due to the Kutta trailing edge condition, which forces the pressure to be continuous at the trailing edge, a flow discontinuity occurs at the leading edge which allows the Kutta condition to be satisfied. Analysis within the leading edge region shows that a velocity and pressure jump occurs in the region, causing a rapid deflection of the streamlines at the leading edge. The full viscous problem relies on this region to determine a starting condition for the flow just after the leading edge. Numerical solutions for varying blade shapes are then found to include boundary-layer separation through flow reversal between the blade and the ground and calculations of lift and drag. Extremal cases of very large or small ground clearance are investigated analytically, using asymptotic methods. For very small ground clearances, there are two streamwise scales of importance, one small scale just after the leading edge where the full boundary-layer equations hold and the other, a larger scale spanning the remainder of the blade governed by a lubrication approximation. For large ground clearances, an inner-outer interaction prevails between the viscous boundary-layer and inviscid free-stream beneath the blade.

Purvis & Smith (2004) investigate the fluid flow past many blades with ground effect. The ground clearance is taken to be of $O(1)$, much larger than the extreme ground effect analysis of Jones & Smith (2003) discussed above. Since the ground clearance is now much larger than the boundary-layer growth, the boundary-layer does not directly interact with the ground in the same way as Jones & Smith (2003). The model presented has an inviscid flow everywhere except close to the blade surfaces where a viscous boundary-layer is located. Global inner-outer interaction occurs whereby the boundary-layer and free-stream are coupled and must be solved simultaneously. This viscous-inviscid coupling is seen in the model through unknown wake centreline shapes and pressure differences in the viscous and inviscid problems respectively. Computational results of the coupled problem are given for various symmetric and non-symmetric blade configurations and numbers of blades. A main result is that blades positioned downstream experience less drag, whilst creating less lift, known as a slip-streaming effect. Cases of large and small ground clearances were analysed analytically. For

large ground clearances, all interaction with the ground is lost at leading order, with the problem given by that of Smith & Timoshin (1996b). As the ground clearance decreases (but still of $O(1)$), the pressure between the blade and ground increases so that the solution, at least for one blade, agrees with that presented by Jones & Smith (2003) for large ground clearances. There is also a many-blade limit, where periodicity is found in the boundary-layer.

In this chapter, we take the multiple blade stance adopted by Purvis & Smith (2004) and allow the non-dimensionalised ground clearance to become $O(Re^{-1/2})$, that of Jones & Smith (2003). The latter authors pointed out that this would be an interesting extension to their work. We consider an array of N flat blades positioned in an otherwise undisturbed uniform flow, with the governing equations given by the Navier-Stokes relations (1.1) - (1.3). The array of N blades lie within a non-dimensional ground clearance of $O(Re^{-1/2})$ in this chapter. Our aim is to describe the flow in this regime, past all N blades and within each wake. It is interesting to see how the inner-outer interaction of Purvis & Smith (2004) carries into this new regime.

2.1 Formulation

The streamwise extent of the problem is taken to be $x = O(1)$. Since all blades lie within an $O(Re^{-1/2})$ distance of the ground, we define the normal coordinate in the problem to be given by $Y = O(1)$, where $y = Re^{-1/2}Y$. All the flat blades lie at $Y = H$, so that the correct scaling for the ground clearance is achieved. The leading edge of the first blade is taken to lie at a position $(0, H)$ within a moving frame of reference and each blade to be of length $l = O(1)$. The oncoming uniform flow is taken to be $U = 1$, $V = 0$, $P = 0$.

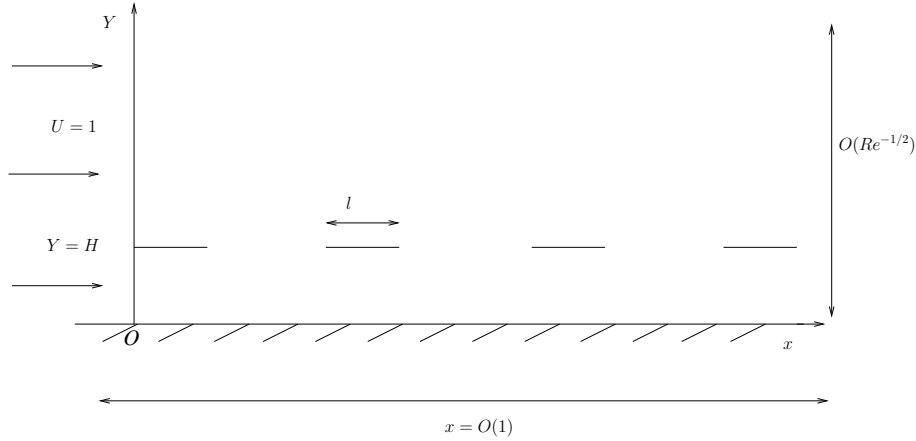


Figure 2.1: The flow problem under consideration. The total normal distance $y = O(Re^{-1/2})$ and the streamwise distance $x = O(1)$. The coordinate of the first leading edge is taken as $(0, H)$. The blade length l is taken to be an $O(1)$ non-dimensional length.

2.1.1 Velocity expansions

The flow velocity components and the pressure are expanded as

$$U = u(x, Y) + \dots, \quad (2.1)$$

$$V = Re^{-1/2}v(x, Y) + \dots, \quad (2.2)$$

$$P = p(x, Y) + \dots, \quad (2.3)$$

in the problem, with any further terms (of lower order) tending to zero in the limit $Re \rightarrow \infty$. We have that $U = O(1)$ due to the uniform oncoming flow and hence by the continuity equation, $V = O(Re^{-1/2})$. The pressure, P , is $O(1)$ in our expansions. We substitute these expansions into the governing Navier-Stokes equations, to reveal the leading order problem

$$u \frac{\partial u}{\partial x} + v \frac{\partial u}{\partial Y} = -\frac{\partial p}{\partial x} + \frac{\partial^2 u}{\partial Y^2}, \quad (2.4)$$

$$0 = -\frac{\partial p}{\partial y}, \quad (2.5)$$

$$\frac{\partial u}{\partial x} + \frac{\partial v}{\partial y} = 0. \quad (2.6)$$

We see immediately from (2.5) that $p(x, Y) = p(x)$, meaning that the leading order problem for u, v and p is governed by the boundary layer equations

$$u \frac{\partial u}{\partial x} + v \frac{\partial u}{\partial Y} = -\frac{dp}{dx} + \frac{\partial^2 u}{\partial Y^2}, \quad (2.7)$$

$$\frac{\partial u}{\partial x} + \frac{\partial v}{\partial y} = 0, \quad (2.8)$$

subject to the boundary conditions

$$u = v = 0 \quad \text{on } Y = H \text{ on the blades,} \quad (2.9)$$

$$u = 1, v = 0 \quad \text{on } Y = 0, \forall x, \quad (2.10)$$

$$u \rightarrow 1 \quad \text{as } Y \rightarrow \infty. \quad (2.11)$$

Here, condition (2.9) represents the no-slip and no-normal flow conditions on the blades and (2.10) the no-slip and no-normal flow conditions at the ground. The latter condition is needed since within our moving frame of reference, the blades appear stationary with the ground moving beneath. The final condition is to match with the free-stream. Upstream of the array of blades, the solution is given by the uniform flow $u = 1, v = 0, p = 0$. Consider the flow in the far-field as $Y \rightarrow \infty$ over each blade and wake. We have that $u \rightarrow 1$ and so by substitution into (2.7), we deduce that

$$-\frac{dp}{dx} \rightarrow 0. \quad (2.12)$$

Hence over each blade and wake, the pressure $p = \text{constant}$. If the constant free-stream pressure is zero, then to match as $Y \rightarrow \infty$, we must take $p(x) = 0$ to leading order in the wakes and above the blades.

However, we cannot apply this argument between the blade and the ground, due to the boundary conditions imposed on the blades. Here, the pressure remains an $O(1)$ unknown. The pressure beneath the blade must satisfy the Kutta condition, requiring pressure continuity at the trailing edge. Hence, just above and below each trailing edge, the pressures must match. Since $p = 0$ above the trailing edge and beneath the blade we have that $p = p(x)$, we have that

$$p = 0, \quad \text{at every trailing edge.} \quad (2.13)$$

Between any particular blade and the ground, the pressure gradient there relies on the geometry created by that blade and the ground. Given the flat blades considered here and with the expectation of forward flow, the pressure gradient is favourable. Thus the pressure is expected to fall between the blade and the ground from the leading edge to the trailing edge. So in general, the Kutta condition at the trailing edge is not satisfied. To ensure this condition

is satisfied, there must be a jump in the velocity and pressure somewhere in the flow. A jump in velocity and pressure may occur at the leading and trailing edges due to the changes in boundary conditions at $Y = H$. Since the Kutta condition forces continuity in the pressure and velocities at the trailing edge, the only place where this jump may occur is at the leading edge. Thus, as the flow passes the leading edge, the pressure must jump from its upstream value of zero to a new value between the blade and the ground downstream, accompanied by adjustments in the velocity. Above the blade, no jump in pressure occurs since $p = 0$ there, although there is an adjustment in velocity. The magnitude of the pressure jump beneath the blade is chosen by the flow so that the prescribed starting condition means that the Kutta condition is satisfied. In the current problem where $p = 0$ at every trailing edge, a leading edge region must occur at the onset of every blade.

2.2 Discontinuity region

To determine the nature of the jumps across each leading edge discontinuity, we seek a formulation valid for each leading edge region. The oncoming flow in U is $O(1)$ and the normal coordinate is $y = O(Re^{-1/2})$. The pressure $P = O(1)$ to match with the pressure between the blade and the ground in the main flow problem above. To determine the streamwise extent in x of the region, we consider the limit $x - x_{le} \rightarrow 0$ of the Navier-Stokes equations, with the above scales. Here, x_{le} represents the leading edge of a particular blade. We find that inertial forces balance with the pressure gradient in the normal momentum equation when $x - x_{le} = O(Re^{-1/2})$. Thus from the continuity equation, we have $V = O(1)$ in the leading edge regions. We define $X = O(1)$ to be the streamwise variable here, where $x - x_{le} = Re^{-1/2}X$, and expand the velocities and pressure as

$$U = \bar{u}(X, Y) + \dots, \quad (2.14)$$

$$V = \bar{v}(X, Y) + \dots, \quad (2.15)$$

$$P = \bar{p}(X, Y) + \dots. \quad (2.16)$$

Substitution into the Navier-Stokes equations yields the inviscid Euler equations holding to leading order. Furthermore, there is a small boundary-layer created on the blade and ground surfaces in the leading edge region, due to the no-slip conditions. By considering the balance $UU_x \sim U_{yy}$ within the region, we deduce that the thickness of these boundary-layers is $O(Re^{-3/4})$. This normal estimate is much smaller than the current normal scale (of $O(Re^{-1/2})$) and so the contribution to the leading order problem is negligible. We do not formulate this problem further, instead concentrating on the inviscid solution.

The leading order streamfunction in the region, ψ , is defined as

$$\bar{u} = \frac{\partial\psi}{\partial Y}, \quad \bar{v} = -\frac{\partial\psi}{\partial X}, \quad (2.17)$$

with the vorticity of the flow in this region given by

$$\omega = \frac{\partial\bar{v}}{\partial X} - \frac{\partial\bar{u}}{\partial Y}. \quad (2.18)$$

For a general incoming flow profile, each streamline has a different value of vorticity. Given the inviscid nature of the flow to leading order, by the Cauchy-Lagrange theorem (see Acheson (1990)) the vorticity of the incoming flow persists throughout the entire region. Hence, the vorticity on each incoming streamline is conserved throughout the region. We substitute (2.17) into (2.18) to find that the streamfunction in the region is governed by the Poisson equation

$$\nabla^2\psi = -\omega(\psi), \quad (2.19)$$

where $\omega(\psi)$ represents the vorticity on a particular streamline. The boundary conditions for the problem are given by

$$\psi = 0, \quad \text{on } Y = 0, \forall X, \quad (2.20)$$

$$\psi = \psi_0, \quad \text{on } Y = H, \text{ for } X > 0. \quad (2.21)$$

$$\psi = \psi(Y), \quad \text{as } X \rightarrow -\infty. \quad (2.22)$$

The value of ψ_0 is the unknown flux entering the blade-ground gap. Applying Bernoulli's equation to each streamline gives us that

$$\bar{p} + \frac{1}{2}(\psi_X^2 + \psi_Y^2) = B(\psi), \quad (2.23)$$

with $B(\psi)$ fixed by applying Bernoulli's equation to each streamline. Thus, both functions ω and B are fixed by the incoming flow profile and further are related by

$$B'(\psi) = \omega(\psi). \quad (2.24)$$

The result (2.24) follows by employing the chain rule to find the total derivative

$$\frac{dB}{d\psi} = \frac{\partial X}{\partial\psi} \frac{\partial B}{\partial X} + \frac{\partial Y}{\partial\psi} \frac{\partial B}{\partial Y}, \quad (2.25)$$

along each streamline. We evaluate the partial derivatives of (2.23) with respect to X and Y and substitute these into the above equation to find

$$\frac{dB}{d\psi} = (\bar{p}_X + \bar{u}\bar{u}_X + \bar{v}\bar{v}_X) \frac{\partial X}{\partial\psi} + (\bar{p}_Y + \bar{u}\bar{u}_Y + \bar{v}\bar{v}_Y) \frac{\partial Y}{\partial\psi}. \quad (2.26)$$

From the governing Euler equations, we have that

$$\bar{p}_X + \bar{u}\bar{u}_X = -\bar{v}\bar{u}_Y, \quad (2.27)$$

$$\bar{p}_Y + \bar{u}\bar{u}_Y = -\bar{u}\bar{v}_X, \quad (2.28)$$

which when substituted into (2.26) yield

$$\frac{dB}{d\psi} = \bar{u}_Y \left(\bar{u} \frac{\partial Y}{\partial\psi} - \bar{v} \frac{\partial X}{\partial\psi} \right) - \bar{v}_X \left(\bar{u} \frac{\partial Y}{\partial\psi} - \bar{v} \frac{\partial X}{\partial\psi} \right). \quad (2.29)$$

By finding the total derivative $d\psi/d\psi$, we find that

$$1 = \bar{u} \frac{\partial Y}{\partial\psi} - \bar{v} \frac{\partial X}{\partial\psi}, \quad (2.30)$$

and hence the result follows.

Equations (2.19) and (2.23) with boundary conditions (2.20) - (2.22) give the formulation for the leading edge problem. For an arbitrary oncoming velocity profile, with streamfunction $\psi(X, Y)$, the full solution of these equations is a numerical problem in general. In our problem of multiple blades, we assume that the blades are well separated as this is seen in some of the applications outlined earlier. A large wake size and the boundary conditions in the wake allows fluid to accelerate back towards $\bar{u} = 1$. This means that the magnitude of the normal velocity \bar{v} decreases. We will choose the length of the wake to be large enough such that \bar{v} is much smaller than \bar{u} . Thus the contribution of \bar{v} in the flow is negligible compared to \bar{u} and consequently we approximate the oncoming velocity and pressure to each leading edge region by the form $\bar{u} = \bar{u}(Y)$, $\bar{v} = 0$ and $\bar{p} = 0$.

2.2.1 Non-uniform oncoming velocity

For approaching non-uniform flow of the form $\bar{u} = \bar{u}(Y)$, $\bar{v} = 0$, $\bar{p} = 0$, let the approaching streamfunction profile be given by ψ_1 . This means that

$$\omega(\psi) = -\psi_1''(Y(\psi)), \quad B(\psi) = \frac{1}{2}\psi_1'(Y(\psi))^2, \quad (2.31)$$

where on any given streamline, $Y(\psi)$ is the normal position of that streamline. In the leading edge region, we are concerned with the solution of the flow as $X \rightarrow \infty$. Hence we can determine the jumps in velocity and pressure over the leading edge to give appropriate starting conditions for the flow above and beneath each blade, without needing to determine the full leading edge solution.

Between the blade and the ground, the solution as $X \rightarrow \infty$ is given by

$$\psi \rightarrow \psi_*(Y(\psi)), \quad \bar{p} \rightarrow p_0 \quad (2.32)$$

due to the boundary conditions (2.20) and (2.21) requiring the streamlines to be tangential to the blade and ground surfaces. The downstream position $Y(\psi)$ of each streamline ψ is unknown and is to be found as part of the solution. The constant p_0 is also unknown, but fixed by the Kutta condition so that $p = 0$ at the trailing edge. We substitute equation (2.32) into (2.19) and integrate once with respect to ψ to find that

$$\psi_*'^2(Y(\psi)) = \psi_1'^2(Y(\psi)) + C, \quad (2.33)$$

with C a constant of integration. As $X \rightarrow -\infty$, the incoming streamfunction satisfies $\psi_1' = 1$ on $Y = 0$. Given the jump in pressure to p_0 as $X \rightarrow \infty$, there is a jump in velocity to u_0 on $Y = 0$ as a result of applying Bernoulli's equation to the ground, with u_0 and p_0 related by

$$u_0 = \sqrt{1 - 2p_0}. \quad (2.34)$$

With the jump in velocity u_0 , we find that the constant $C = u_0^2 - 1$. Thus the flow as $X \rightarrow \infty$ between the blade and the ground is given by

$$\bar{u}(Y(\psi)) = \sqrt{\psi_1'^2(Y(\psi)) - 1 + u_0^2}. \quad (2.35)$$

The final task is to find the location $Y(\psi)$ of the streamline ψ downstream. Since $\bar{u} = \bar{u}(Y)$, we have that $dY/d\psi = 1/\bar{u}(Y(\psi))$ and upon integration using (2.35)

$$Y(\psi) = \int_0^\psi \frac{1}{\sqrt{\psi_1'^2(Y(\psi)) - 1 + u_0^2}} d\bar{\psi}. \quad (2.36)$$

Equations (2.35) and (2.36) are valid for all values of ψ satisfying $0 \leq \psi \leq \psi_0$.

Above the blade, there is no pressure jump and the equations for the flow as $X \rightarrow \infty$ are given by

$$\bar{u}(Y(\psi)) = \psi_1'(Y(\psi)), \quad (2.37)$$

$$Y(\psi) = \int_{\psi_0}^\psi \frac{1}{\bar{u}(Y(\bar{\psi}))} d\bar{\psi}, \quad (2.38)$$

which are found in a similar way to before.

Given an incoming flow of the form $\bar{u} = \bar{u}(Y)$, $\bar{v} = 0$, $\bar{p} = 0$ and pressure jump p_0 , we can now determine the jumps in velocity and pressure as $X \rightarrow \infty$ in the leading edge region. This analysis must be incorporated into the larger flow problem (on the $x = O(1)$ scale) through the parameter p_0 and to find the correct starting conditions so that the Kutta condition is satisfied.

2.2.2 Uniform oncoming flow

The flow approaching the first blade is given by $\bar{u} = 1$, $\bar{v} = 0$, $\bar{p} = 0$ and is a special case for which we gain an analytical solution throughout the leading edge region. Since the flow upstream is uniform, the vorticity is zero everywhere in the leading edge region and hence the streamfunction ψ satisfies Laplace's equation

$$\nabla^2 \psi = 0, \quad (2.39)$$

subject to the conditions

$$\psi = 0, \quad \text{on } Y = 0, \forall X, \quad (2.40)$$

$$\psi = \psi_0, \quad \text{on } Y = H, \text{ for } X > 0, \quad (2.41)$$

$$\psi \rightarrow Y, \quad \text{as } X \rightarrow -\infty. \quad (2.42)$$

By applying the same arguments as above, the solution of the flow as $X \rightarrow \infty$ in the blade-ground gap now takes on the form $\bar{u} \rightarrow u_0$, $\bar{v} \rightarrow 0$, $\bar{p} \rightarrow p_0$, where u_0 and p_0 are constants and equation (2.34) holds everywhere. The value of

$\psi_0 = u_0 H$ in this problem and is found by evaluating the flux q in the blade-ground gap. If $p_0 \neq 0$ (hence $u_0 \neq 0$), then the streamline ψ_0 upstream lies at $Y = u_0 H$, whilst downstream lies at $Y = H$. This means that for any value of pressure jump $p_0 \neq 0$ a deflection of the streamlines occurs through the leading edge region.

To find the solution to the problem, we turn to the complex plane and use a conformal mapping technique. We write the streamfunction ψ as

$$\psi(X, Y) = Y + \Psi(X, Y), \quad (2.43)$$

and by substitution, Ψ satisfies Laplace's equation subject to the boundary conditions

$$\Psi(X, 0) = 0 \quad \forall X, \quad (2.44)$$

$$\Psi(X, H) = \psi_0 - H \quad \text{for } X > 0, \quad (2.45)$$

$$\Psi \rightarrow 0 \quad \text{as } X^2 + Y^2 \rightarrow \infty. \quad (2.46)$$

We map the upper half \bar{Z} -plane to the leading edge (Z -plane) region using the Schwarz-Christoffel transformation (see Carrier *et al.* (1966)). In the leading edge and upper half plane problems, we introduce the complex variables $Z = X + iY$ and $\bar{Z} = \bar{X} + i\bar{Y}$ respectively. The conformal mapping from the \bar{Z} -plane to the Z -plane is given by

$$Z = f(\bar{Z}) = Hi + \frac{H}{\pi} (\bar{Z} - \text{Ln}(\bar{Z}) - 1). \quad (2.47)$$

Although in this instance, the conformal mapping is stated, not derived, we will discuss how to apply the transformation in chapter 8 later in a similar but more technical problem. The \bar{X} -axis in the \bar{Z} -plane maps onto the ground and leading edge geometry in the Z -plane and so the boundary conditions for the problem in the upper half plane are given by

$$\Psi = 0 \quad \text{for } \bar{X} < 0, \quad (2.48)$$

$$\Psi = \psi_0 - H \quad \text{for } \bar{X} > 0, \quad (2.49)$$

$$\Psi \rightarrow 0 \quad \text{as } Y \rightarrow \infty. \quad (2.50)$$

The boundary conditions give us a Dirichlet problem in the upper half plane

for Ψ and means that we can write down the solution immediately (see Mathews & Howell (2001)) as

$$\Psi(\bar{X}, \bar{Y}) = (\psi_0 - H) - \left(\frac{\psi_0 - H}{\pi} \right) \arctan\left(\frac{\bar{Y}}{\bar{X}}\right), \quad (2.51)$$

choosing $0 < \arctan(\bar{Y}/\bar{X}) < \pi$. Thus, the total solution for ψ is defined implicitly as

$$X = \frac{H}{\pi} \left(\bar{X} - \frac{1}{2} \log(\bar{X}^2 + \bar{Y}^2) - 1 \right), \quad (2.52)$$

$$Y = H + \frac{H}{\pi} \left(\bar{Y} - \arctan\left(\frac{\bar{Y}}{\bar{X}}\right) \right), \quad (2.53)$$

$$\psi(X, Y) = Y + (\psi_0 - H) - \left(\frac{\psi_0 - H}{\pi} \right) \arctan\left(\frac{\bar{Y}}{\bar{X}}\right). \quad (2.54)$$

In figure 2.2, we plot an example streamfunction solution. Here, we set the pressure $p_0 = 0.3621$ in the blade-ground gap, meaning that the value of $\psi_0 = 0.5252$. The reported deflection of the oncoming streamlines within this region is seen. The dividing streamline within figure 2.2(b) is given by ψ_0 for this case.

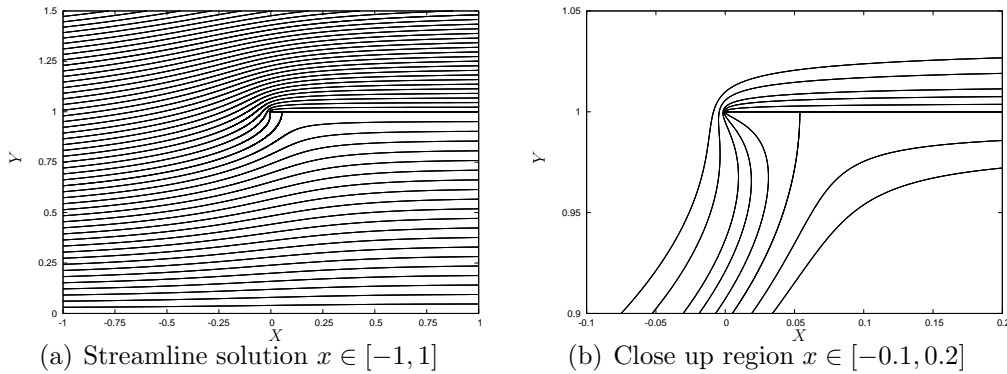


Figure 2.2: Streamfunction solution for the leading edge region when $p_0 = 0.3621$, $u_0 = 0.5252$. The blade lies at $H = 1$. In (a), streamlines are plotted in increments of 0.025. In (b), various streamlines showing the behaviour close to the leading edge of the blade are plotted.

2.3 Summary of the full problem

Now that the leading edge problem has been outlined, we state the full problem to be solved. We must solve the boundary-layer equations

$$u \frac{\partial u}{\partial x} + v \frac{\partial u}{\partial Y} = -\frac{dp}{dx} + \frac{\partial^2 u}{\partial Y^2}, \quad (2.55)$$

$$\frac{\partial u}{\partial x} + \frac{\partial v}{\partial y} = 0. \quad (2.56)$$

within each blade-ground gap, subject to the boundary conditions

$$u = 1, v = 0, \quad \text{on } Y = 0, \forall x, \quad (2.57)$$

$$u = 0, v = 0, \quad \text{on } Y = H \text{ on the blades}, \quad (2.58)$$

$$p = 0, \quad \text{at each trailing edge}, \quad (2.59)$$

$$u = u(Y), v = 0, p = p_0, \quad \text{at each leading edge}. \quad (2.60)$$

For an oncoming streamfunction ψ_1 and pressure jump downstream p_0 of a particular blade ground gap, the leading edge flow between the blade and the ground may be found through the equations

$$u(Y(\psi)) = \sqrt{\psi_1'^2(Y(\psi)) - 1 + u_0^2}, \quad (2.61)$$

$$Y(\psi) = \int_0^\psi \frac{1}{\sqrt{\psi_1'^2(Y(\psi)) - 1 + u_0^2}} d\bar{\psi}, \quad (2.62)$$

$$p_0 + \frac{1}{2}u_0^2 = \frac{1}{2}, \quad (2.63)$$

as outlined in the previous section.

Above each blade and in each wake, we solve the same equations (2.55) and (2.56) but with $p = 0$. The boundary conditions for the problem above each blade and in the wakes are given by

$$u = 0, v = 0, \quad \text{on } Y = H \text{ on the blades}, \quad (2.64)$$

$$u = 1, v = 0, \quad \text{on } Y = 0 \text{ in the wake}, \quad (2.65)$$

$$u \rightarrow 1 \quad \text{as } Y \rightarrow \infty, \quad (2.66)$$

$$u = u(Y), v = 0, p = 0, \quad \text{at each leading edge}. \quad (2.67)$$

After the first leading edge is passed, given the uniform oncoming profile, the governing boundary-layer equations and the boundary conditions (2.64) and (2.66), we have Blasius boundary-layer flow (see Blasius (1908)) at a shifted

position $Y + H$ on top of the first blade. This is not the case for any other blade, since the oncoming flow to subsequent blades is not uniform. The leading edge flow is given by the equations (2.37) and (2.38) once the value of ψ_0 is determined for the flow beneath the blade.

2.4 Numerical methods

We now outline the numerical solution procedure. We begin by discussing the solution of the problem in the leading edge region, followed by solution at any position x . Then we describe the algorithm to solve the full problem.

2.4.1 Leading edge solution

We firstly describe the method to find the far-field solution as $X \rightarrow \infty$ in the leading edge region, to give starting conditions just after each leading edge.

For a given pressure jump p_0 , and incoming streamfunction ψ_1 , we calculate the value of u_0 , the jump in velocity at the ground. Next, we determine the value of ψ_0 , the streamline that lies at a downstream position of $Y = H$ to allow the pressure to jump to p_0 beneath the blade. We do this iteratively, by guessing a value for ψ_0 and using cubic splines to interpolate $\psi_1(Y(\psi))$ between 0 and ψ_0 upstream. We then integrate equation (2.62) to find $Y(\psi_0)$ downstream and test whether

$$|Y(\psi_0) - H| < 10^{-10}, \quad (2.68)$$

for convergence. If convergence is not achieved, then we update the value of ψ_0 using the secant method and recompute $Y(\psi_0)$ using the method above, until convergence is achieved. Once the value of ψ_0 is found, the starting condition beneath the blade is determined. The flow above the blade is found by integrating equations (2.37) and (2.38) afterwards.

We tested the numerical method against exact solutions arising for a uniform flow, for various cases of p_0 . In the exact solution presented in figure 2.2, we know the value of ψ_0 immediately in the problem, whilst the numerical method must calculate that value. The value returned by the

numerical technique is $\psi_0 = 0.5251960$, showing very good agreement with the exact solution.

2.4.2 Blade-ground gap solution

The solution of the boundary-layer equations (2.55) and (2.56) with boundary conditions (2.57) and (2.58) at a particular value of x is found using a finite-difference technique. Each gap is discretised into a regularly spaced grid in x and Y with spacings Δx and ΔY respectively. Thus, the i^{th} x - and j^{th} Y -stations are given by $x_i = i\Delta x$ and $Y_j = j\Delta Y$ respectively.

To discretise the governing equations, we use first-order accurate backward differences in x and second-order accurate centred differences in Y . Equations (2.55) and (2.56) are then discretised as

$$u_{i-1}^j \frac{u_i^j - u_{i-1}^j}{\Delta x} + v_{i-1}^j \frac{u_i^{j+1} - u_i^{j-1}}{2\Delta Y} = -\frac{(p_i - p_{i-1})}{\Delta x} + \frac{u_i^{j+1} - 2u_i^j + u_i^{j-1}}{(\Delta Y)^2}, \quad (2.69)$$

$$\frac{u_i^j - u_{i-1}^j}{\Delta x} + \frac{v_i^{j+1} - v_i^{j-1}}{2\Delta Y} = 0, \quad (2.70)$$

where u_i^j and v_i^j are the unknown streamwise and normal velocities at (x_i, Y_j) and p_i is the unknown pressure at x_i . We find the values of u_i^j first, by rearranging equation (2.69) into a tridiagonal matrix problem

$$a_j u_i^{j+1} + b_j u_i^j + c_j u_i^{j-1} = d_j, \quad (2.71)$$

where a_j, b_j, c_j and d_j are given by

$$a_j = \frac{v_{i-1}^j}{2\Delta Y} - \frac{1}{\Delta Y^2}, \quad (2.72)$$

$$b_j = \frac{u_{i-1}^j}{\Delta x} + \frac{2}{\Delta Y^2}, \quad (2.73)$$

$$c_j = \frac{-v_{i-1}^j}{2\Delta Y} - \frac{1}{\Delta Y^2}, \quad (2.74)$$

$$d_j = \frac{(u_{i-1}^j)^2 - (p_i - p_{i-1})}{\Delta x}. \quad (2.75)$$

Solution of the tridiagonal problem (2.71) is found using a Thomas algorithm with boundary conditions $u = 1$ at $Y = 0$ and $u = 0$ at $Y = H$. The values of a_j, b_j, c_j are known from the velocities at the previous x -station, but p_i and hence all the d_j values are unknown. We treat p_i as an unknown parameter

and seek to determine it iteratively. At any x_i , p_i is set as p_{i-1} on the first iteration and hence we may solve (2.71) to give the values of u_i^j . Once u_i^j is determined, v_i^j follows from the discretised continuity equation (2.70). In finding v_i^j , the conditions $v = 0$ at $Y = 0$ and $Y = H$ are set and then a march to the centre of the blade-ground gap from $Y = 0$ and $Y = H$ ensues, yielding two values for the normal velocity at $Y = H/2$. The normal velocity must be continuous at $Y = H/2$ and so we test for equality between the two values for v_i^j there by requiring that their absolute error is less than 10^{-10} . To gain convergence, the value of p_i is updated at each x_i using a secant method, followed by resolution of the tridiagonal problem and the continuity equation until convergence is achieved. Typically, we needed only five or six iterations of p_i at each x_i .

2.4.3 Over blade and wake solution

The solution method at x_i in these areas is very similar to that of the previous subsection. In these areas, $p = 0$ and so no pressure gradient term appears in (2.75). We solve a similar tridiagonal problem, with d_j replaced by

$$d_j^* = \frac{(u_{i-1}^j)^2}{\Delta x}, \quad (2.76)$$

together with the relevant no-slip condition and matching condition as $Y \rightarrow \infty$. Once the solution to the tridiagonal system is found, we apply the no-normal flow condition at the blade or the ground and use the continuity equation to find v . The solution at x_i is then found.

2.4.4 Solution algorithm

Above, we have outlined how to solve the leading edge region and boundary-layer equations at a particular value of x in the flow domain. This final subsection deals with solving the full problem, encompassing all the numerical techniques outlined above.

To obtain the solution beneath any blade and the ground, we proceed as follows. As yet, we have not applied the Kutta condition, requiring that $p = 0$ at the trailing edge. To satisfy this condition requires us to find the

pressure jump p_0 beneath the leading edge such that once the flow reaches the trailing edge, the Kutta condition is satisfied. We begin by guessing a value of $p_0 = 0$ and then solve the leading edge problem to construct the first starting condition. We then exploit the parabolicity of the governing equations and employ a streamwise sweep from the leading edge to the trailing edge to find the solution at each x_i . The absolute value of p at the trailing edge is tested to see if the Kutta condition (2.59) is satisfied to within a convergence tolerance of 10^{-10} . If the tolerance is not met, the value of p_0 at the leading edge is updated using a secant method, followed by recomputing the starting conditions for the current blade-ground gap and resweeping. Once the convergence tolerance is met, we solve the problem above the blades. We found that this outer iteration requires between five and ten sweeps for convergence to be achieved. Recall that $p = 0$ everywhere above the blade, and so one sweep is needed to the trailing edge.

At the trailing edge, we then obtain the starting condition for the wake, given by the emerging flow from beneath the blade and the flow at the trailing edge above the blade. To construct the starting conditions in u and v , we use cubic splines. Now we may sweep through the wake up to the next leading edge, ready to solve the leading edge problem for the next blade. The whole process above is repeated over each of the blades and wakes in the problem.

In performing the sweep, the equations (2.69) and (2.70) in discretised form are second order accurate in Y but only first order accurate in x . To gain second-order accuracy in x , we adopt the double stepping method of Smith & Timoshin (1996b). This method is chosen as it is robust, accurate, easy to program and deals easily with the continual leading and trailing edge adjustments present in the multiple blade flow. First, we obtain a first-order accurate solution for the velocities and pressure. Then, we apply a half-step solution, from x_{i-1} to $x_{i-\frac{1}{2}}$ and then from $x_{i-\frac{1}{2}}$ to x_i . If u^f and u^h are the first-order accurate and half-stepping solutions for u respectively, then the second-order accurate solution u^c is given by

$$u^c = 2u^h - u^f. \quad (2.77)$$

This method is completed similarly for v and p and is carried out for all Y

at every x -station.

In developing the numerical code, we find that values of $\Delta x = 10^{-3}$ with $\Delta Y = 10^{-6}$ are needed to gain accuracy in the solutions of u, v and p beneath the blade. Accuracy in the solutions is confirmed by adopting much finer grid resolutions in x and Y . We halved and quartered the x and Y grid resolutions with the numerical solutions found being almost identical. We also tested our numerical results from the first blade and wake against those appearing in Jones (2000) and Jones & Smith (2003), who consider the one blade case. Although we do not present graphical comparisons, the results are very similar. Above the blade, a much coarser resolution of $\Delta x = 0.01$ and $\Delta Y = 0.001$ can be used, but in the wake we retain the finer grid resolutions to accurately capture the flow behaviour just after the trailing edge when H is small.

2.5 Results

We present results for an $N = 6$ blade case at scaled ground clearances H between 32 and $1/16$, which captures the majority of the underlying physics. We take the length of each blade to be unity and the wake of length three in all our calculations. This allows the flow approaching the next blade downstream to be such that $v \ll u$ and hence the leading edge formulation described earlier can be used. In figure 2.3 we compare the u and v solutions at the leading edge of blade 2 with $H = 1/16$. We see that v (dotted line) is much smaller in magnitude than u (solid line).

We begin with two examples of the flow adjustments close to the entrance of a blade-ground gap. Next, we summarise the values of the pressure jump p_0 calculated under each leading edge, along with the friction drag, τ and lift, L . We then consider the extremal cases of very small and very large ground clearances asymptotically.

2.5.1 Flow characteristics

In figure 2.4 we present three u velocity profiles close to the leading edge of a blade. We see that the growth of the top and bottom boundary-layers as x

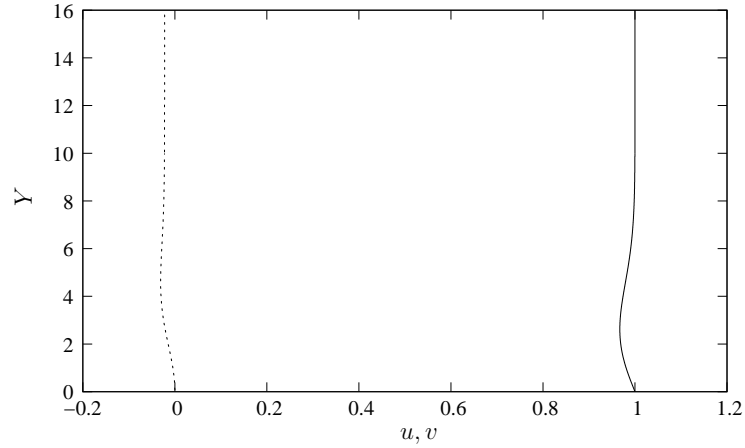


Figure 2.3: Velocity solutions u (solid line) and v (dotted line) at the leading edge of blade 2 for a wake of length 3.

increases downstream quickly engulfs the inviscid bulk flow within the centre of the gap. After only a short distance in figures 2.4(a), (b) and (c), the flow settles into a Pouseuille-Couette type flow. This velocity profile gives the solution as the flow progresses downstream to the trailing edge, under every blade.

In figure 2.5, we outline the pressure solutions beneath each of the $N = 6$ blades. When the ground clearance H is small the pressure gradient is constant for the majority of the flow between the blade and the ground for each blade. As we increase H , the linear nature of the pressure profile is lost. It is interesting to note that for large H and many N , the pressure beneath the blades starts to take on a periodic nature as N increases downstream.

Next, we define the total lift L and friction drag τ experienced by each blade as

$$L = \int_{x_{le}}^{x_{le}+1} p(x) dx, \quad (2.78)$$

$$\tau = \int_{x_{le}}^{x_{le}+1} \frac{\partial u_+}{\partial Y} dx + \int_{x_{le}}^{x_{le}+1} \frac{\partial u_-}{\partial Y} dx, \quad (2.79)$$

where u_+ and u_- are the flow profiles just above and below the blade at $Y = H$ respectively. The total lift and friction drag experienced by each blade is plotted in figure 2.6, along with the computed pressure jumps p_0 under each leading edge. Slip-streaming effects are observed in the lift and friction drag for larger values of H . When H is small, we see that the total

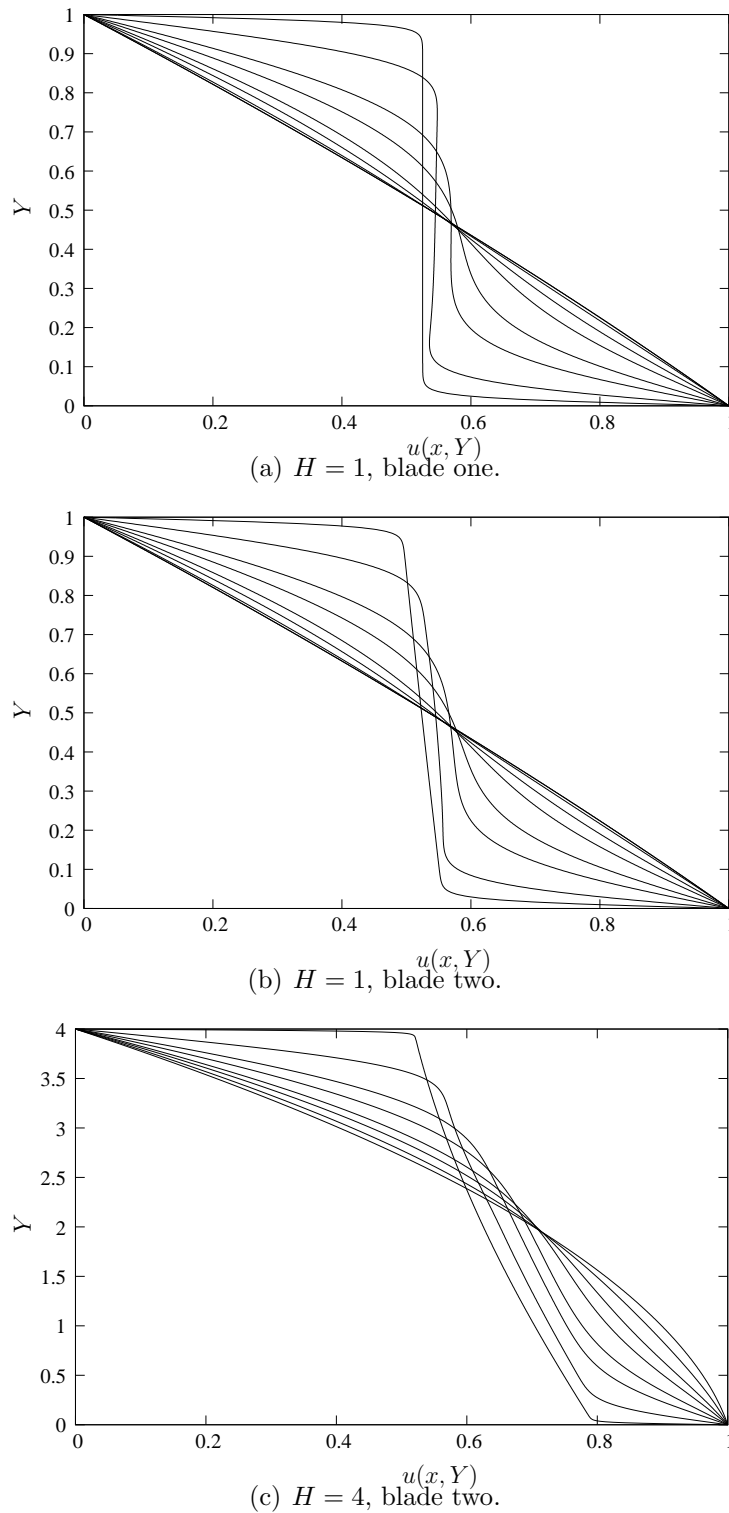


Figure 2.4: Viscid-inviscid interaction in the u velocity profiles at small stream-wise distances $x = 0.001, 0.005, 0.01, 0.02, 0.03, 0.05, 0.1, 0.2$ beneath the blade leading edge. In (a) flow profiles are taken from beneath the first blade with $H = 1$, (b) from under the second blade with $H = 1$ and (c) from beneath the second blade with $H = 4$.

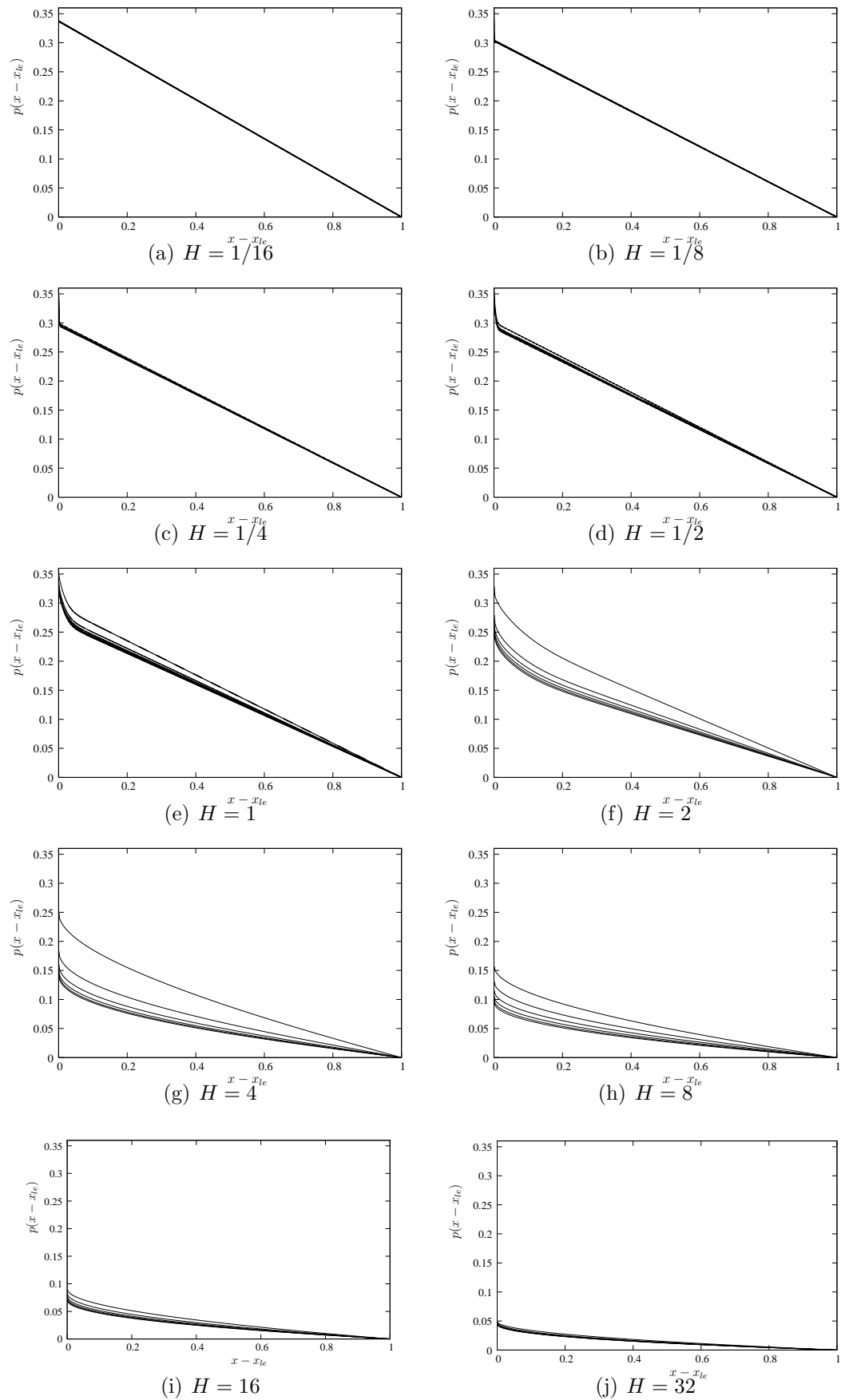


Figure 2.5: Pressure solutions between the blade and ground for each of the $N = 6$ blades for different values of H .

lift and friction drag experienced by each blade is approximately constant for the first six blades. Slip-streaming behaviour is visible in the value of p_0 for larger values of H . As we let $H \rightarrow 0$, the slip-streaming effect in p_0 becomes more obvious before approaching a constant level under each of the $N = 6$ blades. Numerically, we find that $p_0 = 0.3748, 0.3734, 0.3730, 0.3728, 0.3726$ and 0.3725 (to 4 s.f.) for the six blades with $H = 1/16$.

2.5.2 Small H

In the previous section, we saw that as $H \rightarrow 0$ a near constant value of the total lift and friction drag and pressure p_0 occurred for each blade and that slip-streaming effects are lost. In figure 2.7, the streamwise velocity profile u is plotted mid-blade in the blade-ground gap. We see that in each case, we have a linear profile in u . We noted earlier that the pressure solutions for the small ground clearance take on a linear profile also. Figure 2.8 shows the solution for $p(x)$ very close to the leading edge. We see that there is a small x -zone where a rapid change in pressure occurs, before the negative pressure gradient becomes constant. To understand the nature of the flow close to the leading edge, we seek a further asymptotic approximation based on two x -scales for the flow beneath each blade.

Consider the flow very close to the leading edge. The ground clearance $Y = O(H)$ and $u = O(1)$. Here, the x -scale is determined by the balance of the inertial and diffusive operators

$$u \frac{\partial}{\partial x} = \frac{\partial^2}{\partial Y^2} \quad (2.80)$$

yielding $x = O(H^2)$ and by continuity, $v = O(H^{-1})$. Defining the scaled coordinates $\tilde{x} = O(1)$ and $\tilde{Y} = O(1)$ where $x - x_{le} = H^2 \tilde{x}$ and $Y = H \tilde{Y}$ respectively, we expand the velocities and pressure as

$$u(x, Y) = \tilde{u}(\tilde{x}, \tilde{Y}) + \dots, \quad (2.81)$$

$$v(x, Y) = \frac{1}{H} \tilde{v}(\tilde{x}, \tilde{Y}) + \dots, \quad (2.82)$$

$$p(x) = \tilde{p}(\tilde{x}) + \dots, \quad (2.83)$$

where any lower order terms tend to zero as $H \rightarrow 0$. These expansions are substituted into the governing equations (2.55) and (2.56) to reveal the

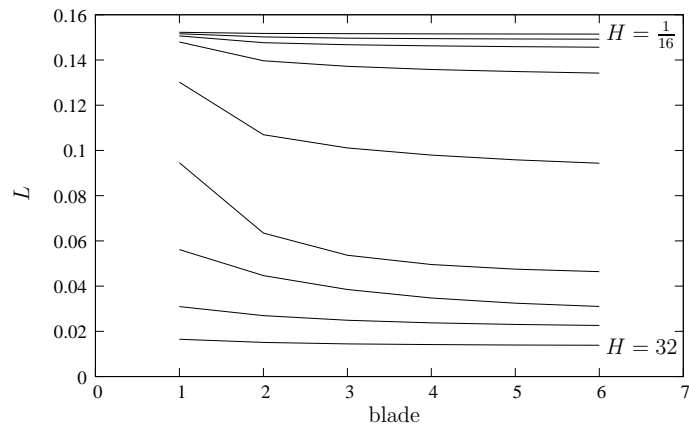
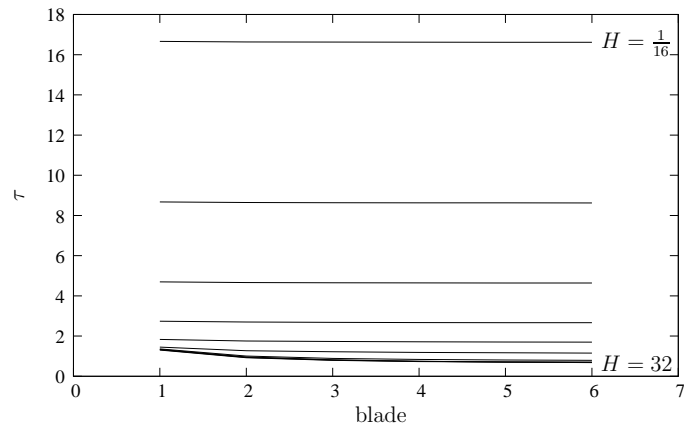
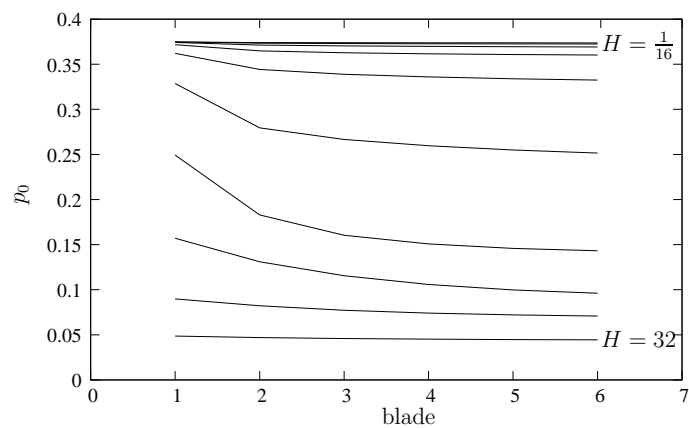
(a) Values of L for each blade at varying H (b) Values of τ for each blade at varying H (c) Values of p_0 for each blade at varying H

Figure 2.6: Calculated values of lift, L , friction drag, τ , and p_0 for every blade with values of $H = 32, 16, 8, 4, 2, 1, 1/2, 1/4, 1/8, 1/16$.

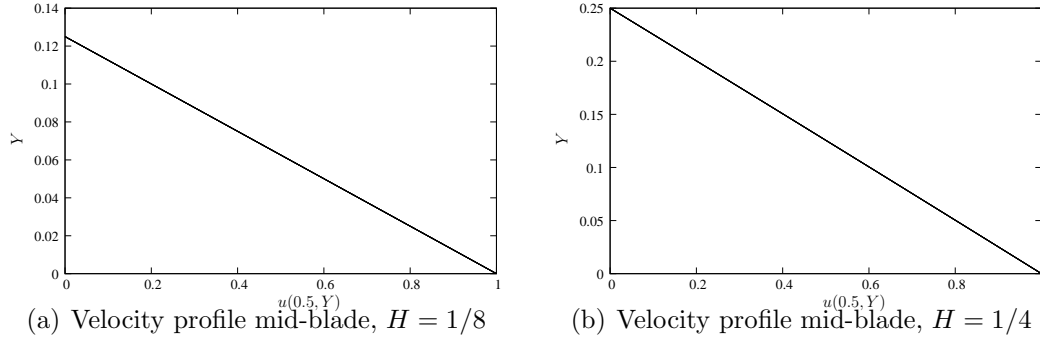


Figure 2.7: Calculated u velocity profiles between the blade and the ground. The profiles are taken from the mid-blade positions of each of the $N = 6$ blades.

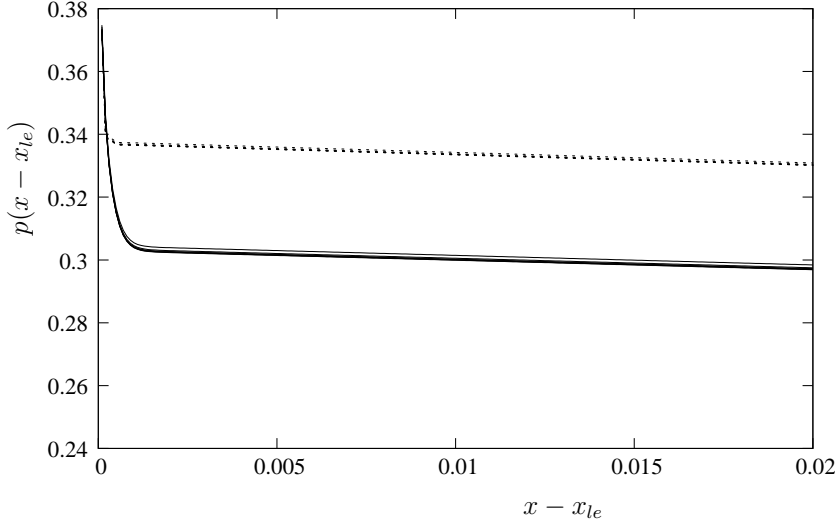


Figure 2.8: The pressure solutions $p(x)$ under each blade in the six-blade case for small x . Solutions plotted are for $H = 1/16$ (dotted line) and $H = 1/8$ (solid line).

leading order balances

$$\tilde{u} \frac{\partial \tilde{u}}{\partial \tilde{x}} + \tilde{v} \frac{\partial \tilde{u}}{\partial \tilde{Y}} = -\frac{d\tilde{p}}{d\tilde{x}} + \frac{\partial^2 \tilde{u}}{\partial \tilde{Y}^2}, \quad (2.84)$$

$$\frac{\partial \tilde{u}}{\partial \tilde{x}} + \frac{\partial \tilde{V}}{\partial \tilde{Y}} = 0, \quad (2.85)$$

and are subject to the boundary conditions

$$\tilde{u} = \tilde{v} = 0 \quad \text{on } \tilde{Y} = 1, \quad (2.86)$$

$$\tilde{u} = 1, \tilde{v} = 0 \quad \text{on } \tilde{Y} = 0, \quad (2.87)$$

$$\tilde{u} = \tilde{u}(\tilde{Y}), \tilde{p} = p_0 \quad \text{at every leading edge.} \quad (2.88)$$

On this short scale, the full balance of streamwise advection with pressure

gradient and diffusion holds, leading to a non-linear interaction at the leading edge. This corresponds to the viscid-inviscid interaction seen in figures 2.4(a) and (b).

The second x -scale covers the remainder of the blade-ground gap on an $x = O(1)$ scale. For the remainder of the gap, the pressure gradient is a negative constant. Since the gap width is very small ($Y = O(H)$) in comparison to the blade length ($x = O(1)$), we expect a lubrication approximation governed by viscous diffusion and pressure gradient. The streamwise velocity $u = O(1)$ still due to the no-slip boundary conditions, and so by continuity we have $v = O(H)$. By considering the balance

$$\frac{dp}{dx} = \frac{\partial^2 u}{\partial Y^2}, \quad (2.89)$$

we find that $p = O(H^{-2})$. Thus, the expansions for the velocity and pressure take the form

$$u(x, Y) = \hat{u}(\hat{x}, \tilde{Y}) + \dots, \quad (2.90)$$

$$v(x, Y) = H\hat{v}(\hat{x}, \tilde{Y}) + \dots, \quad (2.91)$$

$$p(x) = \frac{1}{H^2}\hat{p}(\hat{x}) + \dots, \quad (2.92)$$

with $\hat{x} = x - x_{le}$. Substitution into equations (2.55) and (2.56) gives the governing equations

$$0 = -\frac{d\hat{p}}{d\hat{x}} + \frac{\partial^2 \hat{u}}{\partial \tilde{Y}^2}, \quad (2.93)$$

$$\frac{\partial \hat{u}}{\partial \hat{x}} + \frac{\partial \hat{v}}{\partial \tilde{Y}} = 0, \quad (2.94)$$

at leading order and are subject to

$$\hat{u} = \hat{v} = 0 \quad \text{on } \tilde{Y} = 1, \quad (2.95)$$

$$\hat{u} = 1, \hat{v} = 0 \quad \text{on } \tilde{Y} = 0, \quad (2.96)$$

$$\hat{p} = 0 \quad \text{at each trailing edge.} \quad (2.97)$$

We integrate equation (2.93) twice with respect to \tilde{Y} to obtain

$$\hat{u}(\hat{x}, \tilde{Y}) = \frac{d\hat{p}}{d\hat{x}} \frac{\tilde{Y}^2}{2} + \tilde{Y}F(\hat{x}) + G(\hat{x}), \quad (2.98)$$

where F, G are arbitrary functions of integration. The arbitrary functions are fixed by the no-slip conditions at $\tilde{Y} = 1$ and $\tilde{Y} = 0$ as $F(\hat{x}) = -(\hat{p}'/2 + 1)$

and $G(\hat{x}) = 1$. Hence, we find that $\hat{u} = \hat{u}(\tilde{Y})$ in this problem and is given by

$$\hat{u}(\tilde{Y}) = \frac{1}{2} \frac{d\hat{p}}{d\hat{x}} \tilde{Y}(\tilde{Y} - 1) - \tilde{Y} + 1, \quad (2.99)$$

with $\hat{v} = 0$ by continuity.

To find the pressure, we integrate (2.99) with respect to \tilde{Y} to reveal the streamfunction

$$\psi(\tilde{Y}) = \frac{1}{24} \frac{d\hat{p}}{d\hat{x}} \tilde{Y}^2(4\tilde{Y} - 6) - \frac{\tilde{Y}^2}{2} + \tilde{Y} + c. \quad (2.100)$$

The constant $c = 0$ by the condition that $\psi = 0$ at the ground. To find the pressure, let $\psi = \psi_0$ at $\tilde{Y} = 1$, where ψ_0 represents the total mass flux in the blade-ground gap, and integrate with respect to x to obtain

$$\frac{d\hat{p}}{d\hat{x}} = -12(\psi_0 - \frac{1}{2}). \quad (2.101)$$

We integrate with respect to \hat{x} and apply the Kutta condition $\hat{p} = 0$ at $\hat{x} = x_{te} = x_{le} + 1$, where x_{te} represents the position of each trailing edge to find

$$\hat{p}(\hat{x}) = -12(\psi_0 - \frac{1}{2})(\hat{x} - x_{te}), \quad (2.102)$$

completing this part of the asymptotic solution. If, to match to the smaller $x = O(H^2)$ region we have that $\hat{p} = 0$ at each leading edge (and so $\hat{p} = 0$ everywhere), then we find that the flux $\psi_0 = H/2$. Thus, the velocity may jump to a minimum value of $u_0 = 1/2$ at the ground and hence by Bernoulli's equation, the largest pressure jump allowed in the entrance to any channel is $p_0 = 3/8$. This is suggested by the listed numerical results earlier. Furthermore, if $\hat{p} = 0$ on the $x = O(1)$ scale, then the solution for $\hat{u}(\tilde{Y}) = 1 - \tilde{Y}$, a Couette flow. This type of flow is seen for small H in figure 2.7.

In the wake, the emerging flow from within the blade-ground gap is quickly engulfed by the boundary layer created at the ground, leaving a near linear velocity profile approaching every subsequent blade. Mid-wake u velocities for small h are shown in figure 2.9. Figure 2.9(a) is the case where $H = 0$. Here, the boundary-layer equations are solved with $p = 0$ over an infinite flat plate with the same matching condition as $Y \rightarrow \infty$ and the

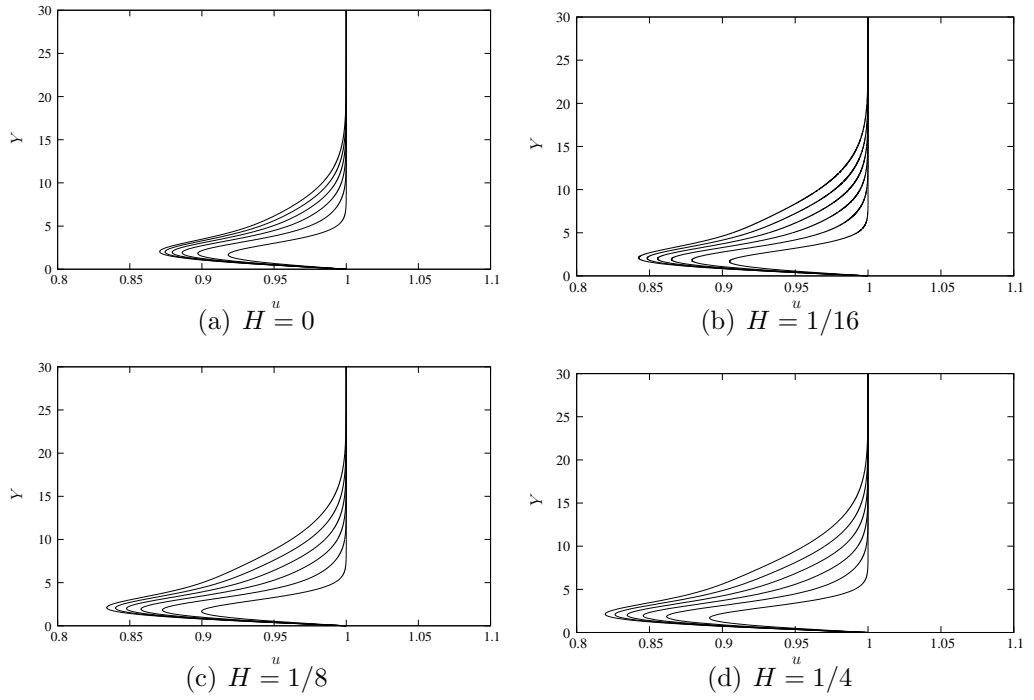


Figure 2.9: Streamwise u -velocity profiles taken at the midpoint of each wake ($N = 6$) for various ground clearances H .

no-slip conditions

$$u = 1 \quad \text{upstream and in each wake,} \quad (2.103)$$

$$u = 0 \quad \text{over each blade.} \quad (2.104)$$

We see increasing qualitative agreement in the streamwise velocity profiles midwake as $H \rightarrow 0$. For flow away from the leading and trailing edge singularities, it is expected that the special case $H = 0$ will give good representations of the flow behaviour for small H .

2.5.3 Large H

We now turn to the other extreme of a large ground clearance parameter H , which is likely to be more physically relevant. For larger values of H , the pressure solution results plotted in figure 2.5 suggest that as H increases, the pressure jumps p_0 are inversely proportional to H . Figure 2.5(j) also shows an approximately equal pressure beneath each blade. In figure 2.6, we saw that as the ground clearance increases, the total lift and friction drag

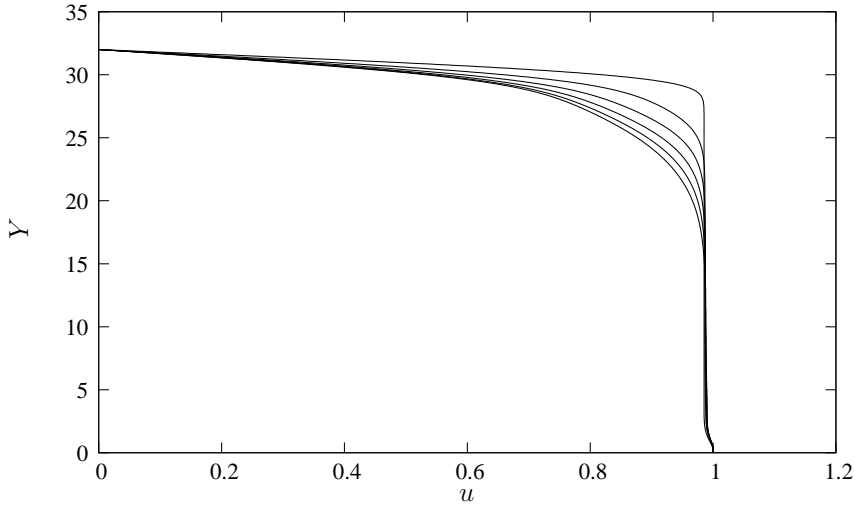


Figure 2.10: Streamwise velocity profiles taken from the mid-blade positions beneath each blade. The uppermost profile corresponds to the solution taken from the first blade.

decreases. Slip-streaming effects, where the friction drag experienced by each blade downstream returns.

We seek an asymptotic approximation to the flow behaviour for large H beneath each blade. In figure 2.10 we present the u velocity solutions at a mid-blade position between each blade and the ground. We see that there is a boundary-layer close to the underside of each blade in these profiles with the remainder of the flow for being a largely uniform, inviscid flow. This suggests that there are two normal scales present over the whole blade.

We begin with the boundary-layer on the underside of the blade. We introduce the normal coordinate y_1 in the boundary layer as $Y = H - y_1$ and then expand the velocities and pressure as

$$u(x, Y) = u_1(x, y_1) + \dots, \quad (2.105)$$

$$v(x, Y) = v_1(x, y_1) + \dots, \quad (2.106)$$

$$p(x) = \frac{1}{H}p_1(x) + \dots, \quad (2.107)$$

with the scale for p_1 suggested from the results above. Substitution into (2.55) and (2.56) reduces the governing equations to

$$u_1 \frac{\partial u_1}{\partial x} + v_1 \frac{\partial u_1}{\partial y_1} = \frac{\partial^2 u_1}{\partial y_1^2}, \quad (2.108)$$

$$\frac{\partial u_1}{\partial x} + \frac{\partial v_1}{\partial y_1} = 0, \quad (2.109)$$

at leading order. The boundary conditions to be satisfied by u_1 and v_1 are

$$u_1 = v_1 = 0 \quad \text{on } y_1 = 0, \quad (2.110)$$

$$u_1 = u_1(y_1) \quad \text{at each leading edge}, \quad (2.111)$$

$$u_1 \rightarrow 1 \quad \text{as } y_1 \rightarrow \infty. \quad (2.112)$$

For the first blade, where $u_1 = 1$, these equations and boundary conditions are exactly those consistent with a Blasius solution.

On the second normal scale, we define $\tilde{Y} = O(1)$, where $Y = H\tilde{Y}$. The flow is given by $u = 1$ subject to an $O(Re^{-1/2})$ ($= O(H^{-1})$) perturbation from the blade boundary-layer. We expand the velocity and pressure beneath each blade as

$$u(x, Y) = 1 + \frac{1}{H}u_2(x, \tilde{Y}) + \dots, \quad (2.113)$$

$$v(x, Y) = v_2(x, \tilde{Y}) + \dots, \quad (2.114)$$

$$p(x) = 0 + \frac{1}{H}p_2(x) + \dots. \quad (2.115)$$

In this instance, it is assumed that any lower order terms tend to zero as $H \rightarrow \infty$. These equations are substituted into the governing equations (2.55) and (2.56), to reveal the leading order balances

$$\frac{\partial u_2}{\partial x} = -\frac{dp_2}{dx}, \quad (2.116)$$

$$\frac{\partial u_2}{\partial x} + \frac{\partial v_2}{\partial \tilde{Y}} = 0. \quad (2.117)$$

Substituting the continuity equation (2.117) into the linearised momentum equation (2.116), followed by differentiation with respect to \tilde{Y} yields the equation

$$\frac{\partial^2 v_2}{\partial \tilde{Y}^2} = 0, \quad (2.118)$$

subject to $v_2(x, 0) = 0$ and $v_2(x, 1) = v_-^e(x)$ on $\tilde{Y} = 1$. The latter condition is a matching condition to the boundary-layer on the underside of the blade and is given by $v_-^e(x) = \delta'(x)$. Here, $\delta(x)$ is the displacement thickness of the boundary-layer on the underside of the blade, defined in this instance by

$$\delta(x) = \int_0^\infty \{1 - u_1(x, y_1)\} dy_1. \quad (2.119)$$

Integrating twice with respect to \tilde{Y} and using the boundary conditions, we find that

$$v_2(x, \tilde{Y}) = \tilde{Y} \delta'(x). \quad (2.120)$$

Hence, by continuity we have $u_2(x, \tilde{Y}) = -\delta(x) + F(\tilde{Y})$, where F is an arbitrary function of integration. The function $F = 0$ using the boundary condition $u_2 = 0$ at $\tilde{Y} = 0$. We then find that $p_2(x) = \delta(x) + c$, under each blade, with c an arbitrary constant of integration. This constant c is fixed as p_0 so that the pressure satisfies the Kutta condition at each trailing edge. The analysis for large H here agrees with the small h case presented in Purvis (2002) where an asymptotic description of the flow beneath every blade is found. As we let $H \rightarrow \infty$ in our problem, we enter the regime of Purvis (2002) and so we should expect both our analyses to agree. This is exactly the case, with the same governing equations and boundary conditions for large H (our problem) and small h (Purvis (2002)) being found.

However, in our case, after many blades have been passed, the boundary-layer will have grown large enough to interact directly with the ground, so that the two-normal scale analysis above does not hold. After N blades, with $N \gg 1$, the boundary-layer thickness will have grown beneath the blade to be of $O(N^{1/2})$. Thus, we must assure that $H \gg N^{1/2}$ for the above analysis to hold.

As we move from a blade into a wake, the pressure $p_2 = 0$. If we take the same expansions above for the second normal scale, then from (2.116), we have that $u_2 = G(\tilde{Y}) = 0$ (due to the ground boundary condition) and hence by continuity, $v_2 = F(x) = 0$, due to no normal flow at the ground. This shows that as $H \rightarrow \infty$ in our analysis, at leading order no flow is entrained into the central part of the wake and the velocity profile present at the trailing edge persists over the wake. In figure 2.11 we compare this simple result to some numerical u solutions taken from downstream distances of 0.5, 1, 1.5 from the trailing edge in wakes 3, 4, 5 and 6 of the $H = 32$ case. We see that the leading order behaviour just described agrees nicely with the result obtained. Across the wake centreline area, there is a difference in the profiles as x increases. This is explained by the fact that the boundary-layer

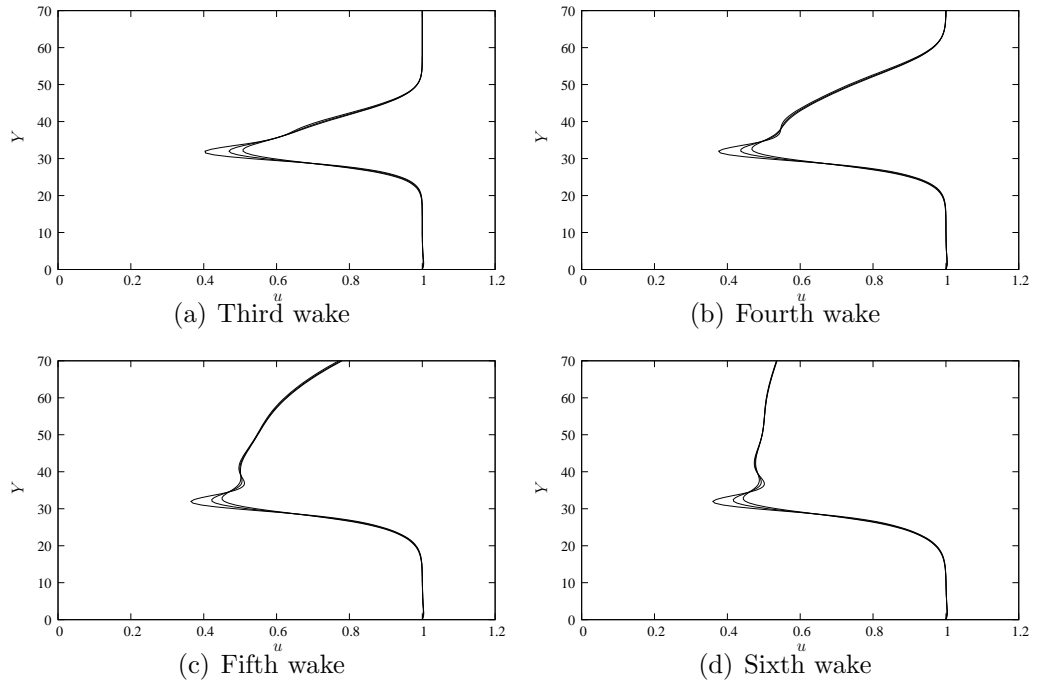


Figure 2.11: Streamwise velocity profiles at distances $x = 0.5, 1, 1.5$ downstream of the trailing edge in the third, fourth, fifth and sixth wakes. In figures (c) and (d), matching to $u = 1$ in the far-field is not shown for clarity.

equations (2.108) and (2.109) hold in this area. Fluid is entrained into this area at lower order in the expansions, allowing the slow increase in u there.

2.6 Summary

In this chapter we have extended the work by Jones & Smith (2003) to include many blades in extreme ground effect. We formulated the problem to find that the boundary-layer equations held everywhere, with an $O(1)$, non-zero pressure gradient beneath each blade and wake. We also found that a flow discontinuity arises at each leading edge to satisfy the Kutta trailing edge condition. The flow problem was solved numerically for a case of $N = 6$ blades and found that there is a viscous-inviscid interaction close to the leading edge. For small values of H , the pressure solution beneath each blade was dominated by a constant, negative pressure gradient. The lift and friction drag were found to increase as $H \rightarrow 0$, becoming constant beneath each blade considered. For larger values of H , slip-streaming was observed in

both the lift and friction drag. We then applied asymptotic analysis to the extremal cases of very small and very large H . In the small H analysis, we found that two x -scales occurred: one short scale close to the leading edge where viscous-inviscid interaction dominates, whilst the other x -scale spans the remainder of the blade and is governed by a lubrication approximation. In the case of large H , we found that two normal scales in Y dominate the flow beneath the blade: one a boundary-layer and the other a larger, inviscid scale.

In our results, we took the wake to be of length 3. We found that reducing the wake length meant that $v(x, Y)$ at the next leading edge was large enough such that the assumption $v \ll u$ was not true. Therefore, an extension would be to solve the leading edge problem for an incoming velocity profile of the form $u = u(x, Y), v = v(x, Y)$. The formulation of the leading edge region would be the same as in this chapter, although the full equations (2.19) and (2.23) would need to be solved. This would allow the effects of shorter wakes to be analysed. The slip-streaming effects seen would be increased with decreasing wake length as the oncoming velocity profile in u has less time to accelerate back towards unity. Further extensions to this work include adding shape to the blades, like in the one blade case of Jones & Smith (2003). This could be achieved by solving the problem in the same way as in that paper, or developing a different method to allow extension of the numerical techniques in this chapter. This may allow adverse pressure gradients and separation to occur if the blade shape has significant camber. It would be interesting to see whether separation would still occur downstream and whether slip-streaming effects are seen in these cases. It would also be interesting to develop an analytical short blade limit, where the wake is much longer than the blade and would still have applications within the scope of this current chapter. Blades positioned at differing heights downstream is another valid extension.

Chapter 3

Flow past many blades at a global angle of attack

3.1 Introduction

In this chapter, we consider two-dimensional high Reynolds number flow past an aligned array of blades at a global angle of attack. A global angle of attack is defined by tilting the whole horizontal alignment of blades by an angle α to the oncoming uniform stream. Ground effect, as considered in the previous chapter, is dropped in this problem.

The work in this chapter is directly motivated from applications to helicopter aerodynamics and understanding further the flow interactions caused by the continually spinning rotor blades. This chapter is relevant to a rotor blade problem where the entire helicopter rotor is tilted, as seen in forward flight. Another application arises in the correct prediction of aircraft take-off and arrival spacings, in understanding the creation of wing-tip vortices and vortex shedding and their interactions with other nearby aircraft. In particular, this work is relevant to the departure from an airport, where all aircraft ascend at an angle to the oncoming air.

Smith & Timoshin (1996a) consider the fluid flow past a symmetric rotor blade in three-dimensions. Firstly, the authors derive a similarity solution for a configuration of blades with an infinite radial span away from the central hub. The model derived is an extension of the von Karman disc-flow system of ordinary differential equations. Within this model, the radial dependence

of the radial and azimuthal velocity components is linear and is scaled out so that the governing equations for the boundary-layer problem rely on the azimuthal and normal co-ordinates, thus making this a two-dimensional problem. Then, the authors introduce a central hub to the system and consider the problem with an unbounded blade span to include radial derivatives in the flow. The effect of adding the radial velocity means that fluid flows away from the central hub and a terminal form appears numerically as distance from the central hub increases. This terminal form shows that away from the hub, the radial and azimuthal velocities increase linearly with respect to r and so the similarity solution mentioned earlier is approached. As a result, the authors are able to show that away from the central hub in the limit $r \rightarrow \infty$, the problem reduces to a quasi-two-dimensional one. Using the linear dependence in r of the radial and azimuthal velocities, the radial derivatives of velocity are removed from the governing three-dimensional boundary-layer equations. The now quasi-two-dimensional boundary-layer equations are still coupled with a three-dimensional potential flow problem in the free-stream. The authors also consider bounded blade span behaviour numerically and discuss analytical properties associated with the blade tips.

Smith & Timoshin (1996b) consider the two-dimensional problem arising in Smith & Timoshin (1996a) to include blade asymmetries through a local angle of attack. Due to the asymmetry, the boundary-layer and free-stream problems become coupled, necessitating simultaneous solution. This viscous-inviscid coupling between the inner boundary-layer and outer free-stream problem is global, spanning all blades and wakes. Numerical solutions show the appearance of slip-streaming effects on blades downstream, similar to those seen in the last chapter. There is also the appearance of a periodic many-blade limit, arising after many rotations of the rotor blades. In this limit, there is a double viscous structure in the boundary-layer, consisting of a rapidly varying region close to the blade and a larger bulk region containing mean Blasius flow. Smith & Timoshin (1996b) point out that after very many blades are passed (a number $n = O(Re^{3/5})$), an interactive multi-blade limit occurs. These far downstream effects are considered by Bowles & Smith (2000a,b). Here, the global inner-outer interaction still exists but a pressure

gradient through the boundary-layer is now supported. The full details of how the global angle of attack effects these periodic limits is addressed in later chapters.

Thus, a solid foundation of analytical and numerical work has been carried out in the previous studies above. As yet, no study has focused on features associated with a global angle of attack, a different type of asymmetry. In the studies above, this asymmetry is highlighted as an important and interesting extension to work already undertaken and furthers the general understanding of many-blade flows. This chapter includes a global angle of attack into the formulation of a multi-blade problem, to reveal for the first time what types of interaction occur between the blades.

3.2 Formulation

The current problem is that of N blades aligned at a global angle of attack α . The streamwise extent of the whole array of blades and each blade length are taken to be $x = O(1)$. The leading and trailing edge positions of the i^{th} blade are given by $x = a_i$ and $x = b_i$ respectively. For convenience, a_1 is taken to be at the origin.

The oncoming free-stream is given by $U = 1, V = 0, P = 0$. We turn the free-stream by an amount $-\alpha$, so that the blades lie along the x -axis and the free-stream velocity is given by $U = \cos \alpha, V = \sin \alpha$. This analysis takes α to be small, so that we may expand the oncoming free-stream velocity components as

$$\cos \alpha = 1 - \frac{\alpha^2}{2} + O(\alpha^4), \quad (3.1)$$

$$\sin \alpha = \alpha + O(\alpha^3). \quad (3.2)$$

In this study, α is taken to be $O(Re^{-1/2})$. Later, we will see that by choosing $\alpha = O(Re^{-1/2})$ causes a leading order change in the free-stream problem. If α is chosen to be smaller than this, then no leading order change occurs within the free-stream and hence the leading order problem is that given by Smith & Timoshin (1996b). If α is larger than this, say of $O(1)$, then we have the possibility of large scale leading and trailing edge separations.

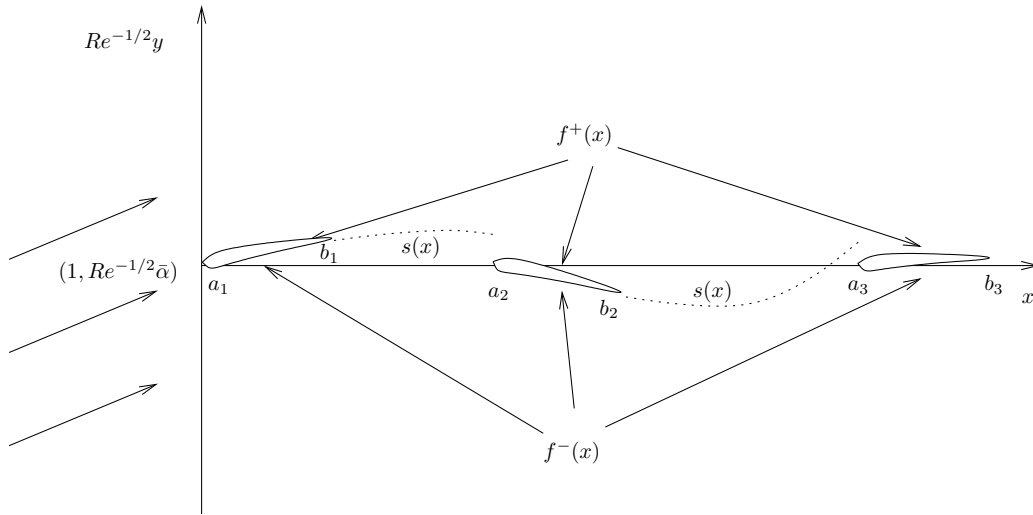


Figure 3.1: The flow configuration close to $N = 3$ thick blades considered in this analysis.

We introduce $\bar{\alpha} = O(1)$ such that $\alpha = Re^{-1/2}\bar{\alpha}$ and so to leading order the free-stream is given by $(1, Re^{-1/2}\bar{\alpha})$. In this analysis, $\bar{\alpha}$ is measured positive in an anti-clockwise direction from the aligned blades along the x -axis (see figure 3.1).

This analysis allows for slender thickness and camber to be applied to each blade, through the functions f_+ and f_- , each of $O(1)$, where $y = Re^{-1/2}f_{\pm}(x)$ gives a particular blade surface. The functions f_+ and f_- represent the shape of the upper and lower blade surfaces respectively and must satisfy $f_+(x) = f_-(x)$ at all leading and trailing edges. By scaling f_{\pm} in this way means the maximum thickness of the blades is of the same magnitude as the boundary-layer thickness and large-scale leading and trailing edge separations do not occur. The configuration close to the blades is illustrated in figure 3.1. The assumptions in the problem suggest a coupling between a viscous boundary-layer close to the blades, which is buried within and continually perturbs an inviscid free-stream.

3.2.1 The viscous boundary-layer

First, we consider the viscous boundary-layer problem. The x co-ordinate for the boundary-layer is $O(1)$ due to the streamwise extent of the blades

and $U = O(1)$ due to the oncoming free-stream. We consider the balance

$$U \frac{\partial}{\partial x} \sim \frac{1}{Re} \frac{\partial^2}{\partial y^2}, \quad (3.3)$$

within the boundary-layer due to the expected balance of inertial and diffusive streamwise terms. Hence, we deduce that the normal scale of the boundary-layer is $y = O(Re^{-1/2})$ and by continuity we have $V = O(Re^{-1/2})$. We apply a Prandtl shift to the problem, by firstly defining $Y = O(1)$ as the normal co-ordinate within the boundary-layer, where $y = Re^{-1/2}(Y + f(x))$ and $f(x)$ is given by

$$f(x) = \begin{cases} f_{\pm}(x) & \text{if } x \text{ is on a blade,} \\ s(x) & \text{if } x \text{ is in a wake.} \end{cases} \quad (3.4)$$

This allows us to remove thickness and camber effects associated with the blades from the boundary-layer calculations. Above, $y = Re^{-1/2}s(x)$ is the shape of the wake centreline which is unknown. We substitute the scaled velocity components $U = \bar{u}$ and $V = Re^{-1/2}(\bar{v} + \bar{u}f'(x))$ into the Navier-Stokes equations to obtain

$$\bar{u} \frac{\partial \bar{u}}{\partial x} + \bar{v} \frac{\partial \bar{u}}{\partial Y} = \frac{\partial^2 \bar{u}}{\partial Y^2}, \quad (3.5)$$

$$0 = \frac{\partial \bar{p}}{\partial Y}, \quad (3.6)$$

$$\frac{\partial \bar{u}}{\partial x} + \frac{\partial \bar{v}}{\partial Y} = 0, \quad (3.7)$$

which are the classical boundary-layer equations. The pressure, P , is expanded as

$$P(x, y) = 0 + Re^{-1/2}\bar{p}(x) + O(Re^{-1}), \quad (3.8)$$

due to matching with the constant free-stream pressure (taken as zero to leading order) and the leading order perturbation being of $O(Re^{-1/2})$. We have that $\bar{p} = \bar{p}(x)$ in the expansion above due to the normal momentum balance (3.6) yielding the result that \bar{p} is independent of Y . The boundary conditions to be satisfied by (3.5) and (3.7) are

$$\bar{u} = \bar{v} = 0 \quad \text{on } Y = 0 \text{ on the blades,} \quad (3.9)$$

$$\bar{u} \rightarrow 1 \quad \text{as } Y \rightarrow \pm\infty, \quad (3.10)$$

representing zero flow on the blades and matching to the free-stream. There is also a requirement of continuous velocities across each wake and a starting condition at the first leading edge, requiring

$$\bar{u} = 1, \quad \bar{v} = \bar{\alpha} \quad \text{at} \quad x = 0, \quad Y \neq 0. \quad (3.11)$$

The Prandtl shift used earlier is known across the blades through the specified blade shape functions f_{\pm} but is unknown across the wakes, due to the unknown function $s(x)$. In the case of a single blade and wake this does not affect the boundary-layer calculation, since equations (3.5) and (3.7) along with the boundary conditions (3.9) and (3.10) give a Prandtl shifted Blasius boundary-layer solution on the blade surfaces with a Goldstein wake (see Blasius (1908) and Goldstein (1930) respectively). To determine the wake-shape and complete the Prandtl shift, we would examine the free-stream problem once the boundary-layer solution is known. In the current problem of many-blades, the wake-shapes are of crucial importance. For the first blade and wake, the boundary-layer solution is exactly that described just above. However, if we do not know the position of the wake centreline at the leading edge of a subsequent blade, we cannot determine the starting conditions for the boundary-layer solution past the next blade and wake. The Y -shift of each wake flow, that is the distance between the wake centreline and position of the next leading edge, must be determined by considering the disturbances to the outer, inviscid free-stream. These disturbances are driven by entrainment velocities into the boundary-layer which cannot be determined until the boundary-layer solution is found. It is this that causes the inner-outer interaction between the viscous boundary-layer and inviscid free-stream.

To determine the entrainment velocities into the boundary-layer, we consider the normal velocity V as $Y \rightarrow \infty$. Firstly, the displacement thicknesses above (δ_+) and below (δ_-) the blade are given by

$$\delta_{\pm}(x) = \pm \int_0^{\pm\infty} \{1 - \bar{u}(x, Y)\} dY. \quad (3.12)$$

Differentiating this expression with respect to x , using the continuity equation and integrating with respect to Y , we find that as $Y \rightarrow \infty$, we have that

the normal velocity

$$\bar{v} \rightarrow \pm \delta'_{\pm}(x). \quad (3.13)$$

By using this result and the Prandtl shift equation for V given earlier, the entrainment velocity into the boundary-layer is given by

$$V = Re^{-\frac{1}{2}}(\pm \delta'_{\pm}(x) + f'(x)). \quad (3.14)$$

and provides the matching condition for the free-stream problem.

3.2.2 The inviscid free-stream

The free-stream is driven by the presence of the boundary-layer and by matching the normal velocity, the velocities and pressure are expanded as

$$U = 1 + Re^{-\frac{1}{2}}u(x, y) + O(Re^{-1}), \quad (3.15)$$

$$V = Re^{-\frac{1}{2}}(\bar{\alpha} + v(x, y)) + O(Re^{-1}), \quad (3.16)$$

$$P = 0 + Re^{-\frac{1}{2}}p(x, y) + O(Re^{-1}). \quad (3.17)$$

We see that the global angle of attack appears at leading order in the free-stream expansion, forming the rationale for taking $\alpha = O(Re^{-1/2})$. Substitution into the Navier-Stokes equations reveals the linearised Euler equations at leading order

$$\frac{\partial u}{\partial x} = -\frac{\partial p}{\partial x}, \quad (3.18)$$

$$\frac{\partial v}{\partial x} = -\frac{\partial p}{\partial y}, \quad (3.19)$$

$$\frac{\partial u}{\partial x} + \frac{\partial v}{\partial y} = 0, \quad (3.20)$$

and substituting the mass conservation equation (3.20) into (3.18) yields

$$\frac{\partial v}{\partial x} = -\frac{\partial p}{\partial y}, \quad (3.21)$$

$$\frac{\partial v}{\partial y} = \frac{\partial p}{\partial x}. \quad (3.22)$$

Hence, the leading order responses for v and p in the free-stream are governed by the Cauchy-Riemann equations. We note that (3.18) gives the solution $u = -p$, by integrating with respect to x and noting that there is no match

for u as $y \rightarrow 0$. To find v and p , we adopt a similar method used by Purvis (2002). We consider the problem in the complex plane and define the holomorphic, complex function w which is required to be bounded in the far-field as

$$w(x + iy) = p(x, y) + iv(x, y), \quad (3.23)$$

and we denote

$$w(x + i0) = p_+(x) + iv_+(x), \quad (3.24)$$

$$w(x - i0) = p_-(x) + iv_-(x), \quad (3.25)$$

as the values of w just above and below $y = 0$ respectively. The real and imaginary parts of w must satisfy the boundary conditions for the problem which are found upon matching with the boundary-layer as $y \rightarrow 0$.

The normal velocity v must match with the entrainment velocities into the boundary-layer as $y \rightarrow 0^\pm$. The boundary-layer entrainment velocities are given by equation (3.14) and so to match we require

$$\bar{\alpha} + v_\pm(x) = f'(x) \pm \delta'_\pm(x). \quad (3.26)$$

Simple rearrangement gives the boundary conditions for v in this problem as

$$v_\pm(x) = \begin{cases} s'(x) - \bar{\alpha} & \text{for } x < 0, \\ f'_\pm(x) \pm \delta'_\pm(x) - \bar{\alpha} & \text{for } x \text{ on a blade,} \\ s'(x) \pm \delta'_\pm(x) - \bar{\alpha} & \text{for } x \text{ in a wake.} \end{cases} \quad (3.27)$$

The derived boundary conditions for v differ from previous research, such as Smith & Timoshin (1996b) and Purvis (2002), through the appearance of the $\bar{\alpha}$ term. On the other hand, the conditions for the pressure are given by

$$p_+(x) = p_-(x) \quad \forall x \text{ in the wakes,} \quad (3.28)$$

$$p_+(b_i) = p_-(b_i) \quad \forall i. \quad (3.29)$$

The first condition represents pressure continuity across each wake. This is because the biggest jump in pressure across the wake centre-line is at most $O(Re^{-1})$ and applies here as $\bar{p} = \bar{p}(x)$ at leading order in the boundary-layer. The second condition represents the Kutta condition at each trailing edge. The pressures p_\pm are unknown over the blades.

3.3 Solution of the inviscid problem

3.3.1 Finding the complex function w

To solve the inviscid problem, we must solve the Cauchy-Riemann equations for v and p . We use Cauchy's integral formula, which states for a holomorphic, complex function g , in a simply connected region with closed contour Γ , described anticlockwise, and fixed point z_0 inside Γ

$$g(z_0) = \frac{1}{2\pi i} \int_{\Gamma} \frac{g(z)}{z - z_0} dz. \quad (3.30)$$

For our multi-blade problem, we take the contour Γ to be produced by the contours γ_+ and γ_- , each composed of a straight line segment from $x = -R$ to $x = R$ and a semi-circle of radius R centred on the origin in the upper and lower half planes respectively (see figure 3.2). Applying (3.30) with $z_0 = x_0 + iy_0$ lying strictly inside either γ_+ or γ_- , considering the limit $R \rightarrow \infty$ and comparing real and imaginary parts leads to

$$p(x_0, y_0) = \frac{1}{2\pi} \int_{-\infty}^{\infty} \frac{y_0[p](x) + (x - x_0)[v](x)}{(x - x_0)^2 + y_0^2} dx, \quad (3.31)$$

$$v(x_0, y_0) = \frac{1}{2\pi} \int_{-\infty}^{\infty} \frac{y_0[v](x) - (x - x_0)[p](x)}{(x - x_0)^2 + y_0^2} dx, \quad (3.32)$$

where

$$[p](x) = p_+(x) - p_-(x), \quad (3.33)$$

$$[v](x) = v_+(x) - v_-(x), \quad (3.34)$$

denote the difference between the values of p and v above and below $y = 0$. The values of $[v](x)$ for all x are given by subtraction of the boundary conditions (3.27) as

$$[v](x) = \begin{cases} 0 & \text{for } x < 0, \\ (f'_+ - f'_-)(x) + (\delta'_+ + \delta'_-)(x) & \text{on blades,} \\ (\delta'_+ + \delta'_-)(x) & \text{in wakes.} \end{cases} \quad (3.35)$$

$$(3.36)$$

Moreover, for a given boundary-layer solution these conditions are known,

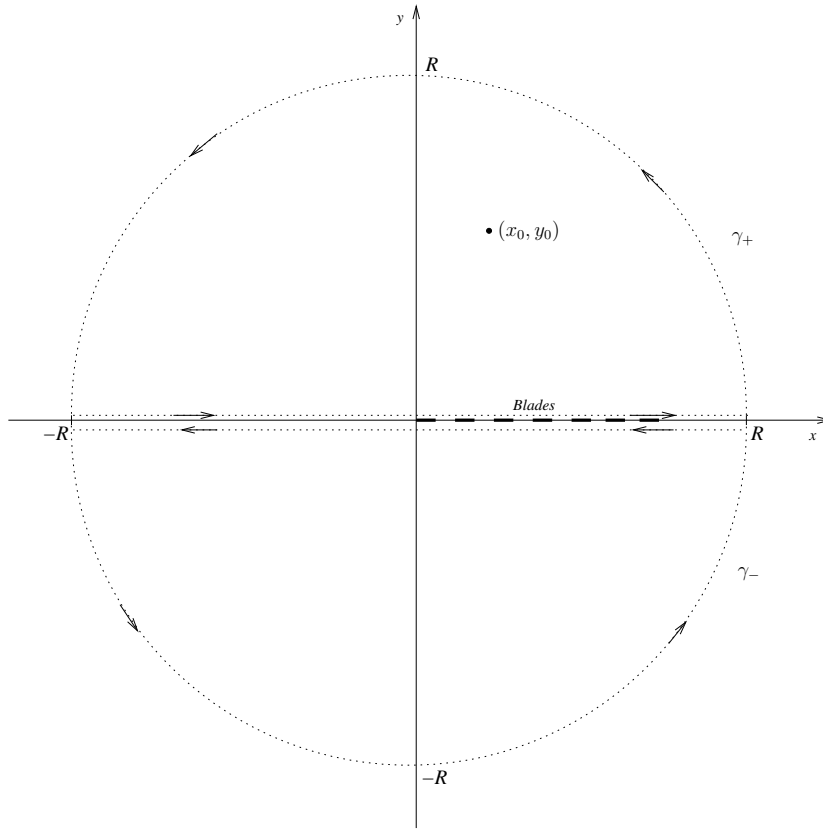


Figure 3.2: The contours γ_+ and γ_- used with Cauchy's integral formula for (x_0, y_0) lying strictly inside either γ_+ or γ_- with $y_0 \neq 0$.

since the unknown $s'(x)$ terms disappear. We also have that

$$[p](x) = 0 \quad \forall x \text{ in the wakes,} \quad (3.37)$$

$$[p](b_i) = 0 \quad \forall i \text{ (Kutta),} \quad (3.38)$$

through subtraction of the pressure continuity conditions (3.28) and (3.29). However, we do not know $[p](x)$ for any $a_i < x < b_i, \forall i$, and hence we cannot solve either of (3.31) or (3.32) for any (x_0, y_0) . To rectify this problem, the original evaluation point z_0 is now taken to lie on $y = 0$. Care must be taken as z_0 now lies on the straight line segment of the original closed contours γ_+ and γ_- in figure 3.2. Therefore, we deform the contours γ_+ and γ_- to include another small semi-circle of radius ϵ centred on $(x_0, 0)$, see figure 3.3.

We now apply Cauchy's integral formula with the double limit $R \rightarrow \infty$

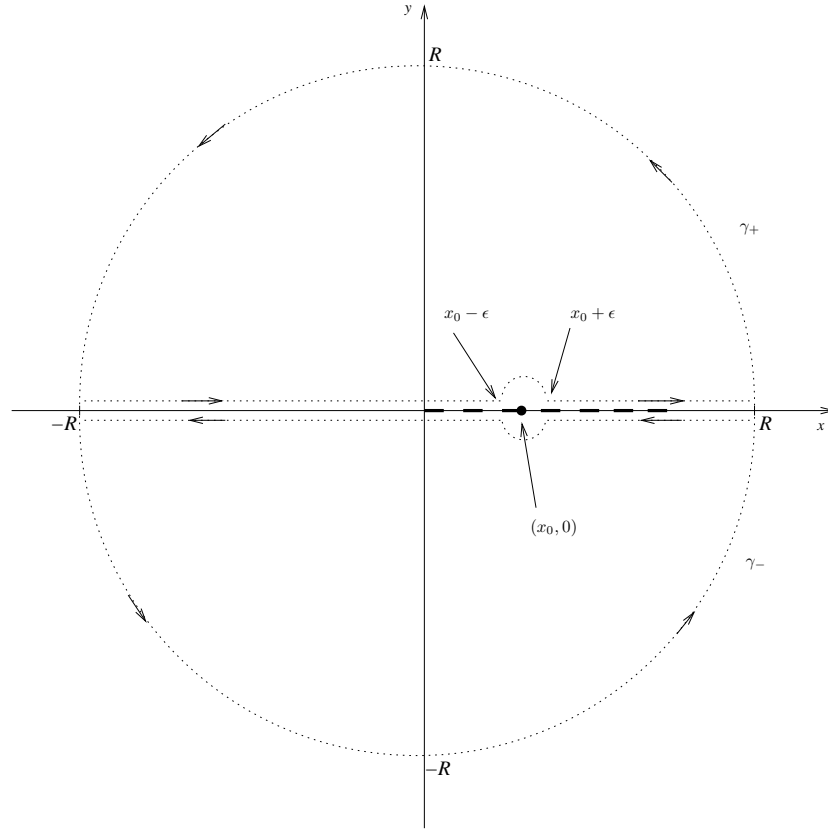


Figure 3.3: The deformed contours γ_+ and γ_- used for Cauchy's integral formula at the point $(x_0, 0)$.

and $\epsilon \rightarrow 0$ to each of $w(x + i0)$ and $w(x - i0)$ in turn, revealing

$$w(x_0 + i0) = \frac{1}{\pi i} \int_{-\infty}^{\infty} \frac{w(x + i0)}{x - x_0} dx, \quad (3.39)$$

$$w(x_0 - i0) = -\frac{1}{\pi i} \int_{-\infty}^{\infty} \frac{w(x - i0)}{x - x_0} dx. \quad (3.40)$$

By substituting $w(x + i0) = p_+(x) + iv_+(x)$ and $w(x - i0) = p_-(x) + iv_-(x)$ into the above equations (3.39) and (3.40) and adding the results we obtain

$$p_+(x_0) + iv_+(x_0) + p_-(x_0) + iv_-(x_0) = \frac{1}{\pi i} \int_{-\infty}^{\infty} \frac{[p](x) + i[v](x)}{x - x_0} dx, \quad (3.41)$$

and by comparing real and imaginary parts, we have

$$\langle p \rangle(x_0) = \frac{1}{\pi} \int_{-\infty}^{\infty} \frac{[v](x)}{x - x_0} dx, \quad (3.42)$$

$$\langle v \rangle(x_0) = -\frac{1}{\pi} \int_{-\infty}^{\infty} \frac{[p](x)}{x - x_0} dx. \quad (3.43)$$

Here

$$\langle p \rangle(x) = p_+(x) + p_-(x), \quad (3.44)$$

$$\langle v \rangle(x) = v_+(x) + v_-(x), \quad (3.45)$$

represent the sum of p and v across $y = 0$. The pressure sums $\langle p \rangle$ are given by equation (3.42) since $[v]$ is known everywhere through (3.35). By adding the boundary conditions for v_{\pm} in equation (3.27), we have that

$$\langle v \rangle(x) = \begin{cases} 2s'(x) - 2\bar{\alpha} & \text{for } x < 0, \\ (f'_+ + f'_-)(x) + (\delta'_+ - \delta'_-)(x) - 2\bar{\alpha} & \text{on blades,} \\ 2s'(x) + (\delta'_+ - \delta'_-)(x) - 2\bar{\alpha} & \text{in wakes.} \end{cases} \quad (3.46)$$

In condition (3.46), the velocity sums are unknown across each wake and for $x < 0$ due to the derivative of the unknown wake-shape appearing in the boundary conditions. Equation (3.43) may be used to find $\langle v \rangle(x)$ in the wakes, once $[p](x)$ is known for all x . The pressure differences are zero at each trailing edge and in each wake by the Kutta condition (3.38) and pressure continuity (3.37) respectively but is unknown over each blade. We may recover the pressures $p_+(x)$ and $p_-(x)$ once $\langle p \rangle(x)$ and $[p](x)$ are known at all x using the simple relation

$$p_{\pm}(x) = \frac{1}{2}(\langle p \rangle(x) \pm [p](x)), \quad (3.47)$$

and similarly for v_{\pm} .

Equation (3.43) is a Fredholm equation of the first kind for $[p]$ and the integrand has a Cauchy kernel containing a singularity at $x = x_0$. This makes (3.43) very difficult to solve, given the possibility of non-unique solutions. However, the known boundary conditions on $[p]$ allow progress to be made. On applying pressure continuity across the wakes (3.37), (3.43) reduces to

$$\langle v \rangle(x_0) = -\frac{1}{\pi} \sum_{i=1}^N \int_{a_i}^{b_i} \frac{[p](x)}{x - x_0} dx. \quad (3.48)$$

Now, Muskhelishvili (1946) gives the solution of

$$k(x_0) = \frac{1}{\pi} \int_L \frac{\kappa(x)}{x - x_0} dx, \quad (3.49)$$

where L is composed of N line segments running from a_i to b_i , with the constraint $\kappa(b_i) = 0$ as

$$\kappa(x_0) = -\frac{S^{-\frac{1}{2}}(x_0)}{\pi} \int_L \frac{S^{\frac{1}{2}}(x)k(x)}{x - x_0} dx, \quad (3.50)$$

where

$$S(x) = \prod_{i=1}^N \left| \frac{x - a_i}{x - b_i} \right|. \quad (3.51)$$

This is exactly the problem here, with $k \equiv \langle v \rangle$, $\kappa \equiv -[p]$ and L is all of the blade surfaces. The constraint $\kappa(b_i) = 0$ is exactly the Kutta condition (3.38) for the differences in pressure being zero at each trailing edge. Thus,

$$[p](x_0) = \frac{S^{-\frac{1}{2}}(x_0)}{\pi} \sum_{i=1}^N \int_{a_i}^{b_i} \frac{S^{\frac{1}{2}}(x) \langle v \rangle(x)}{x - x_0} dx, \quad (3.52)$$

is an integral equation for the values of $[p]$ relying on $\langle v \rangle$ over the blades, which are known through (3.46). Once the pressure differences are calculated for a point on the blades, (3.48) gives the velocity sums $\langle v \rangle(x)$ across the wakes.

To determine $s(x)$, the unknown wake-shapes in the Prandtl-shift, we rearrange (3.46) in the wakes for $s'(x)$, and integrate with respect x to reveal an equation for the i^{th} wake-shape as

$$s(x) = s(b_i) + \frac{1}{2} \int_{b_i}^x \{ \langle v \rangle(x') - (\delta'_+ - \delta'_-)(x') + 2\bar{\alpha} \} dx', \quad (3.53)$$

which completes the Prandtl-shift and the whole viscous solution.

3.3.2 Summary of the full problem

To summarise the full problem, we must solve the boundary-layer equations

$$\bar{u} \frac{\partial \bar{u}}{\partial x} + \bar{v} \frac{\partial \bar{u}}{\partial Y} = \frac{\partial^2 \bar{u}}{\partial Y^2}, \quad (3.54)$$

$$\frac{\partial \bar{u}}{\partial x} + \frac{\partial \bar{v}}{\partial Y} = 0, \quad (3.55)$$

subject to the boundary conditions

$$\bar{u} = \bar{v} = 0 \quad \text{on } Y = 0 \text{ on the blades,} \quad (3.56)$$

$$\bar{u} \rightarrow 1 \quad \text{as } Y \rightarrow \pm\infty. \quad (3.57)$$

There is a starting condition for the flow at the first blade, given by

$$\bar{u} = 1, \quad \bar{v} = \bar{\alpha} \quad \text{at } x = 0, \quad Y \neq 0, \quad (3.58)$$

whilst for the other blades, the starting conditions are unknown due to the unknown wake-shapes $s(x)$ appearing in the Prandtl shift.

To rectify this problem, we must find the pressure differences across the blades through the integral equation

$$[p](x_0) = \frac{S^{-\frac{1}{2}}(x_0)}{\pi} \sum_{i=1}^N \int_{a_i}^{b_i} \frac{S^{\frac{1}{2}}(x) \langle v \rangle(x)}{x - x_0} dx, \quad (3.59)$$

where

$$S(x) = \prod_{i=1}^N \left| \frac{x - a_i}{x - b_i} \right|. \quad (3.60)$$

This allows us to calculate the unknown velocity sums across the wake and hence the unknown wake-shapes through the relation

$$s(x) = s(b_i) + \frac{1}{2} \int_{b_i}^x \{ \langle v \rangle(x') - (\delta'_+ - \delta'_-)(x') + 2\bar{\alpha} \} dx', \quad (3.61)$$

and complete the Prandtl shift within the boundary-layer.

3.4 Numerical methods

3.4.1 Boundary-layer

To solve the boundary layer problem, we use a finite difference approach, akin to that used in the previous chapter, Smith & Timoshin (1996b) and Purvis (2002). A regular grid with spacings Δx and ΔY in the x and Y directions is set up, so that $(x_i, Y_j) = (i\Delta x, j\Delta Y)$ represents the $i^{\text{th}}, j^{\text{th}}$ mesh point. Backward differences in x and centred differences in Y derivatives are used to discretise (3.54) and (3.55) as

$$\bar{u}_{i-1}^j \left(\frac{\bar{u}_i^j - \bar{u}_{i-1}^j}{\Delta x} \right) + \bar{v}_{i-1}^j \left(\frac{\bar{u}_i^{j+1} - \bar{u}_i^{j-1}}{2\Delta Y} \right) = \frac{\bar{u}_i^{j+1} - 2\bar{u}_i^j + \bar{u}_i^{j-1}}{(\Delta Y)^2}, \quad (3.62)$$

$$\frac{\bar{u}_i^j - \bar{u}_{i-1}^j}{\Delta x} + \frac{\bar{v}_i^{j+1} - \bar{v}_i^{j-1}}{2\Delta Y} = 0, \quad (3.63)$$

where \bar{u}_i^j and \bar{v}_i^j represent the values of \bar{u} and \bar{v} at $(i\Delta x, j\Delta Y)$. We use the same method as outlined in Chapter 2 to find the solution at each x_i , to first find \bar{u} using (3.62) and the boundary conditions (3.56) and (3.57). Once \bar{u} is known, \bar{v} may be calculated using the discretised continuity equation (3.63). The solution for all x_i is obtained by employing a streamwise sweep in x and using the double-stepping method of Smith & Timoshin (1996b) used in Chapter 2 to gain second-order accuracy in x .

As we encounter each leading edge within the sweep, we must apply a Y -shift to the incoming velocity profile. This is because all the wake-shapes are unknown and upon applying the Prandtl shift we do not know the position of the next leading edge in relation to the oncoming flow within

the boundary-layer. The correct boundary layer solution is determined by Y -shifting the entire oncoming velocity profiles at the leading edge before the sweep continues over the next blade-wake. Applying each Y -shift is achieved using cubic splines on the velocity components, followed by shifting the profiles by an amount Y_s . To do this, each Y_j is shifted by an amount Y_s at the leading edge to set the new starting condition. This is how the influence of $\bar{\alpha}$ permeates through the boundary-layer solution, via the viscous-inviscid coupling. The Y -shifts are calculated using (3.61) in the inviscid solution and is described in the next section.

To achieve accuracy in \bar{u} and \bar{v} it was necessary to set values of $\Delta x = 0.005$, $\Delta Y = 0.05$ and $-400 \leq j \leq 400$, with finer grid resolutions taken as a check to confirm accuracy. If $\bar{\alpha} > 1$ with $N \geq 5$, a finer grid resolution of $\Delta x = 0.001$, $\Delta Y = 0.01$ and $-4000 \leq j \leq 4000$ was needed for accuracy, especially far downstream.

3.4.2 Inviscid Solution

To determine the Y -shifts, the values of $[p]$ across each blade must first be found from the integral equation (3.52). The integrand in equation (3.59) has a singularity at $x = x_0$ and a removable square-root singularity in S at each trailing edge. To remove the square root singularity, we introduce $\hat{S}(x)$ such that

$$S(x) = \left| \frac{x - a_i}{x - b_i} \right| \hat{S}(x), \quad (3.64)$$

$$\hat{S}(x) = \prod_{j=1, j \neq i}^N \left| \frac{x - a_j}{x - b_j} \right|, \quad (3.65)$$

and make the change of variables

$$x = l_j \sin^2 \theta + a_j, \quad (3.66)$$

$$x_0 = l_i \sin^2 \phi + a_i, \quad (3.67)$$

as used by Purvis (2002). Here $l_j = b_j - a_j$ represents the length of the j^{th} blade. Consequently, (3.59) becomes

$$[p](l_i \sin^2 \phi + a_i) = -\frac{2S(l_i \sin^2 \phi + a_i)^{-\frac{1}{2}}}{\pi} \sum_{j=1}^N \int_0^{\frac{\pi}{2}} \frac{l_j \sin^2 \theta \langle v \rangle (l_j \sin^2 \theta + a_j) \hat{S}^{\frac{1}{2}}(l_j \sin^2 \theta + a_j)}{l_j \sin^2 \theta - l_i \sin^2 \phi + a_j - a_i} d\theta. \quad (3.68)$$

The only remaining singularity is when $\theta = \phi$ and $i = j$ and is a Cauchy Principal Value integral. We evaluate the Principal Value integral by choosing all ϕ evaluation points as the mid-points of each pair of θ nodes. By choosing the ϕ evaluation points in this way, all the integrals above can be calculated numerically using a trapezoidal rule. For accuracy in calculating $[p]$, a step-size $\Delta\theta = \pi/1000$ was needed, with tests carried out on smaller grid sizes of $\Delta\theta$ to confirm accuracy.

Calculation of the velocity sums $\langle v \rangle$ is straightforward. We make the same substitution for x as in (3.68) to give the values of the velocity sums across the wake as

$$\langle v \rangle(x_0) = -\frac{1}{\pi} \sum_{j=1}^N \int_0^{\frac{\pi}{2}} \frac{[p](l_j \sin^2 \theta + a_j)}{l_j \sin^2 \theta + a_j - x_0} l_j \sin(2\theta) d\theta. \quad (3.69)$$

Since the evaluation point x_0 now lies in the wake, no singularities exist in any integral and $\langle v \rangle$ can again be found using the trapezoidal rule. Finally, we compute the wake-shapes through (3.61) and hence we calculate the Y -shifts to be applied in the boundary-layer as

$$Y_s(a_{i+1}) = s(b_i) + \frac{1}{2} \int_{b_i}^{a_{i+1}} \left\{ \langle v \rangle(x') - (\delta'_+ - \delta'_-)(x') + 2\bar{\alpha} \right\} dx'. \quad (3.70)$$

3.4.3 Solution algorithm

To solve the discretised problems, we adopt an iterative approach to deal with the coupled nature of the problem and to find the Y -shifts. We find the solution for a particular value of $\bar{\alpha}$ using the following algorithm.

1. Guess all the Y -shifts (initial guesses of 0 everywhere are sufficient).
2. For the current Y -shifts, solve the boundary-layer problem, interpolating the velocity profiles and shifting using cubic splines at each leading edge.

3. Compute the values of $\langle v \rangle(x)$ across the blades arising from the boundary-layer using (3.46).
4. Hence, find $[p](x)$ across each blade using (3.68) and hence $\langle v \rangle(x)$ across each wake using (3.43).
5. Calculate the new Y -shifts and test for convergence by comparing them to the Y -shifts of the previous iteration.
6. If convergence is not achieved in the Y -shifts, then return to 2. and re-sweep, or finish.

In our code, convergence is achieved in the Y -shifts when the absolute error between successive calculations of the Y -shifts is less than 10^{-6} . We find that the number of iterations needed to achieve this varied depending on the value of $\bar{\alpha}$ and the number of blades present. When only two or three blades are present, convergence is achieved after three or four iterations rising to around seven or eight iterations for larger values of $\bar{\alpha}$ in a configuration of ten or more blades. In all our computations, the initial guesses of zero Y -shifts always gave a converged solution.

3.5 Results

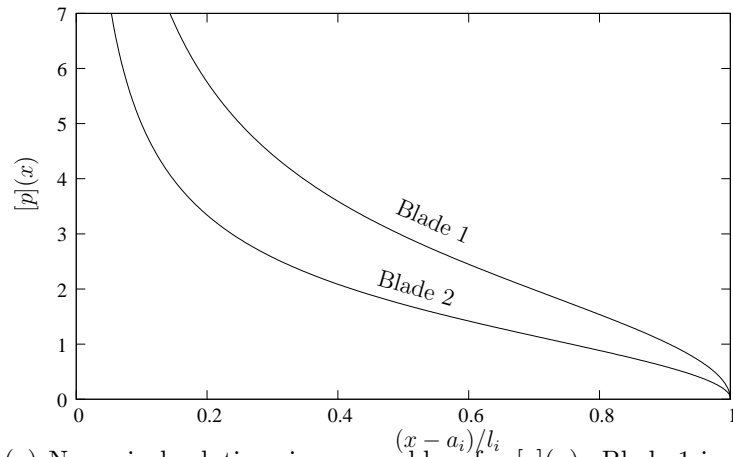
Results are presented in three parts. Firstly, to test for accuracy we compare solutions found using our method to others' previously published results. In the second part, we present solutions for a variety of angles $\bar{\alpha}$ for $N = 5$ flat, horizontal blades ($f_+(x) = f_-(x) = 0$) and wakes all of length unity, although the numerical procedure described in the previous section is suitable for blades and wakes of varying lengths. This configuration helps to pick out the underlying features of such many-blade flows. In the final part, we present solutions for a global angle of attack with $N = 10$ blades, and perform some computations for short and thick blades which are useful in helicopter aerodynamics. There is reflective symmetry in the set of solutions about $y = 0$ with respect to $\bar{\alpha}$ and $-\bar{\alpha}$, so only results for $\bar{\alpha} \geq 0$ are presented.

3.5.1 Method validation

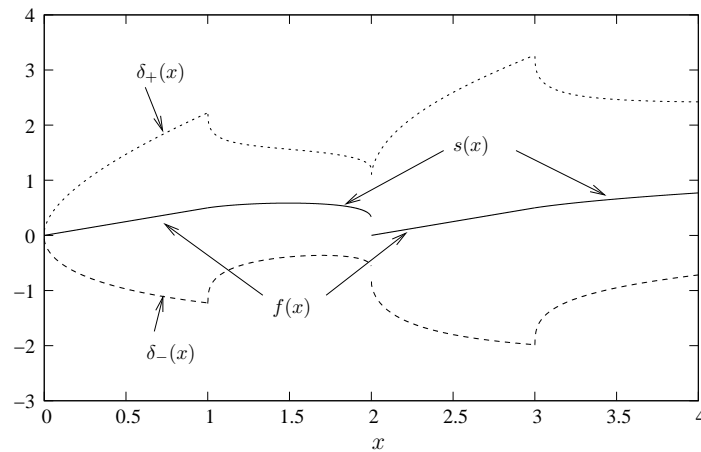
First, we test the numerical code against results illustrated in previous research. The first test case is the blade configuration in figure 5 of Smith & Timoshin (1996b), where there are $N = 2$ blades present with the first and second blades of lengths 0.5 and 1.5 respectively. The wake is of length unity and both blades have a local angle of attack of one. We present the computed result for $[p]$ in figure 3.4(a) and on viewing the solution found by Smith & Timoshin (1996b), we see very good agreement. The second test has blades and wakes of length unity with a local angle of attack of 0.5, as seen in Purvis & Smith (2004). The test case chosen matches that of figure 7(a) of Purvis & Smith (2004) for a large value of the ground clearance parameter h in that paper. Although ground effect is not taken into account in our problem, we see that the result given in figure 3.4(b) shows very good agreement, which is as expected since the ground effect vanishes as $h \rightarrow \infty$. The final comparison was made against the configuration of blades given in figure 3(e) of Bhattacharyya & Smith (2004). The blade and wake lengths are the same as the Smith & Timoshin (1996b) example above, but with the second blade shifted in y by $1.5/\sqrt{200}$. Bhattacharyya & Smith (2004) use full Navier-Stokes simulations to calculate the wake-shapes. Our calculation in figure 3.4(c) shows good agreement to that presented in Bhattacharyya & Smith (2004).

3.5.2 Solutions for $N = 5$ flat blades

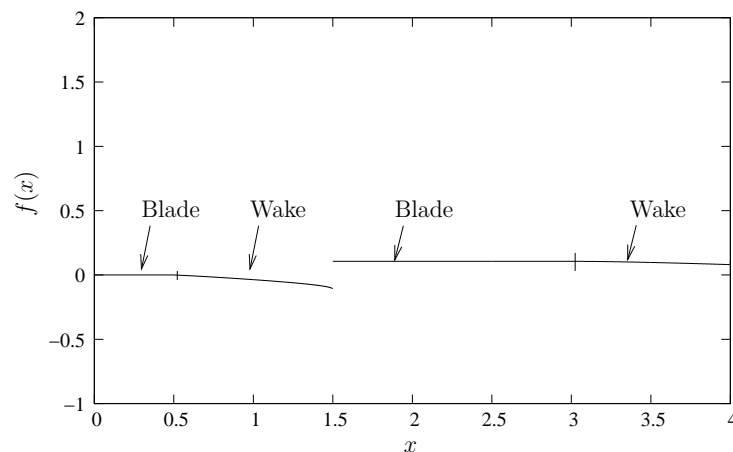
Before introducing a non-zero global angle of attack into the problem, we first outline the symmetric solution found using our numerical code. The symmetric solution is found in our code by setting the parameter $\bar{\alpha} = 0$. The results gained compare well to those seen in Smith & Timoshin (1996b). For the symmetric configuration, the Prandtl shift is known as $s(x) = 0$ in every wake and hence the boundary-layer flow above and below the blades are identical. Since the Prandtl shift is known, then the whole boundary-layer problem may be found separately from the free-stream. The velocity sums $\langle v \rangle(x) = 0$ and so there is no pressure difference $[p](x)$ to find over the



(a) Numerical solutions in our problem for $[p](x)$. Blade 1 is of length 0.5 and blade 2 is of length 1.5.



(b) Wake-shape and displacement thicknesses with a local angle of attack of 0.5 and blade and wake lengths of unity.



(c) Wake-shapes calculated to compare with full Navier-Stokes simulations. Blade 1 has length 0.5, wake 1 has length unity and blade 2 has length 1.5. Blade 2 is shifted in Y by 0.1.

Figure 3.4: Computed results for the test cases taken from (a) Smith & Timoshin (1996b), (b) Purvis & Smith (2004) and (c) Bhattacharyya & Smith (2004).

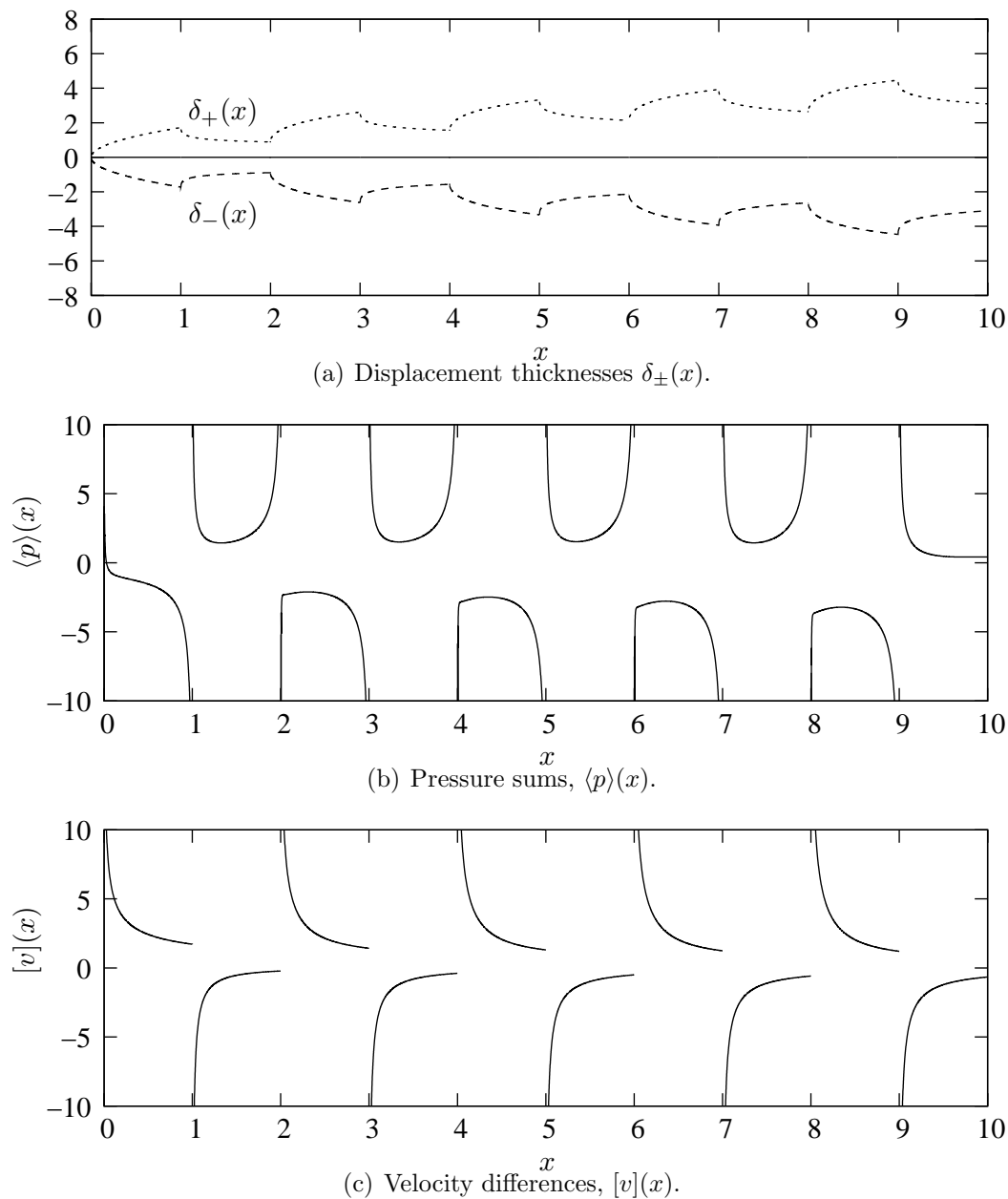


Figure 3.5: Displacement thickness, pressure sums $\langle p \rangle(x)$ and velocity differences $[v](x)$ calculated for the symmetric problem with $N = 5$ flat blades and wakes of length unity. The flat blades lie at x values satisfying $0 \leq x \leq 1, 2 \leq x \leq 3, \dots$.

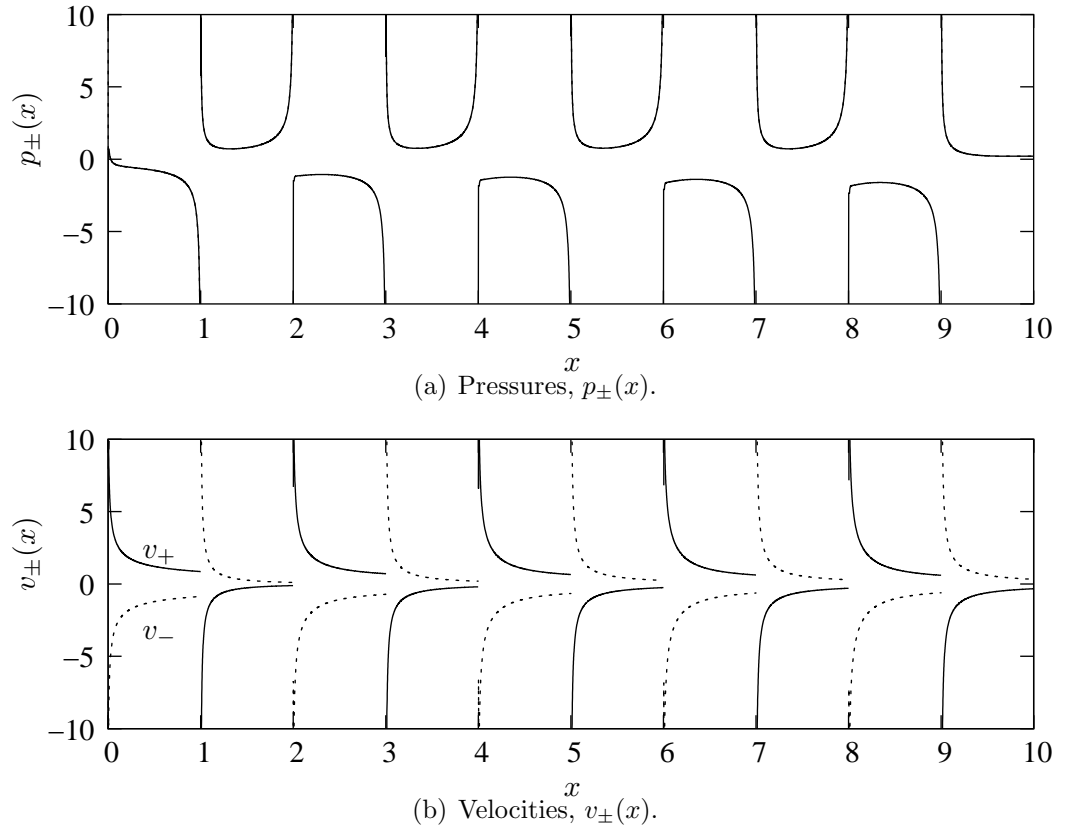


Figure 3.6: Pressures $p_{\pm}(x)$ and velocities $v_{\pm}(x)$ calculated for the symmetric problem with $N = 5$ flat blades and wakes of length unity.

blades. Thus the symmetric case is a decoupled problem. Solutions for the displacement thicknesses $\delta_{\pm}(x)$, velocity differences $[v]$ and pressure sums $\langle p \rangle$ are given in figure 3.5. The displacement thicknesses of the boundary-layer are plotted in figure 3.5(a) and we see that there is reflective symmetry about the x -axis, as expected. The pressure sums calculated in figure 3.5(b) have singularities at each leading and trailing edge. This is caused by the discontinuous nature of the displacement gradient at the leading and trailing edges. We find that the velocity differences, $[v]$ also possess these singularities, with the profile being monotonically decreasing over the blades and monotonically increasing within each wake.

The pressures p_{\pm} and velocities v_{\pm} for the symmetric problem are given in figure 3.6. Since $[p](x) = 0$ in this symmetric problem, we have that $p_+(x) = p_-(x) = \langle p \rangle(x)/2$ and is illustrated in figure 3.6(a). The velocities $v_{\pm}(x)$ are plotted in figure 3.6(b). Since $\langle v \rangle(x) = 0$, then we have that

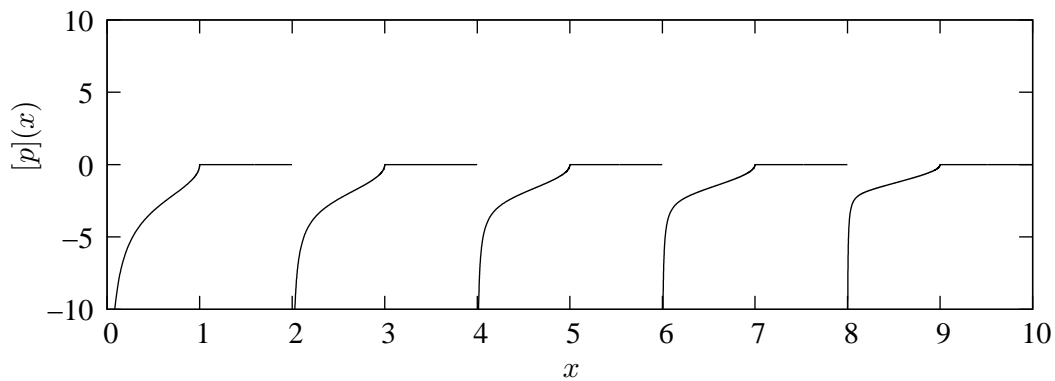
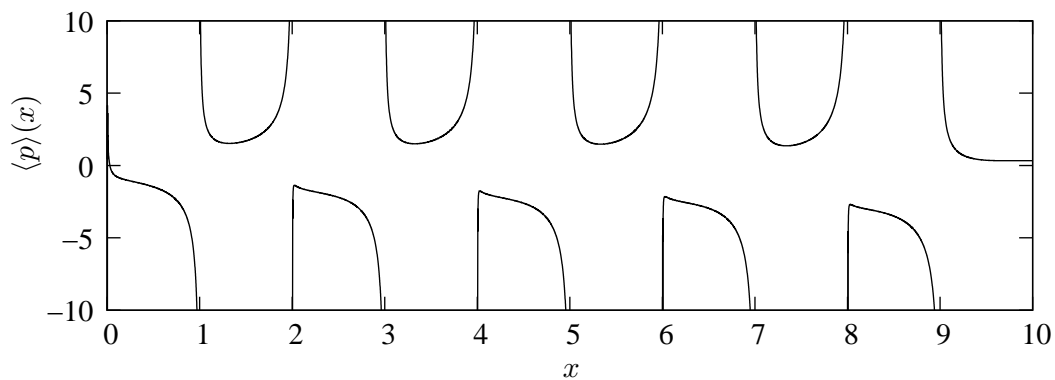
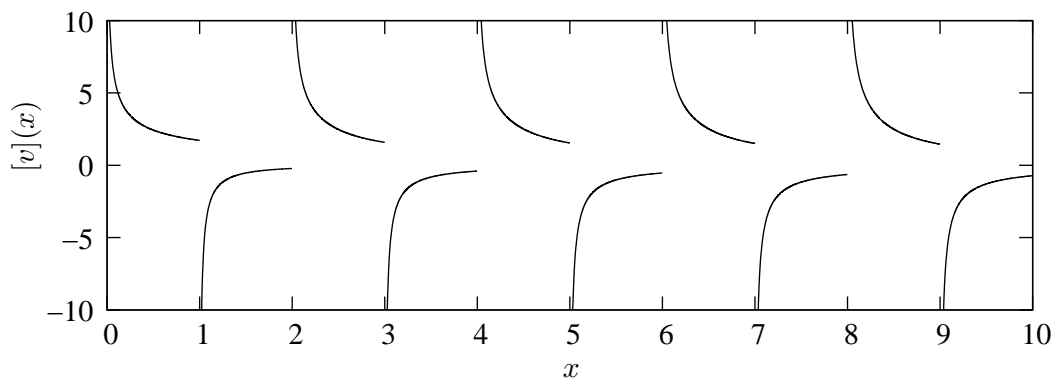
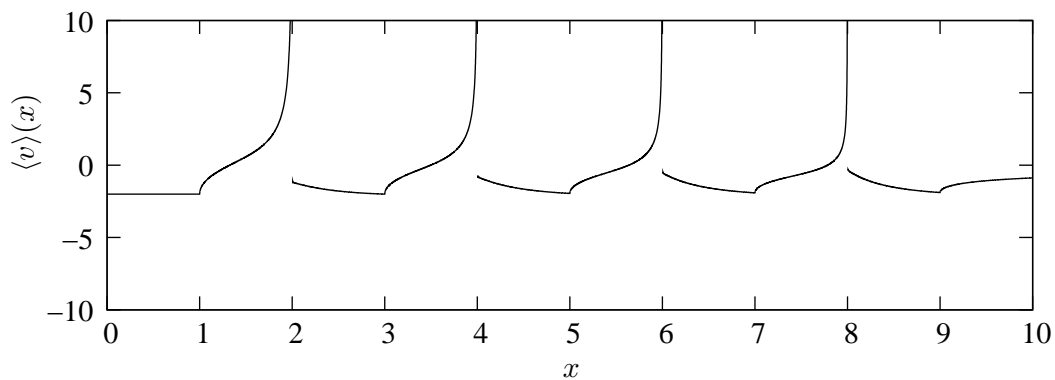
(a) Pressure differences, $[p](x)$.(b) Pressure sums, $\langle p \rangle(x)$.(c) Velocity differences, $[v](x)$.(d) Velocity sums, $\langle v \rangle(x)$.

Figure 3.7: Computed pressure differences and sums, $[p]$ and $\langle p \rangle$ and velocity differences and sums for $[v]$ and $\langle v \rangle$ with $\bar{\alpha} = 1, N = 5$.

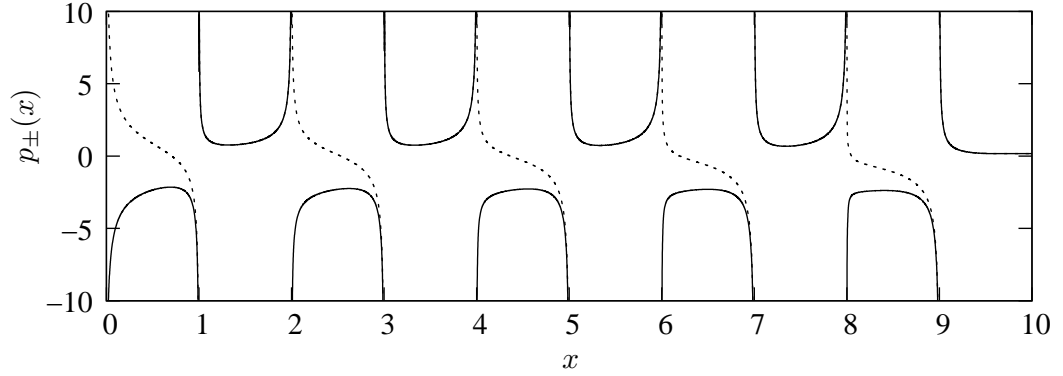
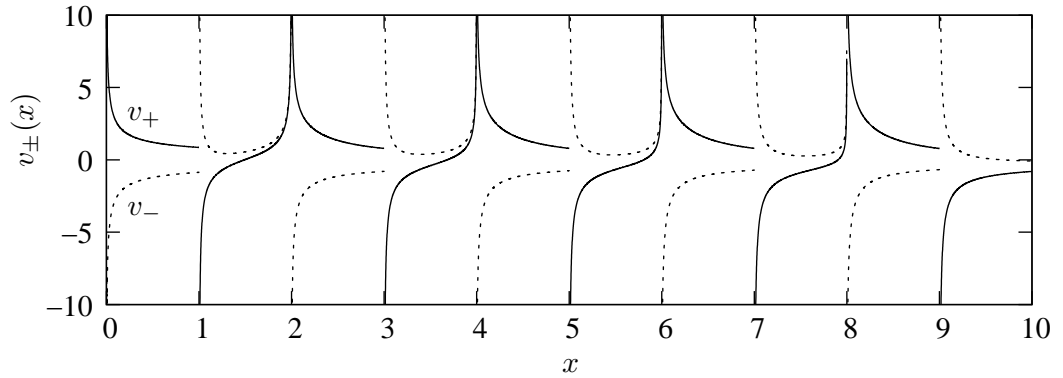
(a) Pressures, $p_{\pm}(x)$.(b) Velocities, $v_{\pm}(x)$.

Figure 3.8: Pressures and velocities $p_{\pm}(x)$ and $v_{\pm}(x)$ for $N = 5$ flat blades at a global angle of attack $\bar{\alpha} = 1$.

$v_{\pm}(x) = \pm[v](x)/2$. The result in figure 3.6(b) shows this through symmetry about the x -axis. The differences $[v]$ are calculated using the derivatives of the displacement thicknesses from the boundary-layer. Over a blade, we expect outflow from the boundary-layer to the free-stream, meaning that $v_+(x) > 0$ and $v_-(x) < 0$ over the blades and hence $[v](x) = v_+(x) - v_-(x) > 0$ over each blade. This situation is reversed in the wakes.

In figure 3.7, we compute and present the solutions for $\langle p \rangle$, $\langle v \rangle$, $[p]$ and $[v]$ found for the case $\bar{\alpha} = 1$, a non-zero global angle of attack. In figure 3.7(a), we see that a pressure difference between the upper and lower surfaces of the blade occurs, with $[p](x) < 0$. We see at the trailing edges (i.e. $x = 1, 3, 5, 7, 9$) that the Kutta condition, requiring the pressure difference to be zero there, is clearly satisfied. The computed pressure sums and velocity differences in figures 3.7(b) and show similar characteristics as described in the symmetric case above. The computed velocity sums $\langle v \rangle$ are monotonic

decreasing over each blade (except the first, where $\langle v \rangle = -2\alpha$) and monotonically increasing in each wake. The velocity sums in each wake are calculated using the integral equation (3.42) after finding the pressure differences in figure 3.7(a).

The actual pressures $p_{\pm}(x)$ and velocities $v_{\pm}(x)$ using the computed sums and differences are given in 3.8. As seen in the symmetric case, the singularities present at the leading and trailing edges still reside in the inviscid problem. An analysis valid close to the singularities is given by Smith & Timoshin (1996b). The analysis models the boundary-layer flow close to the leading and trailing edges in two normal flow regions. At the leading edge, the first normal scale is small with $Y = O(Re^{-1/4})$ and is viscous due to the onset of the no-slip boundary condition at the leading edge. The second normal scale is $Y = O(1)$ and is predominantly inviscid. The analysis was undertaken to confirm that the correct behaviour of the solutions had been properly captured by the numerical code as flow passes over the singularities. Since our test cases agree well with the solutions found in Smith & Timoshin (1996b), this same analysis is expected to hold close to the singularities in this instance.

In figures 3.9 - 3.12, the boundary-layer solution through displacement thicknesses, computed wake-shapes and the pressures p_{\pm} for various values of $\bar{\alpha}$ are presented. As expected, greater deflections in the wake-shape are observed when $\bar{\alpha}$ is increased. The presence of a non-zero value of $\bar{\alpha}$ in the code now couples the outer free-stream and inner boundary-layer solution procedures.

The results show sheltering effects for each value of $\bar{\alpha}$, as in each case, the Y -shift at each leading edge decreases after passing a few blades. For $\bar{\alpha} = 0.05$ in figure 3.9(a), only a small deflection of the wake-shape is seen, as expected. As $\bar{\alpha}$ is increased to $\bar{\alpha} = 0.5$, greater deflection of the wake-shape is seen. In figure 3.11, solutions for larger values of $\bar{\alpha}$ are presented. For the values of $\bar{\alpha} = 4, 8$, we see that a Blasius boundary-layer forms beneath each blade. For these cases of $\bar{\alpha}$, the wake-shape is considerably deflected and hence the incoming flow to each subsequent leading edge is a uniform flow. As downstream distance is increased, the sheltering effects observed

on passing more blades causes the Y -shift to drop. When this happens, the Blasius behaviour observed under each blade will cease, due to the non-uniform incoming flow now present there.

The pressures p_+ and p_- in figures 3.10 and 3.12 are discontinuous at all leading and trailing edges (but still satisfy the Kutta condition at the trailing edge), as seen in the symmetric case. As $\bar{\alpha}$ is increased, the pressure solutions show a general increase in the difference between p_+ and p_- over the blades. As with the wake-shapes, slip-streaming effects are apparent as the difference between p_+ and p_- solutions becomes less after more blades are passed. Results for the total lift felt by each blade, given by the integral of $-[p]$ over the whole blade is given in figures 3.13(a) and (b). Slip-streaming effects are clear, with the decrease of lift on blades downstream. For large values of $\bar{\alpha}$, the friction drag on each blade, τ , (given by equation (2.79) in Chapter 2) appears equal for each blade. This suggests a near Blasius boundary-layer is created above and below the first few blades. For smaller $\bar{\alpha}$, the friction drag calculated agrees with the symmetric case of blades in Smith & Timoshin (1996b).

3.5.3 Short, thick and many blades

With the code developed for blades of variable length and blade thicknesses, we turn to finding solutions to a problem where the blade is much shorter than the wake. This configuration has applications to the spinning rotor on a helicopter. Solutions to problems with $\bar{\alpha} = 0.5$ and $\bar{\alpha} = 2$ are presented in figure 3.14. The length of each blade is taken to be 0.25 with the wake of length 1.75. We see that the wake-shape and pressure solutions take on a very similar form past all blades in the configuration. The shortness of the blades means that, compared to the previous case, the boundary-layer created over the blades has less streamwise distance to grow. With a long wake, the global angle of attack exerts itself on the wake-flow over a longer distance in x . This causes a greater deflection of the wake-shapes compared to the solutions for the same values of $\bar{\alpha}$ in the previous section. Then, each blade experiences a uniform flow close to both the upper and lower blade surfaces. Hence, the sheltering effects present (reported in the previous section) are reduced, by

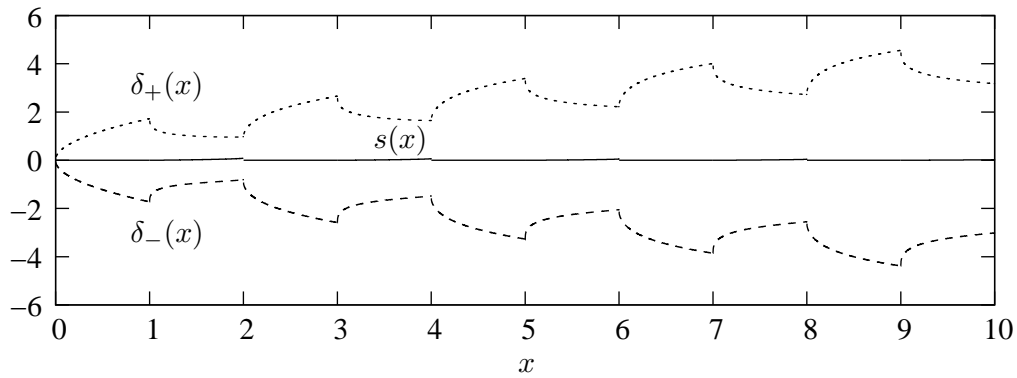
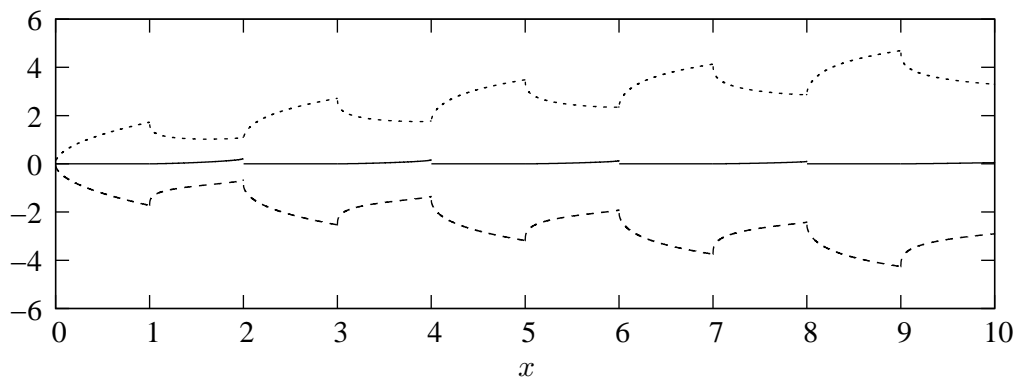
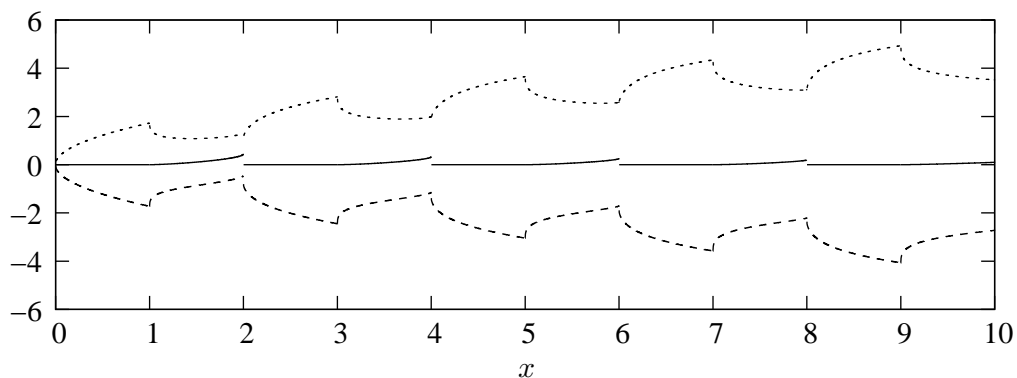
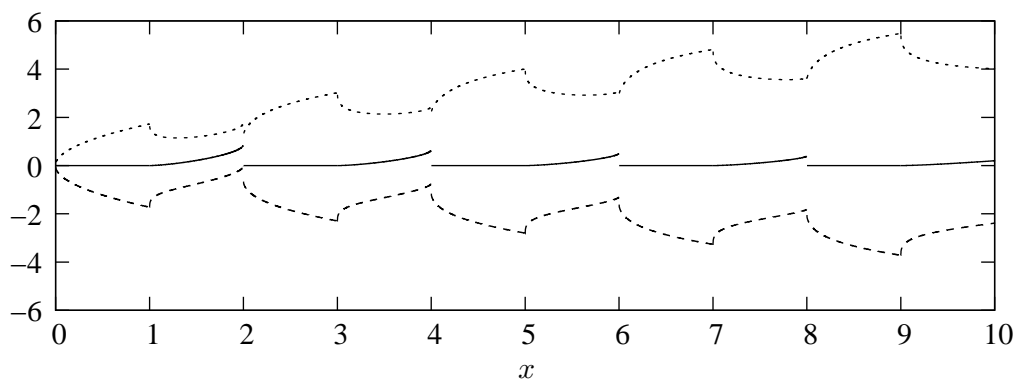
(a) $\bar{\alpha} = 0.05$.(b) $\bar{\alpha} = 0.125$.(c) $\bar{\alpha} = 0.25$.(d) $\bar{\alpha} = 0.5$.

Figure 3.9: Boundary-layer displacement thicknesses δ_+ , δ_- and computed wake-shapes $s(x)$ for values of small $\bar{\alpha}$ for $N = 5$ flat blades and wakes of length unity.

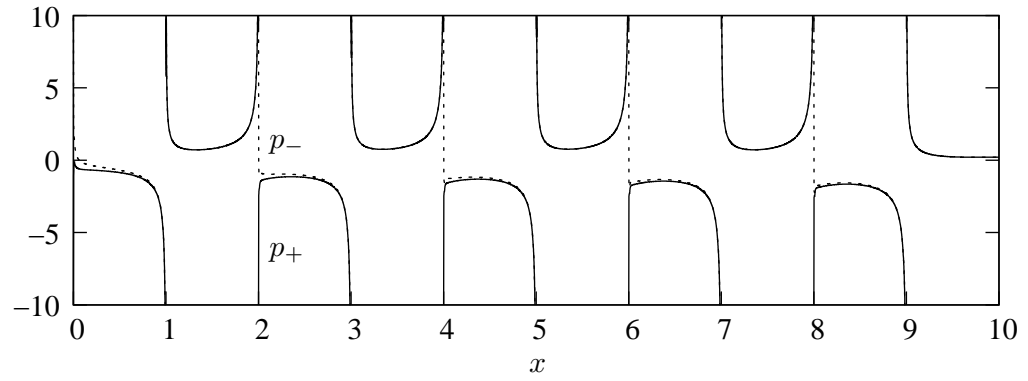
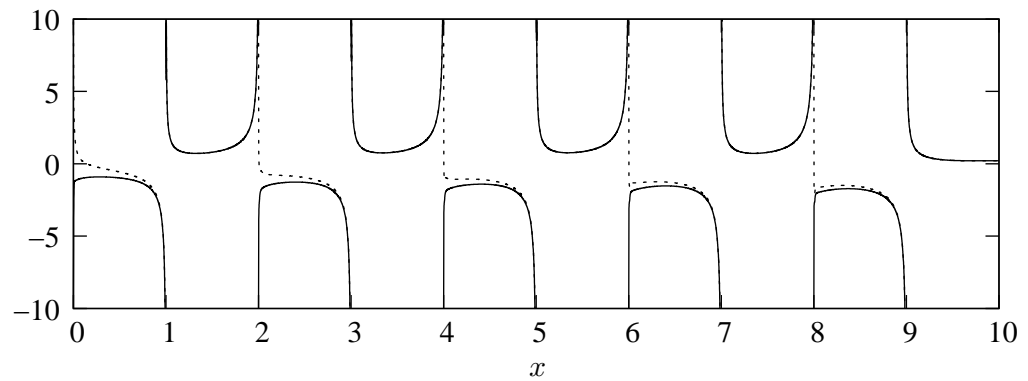
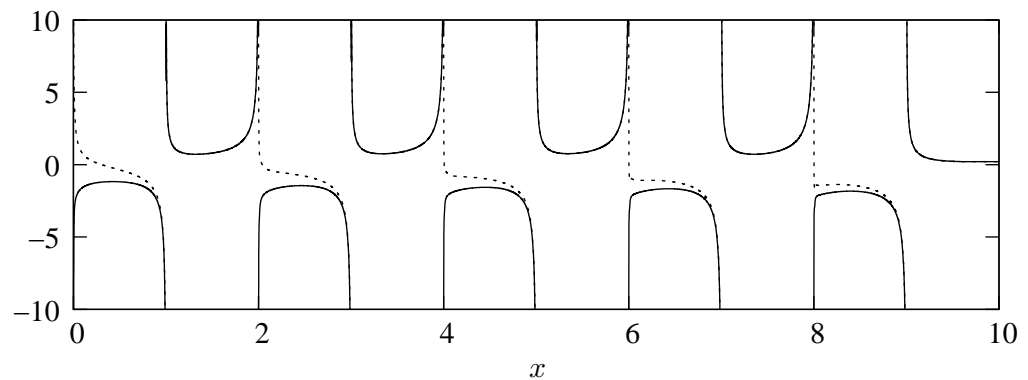
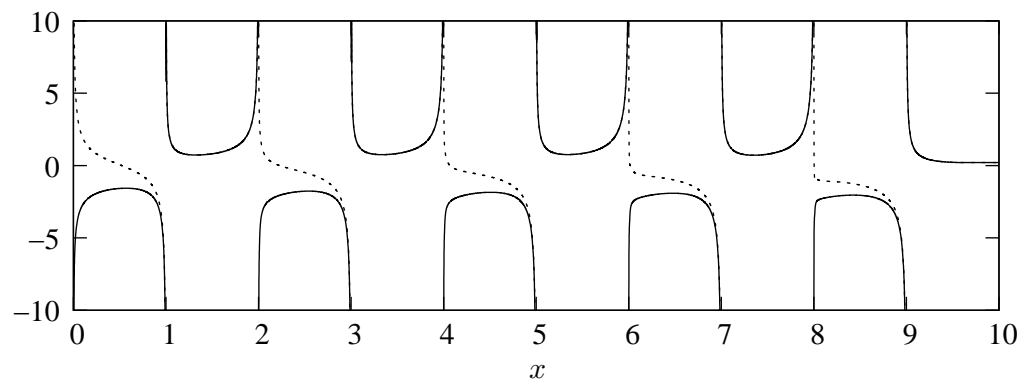
(a) $\bar{\alpha} = 0.05$.(b) $\bar{\alpha} = 0.125$.(c) $\bar{\alpha} = 0.25$.(d) $\bar{\alpha} = 0.5$.

Figure 3.10: Corresponding pressures p_+ (solid line) and p_- (dashed line) for the cases in figure 3.9 at $y = 0^\pm$.

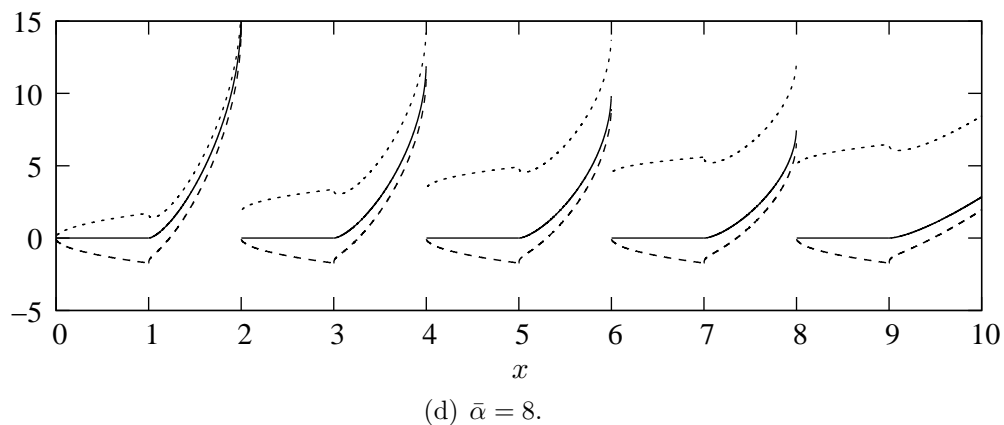
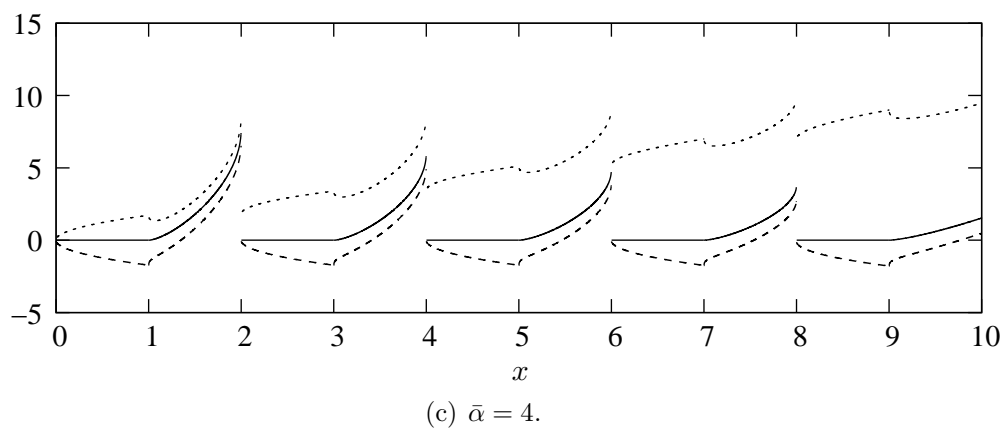
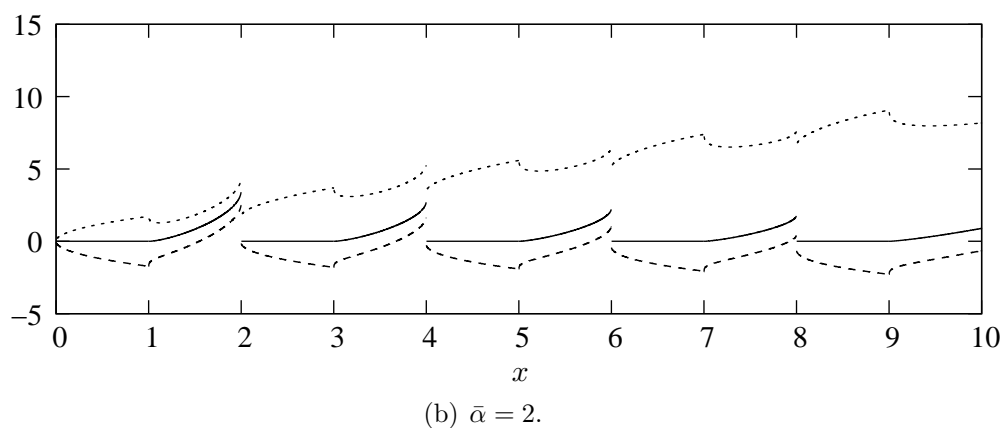
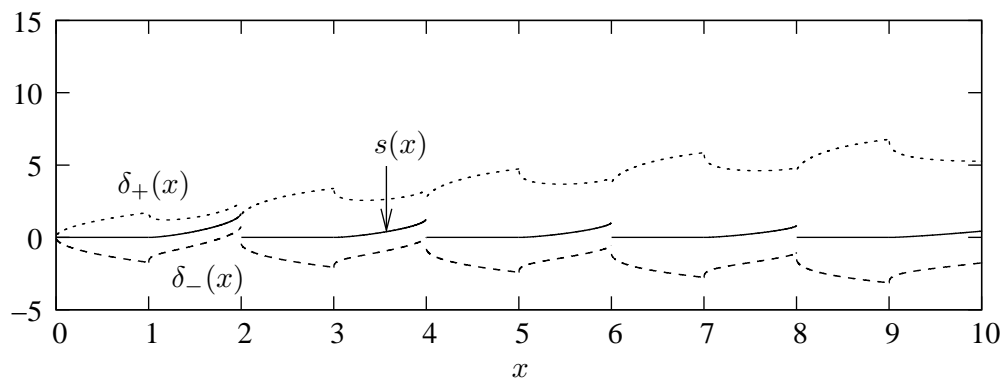


Figure 3.11: Boundary-layer displacement thicknesses δ_+ , δ_- and computed wake-shapes $s(x)$ for larger values of $\bar{\alpha}$ for $N = 5$ flat blades and wakes of length unity.

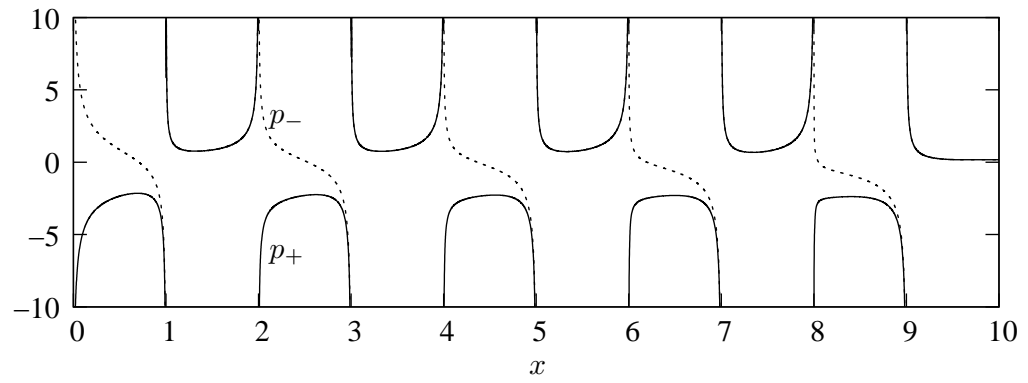
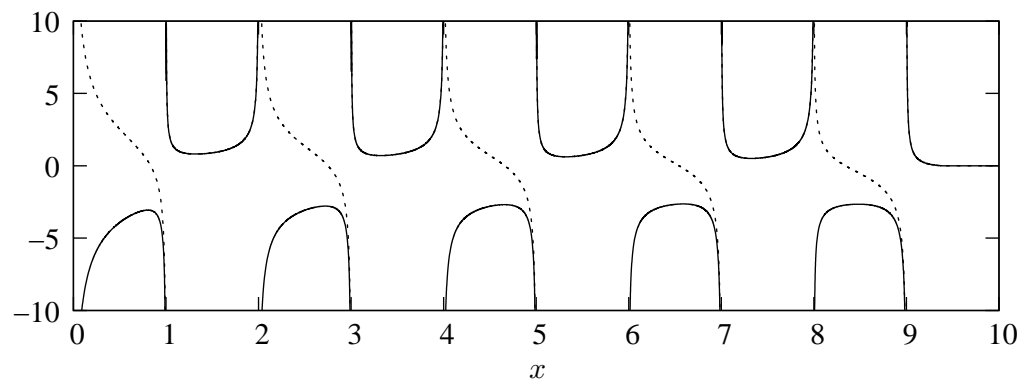
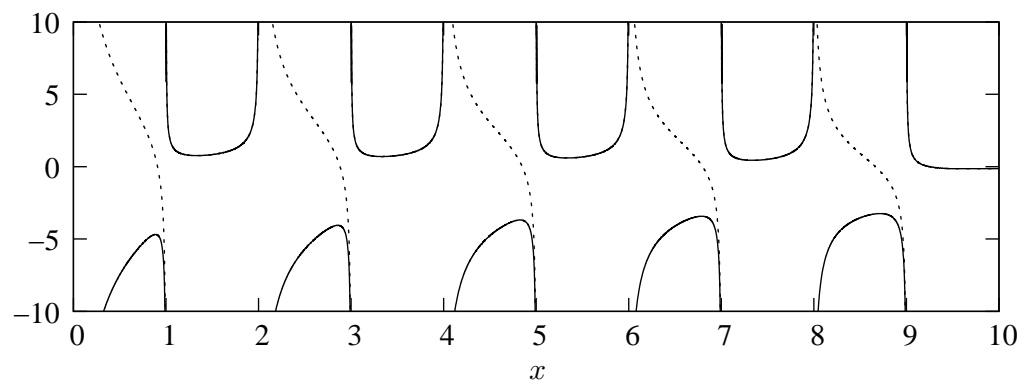
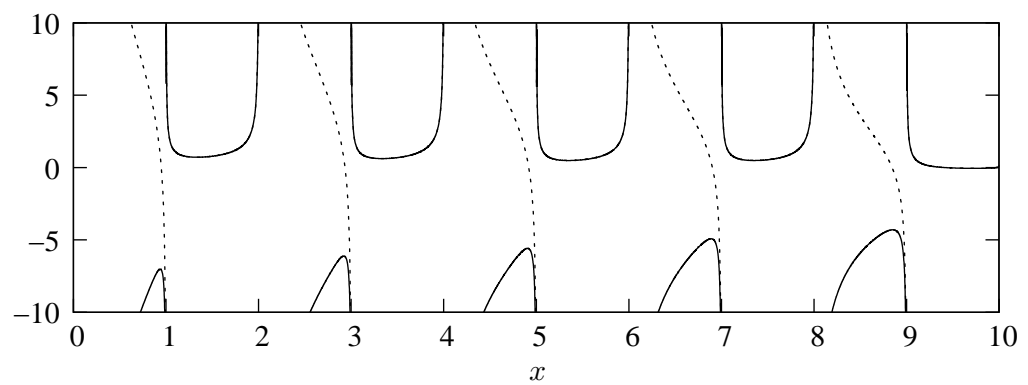
(a) $\bar{\alpha} = 1.$ (b) $\bar{\alpha} = 2.$ (c) $\bar{\alpha} = 4.$ (d) $\bar{\alpha} = 8.$

Figure 3.12: Corresponding pressures p_+ (solid line) and p_- (dashed line) for the cases in figure 3.11 at $y = 0^\pm$.

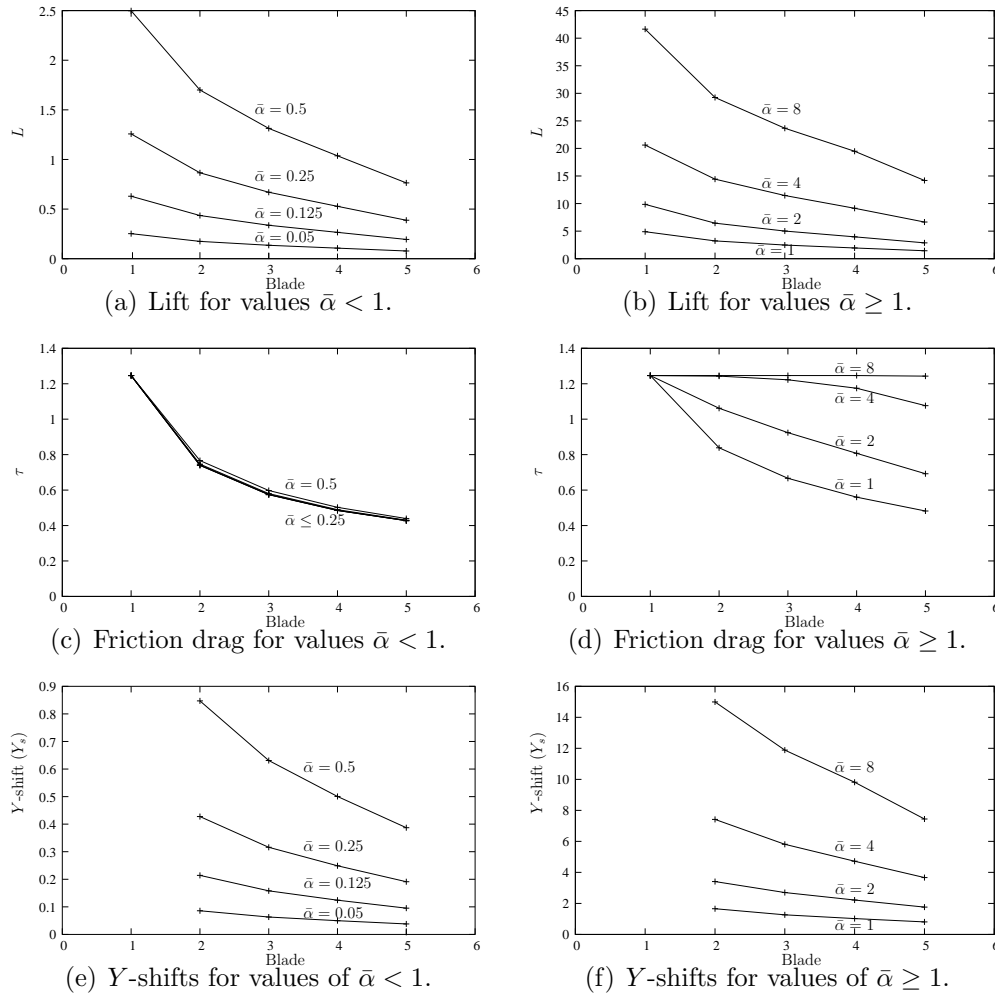


Figure 3.13: Computed values of the scaled lift, L , friction drag, τ and Y -shifts on each blade, Y_s , for the results presented in figures 3.9 - 3.12.

having a larger wake.

Solutions for blades with non-zero thickness are shown in figures 3.15 and 3.16. In figure 3.15 we present the solutions found for a non-symmetric convex shaped blade with global angles of attack $\bar{\alpha} = 0.5, 2$. The blade and wake lengths are unity for each case presented. In each case, a decrease in the Y -shift at each leading edge is observed and suggests that (even with non-zero blade thickness) a sheltering effect occurs, similar to that in the last section. The calculated pressures also show similar behaviour.

In figure 3.16 the calculations described above are repeated, but now the blade has a concave underside. In this case, the Y -shift becomes negative on blades downstream. As the number of blades passed increases in 3.16(b), the signs of the pressure solutions for p_+ and p_- swap close to the leading edge,

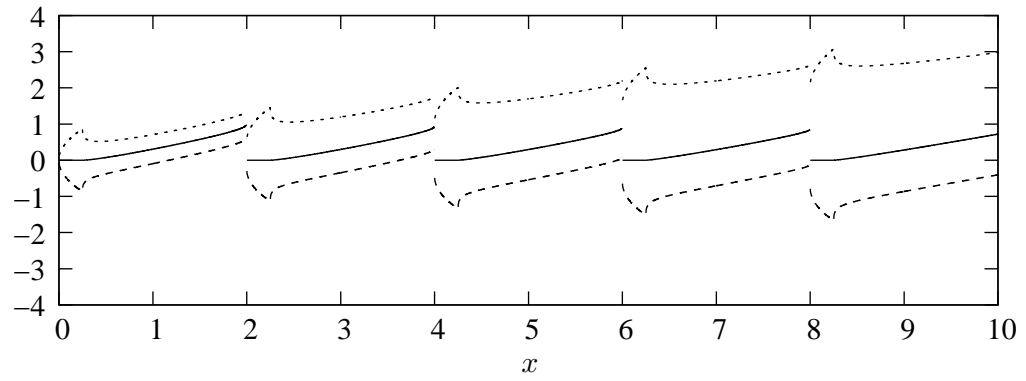
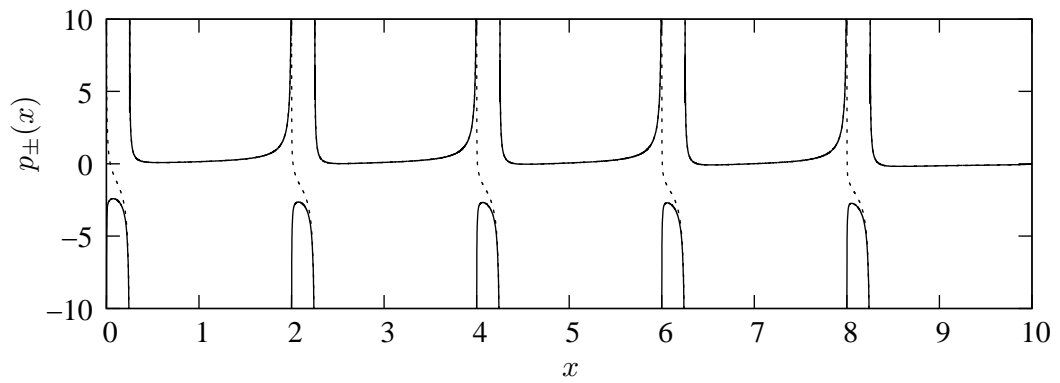
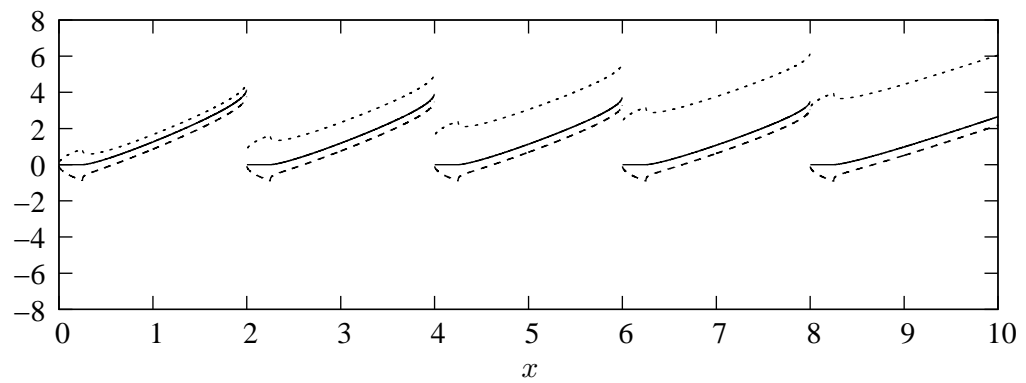
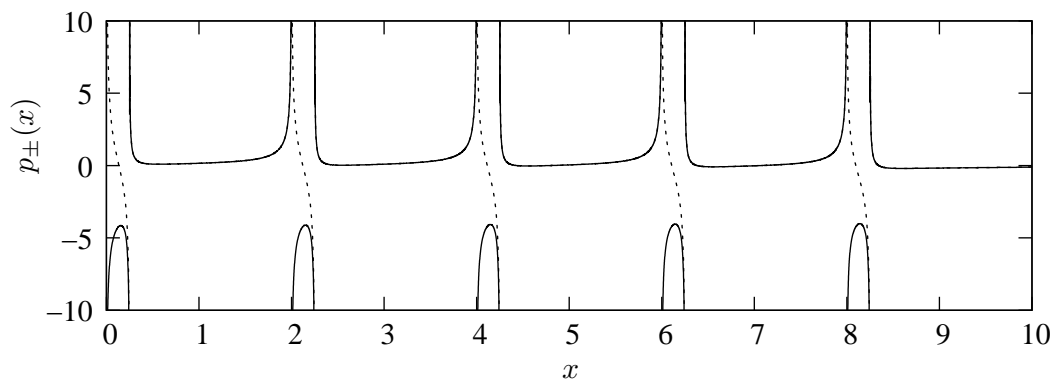
(a) Wake-shapes and displacement thickness, $\bar{\alpha} = 0.5$.(b) Pressures, $\bar{\alpha} = 0.5$.(c) Wake-shapes and displacement thickness, $\bar{\alpha} = 2$.(d) Pressures, $\bar{\alpha} = 2$.

Figure 3.14: Displacement thicknesses and pressures for five flat blades of length $l_j = 0.25$, for the cases of (a) $\bar{\alpha} = 0.5$ and (b) $\bar{\alpha} = 2.0$.

in contrast to the previous results. This is caused by the negative Y -shift occurring at the leading edges of blades downstream. With a larger global angle of attack, we see in figure 3.16(c) that the Y -shift has not yet become negative, although similar behaviour in the pressure is seen as the number of blades passed increases. In general, the flow behaviour seen in the flat blade case of the last section, appears to be similar to these cases.

Finally in figure 3.17, the number of flat blades is increased to $N = 10$ to examine what features arise upon passing many blades. For the case presented, $\bar{\alpha} = 2$ and the blade and wake lengths are equal to one. Beneath the first few blades in figure 3.17, a near Blasius boundary-layer is created. On passing a few more blades, this is not true, since the sheltering effect has now caused the Y -shift at each leading edge to decrease enough so that a more general boundary-layer grows above and beneath each blade. This is as reported in the last section for $N = 5$ blades. Considering the displacement thicknesses above the blades in figure 3.17(a), there is a slow growth of the boundary-layer over the whole array of blades, with a rapid change in the displacement thickness locally over a single blade. These rapid changes over each blade appear to take on a very similar nature. In the fifth to eighth wakes, we see that the wake-shape and pressure solutions are also very similar. All of this evidence gives an indication that a periodic solution for many-blades may occur, something we will discuss in the next chapter.

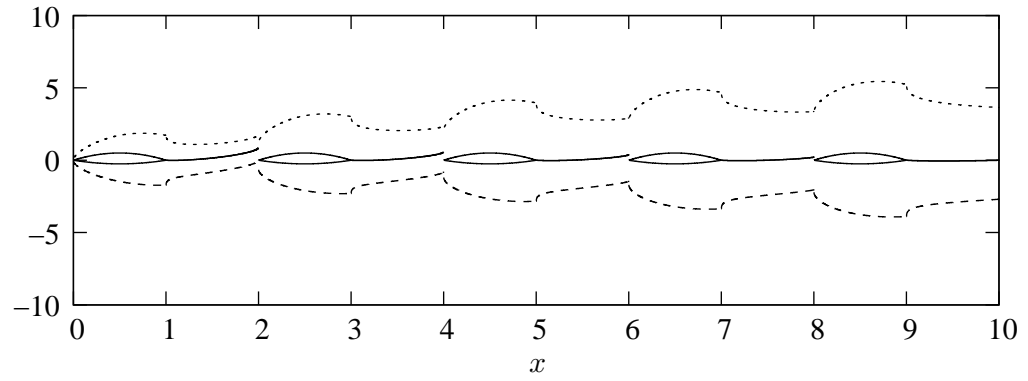
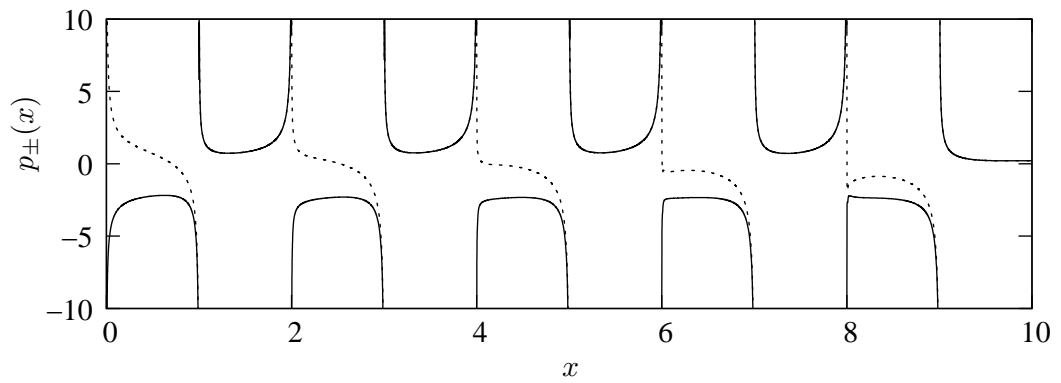
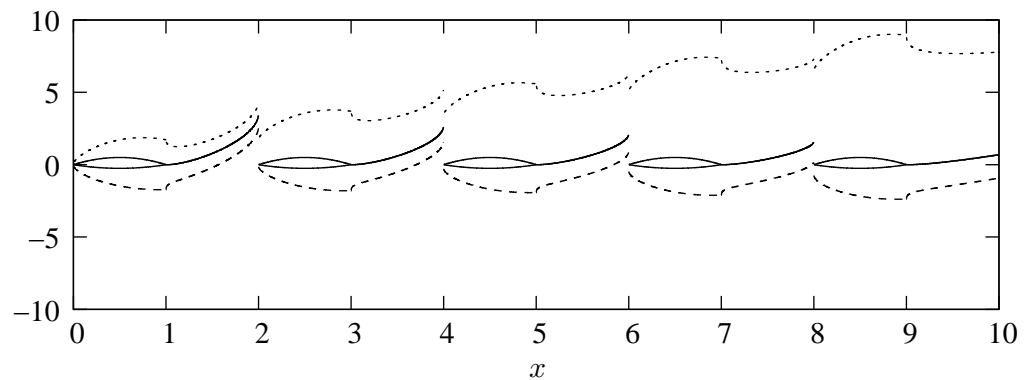
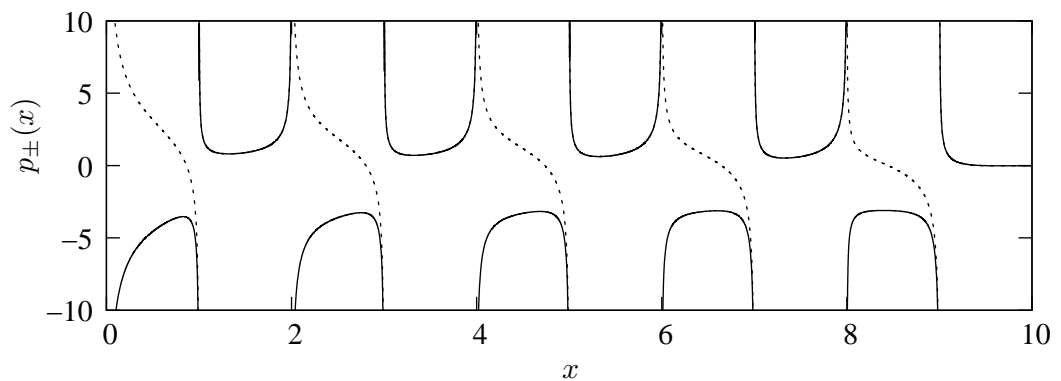
(a) Wake-shapes and displacement thickness, $\bar{\alpha} = 0.5$.(b) Pressures, $\bar{\alpha} = 0.5$.(c) Wake-shapes and displacement thickness, $\bar{\alpha} = 2$.(d) Pressures, $\bar{\alpha} = 2$.

Figure 3.15: Displacement thicknesses and pressures with $\bar{\alpha} = 0.5, 2.0$ and blade thicknesses given by $f_+(x) = 2(x - x^2)$, $f_-(x) = x^2 - x$.

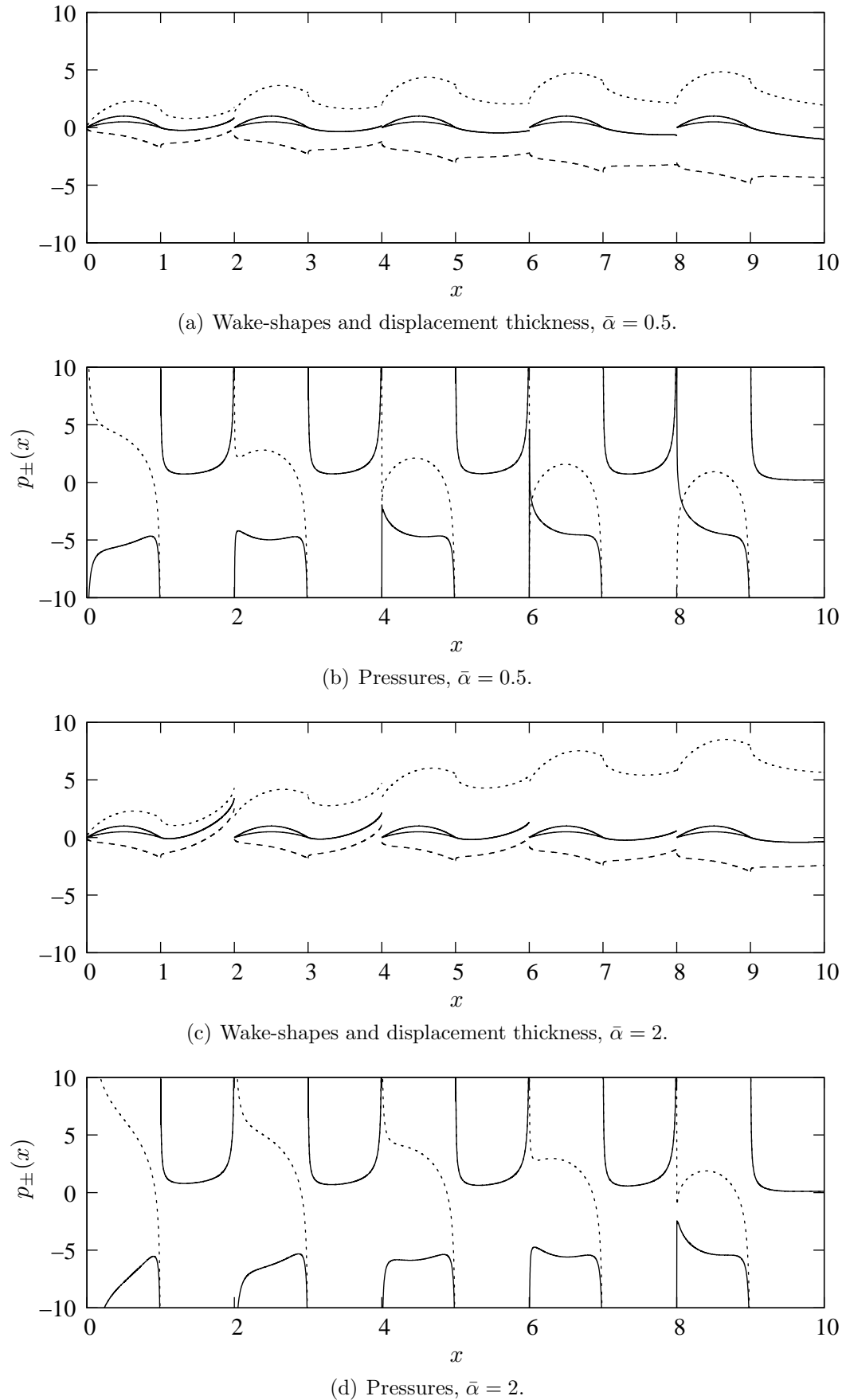


Figure 3.16: Displacement thicknesses for five aerofoils with $\bar{\alpha} = 0.5, 2.0$ and blade thicknesses given by $f_+(x) = 4(x - x^2)$, $f_-(x) = 2(x - x^2)$.

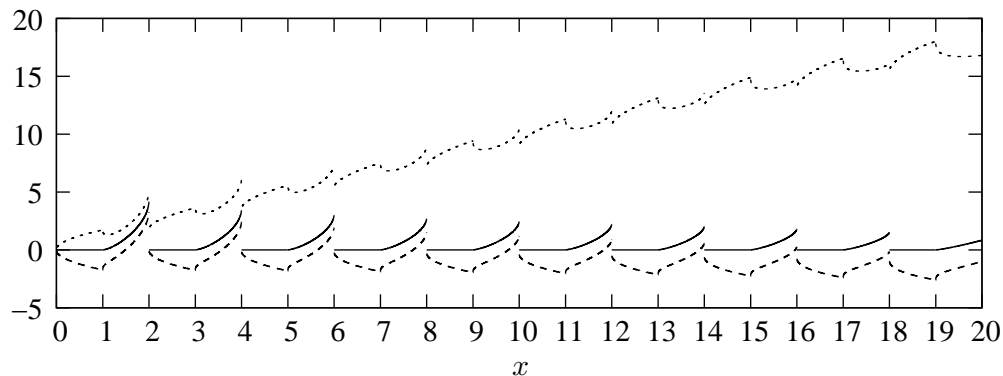
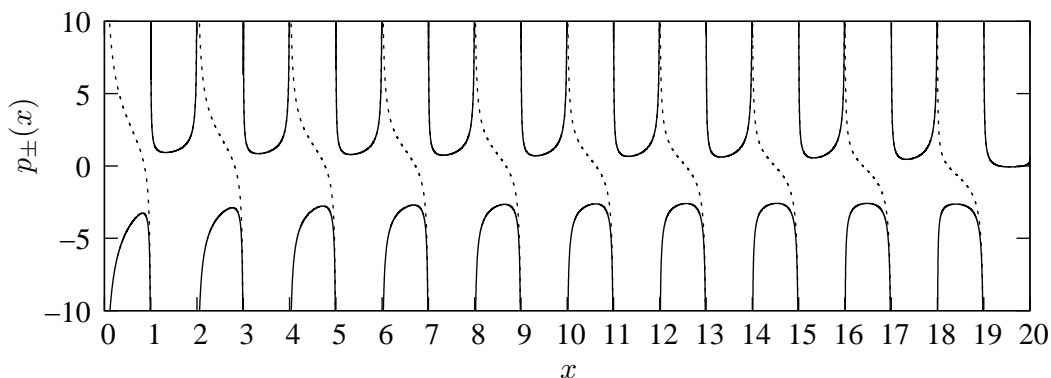
(a) Displacement thicknesses $\delta_{\pm}(x)$.(b) Pressures, $p_{\pm}(x)$.

Figure 3.17: Displacement thicknesses and wake-shapes with corresponding pressure solutions p_+ and p_- (solid and dashed lines respectively) for 10 flat blades, $\bar{\alpha} = 2.0$

3.6 Summary

This chapter has extended Smith & Timoshin (1996b) to include a small global angle of attack to a configuration of blades. Choosing the angle of size $O(Re^{-1/2})$ caused a leading order change to the free-stream. A similar technique to that of Smith & Timoshin (1996b) was applied to solve the coupled boundary-layer free-stream problem. The global inner-outer coupling between the boundary-layer and free-stream was observed through Y -shifts in the boundary layer and unknown pressures across the blades in the free-stream. We presented solutions for the problem past $N = 5$ flat blades and wakes of length unity for various values of $\bar{\alpha}$, to outline the phenomena associated with these multi-blade flows. Slip-streaming effects were seen downstream through decreases in Y -shifts and flattening of each wake-shape, along with decreases in lift and friction drag. We then computed some short and thick blade solutions. Results for the short blade analysis showed that

the wake-shapes and pressures were very similar on each blade and in each wake, whilst the thick blade solutions repeated the sheltering effects seen in the flat blade case. Finally, a configuration of ten blades was presented and seemed to indicate the appearance of a many-blade limit, which will be discussed in the next chapter.

Possible extensions to the work in this chapter include the following. Firstly, the angle of attack within the problem is taken to be very small, so that the normal velocity in the free-stream is affected at leading order. An extension would be to develop a model for flow past blades with a larger angle of attack, say $\alpha = O(1)$. This has implications for the development of both the boundary-layer and free-stream and we may expect large scale separations to occur on the blades if the global angle of attack is large enough. Another extension of interest would be to develop an analytical short blade analysis within the current setting, to better understand the phenomena computed in the solutions presented here. A starting point may be the paper by Bowles & Smith (2000b), where a short blade analysis is sought for a non-symmetric configuration of blades far downstream. Unsteady problems, such as start-up of the rotor system could also be analysed, where very little or no work has been conducted before.

However, the extension with the most personal interest would be to solve a non-symmetric, possibly with a global angle of attack, global viscous-inviscid rotor blade problem in three-dimensions. Smith & Timoshin (1996a) have shown how the boundary-layer problem may be solved for the rotary system, but for non-symmetric configurations of the rotor blades we expect the viscous-inviscid coupling described here. The main difficulty in three-dimensions would be to formulate and solve the outer inviscid problem. In this chapter we were able to use complex analysis to derive an equation for the pressure differences across the blades, which allowed for the solution of the inviscid and hence the whole two-dimensional problem. This complex analysis approach is not possible in three-dimensions. A way to formulate the potential free-stream problem for pressure or normal velocity would be to use a boundary integral method. However, there is a difficulty in knowing where the leading and trailing edges occur on a three-dimensional rotor

blade. This is due to the radial flow outwards from the centre of the rotation being of comparable size to the oncoming flow to the spinning rotor blade. Thus it is very difficult to apply the Kutta trailing edge condition in the correct locations in advance. We can reformulate the free-stream problem in three-dimensions using a boundary integral method to obtain equivalent integral equations to (3.42) and (3.43), but the result we used in this chapter to solve (3.43) for $[p]$ required Muskhelishvili (1946) and used a complex variable technique to solve (3.43). In the three-dimensional case, we need to find a way to transform the integral equation into an equation of the second kind without using complex analysis or solve the first kind equation directly. In either case, this presents considerable difficulty, especially in solving a first kind equation given the non-uniqueness of solutions. If any of the two difficulties could be overcome, a formulation should be possible in three dimensions, at least for infinite blade spans where the Kutta condition may be easier to apply.

Chapter 4

Many-blade limit with a global angle of attack

4.1 Introduction

In this chapter, we explore in more depth the flow behaviour on passing many-blades with a global angle of attack. The analysis carried out in the last chapter holds for the case of many-blades but computation time is increased as the number of blades is increased due to the number of discretisation points required to accurately capture the boundary layer flow. Thus, we seek a limiting case for the flow behaviour on passing many blades.

Results from the previous chapter (particularly figure 3.17, a case of $N = 10$ blades) showed a similar wake-shape across every wake with a decreasing Y -shift as more blades and wakes were passed. There was an overall growth of the boundary layer on passing all the blades with rapid changes to the displacement thickness of the boundary layer over a single blade and wake. The rapid change in the displacement thickness profiles over each blade and wake are caused by the continual adjustments required to account for the no-slip boundary conditions on each blade. This suggests that there may be an underlying structure of the boundary layer, whereby an overall growth is seen over a long x -scale (over all blades and wakes) whilst effects on a much shorter x -scale (over each blade and wake) cause the rapid changes in the local thickness of the boundary layer.

A many-blade limit is reported in Smith & Timoshin (1996b) and Purvis

(2002) for the cases of non-symmetric blades and ground effect respectively. Within these papers, the boundary layer is modelled in two parts. The first part contains the majority of the boundary layer flow which varies slowly in x and accounts for the general overall growth of the boundary layer on passing many blades. Within this bulk part of the boundary layer, the flow is given by a Blasius flow on average at leading order. The second part of the boundary layer is a relatively thin inner, viscous sublayer. The sublayer occurs over a much shorter scale in x , that of one blade and wake. The sublayer deals with the leading- and trailing-edge singularities and the changes to and from the no-slip condition. Furthermore, a periodic nature is revealed when the derived scalings for the velocities in the sublayer are applied to the \bar{u} solutions in the boundary layer. The boundary layer is still coupled to the free-stream through unknown wake-shapes, and the free-stream is coupled to the boundary layer by unknown pressure differences over the blades.

Given that for similar many-blade studies a periodic many-blade limit does occur, we investigate this in the context of having a global angle of attack. Evidence from the calculations in the previous chapter (outlined in the second paragraph of this chapter) suggests that a many-blade limit may occur with a global angle of attack, like that of Smith & Timoshin (1996b) and Purvis (2002). The number, n , of blades passed is now taken to be large where $O(1) \ll n \ll O(Re^{3/5})$. If $n = O(Re^{3/5})$, as documented by Bowles & Smith (2000a,b), the proposed analysis here is no longer valid. A discussion of the breakdown of the many-blade limit is given in later chapters.

4.2 Structure

The approach taken is guided by Smith & Timoshin (1996b) and numerical results gained in the previous chapter. We consider the flow over blade and wake n , buried within a very large streamwise array of blades. The coordinate of the viscous boundary layer is still given by Y , of order unity, where $y = Re^{-1/2}Y$.

To represent the two streamwise scales of significance, we proceed as follows. The long scale in x , after passing n blades is given by $x = nx_l$,

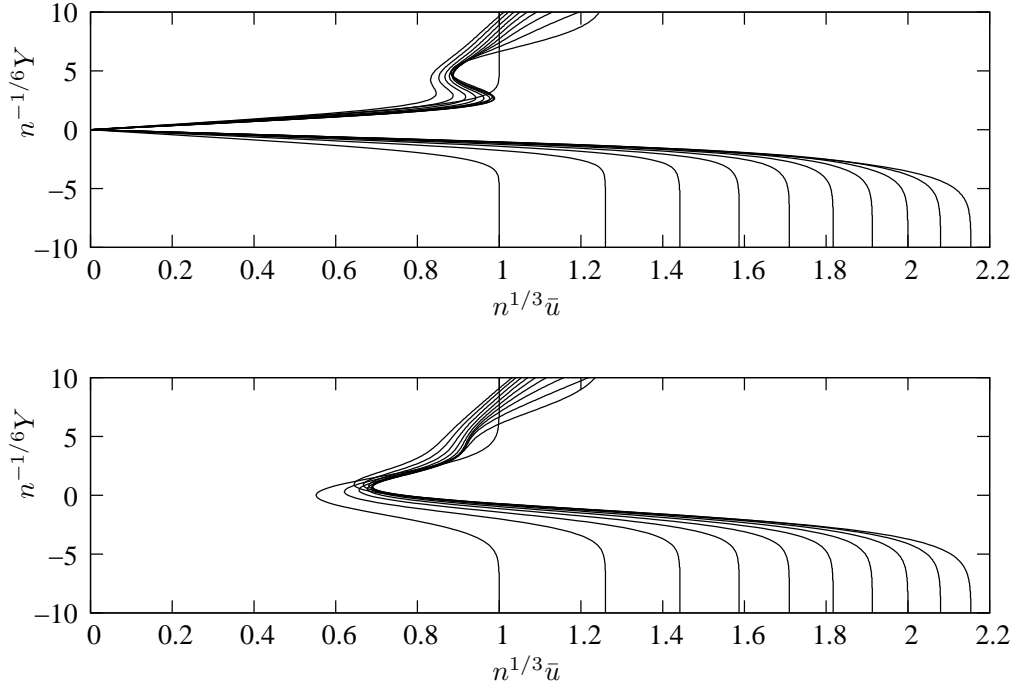


Figure 4.1: Scaled \bar{u} velocities from the previous chapter suggesting the periodic nature of the viscous sub-layer. Profiles are taken from the mid-blade (top figure) and mid-wake (bottom figure) positions taken from the 10 blade computation performed in figure 3.17, where $\bar{\alpha} = 1$.

with $x_l = O(1)$. This longer scale observes an overall growth of the whole boundary layer as more blades are passed. The other is a local, fast scale of $O(1)$ over each blade and wake and is given by $x = x_s$. This shorter scale accommodates the change in boundary conditions at the blade surface and wake centreline from that of no-slip to no-shear, and vice-versa. Therefore, to represent both x dependencies in the boundary layer, we write

$$x = x_s + nx_l. \quad (4.1)$$

Within the boundary layer, the velocity $\bar{u} = O(Yn^{-1/2})$. The normal scales of the bulk-layer and the sublayer are deduced by the inertial-diffusive balance of operators

$$\bar{u} \frac{\partial}{\partial x} \sim \frac{\partial^2}{\partial Y^2}. \quad (4.2)$$

At an $O(n)$ distance downstream, we find that the normal scale of the bulk-layer is $O(n^{1/2})$ as expected. Hence, $\bar{u} = O(1)$ and by continuity, $\bar{v} = O(n^{-1/2})$ in the bulk-layer. Over the shorter, $O(1)$ scale x_s , (4.2) yields

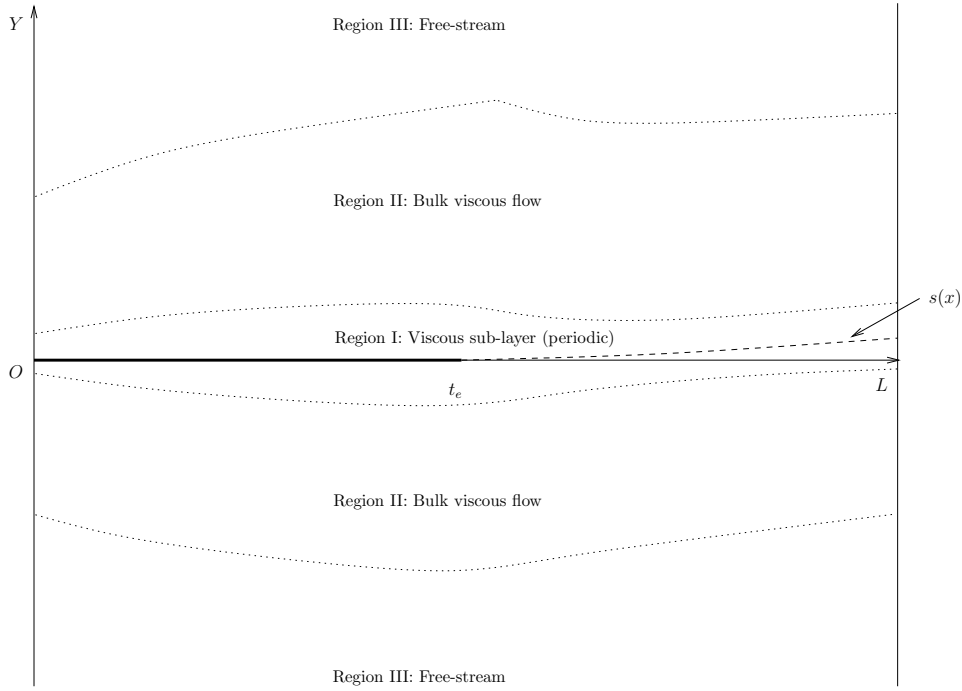


Figure 4.2: The proposed structure of the current many-blade limit showing the three regions of flow over one blade-wake period.

the balance $Yn^{-1/2} \sim Y^{-2}$ and hence the sublayer size $Y = O(n^{1/6})$. Thus the velocities scale as $\bar{u} = O(n^{-1/3})$ and $\bar{v} = O(n^{-1/6})$ in the sublayer.

In figure 4.1, the sublayer scales for \bar{u} and Y are applied to the velocity profiles mid-blade and mid-wake of the $N = 10$ blade case of figure 3.17 in the last chapter. The scaled profiles show that as more blades are passed, the velocity components begin to settle into a near periodic regime close to the blade surface and wake centreline. Thus for the current many-blade limit, we take the sublayer to be periodic. To determine the periodic boundary layer flow, we consider the flow over one particular blade and wake, that leads to the proposed structure in figure 4.2. The blade leading edge is taken to be at $x = 0$, with trailing edge at $x = t_e$ and the would-be next leading edge at $x = L$.

4.2.1 Region II: bulk viscous flow

The bulk viscous layer makes up the majority of the boundary layer flow. A new normal coordinate $Y_b = O(1)$ is introduced such that $Y = n^{1/2}Y_b$ since the normal scale in region II is of $O(n^{1/2})$. The governing equations for region II are the boundary layer equations (3.5) and (3.7) from the last

chapter. The velocities in the boundary layer, \bar{u} and \bar{v} , which must match both the free-stream and viscous sub-layer, are expanded as,

$$\bar{u} = u_0(x_s, Y_b) + n^{-\frac{1}{3}}u_1(x_s, Y_b) + n^{-\frac{2}{3}}u_2(x_s, Y_b) + n^{-1}u_3(x_s, Y_b) + \dots, \quad (4.3)$$

$$\bar{v} = n^{\frac{1}{6}}v_1(x_s, Y_b) + n^{-\frac{1}{6}}v_2(x_s, Y_b) + n^{-\frac{1}{2}}v_0(x_s, Y_b) + \dots. \quad (4.4)$$

Substituting these expressions into the boundary layer equations, we find

$$u_0 \frac{\partial u_1}{\partial x_s} + v_1 \frac{\partial u_0}{\partial Y_b} = 0, \quad (4.5)$$

$$\frac{\partial u_1}{\partial x_s} + \frac{\partial v_1}{\partial Y_b} = 0, \quad (4.6)$$

are the leading order balances. A simple substitution of (4.6) into (4.5), and subsequent solution using separation of variables leads to the solutions

$$u_1 = E_{\pm}(x_s) \frac{\partial u_0}{\partial Y_b}, \quad (4.7)$$

$$v_1 = -E'_{\pm}(x_s)u_0. \quad (4.8)$$

Here and in what follows, the \pm subscripts (and later superscripts) refer to values just above and below $Y_b = 0$ respectively. The functions E_{\pm} are determined upon matching to region I at $Y_b = 0^{\pm}$.

At $O(n^{-1/3})$, the balances

$$u_0 \frac{\partial u_2}{\partial x_s} + u_1 \frac{\partial u_1}{\partial x_s} + v_1 \frac{\partial u_1}{\partial Y_b} + v_2 \frac{\partial u_0}{\partial Y_b} = 0, \quad (4.9)$$

$$\frac{\partial u_2}{\partial x_s} + \frac{\partial v_2}{\partial Y_b} = 0, \quad (4.10)$$

hold for u_2 and v_2 . Substitution of (4.10) along with the solutions (4.7) and (4.8) for u_1 and v_1 into (4.9) give the equation

$$u_0 \frac{\partial v_2}{\partial Y_b} - v_2 \frac{\partial u_0}{\partial Y_b} = E_{\pm}(x_s)E'_{\pm}(x_s) \left\{ \left(\frac{\partial u_0}{\partial Y_b} \right)^2 - u_0 \frac{\partial^2 u_0}{\partial Y_b^2} \right\}, \quad (4.11)$$

for v_2 , which may be solved using the integrating factor $1/u_0$. The solution to this equation is

$$v_2 = -E_{\pm}(x_s)E'_{\pm}(x_s) \frac{\partial u_0}{\partial Y_b} + u_0 G'_{\pm}(x_s). \quad (4.12)$$

Using conservation of mass and integrating with respect to x_s , we obtain

$$u_2 = \frac{E_{\pm}^2(x_s)}{2} \frac{\partial^2 u_0}{\partial Y_b^2} - G_{\pm}(x_s) \frac{\partial u_0}{\partial Y_b}, \quad (4.13)$$

where G_{\pm} , like E_{\pm} match region II to the sublayer region. The unknown functions E_{\pm} and G_{\pm} are actually displacement effects to region II from the sublayer. To see why, we perturb the leading order flow $u_0(x_l, Y_b)$ by a small amount $\epsilon = n^{-1/3}E_{\pm}(x_s) + n^{-2/3}G_{\pm}(x_s)$. Expanding $u_0(x_l, Y_b + \epsilon)$ about Y_b using Taylor's theorem yields

$$u_0(x_l, Y_b + \epsilon) = u_0(x_l, Y_b) + n^{-\frac{1}{3}}E_{\pm}\frac{\partial u_0}{\partial Y_b} + n^{-\frac{2}{3}}\left\{G_{\pm}\frac{\partial u_0}{\partial Y_b} + E_{\pm}\frac{\partial^2 u_0}{\partial Y_b^2}\right\}. \quad (4.14)$$

So, upon applying a small displacement to the leading order flow, the solutions for u_1 and u_2 are recovered at $O(n^{-1/3})$ and $O(n^{-2/3})$ respectively, matching the original expansion for \bar{u} .

Finally, at $O(n^{-2/3})$ the equations

$$u_1\frac{\partial u_1}{\partial x_s} + u_0\frac{\partial u_0}{\partial x_l} + u_1\frac{\partial u_2}{\partial x_s} + u_2\frac{\partial u_1}{\partial x_s} + v_1\frac{\partial u_2}{\partial Y_b} + v_2\frac{\partial u_1}{\partial Y_b} + v_0\frac{\partial u_0}{\partial Y_b} = \frac{\partial^2 u_0}{\partial Y_b^2}, \quad (4.15)$$

$$\frac{\partial u_0}{\partial x_l} + \frac{\partial u_3}{\partial x_s} + \frac{\partial v_0}{\partial Y_b} = 0, \quad (4.16)$$

hold, containing both short and long scale variations in x . The periodicity assumption over the short scale x_s is now applied. Integrating (4.15) and (4.16) with respect to x_s from 0 to L leaves

$$u_0\frac{\partial u_0}{\partial x_l} + v_M\frac{\partial u_0}{\partial Y_b} = \frac{\partial^2 u_0}{\partial Y_b^2}, \quad (4.17)$$

$$\frac{\partial u_0}{\partial x_l} + \frac{\partial v_M}{\partial Y_b} = 0, \quad (4.18)$$

where

$$v_M = \frac{\int_0^L v_0 dx_s}{\int_0^L dx_s}, \quad (4.19)$$

represents the mean value of v_0 over the period. The boundary conditions are

$$u_0 = v_M = 0 \quad \text{at } Y_b = 0^{\pm}, \quad (4.20)$$

$$u_0 \rightarrow 1 \quad \text{as } Y_b \rightarrow \pm\infty, \quad (4.21)$$

as in Smith & Timoshin (1996b). The equations (4.17) and (4.18) along with the constraints (4.20) and (4.21) are exactly the conditions required for the

Blasius boundary layer solution, in this case holding on average for u_0 and v_0 across the whole period. From a physical stance, this layer is largely passive. It is sheltered from the leading and trailing edge singularities by region I and grows slowly over all the blades and wakes, but serves to pass details of the sublayer displacements out to the free-stream over the shorter scale.

4.2.2 Region I: viscous sublayer

In the sublayer, the normal coordinate $Y = O(n^{1/6})$. We define $\hat{Y} = O(1)$ as the normal coordinate of the sublayer such that $Y = n^{1/6}\hat{Y}$. To match with region II, the expansions

$$\bar{u}(x, Y) = n^{-\frac{1}{3}}\hat{u}_0(x_s, \hat{Y}) + n^{-\frac{2}{3}}\hat{u}_1(x_s, \hat{Y}) \cdots, \quad (4.22)$$

$$\bar{v}(x, Y) = n^{-\frac{1}{6}}\hat{v}_0(x_s, \hat{Y}) + n^{-\frac{1}{2}}\hat{v}_1(x_s, \hat{Y}) \cdots, \quad (4.23)$$

are substituted into the boundary layer equations to yield

$$\hat{u}_0 \frac{\partial \hat{u}_0}{\partial x_s} + \hat{v}_0 \frac{\partial \hat{u}_0}{\partial \hat{Y}} = \frac{\partial^2 \hat{u}_0}{\partial \hat{Y}^2}, \quad (4.24)$$

$$\frac{\partial \hat{u}_0}{\partial x_s} + \frac{\partial \hat{v}_0}{\partial \hat{Y}} = 0, \quad (4.25)$$

at leading order. These equations must be solved subject to the boundary conditions

$$\hat{u}_0 = \hat{v}_0 = 0 \quad \text{on } \hat{Y} = 0 \text{ over the blade}, \quad (4.26)$$

$$\frac{\partial \hat{u}_0}{\partial \hat{Y}} \rightarrow \pm \lambda \quad \text{as } \hat{Y} \rightarrow \pm \infty, \quad (4.27)$$

$$L\text{-periodicity in } x_s, \quad (4.28)$$

$$\hat{Y}\text{-shift at } x = L. \quad (4.29)$$

The condition (4.27) is required for the sublayer to match to the leading order flow in the bulk-layer. The leading order solution for u_0 as $Y_b \rightarrow 0^\pm$ in the bulk-layer is given by the shear flow $u_0 = \pm \lambda_\pm Y_b$ since u_0 is given by a mean Blasius solution at leading order. The values of λ_\pm in the small Y_b mean Blasius flow are given by

$$\lambda_\pm = \frac{\partial u_0(x_l, 0^\pm)}{\partial Y_b} = \hat{f}''(0)x_l^{-1/2}, \quad (4.30)$$

where \hat{f} is the Blasius function and $\hat{f}''(0) = 0.3321$. Thus, matching the sublayer to the bulk-layer requires condition (4.27). Further, this condition

fixes the displacements E_{\pm} and their derivatives E'_{\pm} in the bulk-layer solution. By direct integration of (4.27) and use of continuity, we have

$$\hat{u}_0 \rightarrow \pm\lambda(\hat{Y} + b_{\pm}(x_s)), \quad (4.31)$$

$$\hat{v}_0 \rightarrow \mp\lambda b'_{\pm}(x_s)\hat{Y}, \quad (4.32)$$

as $\hat{Y} \rightarrow \infty$. Here, b_{\pm} are functions of integration representing the displacement effects of the sublayer. As $\hat{Y} \rightarrow \infty$, \hat{v}_0 must match to v_0 in the bulk-layer as $Y_b \rightarrow 0$ and so $E_{\pm} \equiv b_{\pm}$. Notice also that over the short periodic scale x_s , λ_{\pm} are approximately constant. The condition (4.29) is how the global angle of attack is felt through the boundary layer.

At next order, the equations

$$\hat{u}_1 \frac{\partial \hat{u}_0}{\partial x_s} + \hat{u}_0 \frac{\partial \hat{u}_1}{\partial x_s} + \hat{v}_1 \frac{\partial \hat{u}_0}{\partial \hat{Y}} + \hat{v}_0 \frac{\partial \hat{u}_1}{\partial \hat{Y}} = \frac{\partial^2 \hat{u}_1}{\partial \hat{Y}^2}, \quad (4.33)$$

$$\frac{\partial \hat{u}_0}{\partial x_s} + \frac{\partial \hat{v}_0}{\partial \hat{Y}} = 0, \quad (4.34)$$

hold, along with the boundary conditions

$$\hat{u}_1 = \hat{v}_1 = 0 \quad \text{on } \hat{Y} = 0 \text{ on the blade}, \quad (4.35)$$

$$\frac{\partial \hat{u}_0}{\partial \hat{Y}} \rightarrow 0 \quad \text{as } \hat{Y} \rightarrow \pm\infty, \quad (4.36)$$

$$L\text{-periodicity in } x_s. \quad (4.37)$$

At this order, the bulk-layer displacements G_{\pm} and it's derivatives G'_{\pm} are determined in a similar way to the leading order method above. By integration of (4.36) and use of continuity, we have

$$\hat{u}_1 \rightarrow \pm\lambda c_{\pm}(x_s), \quad (4.38)$$

$$\hat{v}_1 \rightarrow \mp\lambda c'_{\pm}(x_s)\hat{Y}, \quad (4.39)$$

as $\hat{Y} \rightarrow \pm\infty$. Thus to match the sublayer and bulk-layer requires $G_{\pm} \equiv c_{\pm}$. In this analysis a leading order solution will be sought, so any effects associated with the lower order displacement effects c_{\pm} are neglected.

4.2.3 Region III: free-stream

The final task is to find the perturbation to the free-stream, which will determine the wake-shape required for the boundary layer problem. To ensure

the free-stream matches to region II in the boundary layer requires the expansions

$$u = n^{\frac{1}{6}}U_0(x, y) + \dots, \quad (4.40)$$

$$\bar{\alpha} + v = n^{\frac{1}{6}}V_0(x, y) + \dots, \quad (4.41)$$

$$p = n^{\frac{1}{6}}P_0(x, y) + \dots. \quad (4.42)$$

These expansions are substituted into the governing Cauchy-Riemann equations for the free-stream problem leaving them unchanged at leading order, given here by

$$\frac{\partial V_0}{\partial x_s} = -\frac{\partial P_0}{\partial y}, \quad (4.43)$$

$$\frac{\partial V_0}{\partial y} = \frac{\partial P_0}{\partial x_s}. \quad (4.44)$$

The boundary conditions to be satisfied by P_0 are still continuity across the wakes, with the Kutta condition holding at every trailing edge. The normal velocity component V_0 must once again match the entrainment into the boundary layer, given by

$$V_0(x, 0^\pm) = \begin{cases} \pm b'_\pm(x_s) - n^{-\frac{1}{6}}\bar{\alpha} & \text{on the blade,} \\ s'(x_s) \pm b'_\pm(x_s) - n^{-\frac{1}{6}}\bar{\alpha} & \text{for } x \text{ in a wake.} \end{cases} \quad (4.45)$$

The boundary conditions stated for V_0 are for the case of flat blades. Thickness or camber could be introduced to the blades with the same analysis holding under the constraint that the aerofoil shape is contained entirely within region I. This would introduce an $f'_\pm(x_s)$ term to the boundary condition over the blades.

The free-stream problem is driven by the sublayer displacement effects, since the boundary conditions (4.45) rely only upon the short x_s -scale effects from the sublayer and the global angle of attack term. The $n^{-1/6}$ term multiplying $\bar{\alpha}$ in the boundary conditions gives an explanation for the decrease in the Y -shift on passing more blades. As n increases, the effect of the global angle of attack decreases like $n^{-1/6}$ and so the wake-shape and Y -shift must decrease in the same manner. Thus far downstream, the dominant driving force will be the displacements caused by the geometry in the sublayer region. To illustrate how a solution can be found, results will be presented when the

global angle of attack term is significant in the boundary conditions and it is possible to compare the predictions of the many-blade limit with those arising from the method in the previous chapter.

Solution to the free-stream problem is found using the same method as before. We seek the holomorphic, complex function $W = P_0 + iV_0$ which is bounded in the far-field. Cauchy's integral formula is applied to evaluation points on and away from $y = 0$, to derive similar integral relations for V_0 and P_0 and their sums and differences across $y = 0$. Following the same arguments as the previous chapter, these integral equations must be solved subject to the boundary conditions

$$[V_0](x) = \begin{cases} (b'_+ + b'_-)(x_s) & \text{on the blade,} \\ (b'_+ - b'_-)(x_s) & \text{in the wake.} \end{cases} \quad (4.46)$$

$$\langle V_0 \rangle(x) = \begin{cases} (b'_+ - b'_-)(x_s) - 2n^{-1/6}\bar{\alpha} & \text{on the blade,} \\ 2s'(x_s) + (b'_+ - b'_-)(x_s) - 2n^{-1/6}\bar{\alpha} & \text{in the wake,} \end{cases} \quad (4.47)$$

$$[P_0](x) = 0 \quad \text{in wakes and at trailing edges,} \quad (4.48)$$

where, as in the previous chapter, the $\langle \rangle$ and $[\]$ parentheses represent the sum and difference of the boundary values of V_0 and P_0 respectively. As in the previous chapter, the key quantity is $[P_0]$ across the blades. The integral equation connecting $\langle V_0 \rangle$ and $[P_0]$ is

$$\langle V_0 \rangle(x_0) = -\frac{1}{\pi} \sum_{i=-\infty}^{\infty} \int_{a_i}^{b_i} \frac{[P_0](x)}{x - x_0} dx, \quad (4.49)$$

after using (4.48) in the wakes. This equation can once be inverted using Muskhelishvili (1946), to obtain

$$[P_0](x_0) = \frac{S^{-\frac{1}{2}}(x_0)}{\pi} \sum_{i=-\infty}^{\infty} \int_{a_i}^{b_i} \frac{S^{\frac{1}{2}}(x) \langle V_0 \rangle(x)}{x - x_0} dx. \quad (4.50)$$

In the many-blade limit, S is effectively evaluated over an infinite array of blades in either direction, so that

$$S(x) = \prod_{j=-\infty}^{\infty} \left| \frac{x - a_j}{x - b_j} \right|. \quad (4.51)$$

The new periodicity requirement allows simplification through the exchange of the order of summation and integration. The substitution $x = x_s + jL$ is

made, with the leading and trailing edges given by $a_j = jL$ and $b_j = t_e + jL$ respectively and x_s running over the period $L = a_{j+1} - a_j$. This transforms (4.50), with the periodic boundary conditions (when n is large) to

$$[P_0](x_0) = \frac{\hat{S}^{-\frac{1}{2}}(x_0)}{\pi} \int_0^{t_e} \sum_{i=-\infty}^{\infty} \frac{\hat{S}^{\frac{1}{2}}(x_s) \langle V_0 \rangle(x_s)}{x_s + iL - x_0} dx_s, \quad (4.52)$$

where \hat{S} is given by

$$\hat{S}(x) = \prod_{j=-\infty}^{\infty} \left| \frac{x + jL}{x + jL - t_e} \right|. \quad (4.53)$$

This equation gives $[P_0]$ for a point x_0 on the blade. A similar method can be carried out to find the velocity sums across the wake. By using the same substitution for x and changing the order of summation and integration leads to the integral equation

$$\langle V_0 \rangle(x_0) = -\frac{1}{\pi} \int_0^{t_e} \left\{ \sum_{j=-\infty}^{\infty} \frac{[P_0](x_s)}{x_s + jL - x_0} \right\} dx_s, \quad (4.54)$$

for the velocity sums across the wake. With $\langle V_0 \rangle$ known everywhere, the wake-shape and hence Y -shift can be calculated using (4.47).

4.3 Numerical Solution

To determine the many-blade limit on a particular blade n downstream, we solve the coupled sublayer and free-stream problems using an iterative method. Region I requires the Y -shift through the wake-shape and the free-stream relies on the pressure difference over the blade caused by the displacements of the sublayer.

The sublayer problem is very similar to that in the previous chapter. We discretise the boundary layer equations using the same finite-difference method as before, with the only change being the matching condition as $\hat{Y} \rightarrow \infty$ to satisfy (4.27). The first starting condition for the sublayer is given by a shear flow and an initial guess for the Y -shift on the n^{th} blade of zero is made. The boundary layer equations are solved by performing a streamwise sweep from $x_s = 0$ to $x_s = L$. At $x_s = L$, a check on periodicity is made by comparing the absolute error of successive iterates of \hat{u}_0 and \hat{v}_0 at

$x = L$. Convergence is achieved if the absolute error at each Y_j for successive sublayer sweeps is less than 10^{-3} . If convergence is not achieved on the current sweep, the Y -shifted profiles of \hat{u}_0 and \hat{v}_0 are set as new starting conditions, followed by resweeping until convergence is achieved. Depending on the value of $\bar{\alpha}$, 10 – 20 sweeps were needed to gain convergence in the Y -shift.

Once the sublayer solution is found, we turn to the free-stream problem to find the wake-shape $s(x)$. The problems in evaluating (4.52) are much the same as before, with a Cauchy-type singularity at $x_0 = x_s$ when $j = 0$. To proceed, the $j = 0$ component in \hat{S} is removed, followed by pairing the j^{th} and $-j^{\text{th}}$ terms

$$\hat{S}(x) = \left| \frac{x}{x - t_e} \right| \prod_{j=1}^{\infty} \frac{x^2 - j^2 L^2}{(x - t_e)^2 - j^2 L^2}, \quad (4.55)$$

$$= \left| \frac{x}{x - t_e} \right| \bar{S}(x). \quad (4.56)$$

The substitutions $x_s = t_e \sin^2 \theta$ and $x_0 = t_e \sin^2 \phi$ are made to calculate $[P_0]$ across the blades, which transforms the integral equation to

$$\begin{aligned} [P_0](t_e \sin^2 \phi) &= \\ &= -\frac{2\hat{S}(t_e \sin^2 \phi)^{-\frac{1}{2}} t_e}{\pi} \int_0^{\frac{\pi}{2}} \sum_{i=-\infty}^{\infty} \frac{\sin^2 \theta \langle V_0 \rangle (t_e \sin^2 \theta) \bar{S}^{\frac{1}{2}}(t_e \sin^2 \theta)}{t_e \sin^2 \theta + iL - t_e \sin^2 \phi} d\theta. \end{aligned} \quad (4.57)$$

To compute $[P_0]$ over the blades, all ϕ points are set as the mid-points of each pair of θ points. Various truncations of the sum in the integrand were tested until little change in the solutions for P_0 and V_0 occurred. Typically, a truncation of ten blades in each direction is required for accuracy, with tests against 20 and 100 blades showing very little variation.

The velocity sums across the wakes are computed once the pressure differences are known across the blade using a similar method to the above through (4.54). Finally, the wake-shape and Y -shift are calculated through

$$s(x_s) = s(t_e) + \frac{1}{2} \int_{t_e}^{x_s} \left\{ \langle v \rangle(x') - (b'_+ - b'_-)(x') + 2\bar{\alpha} n^{-1/6} \right\} dx', \quad (4.58)$$

by rearranging condition (4.47) across the wakes. Convergence in the Y -shift is obtained when the absolute error between successive Y -shift iterates

is less than 10^{-6} . If convergence is not achieved, the Y -shift in region I is updated, followed by complete recomputation of the sublayer and free-stream problems. We found that two to six complete cycles were needed until the Y -shift converged.

4.4 Results

Solutions from the current many-blade case are compared to those arising from calculations using the method of Chapter 3 in figures 4.3 - 4.6. In figures 4.3 - 4.5, results for $p_{\pm}(x)$ and the wake-shape $s(x)$ of the many-blade limit are compared to those calculated over blade and wake 6 of a 12 blade array from the previous chapter for $\bar{\alpha} = 0.1, 1, 4$. In figure 4.6, the wake-shapes of wakes 5, 10, 15 of a 20 blade array for both methods are compared.

4.4.1 Comparisons

Varying degrees of agreement are seen throughout the results. For the comparisons of $\bar{\alpha} = 0.1$ in figure 4.3, there is good agreement between the pressure solutions (except perhaps near the leading edge) and wake-shapes. Given that this is for blade $n = 6$ of an $N = 12$ blade array, this shows that for small global angles of attack, the many-blade limit can be reached after passing only a few blades.

When $\bar{\alpha} = 1$ in figure 4.4, some agreement is shown with a slight difference in the wake shape near $x_s = 2$. However, the pressure solutions follow a similar trend and show good agreement. For $\bar{\alpha} = 4$ in figure 4.5, although the wake-shapes are similar there are some areas of noticeable difference. For larger values of $\bar{\alpha}$, we saw in the last chapter that a near Blasius boundary layer formed beneath the first few blades. This is the case here and so the many-blade limit is not such a good approximation in this instance. This varies from previous work, where the many-blade limit is a good approximation to the flow behaviour after only four or five blades have been passed. However, investigation of the flow features on the fiftieth blade (for example) in a 100 blade array would produce much better agreement.

In figure 4.6 the wake-shapes of wakes 5, 10 and 15 in a 20 blade array

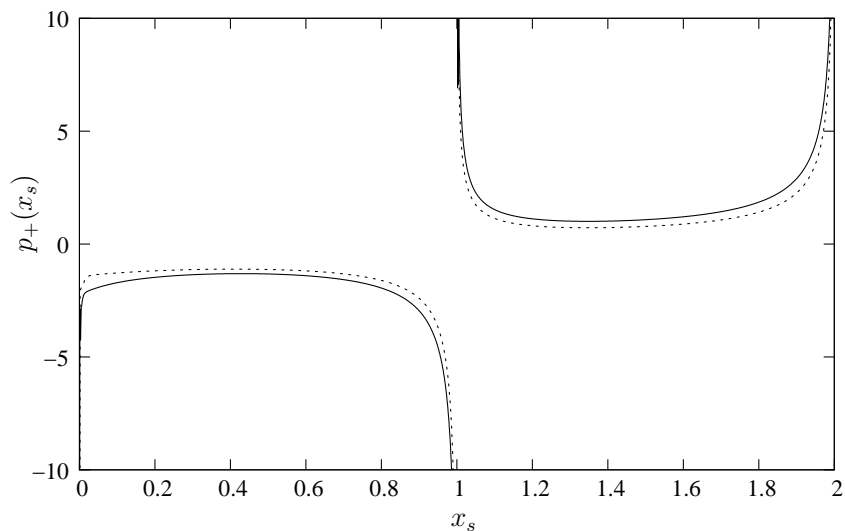
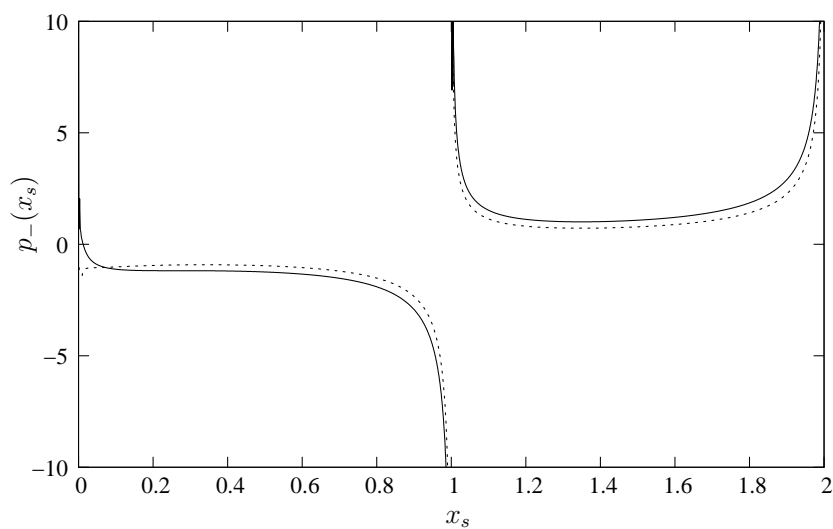
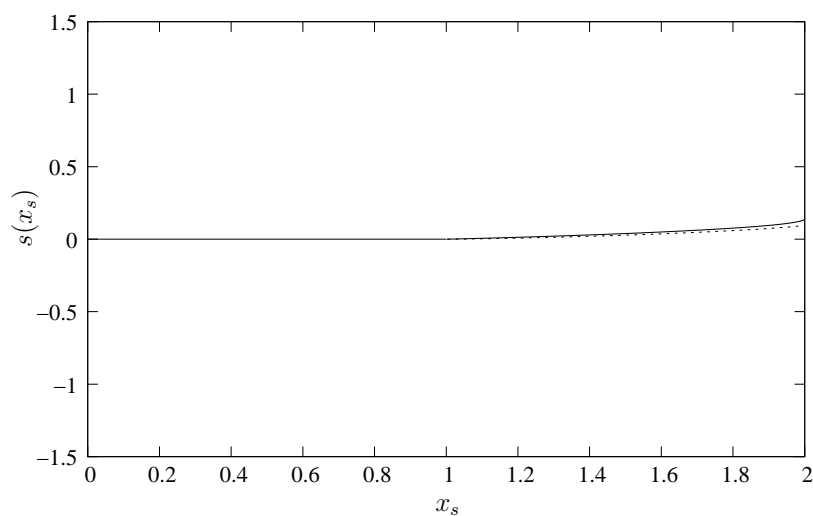
(a) Blade 6, $p_+(x_s)$ (b) Blade 6, $p_-(x_s)$ (c) Blade 6, $s(x_s)$

Figure 4.3: Comparisons of (a) $p_+(x_s)$, (b) $p_-(x_s)$ and (c) $s(x_s)$, the wake-shape between the solutions for the many-blade analysis of this chapter (solid line) and the full problem (dashed line) for the sixth blade of a 12 flat blade array. Here, $\bar{\alpha} = 0.1$.

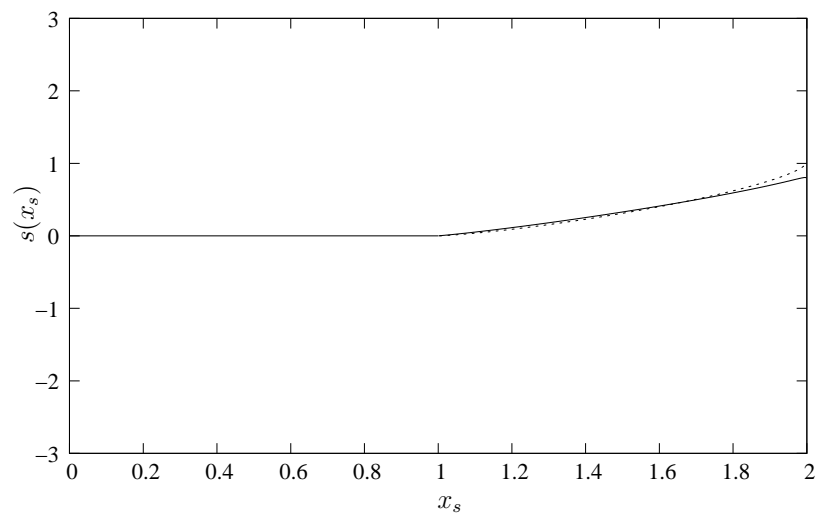
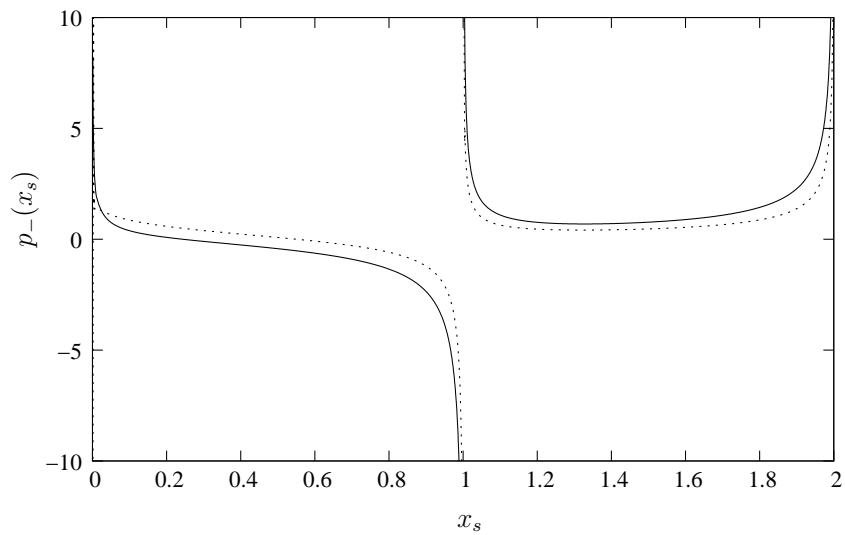
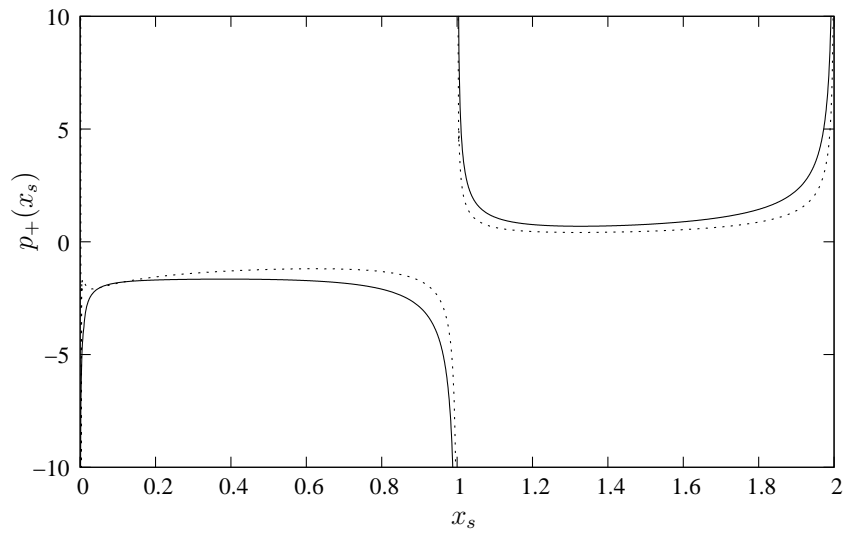
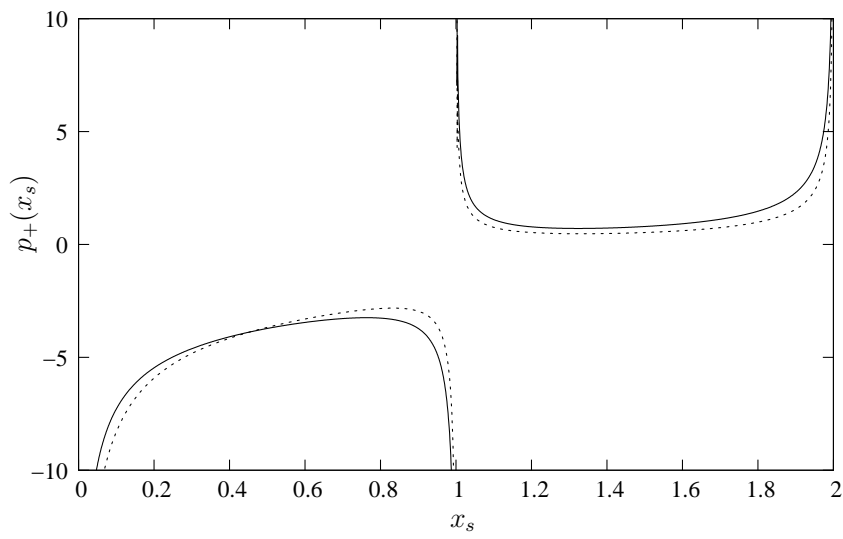
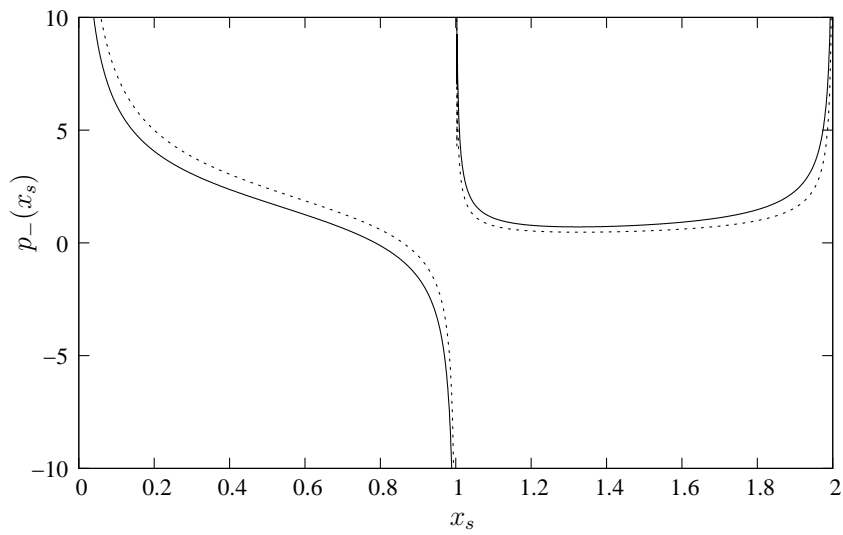
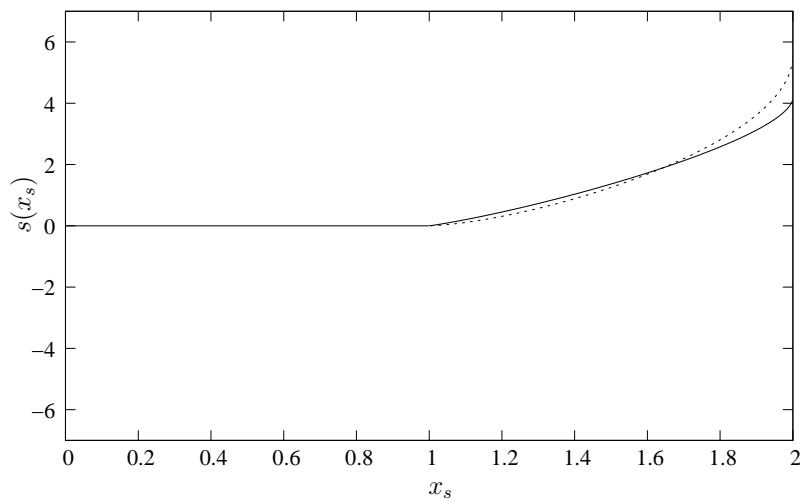
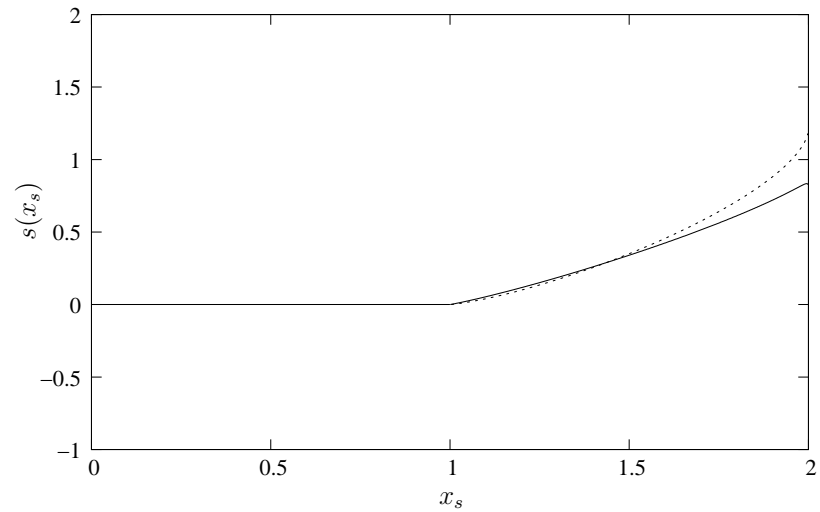
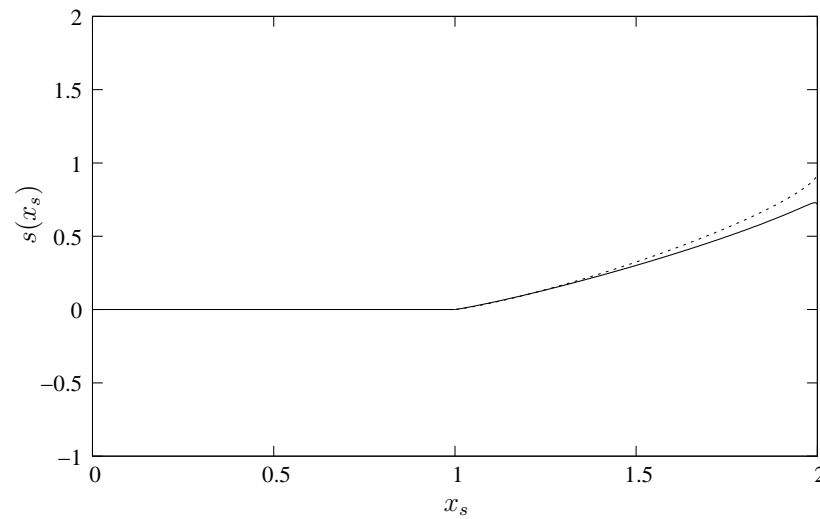


Figure 4.4: As figure 4.3 but $\bar{\alpha} = 1$.

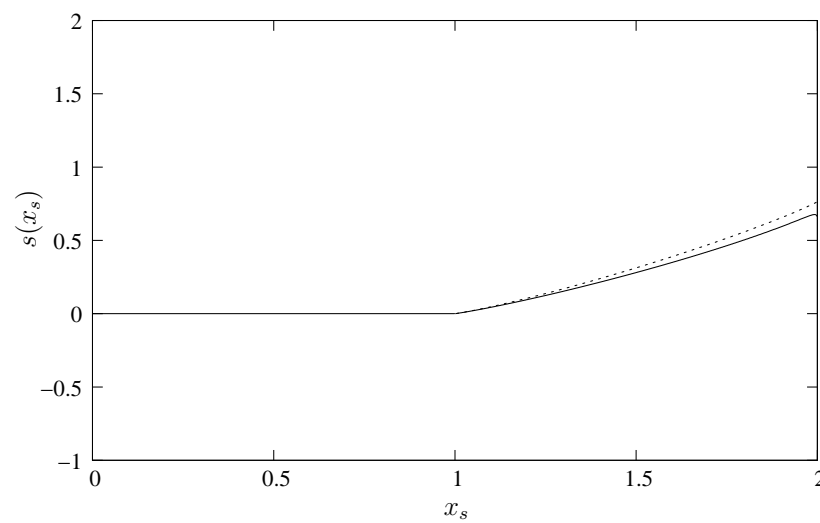
(a) Blade 6, $p_+(x_s)$ (b) Blade 6, $p_-(x_s)$ (c) Blade 6, $s(x_s)$ **Figure 4.5:** As figure 4.3 but $\bar{\alpha} = 4$.



(a) Wake-shape in wake 5



(b) Wake-shape in wake 10



(c) Wake-shape in wake 15

Figure 4.6: Comparisons between the wake-shapes computed using the many-blade limit of this chapter (solid line) and those in wakes 5, 10 and 15 in a 20 blade array using the code from the previous chapter. Here, a flat blade occupies the region $0 \leq x_s \leq 1$ and $\bar{\alpha} = 1$.

calculated using the method in the previous chapter are compared to those arising in the current many-blade limit. We see increasing agreement between the solutions as n increases downstream, as expected, with an overall decrease in the Y -shift.

4.5 Summary

In this chapter, we have extended the many-blade limit of Smith & Timoshin (1996b) to include a global angle of attack. There are two streamwise scales of importance and the boundary layer is modelled as a double viscous structure of a bulk-layer and sublayer. The leading order solution in the bulk-layer is mean Blasius flow over the long scale in x with the full boundary layer equations holding in the sublayer over the short scale in x . Furthermore, the flow in the sublayer is periodic. The global angle of attack appears in the boundary conditions for the free-stream problem, multiplied by an $n^{-1/6}$ term and suggests that as $n \rightarrow \infty$, the global angle of attack drops out of the leading order problem. We presented comparisons between the many-blade limit and the results gained from blade $n = 6$ of an $N = 12$ blade array in the previous chapter. Overall, we found qualitative agreement between the solutions for each method. Lift is still created within this structure with a global angle of attack and can be most easily deduced from figure 4.5, where there is clear evidence that the difference $p_+(x_s) - p_-(x_s) \neq 0$ over most of the blade. Since lift is given by the integral of the non-zero (in general) pressure difference over the blade surface, then lift is generated on each blade downstream. Although some differences in the wake-shapes for the larger cases of $\bar{\alpha}$ are seen, better agreement is observed between the two methods as n increases. This invokes the question of how many blades are required, for some value of $\bar{\alpha}$, for the many-blade limit to be reached. One answer could come from condition (4.47). If $\langle V_0 \rangle = O(1)$, with $\bar{\alpha}$ large and n of moderate size, then the many-blade limit is reached when displacement effects balance with the global angle of attack. Hence an estimate when the many-blade limit may be reached is when

$$n \sim (2\bar{\alpha})^6. \quad (4.59)$$

Chapter 5

The pressure interactive many-blade limit

5.1 Introduction

The periodic many-blade limit of the last chapter gave us a detailed picture of the development of the boundary-layer structure on a particular blade n buried within what is effectively an infinite array of blades. As yet, we have not stated whether this many-blade limit holds for all downstream distances. Thus, the purpose of this chapter is to allow the downstream distance to become very large, by allowing $n \rightarrow \infty$, until a new interaction occurs.

In the previous chapter, we expanded the streamwise component of the velocity in the sublayer as

$$U = n^{-1/3}\hat{u}_0(x_s, \hat{Y}) + \dots, \quad (5.1)$$

where $\hat{Y} = O(1)$ is the normal scale of the sublayer and $y = n^{1/6}\hat{Y}$. To match with the free-stream, the pressure within the sublayer takes the form

$$P = P_\infty + Re^{-1/2}n^{1/6}\hat{p}(x_s) + \dots, \quad (5.2)$$

where P_∞ is the ambient free-stream pressure (zero) and x_s represents the short, fast x -scale across each blade-wake period. Notice that for increasing n the streamwise velocity is decreasing in magnitude whilst the pressure within the sublayer increases. In the boundary-layer momentum equation, we have that the streamwise advection term $UU_{x_s} \sim n^{-2/3}$ whilst the pressure gradient $dP/dx_s \sim Re^{-1/2}n^{1/6}$. In the previous many-blade limit, the

pressure gradient was not present at leading order within the sublayer, but with increasing n we would expect the balance

$$U \frac{\partial U}{\partial x_s} \sim \frac{dP}{dx_s}, \quad (5.3)$$

to be achieved when n is large. This occurs when $n^{-2/3} \sim Re^{-1/2} n^{1/6}$, and by rearrangement we have

$$n \sim Re^{3/5}. \quad (5.4)$$

This means that if n (and hence x) is of $O(Re^{3/5})$, then the previously redundant leading order pressure gradient term exerts itself at leading order in the sublayer problem, thus violating the formulation in the previous chapter. This particular downstream distance was first identified by Smith & Timoshin (1996b) towards the end of that particular study, and the system as a whole was investigated more fully by Bowles & Smith (2000a,b).

Bowles & Smith (2000a) examined symmetric, periodic solutions to the interactive sublayer problem. Solutions for flat blades are found, as well as solutions for thicker blades, in some cases producing reversed boundary-layer flow. The authors devised an interesting short blade analysis, by taking a blade of length $O(\epsilon)$ with $\epsilon \ll 1$ and a wake of length $O(1)$. A five region structure for the short blade limit is developed in the simplest case of a flat blade. The vorticity generated at the blade is assumed to be mostly contained within a thin sublayer surrounding the blade and a portion of the wake. The remaining parts of the flow are taken to be inviscid and globally determined. The flow within the thin sublayer is given by a Blasius-type flow over the blade and a Goldstein-like flow in the near wake. The remainder of the flow is driven by this region just described. Following this short blade limit, an extension is given to include much thicker blades, where care must be taken due to the blade thickness being greater in magnitude than the sublayer thickness. Bowles & Smith (2000b) then looked at a general asymmetry through imposing a local angle of attack and a non-zero thickness. In this paper, a fully non-symmetric model was developed, which included the novel feature of a small leading edge region to satisfy the Kutta trailing edge condition, similar to that seen in Chapter 2. Emphasis is placed in this study on solving the condensed limit, where the displacement caused

by the boundary-layer as a whole is constant over the blade and wake. The authors adapted part of the five tiered short blade limit to include the effects of non-symmetry. For the special case of short flat blades with a local angle of attack, they were able to deduce a linear relationship between the lift and the angle of attack of the blade. In this paper, the authors suggest that a discussion of the effects of a global angle of attack in the pressure interactive limit is an important extension.

The previous chapter introduced a many-blade limit similar to the Smith & Timoshin (1996b) one, and an implication of the velocity expansions that we established in Chapter 4 is that a pressure-interactive many-blade limit should also exist, like the studies outlined above. Our aim over Chapters 5, 6 and 7 is to extend the previous studies by Bowles & Smith (2000a,b) to include a global angle of attack. In this chapter, we will derive the interactive many-blade limit for the case of a general non-symmetric problem of angled and thick blades, and find some new results using an alternative approach to Bowles & Smith (2000b). Then, in Chapters 6 and 7, we will conduct an investigation into the new interactions present within the many-blade limit when a global angle of attack is introduced.

5.2 The boundary-layer structure

As in the non-interactive limit, the same two x -scales operate, the first being the short, fast scale varying across each blade-wake period and the other a long, slow scale over a much larger streamwise extent. The x dependence now takes the form

$$x = x_s + Re^{3/5}x_l, \quad (5.5)$$

from the previous many-blade limit with $n = O(Re^{3/5})$. The flow is periodic over the short scale x_s . The leading edge is taken to lie at $x_s = 0$, with trailing edge at $x_s = l$ within the blade-wake period of length L . The scalings for the sublayer and bulk-layer in the non-interactive many-blade limit of the last chapter are given by $y = O(Re^{-1/2}n^{1/6})$ and $y = O(Re^{-1/2}n^{1/2})$ respectively.

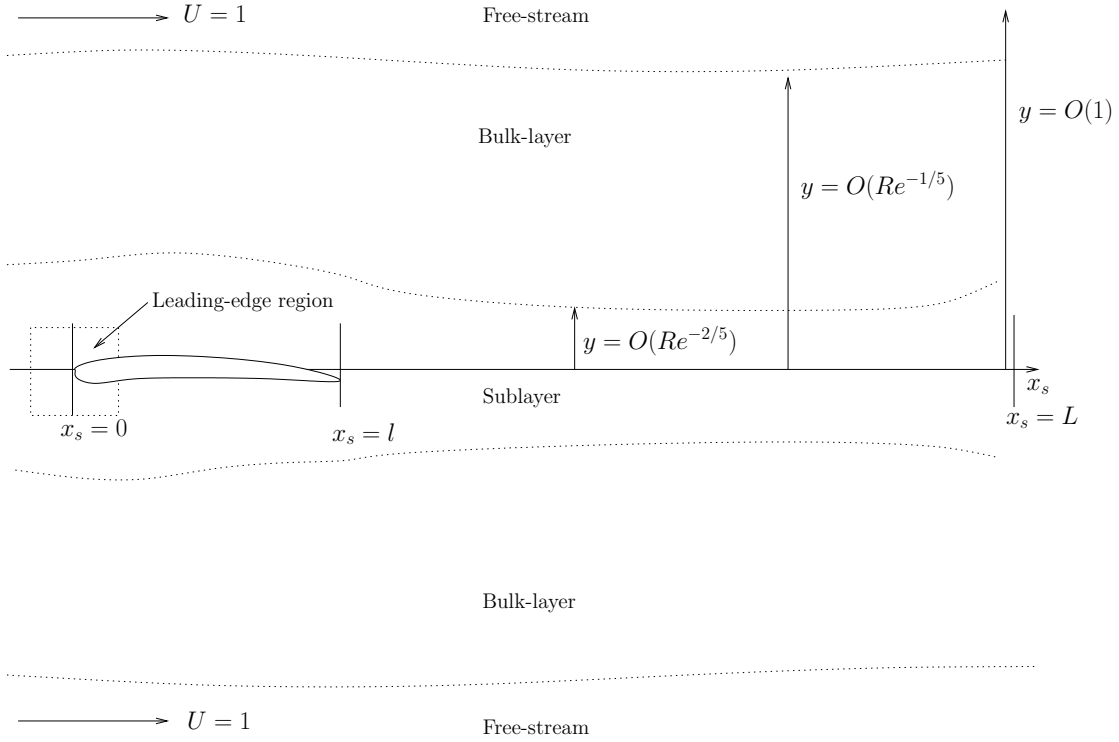


Figure 5.1: Boundary-layer structure over one period ($0 \leq x_s \leq L$) past a thick, non-symmetric blade showing the sublayer, bulk-layer and free-stream. Also shown is a small, leading edge region which is discussed in section 5.2.3.

Hence, the scalings for the sublayer and bulk-layer in the interactive many-blade limit are given by

$$y = Re^{-2/5}\hat{Y} \quad \text{and} \quad y = Re^{-1/5}Y_b, \quad (5.6)$$

respectively, with \hat{Y} and Y_b both of $O(1)$. Local non-symmetry, through a choice of local angle of attack, unequal blade thicknesses or both are taken to lie entirely within the sublayer. These non-symmetries are to be prescribed through the functions $f_{\pm}(x_s)$ such that $y = Re^{-2/5}f_{\pm}(x_s)$ gives the blade geometry. The structure is outlined in figure 5.1, where there is a small leading edge region included and is discussed later. The functions f_{\pm} must be smooth and defined such that $f_+(0) = f_-(0)$ and $f_+(l) = f_-(l)$. We begin our investigation in the bulk-layer.

5.2.1 The bulk-layer

In the bulk-layer, the normal coordinate is given by $Y_b = O(1)$ where $y = Re^{-1/5}Y_b$. The expansions here take the form

$$U = u_0(x_s, Y_b) + Re^{-\frac{1}{5}}u_1(x_s, Y_b) + Re^{-\frac{2}{5}}u_2(x_s, Y_b) + Re^{-\frac{3}{5}}u_3(x_s, Y_b) + \dots, \quad (5.7)$$

$$V = Re^{-\frac{2}{5}}v_1(x_s, Y_b) + Re^{-\frac{3}{5}}v_2(x_s, Y_b) + Re^{-\frac{4}{5}}v_0(x_s, Y_b) + \dots, \quad (5.8)$$

$$P = Re^{-\frac{2}{5}}p_1(x_s) + Re^{-\frac{3}{5}}p_2(x_s) + \dots, \quad (5.9)$$

by substituting $n = Re^{3/5}$ in the expansions from the previous chapter. We substitute these expansions into the governing Navier-Stokes equations, which yields, at leading order

$$u_0 \frac{\partial u_1}{\partial x_s} + v_1 \frac{\partial u_0}{\partial Y_b} = 0, \quad (5.10)$$

$$\frac{\partial u_1}{\partial x_s} + \frac{\partial v_1}{\partial Y_b} = 0. \quad (5.11)$$

This balance matches that of the previous chapter and so has the same solution, which we state here as

$$u_1 = E_{\pm}(x_s) \frac{\partial u_0}{\partial Y_b}, \quad (5.12)$$

$$v_1 = -E'_{\pm}(x_s)u_0, \quad (5.13)$$

where, for now, E_{\pm} are arbitrary functions of integration and are determined by matching to the sublayer. At first order, we have the balances

$$u_0 \frac{\partial u_2}{\partial x_s} + u_1 \frac{\partial u_1}{\partial x_s} + v_1 \frac{\partial u_1}{\partial Y_b} + v_2 \frac{\partial u_0}{\partial Y_b} = -\frac{dp_1}{dx_s}, \quad (5.14)$$

$$\frac{\partial u_2}{\partial x_s} + \frac{\partial v_2}{\partial Y_b} = 0. \quad (5.15)$$

These differ only slightly from the non-interactive limit, in that the pressure gradient dp_1/dx_s appears on the right-hand side. The same method can be applied as in the previous chapter to find the solutions

$$v_2 = -u_0 \int \frac{p'_1(x_s)}{u_0^2} dY_b + E(x_s)E'(x_s) \frac{\partial u_0}{\partial Y} + G'(x_s)u_0, \quad (5.16)$$

$$u_2 = \int \left\{ u_0 \int \frac{p'_1(x_s)}{u_0^2} dY_b \right\} dx_s + \frac{1}{2}E(x_s)^2 \frac{\partial^2 u_0}{\partial Y^2} - G(x_s) \frac{\partial u_0}{\partial Y}, \quad (5.17)$$

where G_{\pm} are functions that match with the sublayer.

At next order, we have

$$u_0 \frac{\partial u_0}{\partial x_l} + u_0 \frac{\partial u_3}{\partial x_s} + \frac{\partial(u_1 u_2)}{\partial x_s} + v_1 \frac{\partial u_2}{\partial Y_b} + v_2 \frac{\partial u_1}{\partial Y_b} + v_3 \frac{\partial u_0}{\partial Y_b} = -\frac{dp_2}{dx_s} + \frac{\partial^2 u_0}{\partial Y_b^2}, \quad (5.18)$$

$$\frac{\partial u_0}{\partial x_l} + \frac{\partial u_3}{\partial x_s} + \frac{\partial v_0}{\partial Y_b} = 0. \quad (5.19)$$

Again, this balance is very similar to the non-interactive balances at the same order in the previous chapter, with numerous short scale derivatives appearing with the long scale derivative terms. The pressure gradient term $-dp_2/dx_s$ now appears on the right-hand side of (5.18), but offers no more difficulty. We apply the periodicity requirement over x_s , to eliminate all of the short scale terms in equations (5.18) and (5.19). Defining the short scale mean value of the normal velocity component, v_M , as

$$v_M = \frac{\int_0^L v_0 dx_s}{\int_0^L dx_s}, \quad (5.20)$$

and integrating (5.18) and (5.19) with respect to x_s over the period L , we have

$$u_0 \frac{\partial u_0}{\partial x_l} + v_M \frac{\partial u_0}{\partial Y_b} = \frac{\partial^2 u_0}{\partial Y_b^2}, \quad (5.21)$$

$$\frac{\partial u_0}{\partial x_l} + \frac{\partial v_M}{\partial Y_b} = 0, \quad (5.22)$$

as the governing equations for u_0 and v_0 . These equations are subject to the boundary conditions

$$u_0 = v_M = 0 \quad \text{on} \quad Y_b = 0^\pm, \quad (5.23)$$

$$u_0 \rightarrow 1 \quad \text{as} \quad Y_b \rightarrow \pm\infty. \quad (5.24)$$

The first condition, (5.23), is found to be required for periodicity, as discussed by Smith & Timoshin (1996a), whilst the second condition (5.24) is required to match to the leading order free-stream solution. In the non-interactive limit, we found that the Blasius solution held throughout the bulk-layer in a mean-sense and this is the case in the interactive limit also. To complete the solution in this region, we need to match with the sublayer through the arbitrary functions of integration E_\pm and G_\pm .

5.2.2 Interactive sublayer

On the current long streamwise scale of $O(Re^{3/5})$, the sublayer is of thickness $O(Re^{-2/5})$. Thus we introduce $\hat{Y} = O(1)$ as the normal sublayer coordinate and $y = Re^{-2/5}\hat{Y}$. To match with the bulk-layer region, we expand the velocities and pressure as

$$U = Re^{-\frac{1}{5}}\hat{u}(x_s, \hat{Y}) + \dots, \quad (5.25)$$

$$V = Re^{-\frac{3}{5}}\hat{v}(x_s, \hat{Y}) + \dots, \quad (5.26)$$

$$P = Re^{-\frac{2}{5}}\hat{p}(x_s) + \dots, \quad (5.27)$$

and substitute these into the Navier-Stokes equations to yield the leading order balances

$$\hat{u}\frac{\partial\hat{u}}{\partial x_s} + \hat{v}\frac{\partial\hat{u}}{\partial\hat{Y}} = -\frac{d\hat{p}}{dx_s} + \frac{\partial^2\hat{u}}{\partial\hat{Y}^2}, \quad (5.28)$$

$$\frac{\partial\hat{u}}{\partial x_s} + \frac{\partial\hat{v}}{\partial\hat{Y}} = 0, \quad (5.29)$$

which are the interactive boundary-layer equations. The boundary conditions to be satisfied by (5.28) and (5.29) are

$$\hat{u} = \hat{v} = 0 \quad \text{on} \quad \hat{Y} = f_{\pm}(x_s), \quad 0 < x_s < l, \quad (5.30)$$

$$\text{Continuity in } \hat{u}, \hat{v} \text{ and } \hat{p} \text{ in the wake,} \quad (5.31)$$

$$\hat{u} \rightarrow \pm\lambda_{\pm}(\hat{Y} + b_{\pm}(x_s)) \quad \text{as} \quad \hat{Y} \rightarrow \pm\infty, \quad (5.32)$$

$$\hat{p}_+(l) = \hat{p}_-(l), \quad (5.33)$$

$$L\text{-periodicity in } \hat{u}, \hat{v}, \text{ and } \hat{p}. \quad (5.34)$$

Condition (5.30) represents the no-slip and no-penetration conditions on the blade. Condition (5.32) is the matching condition to the bulk-layer and is deduced by considering the normal derivative $\partial/\partial y$ as $\hat{Y} \rightarrow \infty$ in the sublayer. The functions b_{\pm} appearing in the boundary condition are the unknown displacement functions associated with the presence of the sublayer. The functions b_{\pm} may be determined by a pressure-displacement relation resulting from the free-stream solution later. The condition (5.33) is the Kutta trailing edge condition, requiring equal pressures just above and just

below the blade at the trailing edge and now appears directly in the sublayer problem.

As a final task, we need to complete the bulk-layer solution by finding the functions E_{\pm} in the leading order solution v_1 . Using (5.32), differentiation with respect to x_s and the continuity equation, followed by integration with respect to \hat{Y} , matching requires that $\hat{v} \rightarrow v_1$ in the bulk-layer and so

$$\mp \lambda_{\pm} b'_{\pm} \hat{Y} \sim \lambda_{\pm} E'_{\pm} Y_b. \quad (5.35)$$

Hence, the bulk-layer functions $E_{\pm} \equiv b_{\pm}$, the displacement gradient of the sublayer.

5.2.3 Leading-edge discontinuity

For a general non-symmetric blade geometry, the Kutta trailing edge condition (5.33) is not satisfied. Given the expectation of primarily forward flow in the sublayer region, the pressure gradient is favourable meaning that the pressure will fall over the blade from the leading edge to the trailing edge. In the non-symmetric case, the pressures above and below the blade will be unequal in general, due to differing blade shapes, and so will violate the Kutta trailing edge condition. The resolution of this problem is that there is a flow discontinuity located in a small region at the leading edge. The discontinuity allows the velocity and pressure to jump from the oncoming wake values to new values above and below the blade just downstream of the leading edge. Similar behaviour was observed in Chapter 2.

To determine the flow behaviour in the leading edge region, we follow the same process as in Chapter 2. The sublayer is of thickness $O(Re^{-2/5})$ and the velocity $\hat{u} = O(Re^{-1/5})$. To determine the x -scale of the region, we consider the limit $x_s \rightarrow 0$ in the Navier-Stokes equations with the above scales to find that the normal inertial and pressure gradient terms balance in a distinguished limit when $x_s = O(Re^{-2/5})$. Thus, by continuity $\hat{v} = O(Re^{-1/5})$ in the local leading edge region. We introduce the leading edge streamwise coordinate $X = O(1)$ such that $x_s = Re^{-2/5}X$ and expand the velocities and

pressure in this region as

$$U = Re^{-\frac{1}{5}}\bar{u}(X, \hat{Y}) + \dots, \quad (5.36)$$

$$V = Re^{-\frac{1}{5}}\bar{v}(X, \hat{Y}) + \dots, \quad (5.37)$$

$$P = Re^{-\frac{2}{5}}\bar{p}(X, \hat{Y}) + \dots, \quad (5.38)$$

which when substituted into the Navier-Stokes equations yield the inviscid Euler equations at leading order throughout the region $-\infty < X < \infty, -\infty < \hat{Y} < \infty$. We discount bluff leading edge geometries, so that locally the leading edge appears as a semi-infinite flat plate.

The governing equations for the full leading order problem of the leading edge region match those of Chapter 2. There, the full equations are given by (2.17) and (2.18), which are repeated here for clarity

$$\nabla^2\psi = -\omega(\psi), \quad (5.39)$$

$$\bar{p} + \frac{1}{2}(\psi_X^2 + \psi_Y^2) = B(\psi), \quad (5.40)$$

$$B'(\psi) = -\omega(\psi). \quad (5.41)$$

In the above equations, ψ is the streamfunction ($\bar{u} = \psi_{\hat{Y}}, \bar{v} = -\psi_X$), ω the vorticity and B the pressure head. In this chapter, we concentrate on the flow in the limit $X \rightarrow \infty$, to provide starting conditions for the sublayer problem such that the Kutta trailing edge condition is satisfied. In keeping with Bowles & Smith (2000a) and to simplify the problem in the leading edge region, the wake length in the sublayer l_W is taken so that on comparison to l_B , the length of the blade, $l_W \gg l_B$. This means that the oncoming velocities in the leading edge region are such that $\bar{u} \gg \bar{v}$, as seen in Chapter 2.

With the assumption that $\bar{u} \gg \bar{v}$ in the oncoming wake profile, we expect the flow to enter and exit the region as $|X| \rightarrow \infty$ unidirectionally and given the inviscid nature of the leading order problem, the incoming vorticity is conserved on each streamline through the region. Thus, we have the Bernoulli and vorticity requirements across the leading edge

$$\bar{p}(0^-) + \frac{1}{2}\bar{u}(0^-)^2 = \bar{p}_+(0^+) + \frac{1}{2}\bar{u}_+^2(0^+) = \bar{p}_-(0^+) + \frac{1}{2}\bar{u}_-^2(0^+), \quad (5.42)$$

$$\frac{\partial \bar{u}}{\partial \hat{Y}} \text{ is conserved along every streamline,} \quad (5.43)$$

in the sublayer problem. Here, $\bar{p}(0^-)$ is the oncoming pressure in the wake, with velocity profile $\bar{u}(0^-)$. The exiting pressures and velocity profiles from the leading edge region above and beneath the blade are given by $\bar{p}_\pm(0^+)$ and $\bar{u}_\pm(0^+)$ respectively. Note, we have neglected \bar{v} in the formulation due to our assumption $\bar{u} \gg \bar{v}$. The relations (5.42) and (5.43) are enough to give the velocity as $X \rightarrow \infty$ in terms of a known incoming flow profile and pressure jumps. We discuss this further in the numerical methods section 5.3 later.

The outgoing \bar{u}_\pm functions are inviscid approximations to the actual solution on passing the leading edge. With the onset of the no-slip condition at the leading edge, there would be a Blasius-like boundary-layer in this region, of normal scale $y = O(Re^{-3/5})$. The thickness of the boundary-layer is asymptotically smaller than the thickness of the leading edge region and thus perturbations to the leading order inviscid problem are small and not considered further.

5.2.4 Inviscid free-stream region

The free-stream, $U = 1$, is perturbed by the presence of the boundary-layer, so that the expansions take on the form

$$U = 1 + Re^{-\frac{2}{5}}u(x_s, y) + \dots, \quad (5.44)$$

$$V = 0 + Re^{-\frac{2}{5}}v(x_s, y) + \dots, \quad (5.45)$$

$$P = Re^{-\frac{2}{5}}p(x_s, y) + \dots, \quad (5.46)$$

with the scales arising on matching with the bulk-layer. Substitution into the Navier-Stokes equations yields the Cauchy-Riemann equations for p and v holding at leading order in the free-stream. We notice that this is the same as in the previous two chapters, but now driven by the interactive sublayer flow above. To solve the Cauchy-Riemann equations, we use exactly the same method as presented in the non-interactive many-blade limit of the last chapter. The bounded, analytic complex function $w(x + iy) = p(x, y) + iv(x, y)$ is

sought using Cauchy's integral formula. This gives the same integral equations as before, for p and v , for a point away from $y = 0$

$$p(x_0, y_0) = \frac{1}{2\pi} \int_{-\infty}^{\infty} \frac{y_0[p](x_s) + (x_s - x_0)[v](x_s)}{(x_s - x_0)^2 + y_0^2} dx_s, \quad (5.47)$$

$$v(x_0, y_0) = \frac{1}{2\pi} \int_{-\infty}^{\infty} \frac{y_0[v](x_s) - (x_s - x_0)[p](x_s)}{(x_s - x_0)^2 + y_0^2} dx_s, \quad (5.48)$$

where

$$[p](x_s) = p_+(x_s) - p_-(x_s), \quad (5.49)$$

$$[v](x_s) = v_+(x_s) - v_-(x_s), \quad (5.50)$$

denote the difference between the values of p and v across the boundary-layer. Matching the normal velocities in the bulk-layer and free-stream yields v_{\pm} as

$$v_{\pm}(x_s) = \mp \lambda_{\pm} b'_{\pm}(x_s) \quad \text{for } 0 \leq x_s \leq L. \quad (5.51)$$

By subtracting the above equations for v_+ and v_- and applying pressure continuity in the wake and the Kutta condition, equations (5.47) and (5.48) are subject to the conditions

$$[v](x_s) = -\lambda_{\pm} b'_{\pm}(x_s) \quad \text{for } 0 \leq x_s \leq L, \quad (5.52)$$

$$[p](x_s) = 0 \quad \text{for } x_s = l \text{ and in the wake.} \quad (5.53)$$

The differences $[v]$ are unknown in advance due to the unknown sublayer displacements and $[p]$ is unknown over the blade. Cauchy's integral formula is now used again, this time for $w(x + i0) = p_+(x_s) + iv_+(x_s)$ and $w(x - i0) = p_-(x_s) + iv_-(x_s)$. We find that the pressures p_{\pm} and the normal velocities v_{\pm} are related by

$$p_+(x_0) = -\frac{1}{\pi} \int_{-\infty}^{\infty} \frac{v_+(x_s)}{x_s - x_0} dx_s, \quad (5.54)$$

$$p_-(x_0) = -\frac{1}{\pi} \int_{-\infty}^{\infty} \frac{v_-(x_s)}{x_s - x_0} dx_s, \quad (5.55)$$

$$v_+(x_0) = \frac{1}{\pi} \int_{-\infty}^{\infty} \frac{p_+(x_s)}{x_s - x_0} dx_s, \quad (5.56)$$

$$v_-(x_0) = \frac{1}{\pi} \int_{-\infty}^{\infty} \frac{p_-(x_s)}{x_s - x_0} dx_s. \quad (5.57)$$

Next, we apply the periodicity argument to (5.54) only, as the same analysis can be carried out for all the other equations. The integral in (5.54) is written

in three parts as follows

$$\int_{-\infty}^{\infty} \frac{v_+(x_s)}{x_s - x_0} dx_s = \int_{-\infty}^0 \frac{v_+(x_s)}{x_s - x_0} dx_s + \int_0^L \frac{v_+(x_s)}{x_s - x_0} dx_s + \int_L^{\infty} \frac{v_+(x_s)}{x_s - x_0} dx_s. \quad (5.58)$$

Since the period in x_s is from 0 to L , we decompose the first and third integrals further into an integral across the k^{th} period

$$\begin{aligned} \int_{-\infty}^{\infty} \frac{v_+(x_s)}{x_s - x_0} dx_s &= \sum_{k=-\infty}^{-1} \int_{kL}^{(k+1)L} \frac{v_+(x_s)}{x_s - x_0} dx_s + \int_0^L \frac{v_+(x_s)}{x_s - x_0} dx_s \\ &+ \sum_{k=1}^{\infty} \int_{kL}^{(k+1)L} \frac{v_+(x_s)}{x_s - x_0} dx_s, \end{aligned} \quad (5.59)$$

and by defining $x_s = x'_s + kL$, we have

$$\begin{aligned} \int_{-\infty}^{\infty} \frac{v_+(x_s)}{x_s - x_0} dx_s &= \sum_{k=-\infty}^{-1} \int_0^L \frac{v_+(x'_s)}{x'_s + kL - x_0} dx'_s + \int_0^L \frac{v_+(x'_s)}{x'_s - x_0} dx'_s \\ &+ \sum_{k=1}^{\infty} \int_0^L \frac{v_+(x'_s)}{x'_s + kL - x_0} dx'_s. \end{aligned} \quad (5.60)$$

Next, the $-k^{\text{th}}$ and k^{th} terms in each of the two sums are paired-off,

$$\begin{aligned} \int_{-\infty}^{\infty} \frac{v_+(x_s)}{x_s - x_0} dx_s &= \sum_{k=1}^{\infty} \int_0^L \frac{v_+(x'_s)}{x'_s - kL - x_0} + \frac{v_+(x'_s)}{x'_s + kL - x_0} dx'_s \\ &+ \int_0^L \frac{v_+(x'_s)}{x'_s - x_0} dx'_s, \end{aligned} \quad (5.61)$$

and on simplification, we have

$$\int_{-\infty}^{\infty} \frac{v_+(x_s)}{x_s - x_0} dx_s = \int_0^L v_+(x'_s) \left\{ \frac{1}{x'_s - x_0} + \sum_{k=1}^{\infty} \frac{2(x'_s - x_0)}{(x'_s - x_0)^2 + (kL)^2} \right\} dx'_s. \quad (5.62)$$

Gradshteyn & Ryzhik (1988) give the summation in the bracketted term in the integrand as

$$\frac{1}{x'_s - x_0} + \sum_{k=1}^{\infty} \frac{2(x'_s - x_0)}{(x'_s - x_0)^2 + (kL)^2} = \frac{\pi}{L} \cot \left\{ \frac{\pi(x'_s - x_0)}{L} \right\}, \quad (5.63)$$

and thus the periodic pressure-displacement law is given by

$$p_+(x_0) = \frac{\lambda_+}{L} \int_0^L b'_+(x_s) \cot \left\{ \frac{\pi(x_s - x_0)}{L} \right\} dx_s, \quad (5.64)$$

upon substituting the condition (5.51) for v_+ . In (5.64) the prime on the x_s term has been dropped for convenience. A similar expression was derived in Bowles & Smith (2000a) and also Tsao *et al.* (1997), where stability and interaction of thin liquid layers on an airfoil were analysed. Applying the periodicity arguments to the equations (5.55) - (5.57) gives the pressure-displacement laws as

$$p_{\pm}(x_0) = \pm \frac{\lambda_{\pm}}{L} \int_0^L b'_{\pm}(x_s) \cot \left\{ \frac{\pi(x_s - x_0)}{L} \right\} dx_s, \quad (5.65)$$

$$b'_{\pm}(x_0) = \mp \frac{1}{\lambda_{\pm} L} \int_0^L p_{\pm}(x_s) \cot \left\{ \frac{\pi(x_s - x_0)}{L} \right\} dx_s. \quad (5.66)$$

5.2.5 Comparisons with the non-interactive limit

Now we have completed the formulation of the pressure interactive many-blade limit, it is worth briefly drawing a few comparisons with the previous many-blade limit of Chapter 4.

The bulk-layer solution is much the same as the previous non-interactive limit. We found identical leading order balances leaving the leading order term for V and first order term for U unchanged. The first-order balances differed to the non-interactive limit through the appearance of a pressure gradient term on the right-hand side of the momentum equation in the bulk-layer. This adds a slight complexity to the solution of the equations, but leaves the behaviour essentially unchanged. Another pressure gradient term appeared in the equations governing the leading order behaviour for U . We integrated the equations and applied the periodicity argument over x_s , which left the mean-Blasius solution governing the leading order behaviour for U in the bulk-layer, as previously seen in the non-interactive limit.

The sublayer problem is now governed by the pressure interactive boundary-layer equations to leading order. Since the pressure gradient appears at leading order within the sublayer equations, the Kutta condition can now be applied directly whereas in the non-interactive limit, this condition was enforced in the free-stream equations. For the Kutta condition to be satisfied, a small leading edge region arises, that allows the pressure and velocity to jump. This is not seen in the non-interactive limit. We can also enforce pressure continuity in the wake through the regularity conditions (5.31) in the

sublayer. As with the Kutta condition, pressure continuity in the wake was applied via the free-stream perturbation in the non-interactive limit. There is a different boundary condition to contend with in this interactive case, as the unknown displacement functions b_{\pm} are unknown in the matching condition for \hat{u} as $\hat{Y} \rightarrow \infty$. These displacement functions are related to the unknown pressure through the pressure-displacement laws (5.65) and (5.66) gained from the free-stream.

The governing equations for the perturbations to the free-stream remain unchanged from the non-interactive limit, but development of the integral equations resulting from using Cauchy's integral formula is undertaken in a slightly different way. The integral equations are used to determine the unknown displacement functions b_{\pm} caused by the sublayer and must be solved in tandem with the sublayer in determining the matching condition (5.32). Thus we see that the boundary-layer and the free-stream remain coupled through the unknown pressure and sublayer displacements.

5.2.6 The condensed limit

To simplify our analysis in finding solutions to the interactive sublayer problem, we will solve a condensed problem. We will explore the condensed limit as a result of finding the relative sizes of each of \hat{Y} , \hat{u} , \hat{v} , \hat{p} and b_{\pm} required to maintain the interactive boundary-layer equations (5.28) and (5.29) and conditions (5.30) - (5.34) over all scales in x_s . Let $x_s = O(L)$, where L represents the streamwise extent of a typical blade-wake period. We look for balances of

$$\hat{u} \frac{\partial \hat{u}}{\partial x_s} \sim \frac{\partial^2 \hat{u}}{\partial \hat{Y}^2} \sim \frac{d\hat{p}}{dx_s}, \quad (5.67)$$

for the given scale of x_s . Within the sublayer, \hat{u} is estimated to be $O(\hat{Y})$ due to the predominantly shear like flow behaviour in the sublayer and boundary condition (5.32). The balance of streamwise advection and diffusion terms, $\hat{u} \hat{u}_{x_s} \sim \hat{u}_{\hat{Y}\hat{Y}}$, gives us that $\hat{Y} = O(L^{1/3})$ and hence $\hat{u} = O(L^{1/3})$. The other balance we seek is $\hat{u} \hat{u}_{x_s} \sim \hat{p}'(x_s)$, yielding the result $\hat{p} = O(L^{2/3})$. Hence, by the continuity equation $\hat{v} = O(L^{-1/3})$ and so $b_{\pm} = O(L^{1/3})$ from the boundary condition (5.32). However, in the pressure-displacement laws

(5.65) the right-hand side scales as $O(L^{-2/3})$ whilst the left-hand side scales like $O(L^{2/3})$. Hence in the limit $L \rightarrow 0$, a mismatch occurs in this law unless $b'_\pm = 0$. The case where $b'_\pm = 0$ is called the condensed limit.

Physically, the condensed limit represents the case where a constant displacement is caused to the free-stream by the sublayer. We now have that $b_\pm(x_s) = \pm c_\pm$ where c_\pm are unknown constants representing the displacement caused by the sublayer over the period L . The condensed flow case gives a simplification to our problem, in that there is no x_s -dependence in our far-field matching condition and furthermore is in keeping with previous works by Bowles & Smith (2000a,b), especially in the latter, where no attempt is made to numerically resolve the full problem.

Bowles & Smith (2000a) use the pressure-displacement law in one sublayer calculation and compare their results with the condensed flow solution, for the same blade geometry, and find that the condensed case gives a good representation of the overall flow features. In particular, we note figures 2 and 3 in that paper, where there seems to be good qualitative agreement between the streamwise velocities, pressure and skin friction. Typical numerical values of the calculated displacement functions there are of $O(10^{-2})$, giving only a small difference to the far-field matching condition (5.32).

Condensed flow problems also appear in internal boundary-layer flows, such as the boundary-layer flow between two flat, parallel plates, encountering a bump (see Smith (1982) for a comprehensive review). Other articles where the condensed limit is studied, are Smith *et al.* (1981) in relation to boundary-layer flow past two-dimensional obstacles, and Smith (1983) where trailing edge separation is considered.

5.3 Numerical formulation

The full problem to be solved is given by (5.28) - (5.29) with the boundary conditions (5.30) - (5.34), a Y -shift at $x_s = L$ and the pressure-displacement laws (5.65) - (5.66). As just mentioned, we solve the condensed flow problem, so that $b_\pm(x_s) = \pm c_\pm$, where c_\pm are unknown constants. A Prandtl shift is applied to simplify the blade geometry defined by $\hat{u} = u_*$, $\hat{v} = v_* - u_* f'(x_s)$,

$\hat{p} = p_*$ and $\hat{Y} = Y_* + f(x_s)$. Substitution of the Prandtl shift into the interactive boundary-layer equations leaves them unchanged at leading order

$$u \frac{\partial u}{\partial x} + v \frac{\partial u}{\partial Y} = -\frac{dp}{dx} + \frac{\partial^2 u}{\partial Y^2}, \quad (5.68)$$

$$\frac{\partial u}{\partial x} + \frac{\partial v}{\partial Y} = 0, \quad (5.69)$$

where the * subscripts have been dropped, x_s replaced by x and the shears $\lambda_{\pm} = 1$ are taken for convenience. The boundary conditions are given by

$$u = v = 0 \quad \text{on} \quad Y = 0, \quad 0 < x_s < l, \quad (5.70)$$

$$\frac{\partial u}{\partial Y} = v = 0, p_+(x) = p_-(x) \quad \text{on} \quad Y = 0, \quad l < x_s < L, \quad (5.71)$$

$$u \rightarrow \pm(Y + f_{\pm}(x)) + c_{\pm} \quad \text{as} \quad Y \rightarrow \pm\infty, \quad (5.72)$$

$$L\text{-periodicity in } u, v, \text{ and } p. \quad (5.73)$$

$$Y\text{-shift at } x = L. \quad (5.74)$$

The functions f_{\pm} are known on the blade, since these describe the blade geometry. Although we have $f_+ = f_-$ in the wake, the functions are unknown and must be determined as part of the solution (see later). The condition (5.74) appears due to the leading edge discontinuity to allow the Kutta trailing edge condition to be satisfied. The numerical method developed is similar to the box scheme used by Keller (1978) and Cebeci *et al.* (1979) in calculating separating boundary-layer flows.

5.3.1 Finite-difference discretisation

We discretise the equations on a uniform grid, such that each x - and y -station is described by $x_i = i\delta x$ and $Y_j = j\delta Y$, where δx and δY represent the uniform grid spacings in the x and Y directions respectively and $i = 0, \dots, N$, $j = -M, \dots, M$. The values of u, v and p at (x_i, Y_j) are given by u_i^j, v_i^j and p_i respectively. The governing equations are discretised using centred differences in Y and backward differences in x as

$$u_i^j \left(\frac{u_i^j - u_{i-1}^j}{\delta x} \right) + v_i^j \left(\frac{u_i^{j+1} - u_i^{j-1}}{2\delta Y} \right) = -\frac{p_i - p_{i-1}}{\delta x} + \frac{u_i^{j+1} - 2u_i^j + u_i^{j-1}}{(\delta Y)^2}, \quad (5.75)$$

$$\frac{u_i^j - u_{i-1}^j}{\delta x} + \frac{v_i^{j+1} - v_i^{j-1}}{2\delta Y} = 0, \quad (5.76)$$

given by

$$\mathbf{A}_j = \begin{pmatrix} \frac{-v_j^n}{2\delta Y} - \frac{1}{(\delta Y)^2} & 0 \\ 0 & -\frac{1}{2\delta Y} \end{pmatrix}, \quad (5.81)$$

$$\mathbf{B}_j = \begin{pmatrix} \frac{2u_j^n - u_{i-1}^j}{\delta x} + \frac{2}{(\delta Y)^2} & \frac{u_{j+1}^n - u_{j-1}^n}{2\delta Y} \\ \frac{1}{\delta x} & 0 \end{pmatrix}, \quad (5.82)$$

$$\mathbf{C}_j = \begin{pmatrix} \frac{v_j^n}{2\delta Y} - \frac{1}{(\delta Y)^2} & 0 \\ 0 & \frac{1}{2\delta Y} \end{pmatrix}, \quad (5.83)$$

$$\mathbf{R}_j = \begin{pmatrix} u_j^n \left(\frac{u_j^n - u_{i-1}^j}{\delta x} \right) + v_j^n \left(\frac{u_{j-1}^n - u_{j+1}^n}{2\delta Y} \right) + \frac{p_{i-1} - p^n}{\delta x} + \frac{u_{j+1}^n - 2u_j^n + u_{j-1}^n}{(\delta Y)^2} \\ \frac{u_{i-1}^j - u_j^n}{\delta x} + \frac{v_{j-1}^n - v_{j+1}^n}{2\delta Y} \end{pmatrix}, \quad (5.84)$$

$$\mathbf{E}_j = \begin{pmatrix} 1 \\ 0 \end{pmatrix}, \quad (5.85)$$

with the 0th block matrices given by

$$\mathbf{B}_0 = \begin{pmatrix} 1 & 0 \\ 0 & 1 \end{pmatrix}, \mathbf{C}_0 = \begin{pmatrix} 0 & 0 \\ 0 & 0 \end{pmatrix},$$

$$\mathbf{R}_0 = \begin{pmatrix} -u_0^n \\ -v_0^n \end{pmatrix}, \mathbf{E}_0 = \begin{pmatrix} 0 \\ 0 \end{pmatrix}, \quad (5.86)$$

representing no-slip and no-normal flow conditions on the blade. To satisfy the matching conditions as $Y \rightarrow \infty$, (5.72) is differentiated with respect to Y and is discretised using a first-order backward difference in Y . The other condition applied is a first-order accurate in Y version of the continuity equation. The linear system is completed by the block matrices

$$\mathbf{A}_M = \begin{pmatrix} -1 & 0 \\ 0 & \frac{-1}{\delta Y} \end{pmatrix}, \mathbf{B}_M = \begin{pmatrix} 1 & 0 \\ \frac{1}{\delta x} & \frac{1}{\delta Y} \end{pmatrix},$$

$$\mathbf{R}_M = \begin{pmatrix} \delta Y + u_{M-1}^n - u_M^n \\ u_{i-1}^M - u_M^n + v_{M-1} - v_M \end{pmatrix}, \mathbf{E}_M = \begin{pmatrix} 0 \\ 0 \end{pmatrix}. \quad (5.87)$$

The conditions as $Y \rightarrow \infty$ above are applied at some Y_M with M taken suitably large to fully capture the sublayer flow. On building the 2×2 block matrix system, it is seen that we have a pentadiagonal system for the values $(\Delta u_j, \Delta v_j)$ for all j at the current x -station. The pentadiagonal system itself

gives $2M + 2$ equations for $2M + 3$ unknowns, the extra unknown being Δp . To solve the linear system we employ the LAPACK subroutine `dgbsv`, which solves a general banded linear system. The subroutine is able to solve the system with two (or more) right-hand sides, and works on LU decomposition of the banded matrix. We solve the system for each of \mathbf{R}_j and \mathbf{E}_j , with Δp arbitrary. After gaining the solutions of the linear system, we need to satisfy the final condition on u , namely

$$u \rightarrow Y + c_+ + f_+(x) \quad \text{as } Y \rightarrow \infty. \quad (5.88)$$

We use this equation to determine Δp . At the M^{th} Y -station, we impose that

$$u_M^n + \Delta u_M = Y_M + c_+ + f_+(x), \quad (5.89)$$

and from the solution of the linear system, we have

$$\Delta u_M = R_M^* - \frac{\Delta p}{\delta x} E_M^*, \quad (5.90)$$

where R_M^* and E_M^* are the first components of the solution vectors to each right-hand side from the banded solver subroutine at Y_M . We substitute for Δu_M in (5.89) to yield the final equation to determine Δp

$$\Delta p = \frac{\delta x}{E_M^*} (u_M^n + R_M^* - (Y_M + c_+ + f_+(x_i))). \quad (5.91)$$

Once Δp is determined, we may calculate all the remaining Δu_j and Δv_j terms and hence the $(n + 1)^{\text{th}}$ iterates.

To employ the Newton iteration technique, we require the solution from the previous and current x -stations. Initially, we guess that the solution at the current x -station is exactly that at the previous x -station and this forms our first iterate. Now, we can numerically formulate the linear system for a given c_+ and $f_+(x_i)$ and solve using the LAPACK subroutine. After gaining the two solution vectors \mathbf{R}_j^* and \mathbf{E}_j^* , Δp is determined so that u satisfies the matching condition as $Y \rightarrow \infty$. This method is repeated at each x -station, by updating the n^{th} iterates for u, v and p and subsequent recomputation of the linear system until

$$\epsilon = \max\{|\Delta u_j|, |\Delta v_j|, |\Delta p| : 0 \leq j \leq M\} < 10^{-6}. \quad (5.92)$$

Once this is achieved, the solution is found at the current x -station and we may proceed to the next station downstream. Typically, in all our calculations we found that only four or five iterations were needed before convergence was achieved.

5.3.3 Solution in the wake

Similar to the solution over the blade, we solve a problem above and below $Y = 0$. In the wake, $f_+ = f_-$ in the wake and must be determined as part of the solution. Let $f_+ = f_- = f$ in the wake.

The Newton iterates are substituted into the boundary-layer equations to form the same linear system (5.85), with the same conditions applied at Y_M . However, another 2×2 matrix, \mathbf{D}_0 , is included in the first row of the new linear system to maintain second order accuracy in Y close to $Y = 0$. The matrix \mathbf{D}_0 arises on applying a three-point forward difference formula to the no-shear condition $u_Y = 0$ at $Y = 0$ in the wake. The final conditions required to complete the linear system are

$$\mathbf{B}_0 = \begin{pmatrix} -3 & 0 \\ 0 & 1 \end{pmatrix}, \quad \mathbf{C}_0 = \begin{pmatrix} 4 & 0 \\ 0 & 0 \end{pmatrix}, \quad \mathbf{D}_0 = \begin{pmatrix} -1 & 0 \\ 0 & 0 \end{pmatrix},$$

$$\mathbf{R}_0 = \begin{pmatrix} 3u_0^n - 4u_1^n + u_2^n \\ -v_0^n \end{pmatrix}, \quad \mathbf{E}_0 = \begin{pmatrix} 0 \\ 0 \end{pmatrix}. \quad (5.93)$$

For a given x_i in the wake, the solution proceeds as follows. We solve the problems for $Y > 0$ and $Y < 0$ in tandem. Initially, a value for $f(x_i)$ is guessed (typically $f(x_{i-1})$) and this then allows us to build a linear system for $Y > 0$ and $Y < 0$. Both systems are solved, for the given $f(x_i)$, using the Newton iteration method, until the same convergence tolerance ϵ is met between all the small changes Δu_j , Δv_j and Δp .

To determine $f(x_i)$, we enforce the regularity condition that u must be continuous across $Y = 0$, to within a specific tolerance. If u is not deemed continuous, the guess at $f(x_i)$ is updated using the secant method, followed by repeating the procedure described above until the velocity satisfies the convergence tolerance. For $Y > 0$ and $Y < 0$, we denote the velocity at $Y = 0$ by u_+ and u_- respectively. The velocity is deemed continuous when

$\epsilon_2 = |u_+ - u_-| < 10^{-10}$. When this tolerance criterion is satisfied, pressure continuity in the wake is satisfied. The solution is then found for the current x_i and we may step forward to x_{i+1} .

The number of Newton iterations needed for convergence in the wake was typically four or five, except close to the trailing edge, due to the discontinuous nature of the pressure gradient. There, up to 12 iterations were needed for the most extreme cases of non-symmetry. A further four or five iterations of the value of $f(x_i)$ were needed to obtain a continuous velocity.

The solution for each x_i on the blade and in the wake was trialled for values of $\epsilon = 10^{-6}, 10^{-8}$ and 10^{-10} , with very little difference between the solutions. In the final code, $\epsilon = 10^{-6}$ was taken, since fewer Newton iterations were needed and this sped up the calculations slightly. The tolerance $\epsilon_2 = 10^{-10}$ was kept very small for continuous velocities in the wake to obtain accurate solutions.

5.3.4 The leading edge solution

The leading edge solution has the vital task of providing the correct leading edge onset conditions such that the Kutta trailing edge condition will be satisfied. Recall the equations (5.42) and (5.43) governing the flow behaviour just before and after the leading edge region

$$\bar{p}(0^-) + \frac{1}{2}\bar{u}(0^-)^2 = \bar{p}_+(0^+) + \frac{1}{2}\bar{u}_+^2(0^+) = \bar{p}_-(0^+) + \frac{1}{2}\bar{u}_-^2(0^+), \quad (5.94)$$

$$\frac{\partial \bar{u}}{\partial \bar{Y}} \text{ is conserved along every streamline.} \quad (5.95)$$

The second condition amounts to there being at most a constant shift Y_s in the position of all the oncoming streamlines as the leading edge is passed over. The unknown Y_s gives us the streamline that is deflected vertically to represent the blade surface in the leading edge region by determining the correct fluxes for $\bar{Y} > 0$ and $\bar{Y} < 0$. With the oncoming velocity profile to the leading edge region, we guess the value of Y_s needed to satisfy the Kutta trailing edge condition, and hence shift all the incoming flow profile by the amount Y_s using cubic splines. After applying the shift, the conditions as $\bar{Y} \rightarrow \pm\infty$ (given by (5.72), the sublayer matching condition) on \bar{u}_+ and \bar{u}_-

are not satisfied in general. We apply the far-field condition

$$\bar{u}_{\pm}(\bar{Y}_{\pm M}) = \pm \bar{Y}_{\pm M} + c_{\pm} \quad (5.96)$$

together with (5.94) to deduce the pressure jumps needed downstream for the far-field condition as $\bar{Y} \rightarrow \infty$ to be satisfied. Once the pressure jumps are determined, we can then adjust the now known $\bar{u}_{\pm}(0^+)$ profiles to ensure that both the Bernoulli relation (5.94) and conservation of vorticity (5.95) are satisfied. Hence, the starting conditions required for the blade sweep in the sublayer region are found.

5.3.5 The streamwise sweep

For the first sweep, the starting condition

$$u = |Y| + c_{\pm}, \quad v = 0, \quad (5.97)$$

is constructed for the sublayer flow with $p_+(0) = p_-(0) = 0$ and furthermore, the values of the constant displacements are set as $c_{\pm} = 0$ and $Y_s = 0$. The solution over the blade is found by marching downstream to the trailing edge, using the method at each x_i described above. At $x = l$, a test is made to see if the Kutta condition is met to within a specified tolerance $\epsilon_3 = |p_+(l) - p_-(l)| < 10^{-10}$. If this is not the case, the Y_s value is adjusted using the secant method followed by returning to the leading edge, updating the starting conditions and resweeping to the trailing edge. This process continues until the tolerance criterion ϵ_3 is met and usually requires less than ten iterations. A sweep through the wake then follows, finding $f(x_i)$ and the pressure $p(x_i)$ until we arrive at $x = L$. Here we record the velocity profiles, pressure and pressure gradients, and a test is made to see if the end velocities and pressure gradient from the current sweep are the same as those from the previous sweep to within a relative error of 1%. If convergence is not met, we use the end velocities and pressure from the current sweep to form new starting conditions for the leading edge region, followed by complete recomputation. This method is repeated until we gain convergence in the velocities and pressure gradient. For a suitable initial guess of c_+ , we needed only six or seven iterations to achieve periodicity in the velocities and pressure gradient.

Once the velocities and pressure gradient are periodic, we test whether the pressure is periodic. We calculate the absolute error between the recorded end pressures from successive sublayer sweeps as our criterion for convergence. To gain pressure periodicity, the values of c_{\pm} are adjusted using the secant method to obtain convergence to within $\epsilon_4 < 10^{-4}$, with this final iteration requiring eight to ten cycles. This leaves only one unknown, c_- , the choice of which is discussed in the results presented later. Once the pressure is periodic, the solution is found.

We took the normal scale to be $-20 \leq Y \leq 20$ in most of our computations, except for very large blade thicknesses where the normal scale $-40 \leq Y \leq 40$ was required to fully capture the sublayer behaviour. The grid spacings $\delta x = 0.01$ and $\delta Y = 0.05$ were chosen with checks carried out on the smaller grid size $\delta x = 0.005$ and $\delta Y = 0.01$, giving results with extremely close agreement. As we have seen in previous chapters, the discretised equations are second-order accurate in Y but only first-order accurate in x . The same double stepping technique (as used in previous chapters) was used to gain second-order accuracy in x .

5.3.6 Flow reversal

The above procedure solves the sublayer problem in cases of forward flow. With the pressure gradient now appearing in the sublayer momentum equation, in contrast to Chapters 3 and 4, flow reversal may occur if the blade thickness or shape is large enough to provoke a significant adverse pressure gradient. In the numerical scheme, flow reversal causes a numerical instability in the solutions due to the uu_x term in the momentum equation. This term becomes positive when flow reversal occurs. To combat this problem, several approaches were tested. Firstly, the Reyhner & Flugge-Lotz (1968) approximation was adopted, whereby whenever u_j is negative for any j , we simply drop the uu_x term from the momentum equations for that particular j . This approximation (sometimes called a FLARE switch) has been widely used in calculating separating flow, for example, in Keller (1978) and Cebeci *et al.* (1979). However, as pointed out by Smith (1983), dropping the uu_x

term means that a slightly different problem is solved and so in this chapter, windward differencing is adopted whenever u_j became negative. This involves changing the discretised version of the uu_x term to

$$uu_x = u_i^j \left(\frac{u_{i+1}^j - u_i^j}{\delta x} \right).$$

The u_{i+1}^j term used comes from the previous sublayer sweep. Ordinarily, windward differencing would require multiple sweeping in the separated region. However, due to the multiple sweeping already present in the numerical method, to satisfy periodicity, no additional computational burden is added. Solutions using both the FLARE and upwinding methods were obtained and compared, each giving very similar results.

5.4 Results

We use the numerical method described above to solve several problems posed in Bowles & Smith (2000a,b) for both symmetric and non-symmetric blade configurations. Throughout this section we present calculations of the skin frictions τ_{\pm} , defined as

$$\tau_{\pm} = \frac{\partial \hat{u}}{\partial \hat{Y}} \Big|_{\hat{Y}=0^{\pm}}, \quad (5.98)$$

for the upper and lower blade surfaces respectively and the lift, L , as

$$L = - \int_0^l \{p_+(x_s) - p_-(x_s)\} dx_s. \quad (5.99)$$

First, we consider symmetric flow problems to include blade thickness and a comparison of the FLARE and upwinding schemes in the advent of flow reversal. Then we discuss non-symmetric problems of blades with a local angle of attack and unequal thickness.

5.4.1 Symmetric flow problems

We begin with solutions to some configurations of a symmetric blade. In the symmetric case, we take $L = 25$ and the trailing- and leading edge positions to be $L/4$ and $3L/4$ respectively, so that direct comparisons can be made with the results presented in Bowles & Smith (2000a). In the symmetric

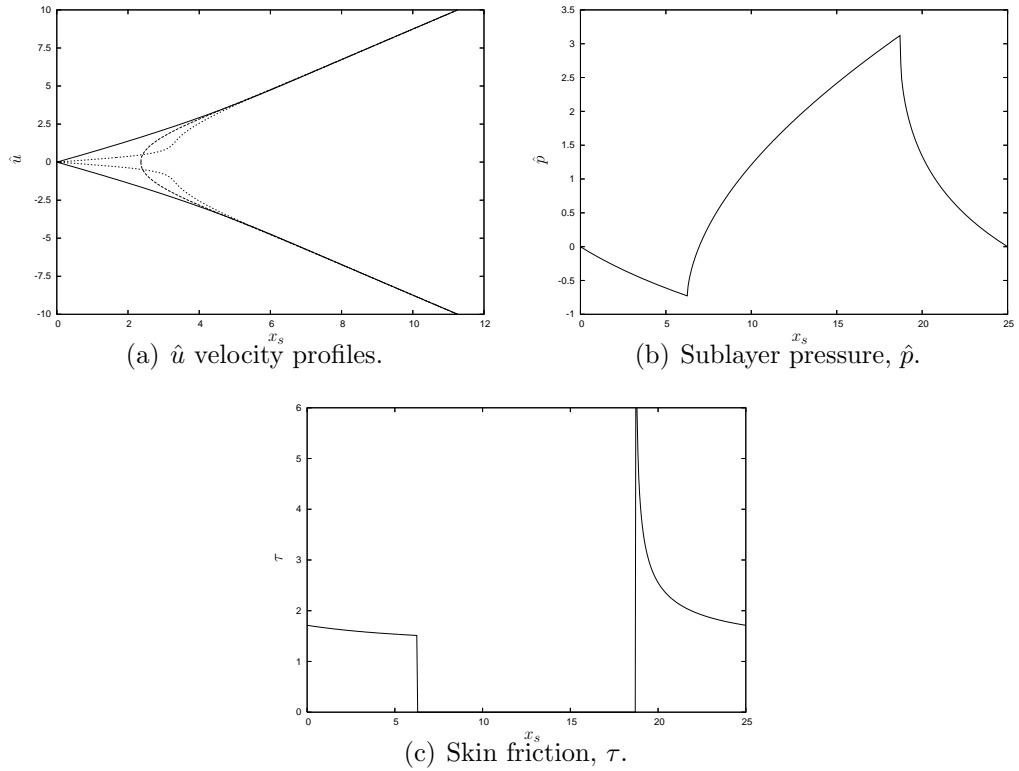


Figure 5.2: Velocity, pressure and skin friction solutions for the case of $f_{\max} = 0$. In (a), the velocity profiles are taken from positions just before the trailing edge (solid line), mid-wake (broken line) and just after the leading edge (dotted line).

case, only one constant c_+ , has to be found as $c_- = c_+$. Furthermore, we do not have to solve the leading edge region as the pressures $\hat{p}_+ = \hat{p}_-$ everywhere and so pressure continuity in the wake and the Kutta condition are already satisfied. We take

$$f_{\pm}(x_s) = \begin{cases} \pm f_{\max} \cos\left(\frac{\pi x_s}{L}\right) & \text{for } 0 \leq x_s \leq L/4, \\ 0 & \text{for } L/4 < x_s < 3L/4, \\ \pm f_{\max} \cos\left(\frac{\pi x_s}{L}\right) & \text{for } 3L/4 \leq x_s \leq L, \end{cases} \quad (5.100)$$

in all the calculations in this subsection, and present solutions for the parameter $f_{\max} = 0, 0.5, 4.9$. We have that $f_{\pm}(x_s) = 0$ throughout the wake due to symmetry and this reduces computational time in the wake section.

In figure 5.2 we take $f_{\max} = 0$ and consider the case of a flat blade. The solutions for \hat{u} are taken from the x -stations just before the trailing edge, mid-wake and just after the leading edge. The pressure solution shows a favourable pressure gradient over the blade surfaces and an adverse pressure gradient in the wake. These results are compared to figure 3 in Bowles &

Smith (2000a) and we see good overall agreement. Figure 5.3 has $f_{\max} = 0.5$. The streamline plot shows only a very slight deceleration of the flow on the backward facing slope of the blade. In the pressure solution, a slight adverse pressure gradient over the last portion of the blade occurs, but no separation is encountered. By comparing the skin friction to that in figure 5.2, we see that the skin friction reduces further before the trailing edge.

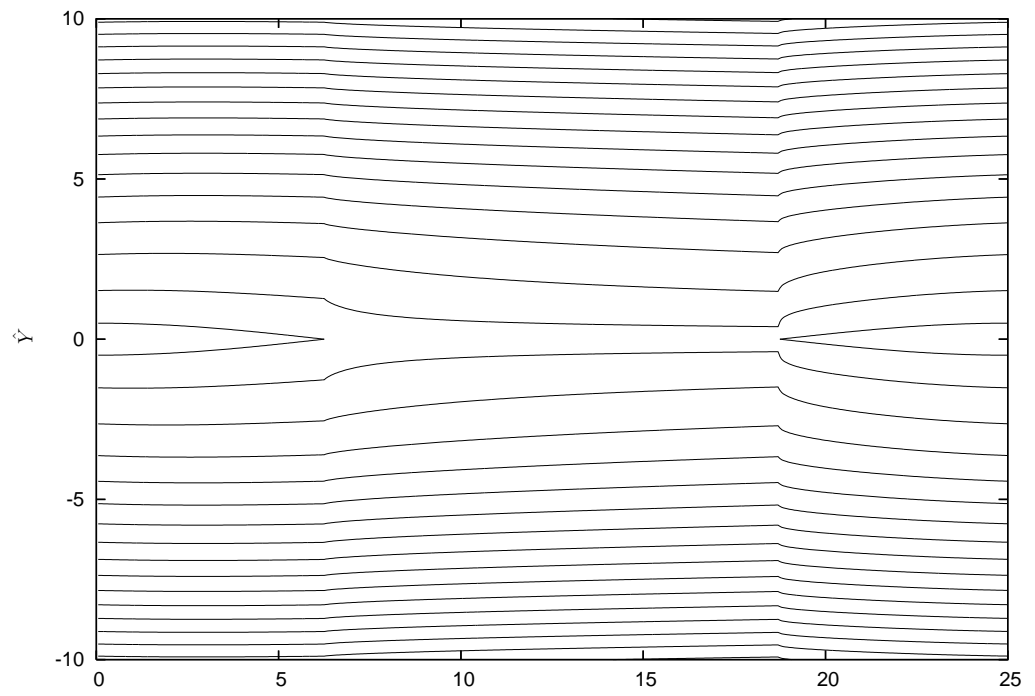
In figures 5.4 and 5.5, solutions for the streamlines and pressure are presented for $f_{\max} = 4.9$ respectively. In figure 5.4, solutions found using the FLARE approximation and the upwinding method are given to allow comparison of each of the methods in the separated region. Separation occurs on the backward facing slope of the blade in both figures 5.4(a) and (b), with a strong adverse pressure gradient, before reattaching on the forward facing slope of the (would-be) next blade in both streamline plots. This forms a large separation eddy which covers the entire wake. Overall, there is good agreement between the streamlines and pressures when using the FLARE approximation and upwinding method, with the slight differences in the separated region due to the loss of the term uu_{x_s} in the FLARE approximation. Furthermore, each method gives excellent agreement in the streamlines and pressure to that given in Bowles & Smith (2000a). The values of c_+ needed to gain periodic solutions in \hat{u} , \hat{v} and \hat{p} in each of the FLARE approximation and upwinding schemes are -3.37 and -3.36 (to three significant figures) respectively. From now on, we adopt the upwinding method if separation is encountered to improve the accuracy of the solution in the separated region.

5.4.2 Non-symmetric flow problems

In Figures (5.6) - (5.11), we take the period $L = 6$ and the leading and trailing edges of the blade to lie at $x_s = 0$ and $x_s = 1$ respectively. Over the blade, thickness and camber effects are prescribed through the functions f_{\pm} as

$$f_{\pm}(x_s) = \pm f_{\max} \sin^2(\pi x_s) - \beta x_s \quad (5.101)$$

with $f = f_{\pm}$ to be found in the wake. The effects of local non-symmetry are produced by adding a local angle of attack and thickness through the



(a) Streamlines.

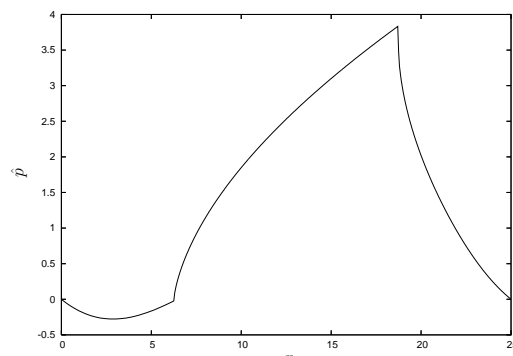
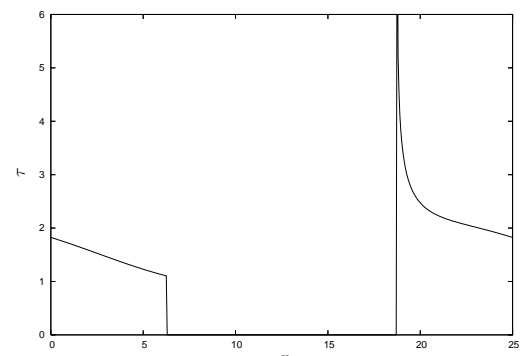
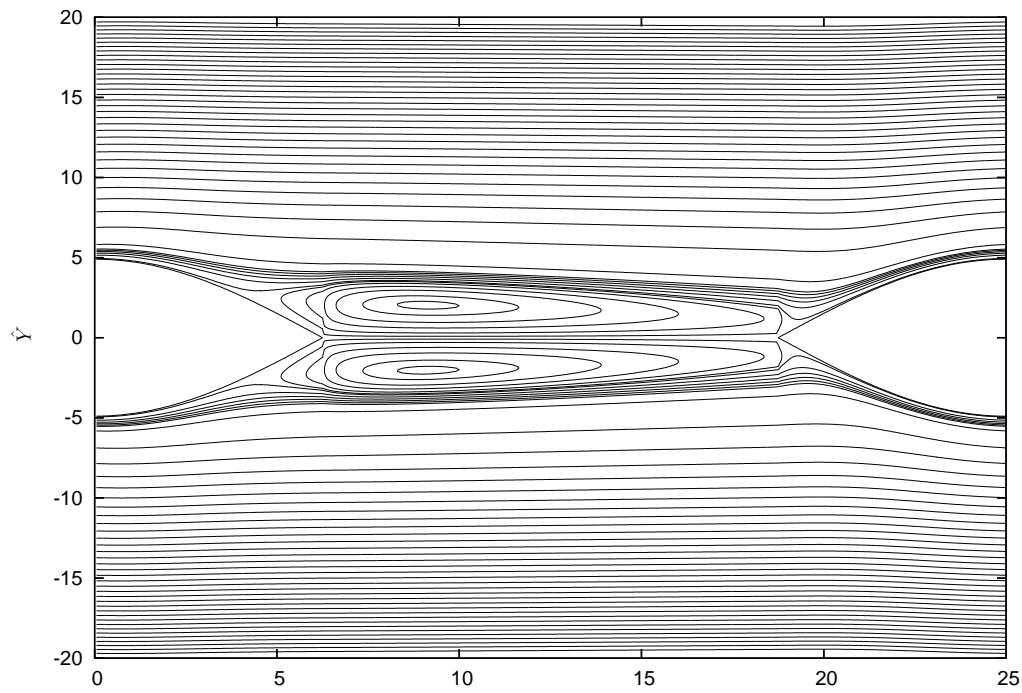
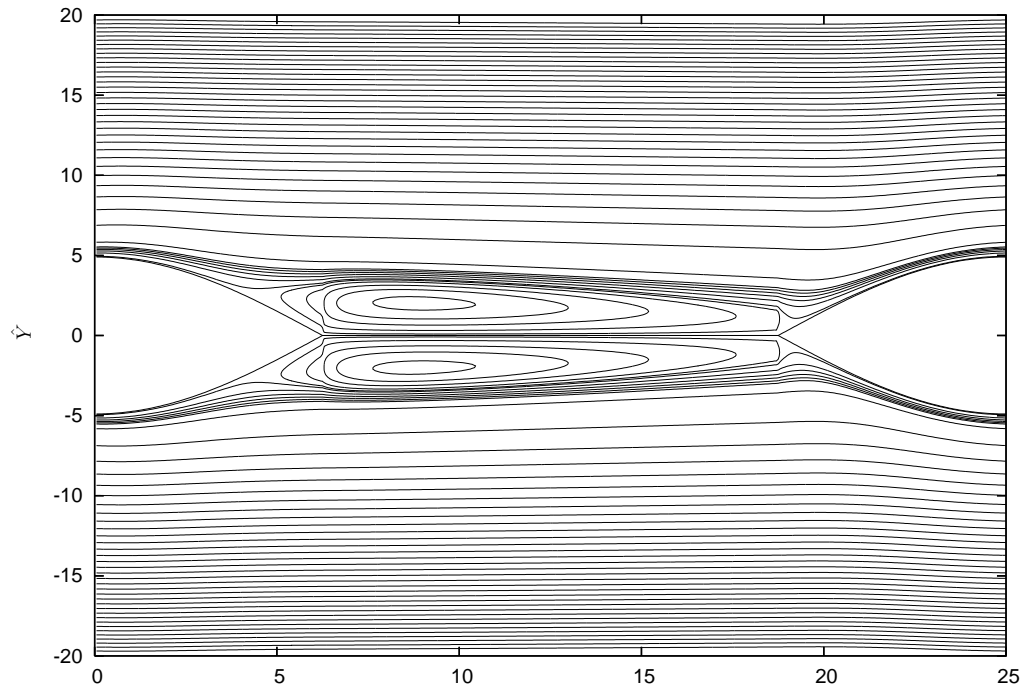
(b) Pressure, \hat{p} .(c) Skin friction, τ .

Figure 5.3: Streamfunction, pressure and skin friction solutions for the case of $f_{\max} = 0.5$.



(a) Streamlines calculated using the FLARE approximation.



(b) Streamlines calculated using upwind differencing.

Figure 5.4: Comparison of the computed streamlines for the case of $f_{\max} = 4.9$ for (a) the FLARE approximation and (b) the upwinding scheme.

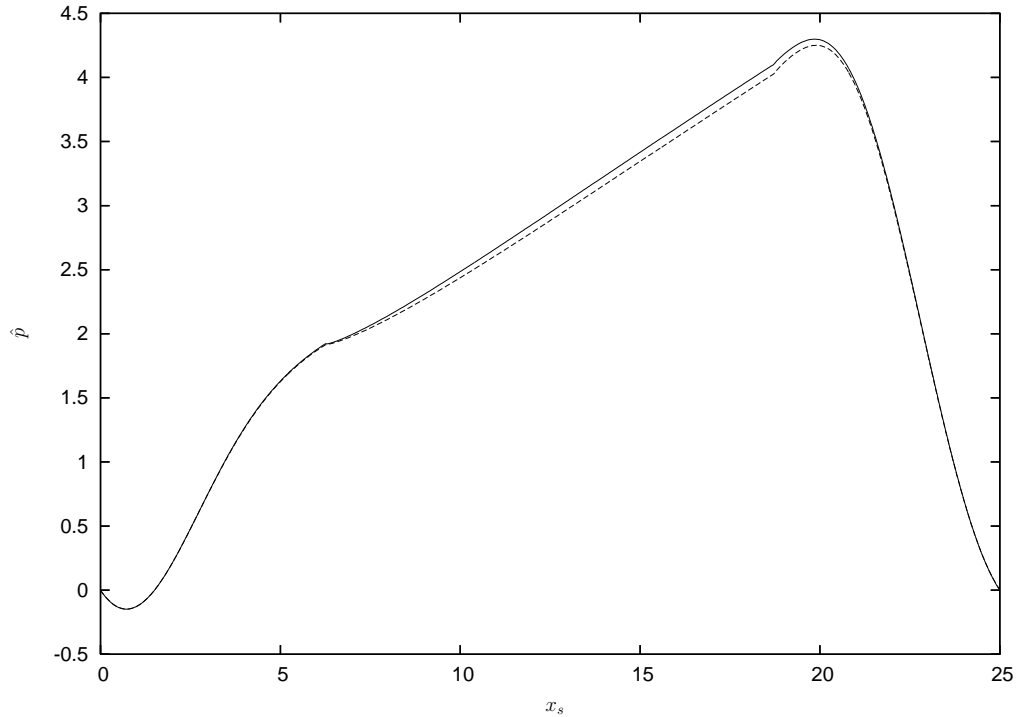


Figure 5.5: Corresponding pressure solutions for $f_{\max} = 4.9$ using the upwinding scheme (solid line) and FLARE approximation (dotted line).

parameters β and f_{\max} , respectively. In all our calculations, we take $c_- = c_+$ to close the system. This choice is taken to analyse the effects produced by the blade geometries to the sublayer alone and was used in some calculations by Bowles & Smith (2000b). Results are presented for some of the configurations used in Bowles & Smith (2000b). They obtained their results using a slightly different method. They prescribe the values for c_{\pm} and the Y -shift Y_s , and instead find a local angle of attack β that satisfies those parameters. In our results, we prescribe the parameters f_{\max} and β and deduce c_{\pm} and Y_s . We find good qualitative agreement between the results in this subsection and those in Bowles & Smith (2000b).

Table (5.1) summarises the values imposed and calculated in figures 5.6 - 5.11. In each figure, we find that for periodicity to be achieved requires $c_+ < 0$. We also notice in the table that the pressure jumps $|\hat{p}_+(0^+)| = |\hat{p}_-(0^+)|$ to three significant figures for every case studied. This is due to the small Y_s , explained in the next paragraph. Figure 5.6 is for the case of a tilted flat blade at angle $\alpha = 0.258$, as shown in figure 3 of Bowles &

Figure	f_{\max}	β	c_+	Y_s	L	$\hat{p}_+(0^+)$	$\hat{p}_-(0^+)$
5.6	0	0.258	-1.21	7.93×10^{-3}	0.301	-0.308	0.308
5.8	0	0.299	-1.84	8.28×10^{-3}	0.326	-0.316	0.316
5.9	0.8	0.575	-2.97	9.86×10^{-3}	0.292	-0.365	0.365
5.10	1.4	0.386	-1.50	7.04×10^{-3}	0.142	-0.271	0.271
5.11	1.6	0.4	-1.81	6.13×10^{-3}	9.92×10^{-2}	-0.234	0.234

Table 5.1: Summary of the values used and calculated in the presented figures (to 3 s.f.).

Smith (2000b). The solutions presented here are over two spatial periods in x_s , so as to illustrate the jump over the small leading edge region. In this case, the calculated $Y_s = 7.93 \times 10^{-3}$ is small, but is seen for $Y < 0$ in figure 5.6(a) through a small upward jump of the streamlines just before $x_s = 6$. The pressure for this particular solution is monotonic decreasing on both the upper and lower surfaces of the blade, with the pressure gradient being favourable on both sides. The pressure difference between the flow above and beneath the blade gives rise to lift. We calculated the lift to be 0.301 to three significant figures. A discontinuity at both the trailing edges in the pressure gradient is clearly visible in this figure, as well as the jump in pressures as flow passes over the leading edge, which are calculated to be $\hat{p}_+(0^+) = -0.308$ and $\hat{p}_-(0^+) = 0.308$ to three significant figures. We notice that $\hat{p}_+(0^+) \approx -\hat{p}_-(0^+)$ for all cases (see table 5.1). The oncoming wake velocities in \hat{u} do not shift by a large amount as the discontinuity is passed, since the Y_s is small for each case. Thus, there is an almost equal flux above and below the blade and so we may expect the pressure jumps to be almost equal to satisfy the matching condition as $Y \rightarrow \infty$. The skin friction was calculated using (5.98) and shows a monotonic decreasing profile on both surfaces of the blade (note that only the solution over one blade is shown). This is as expected and has good qualitative agreement with Bowles & Smith (2000b).

A check on the periodicity of \hat{u} and \hat{v} in the numerical method is given in figure 5.7, where the velocity profiles at $x_s = 6$ for the penultimate and final sweeps of the sublayer are presented for the case in figure 5.6. Periodicity is graphically confirmed by the very good agreement of the \hat{u} and \hat{v}

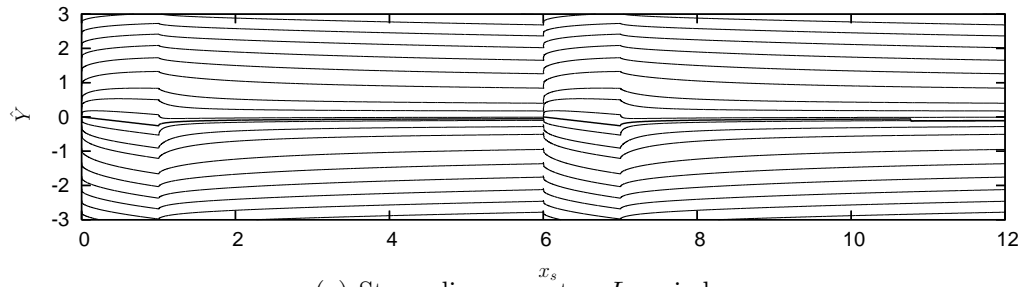
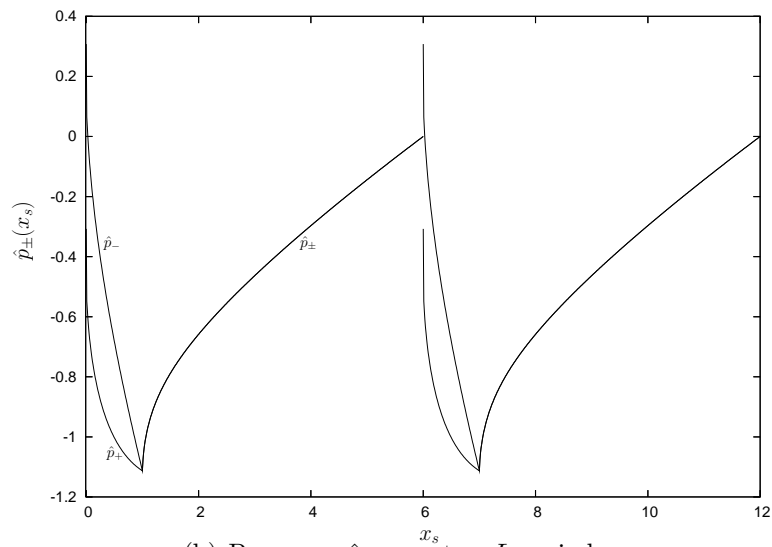
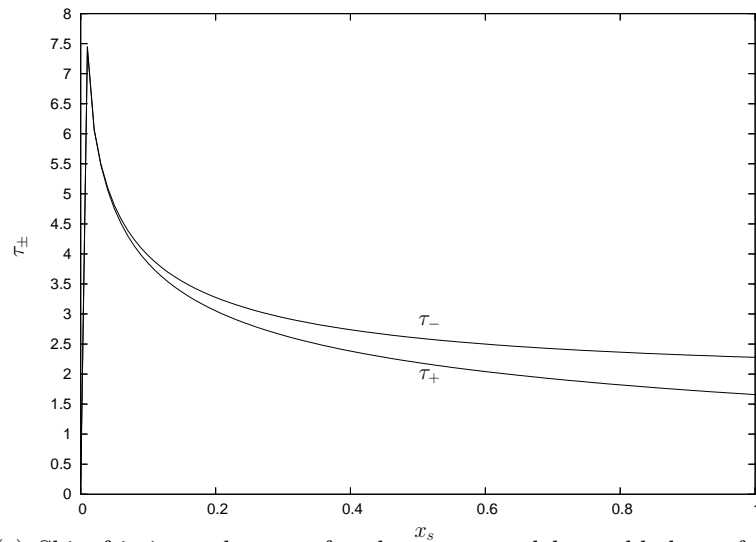
(a) Streamlines over two L -periods.(b) Pressures \hat{p}_{\pm} over two L -periods.(c) Skin friction values τ_{\pm} for the upper and lower blade surfaces respectively.

Figure 5.6: Streamfunction, pressure and skin friction solutions for the case of a flat blade tilted at an angle $\beta = 0.258$. The calculated value of $c_+ = -1.21$. The streamlines and pressure are shown over two L -periods.

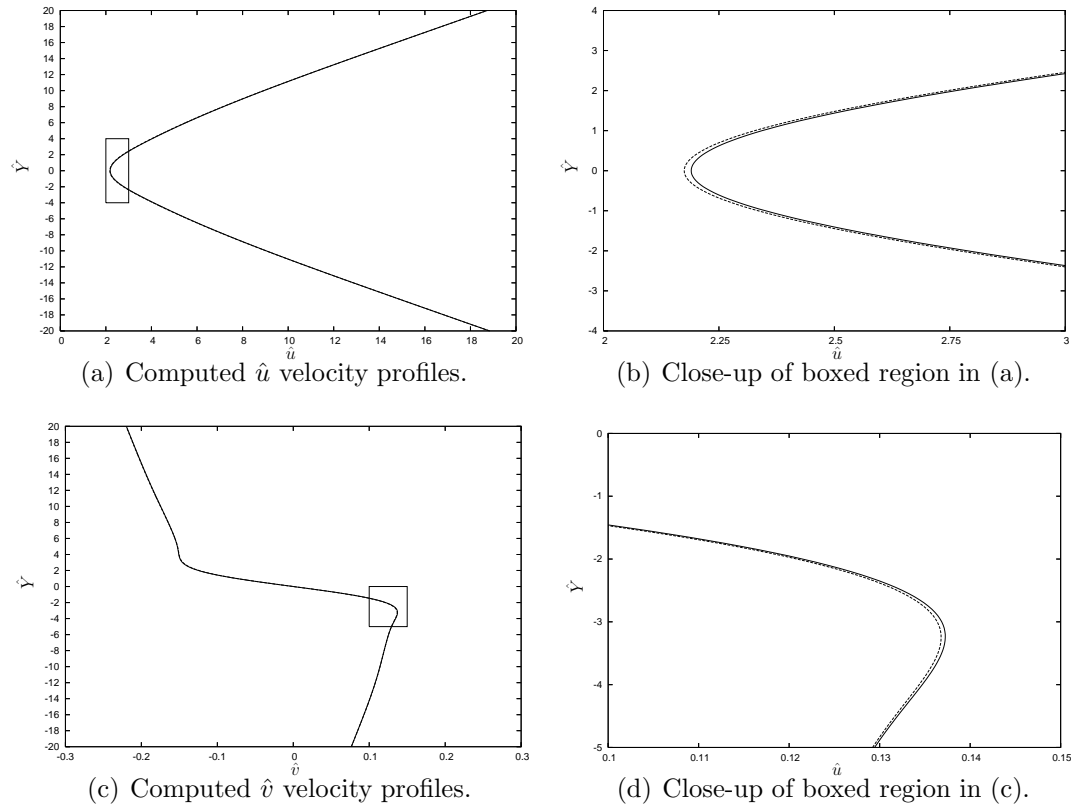


Figure 5.7: Calculated periodic velocity profiles for $\hat{u}(6, Y)$ and $\hat{v}(6, Y)$ on successive sublayer sweeps. The solid and dotted lines are the velocity profiles from the final and penultimate sweeps respectively. Figures (b) and (d) are close-ups of the boxed areas in figures (a) and (c).

velocity profiles. The boxed areas in each of figures 5.7(a) and (c) are given in figures 5.7(b) and (d) respectively. These areas are where the greatest error between the penultimate and final velocity profiles is reported and no significant difference between the profiles is seen.

In figure 5.8 the solution for $\beta = 0.299$ is given, as in figure 5 of Bowles & Smith (2000b). Again, we see similar behaviour in the pressure and skin friction over the blade and in the wake, with the scaled lift calculated in this case as 0.326. In figure 5.9, the solutions for a blade with thickness and local angle of attack is given, with the parameters $f_{\max} = 0.8$ and $\alpha = 0.575$. The pressure gradient remains favourable over most of the blade. However, within the last 40% of the blade, the pressure gradient becomes adverse. Each of τ_{\pm} increase over the first portion of the blade as the flow is accelerated up the forward facing faces of the blade. Over the second portion

of blade, the skin friction decreases as the flow passes over the backward facing sides of the blade, before accelerating slightly before the trailing edge. The deceleration in the flow causes an adverse pressure gradient. These properties are emphasised more in figures 5.10 and 5.11 and show the onset of flow reversal. In figure 5.10, where $f_{\max} = 1.4$ and $\alpha = 0.386$ (as in figure 7 of Bowles & Smith (2000b)), a small separation bubble develops before the trailing edge on the upper blade surface but no reversal occurs underneath. The separation point occurs at a position $x_S = 0.86$ before reattaching at $x_R = 1.01$. This is also seen in the τ_+ profile, where the solution drops below $\tau = 0$. In figure 5.11, two-sided separation occurs. A well-developed eddy is present above the upper surface ($x_S = 0.79, x_R = 1.06$) before the trailing edge and another small eddy develops under the lower surface ($x_S = 0.87, x_R = 0.97$).

In figures 5.12 and 5.13 we set the constants $c_- \neq c_+$ and consider a cambered blade with $f_{\max} = 0$ and $\beta = 0.4$. In figure 5.12 we impose that $c_- = c_+ - 0.5$ and solve using the same method with $f_{\max} = 0$ and $\alpha = 0.4$. We found that $c_+ = -1.63$ (to 3 s.f.) gave us a fully periodic solution. We impose $c_- = c_+ - 1$ in figure 5.13 and find $c_+ = 2.00$. On comparing these two figures, the shear is greater in the flow close to the blade in figure 5.13, due to the fact that $|c_+|$ is larger than that in figure 5.12. Also, there are hints of a slight adverse pressure gradient just before the trailing edge in figure 5.13, even for the case of a flat blade.

This concludes our discussion of the pressure interactive many-blade limit of Bowles & Smith (2000a,b) for a flow with blade non-symmetries. In this chapter, we have outlined the boundary-layer structure and expansions within each region of flow and described the numerical technique to find solutions to the sublayer problem. In the next two chapters, we add the global angle of attack into the interactive many-blade limit. We will find global angles of attack that affect the sublayer, bulk-layer and free-stream regions to leading order and outline how these interactions are embedded into the mathematical analysis.

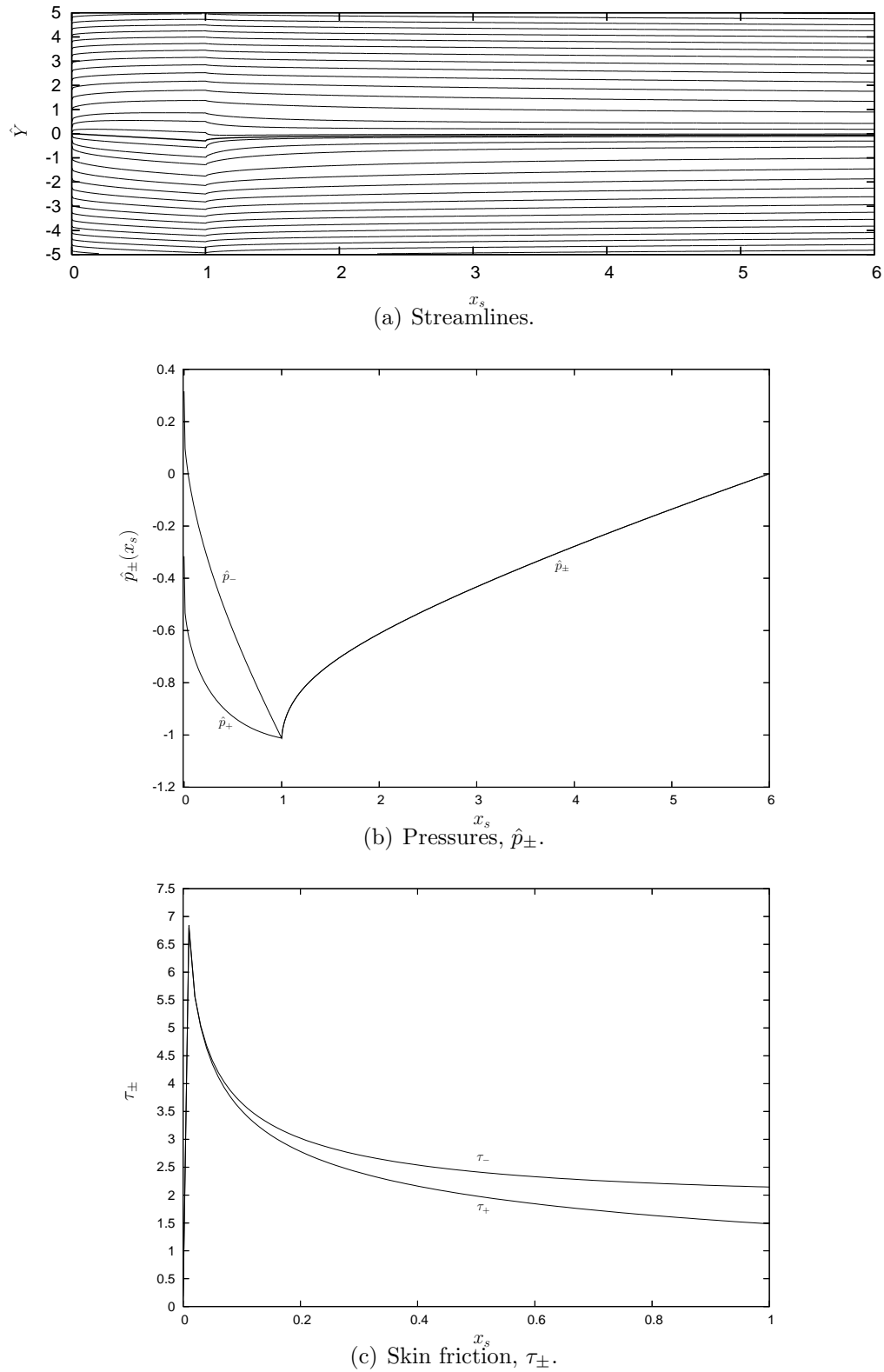
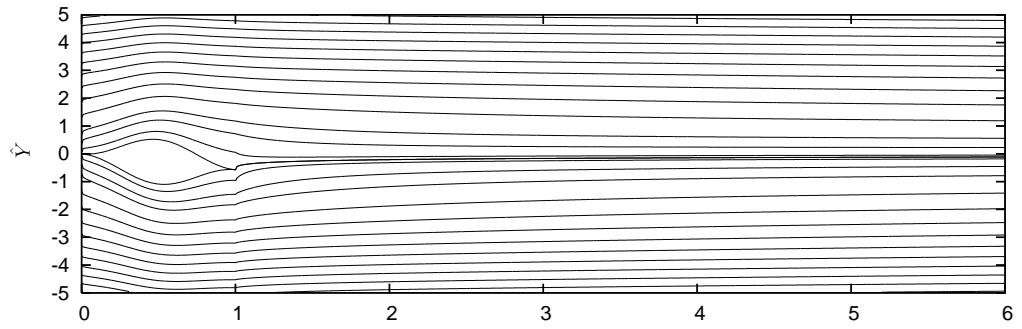


Figure 5.8: Streamfunction, pressure and skin friction solutions for the case of a flat blade tilted at an angle $\beta = 0.299$. Here, the value of $c_+ = -1.84$.



(a) Streamlines.

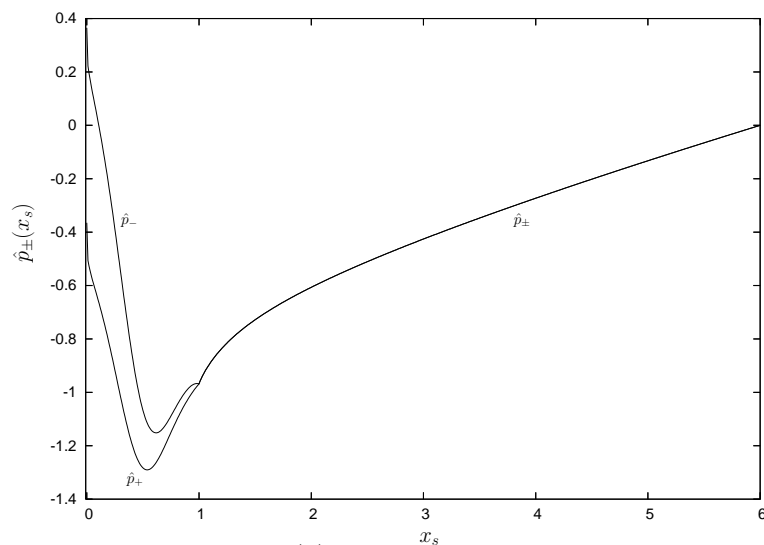
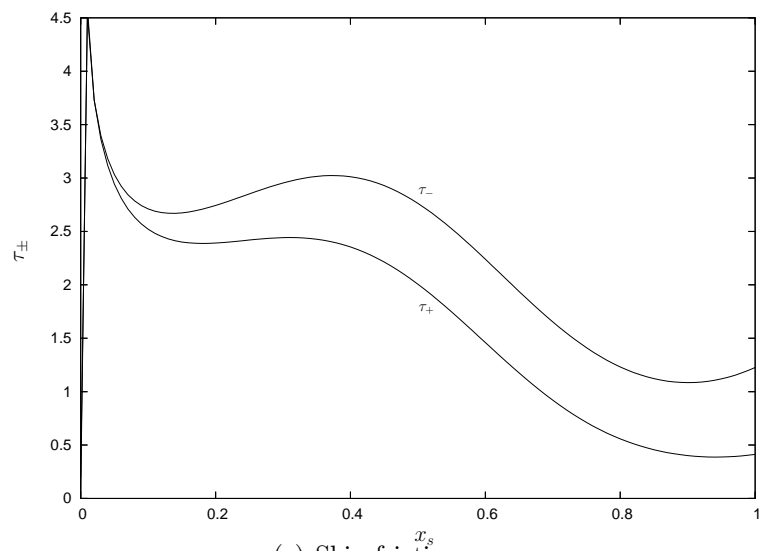
(b) Pressures, \hat{p}_{\pm} .(c) Skin friction, τ_{\pm} .

Figure 5.9: Streamfunction, pressure and skin friction solutions for the case of a thick blade ($f_{\max} = 0.8$) at local angle of attack $\beta = 0.575$. Here, the calculated value of $c_+ = -2.97$.

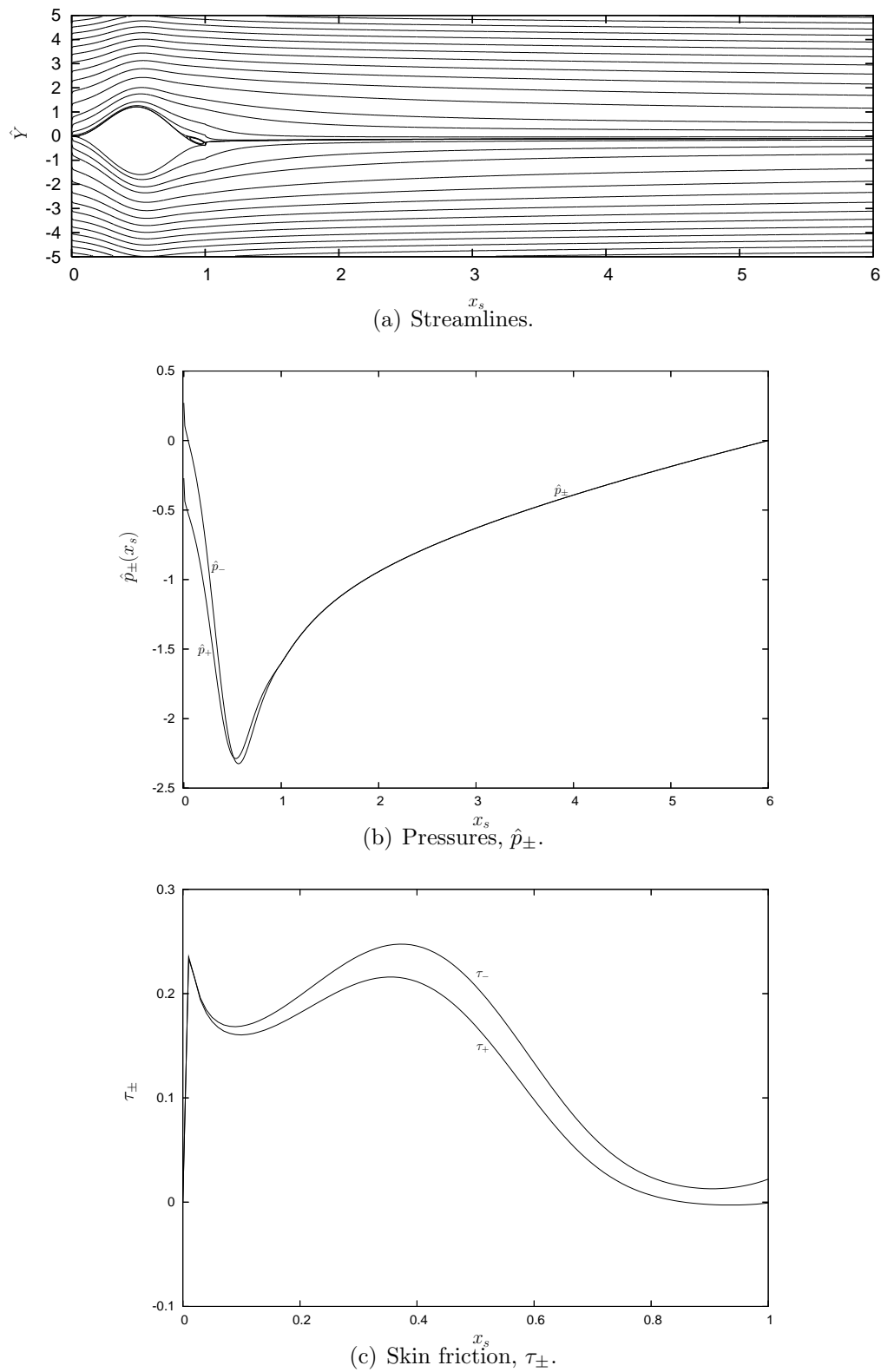
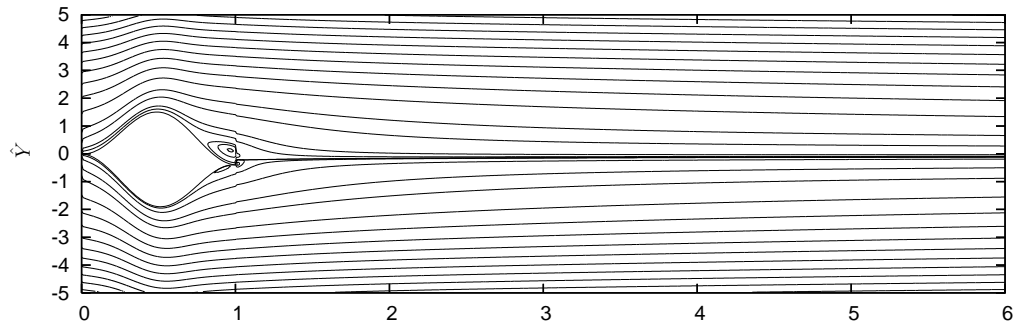


Figure 5.10: Streamfunction, pressure and skin friction solutions for the case of a thick blade ($f_{\max} = 1.4$) at local angle of attack $\beta = 0.386$. Here, the calculated value of $c_+ = -1.50$.



(a) Streamlines.

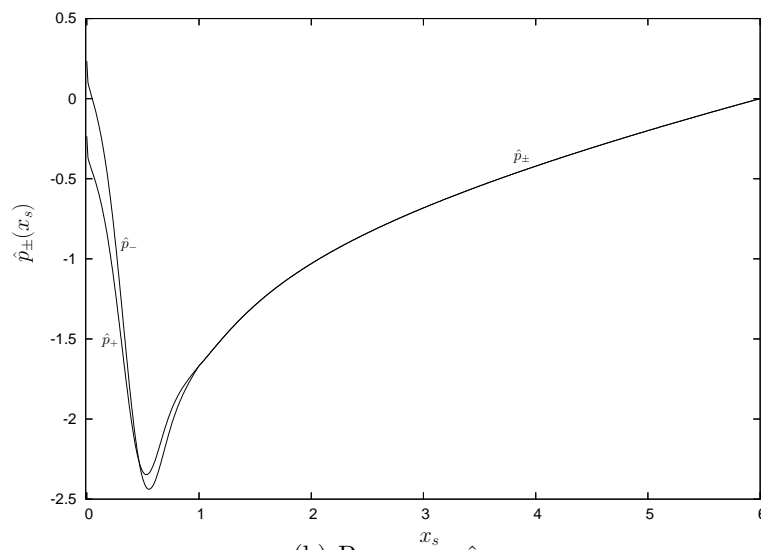
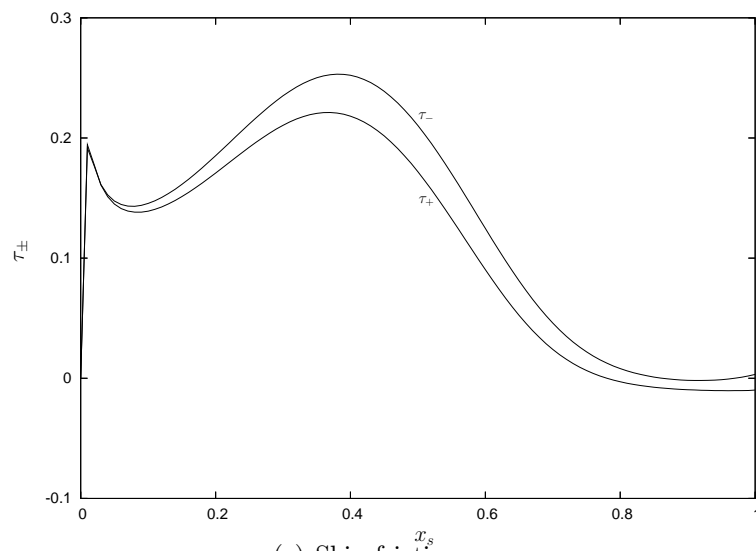
(b) Pressures, \hat{p}_{\pm} .(c) Skin friction, τ_{\pm} .

Figure 5.11: Streamfunction, pressure and skin friction solutions for the case of a thick blade ($f_{\max} = 1.6$) at local angle of attack $\beta = 0.4$. Here, the calculated value of $c_+ = -1.81$.

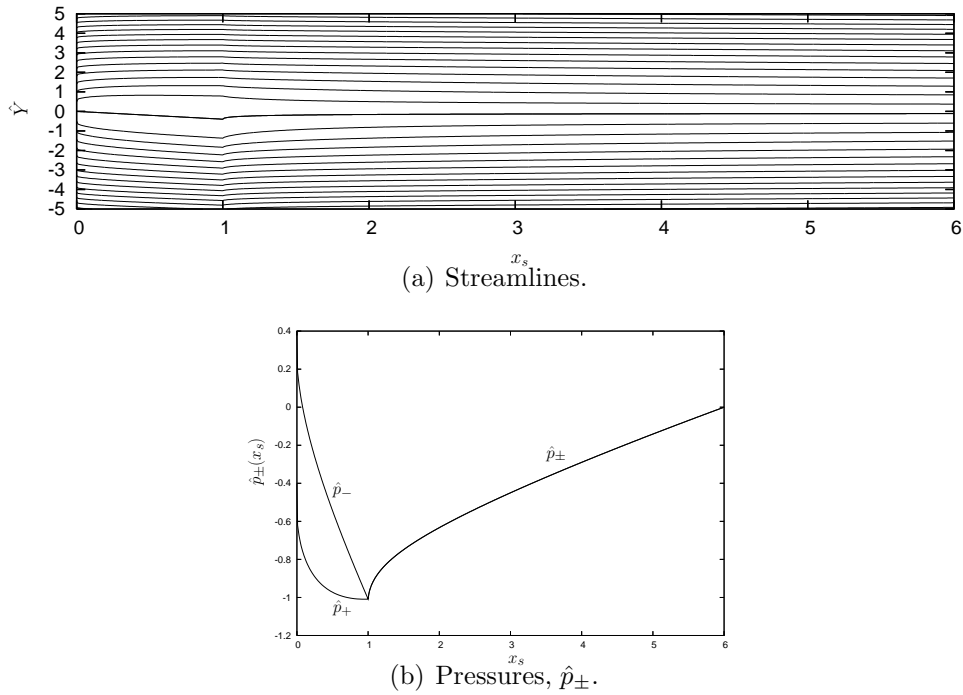


Figure 5.12: Streamfunction and pressure solutions for the case of a flat blade at angle of attack $\beta = 0.4$, with $c_- = c_+ - 0.5$.

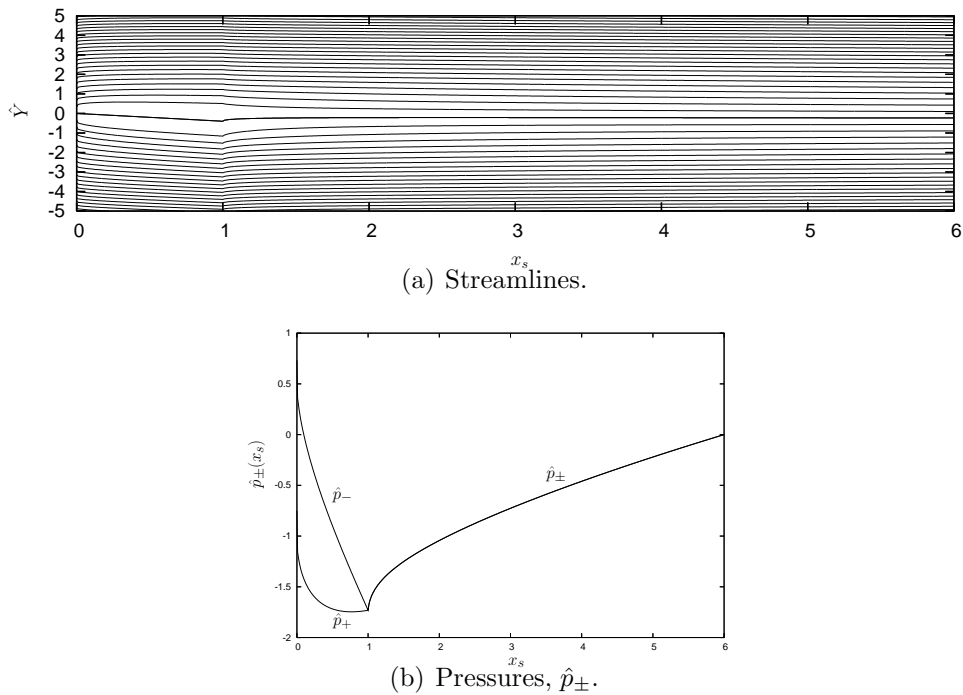


Figure 5.13: Streamfunction and pressure solutions for the case of a flat blade at angle of attack $\beta = 0.4$, with $c_- = c_+ - 1$.

Chapter 6

The pressure interactive many-blade limit with a global angle of attack

6.1 Structure with a global angle of attack

In this chapter, we introduce the global angle of attack α into the non-symmetric, pressure-interactive many-blade limit described in the last chapter. The global angle of attack is taken to be small and we seek a specific angle that causes a leading order change to the sublayer, before a discussion of larger global angles of attack is given in the next chapter.

The succession of many aligned blades and wakes aligned at a global angle of attack is illustrated as dashes and spaces respectively in figure 6.1. In this chapter, α is measured from the positive x -axis to the line of the array of blades and α is positive in an anticlockwise direction from the x -axis (see figure 6.1). For a given downstream distance in x , the corresponding normal position in y of the blade-wake period is given by

$$y = Re^{-\frac{2}{5}} f_{\pm}(x_s) + x \tan \alpha, \quad (6.1)$$

where f_{\pm} are $O(1)$ functions prescribing local non-symmetries to the blade throughout the period and scaled so that the blade geometry is strictly contained within the sublayer. As in the previous chapter, these non-symmetries may represent blade camber or thickness.

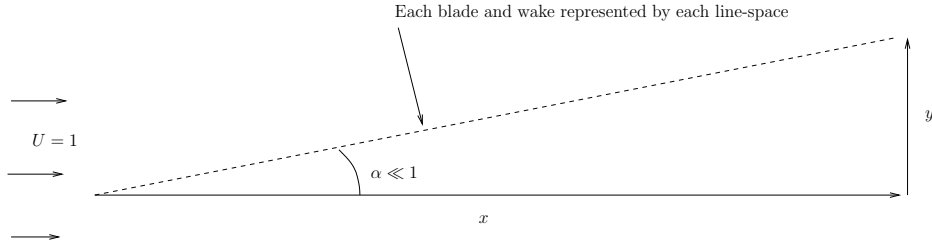


Figure 6.1: Succession of blades and wakes (given by the dashes and spaces respectively) all tilted at the global angle of attack $\alpha \ll 1$.

In the interactive many-blade limit, our horizontal coordinate is described by $x = x_s + Re^{3/5}x_l$. Given $\alpha \ll 1$, we have that $\tan \alpha \approx \alpha$ and further we write $\alpha = Re^{-\kappa}\bar{\alpha}$, where $\bar{\alpha} = O(1)$ and $\kappa > 0$ is a constant to be determined. As before, we seek periodic solutions to the interactive sublayer problem over the short scale x_s and so the long x -scale, x_l , appears approximately constant over x_s . Hence the equation for y in figure 6.1 is given by

$$y = Re^{-\frac{2}{5}}f_{\pm}(x_s) + Re^{-\kappa}\bar{\alpha}x_s + Re^{\frac{3}{5}-\kappa}\bar{\alpha}. \quad (6.2)$$

In the sublayer, the normal coordinate $\hat{Y} = O(1)$ is given by $y = Re^{-2/5}\hat{Y}$. By comparing these two estimates for y , we find that

$$\hat{Y} = f_{\pm}(x_s) + Re^{\frac{2}{5}-\kappa}\bar{\alpha}x_s + Re^{1-\kappa}\bar{\alpha}. \quad (6.3)$$

In order to investigate the case where $\bar{\alpha}$ first influences the sublayer flow, we take $\kappa = 1$ so that $\alpha = Re^{-1}\bar{\alpha}$. Note that we could have chosen $\kappa = 2/5$ in equation (6.3), so that $\alpha = Re^{-2/5}\bar{\alpha}$ and a balance between the normal sublayer coordinate and $\bar{\alpha}x_s$ occurs. This global angle of attack is much larger than the case $\kappa = 1$ and is considered in the next chapter.

It is worth noting that $\alpha = O(Re^{-1})$ is the smallest possible global angle of attack that causes any leading order change within the sublayer at downstream distances $x = O(Re^{3/5})$. For downstream distances $x < O(Re^{3/5})$ and a global angle of attack of $O(Re^{-1})$, the flow behaviour over one blade-wake period is given by the non-interactive limit of Chapter 4. In Chapter

4, $x = x_s + nx_l$ and the sublayer thickness is given by $y = Re^{-1/2}n^{1/6}\hat{Y}$. A similar equation for the normal estimate (6.2) can be derived and in this case, since $n < O(Re^{3/5})$, it can be shown that the first balance with the normal sublayer coordinate occurs when $n = O(Re^{3/5})$. Thus the leading order solution with a global angle of attack of $O(Re^{-1})$ in the non-interactive limit would be given by the non-symmetric problem of Chapter 4 with no global angle of attack present.

6.2 The leading order response for $\alpha = Re^{-1}\bar{\alpha}$

We take equation (6.3) and substitute $\kappa = 1$

$$\hat{Y} = f_{\pm}(x_s) + Re^{-\frac{3}{5}}\bar{\alpha}x_s + \bar{\alpha}, \quad (6.4)$$

and since $Re \gg 1$, the short scale term $Re^{-3/5}\bar{\alpha}x_s$ is small and is neglected. Thus we take

$$\hat{Y} = f_{\pm}(x_s) + \bar{\alpha}, \quad (6.5)$$

to be the leading order balance between the normal sublayer coordinate, the blade geometry and the global angle of attack in the sublayer. The appearance of the $\bar{\alpha}$ term in the above relation represents a vertical shift in the position of the blade within the sublayer at $x = O(Re^{3/5})$ compared to the non-interactive limit and is illustrated in figure 6.2. Furthermore, we note that this global angle of attack is very small, even compared to the thickness of the sublayer.

We begin, as in the previous chapter, with the bulk-layer problem. By comparing the bulk-layer thickness with the right-hand side of equation (6.2), there are no leading order balances between Y_b and the global angle of attack terms. Thus, the bulk-layer lies at $y = 0$ to leading order in this regime. On matching with the sublayer and free-stream, the same expansions hold for the velocities and pressure as in the last chapter, leading to exactly the same solutions. To leading order, U is given by mean-Blasius flow in the bulk-layer, whilst the leading order term in the expansion for V is given by

$$v_1 = -E'_{\pm}(x_s)u_0, \quad (6.6)$$

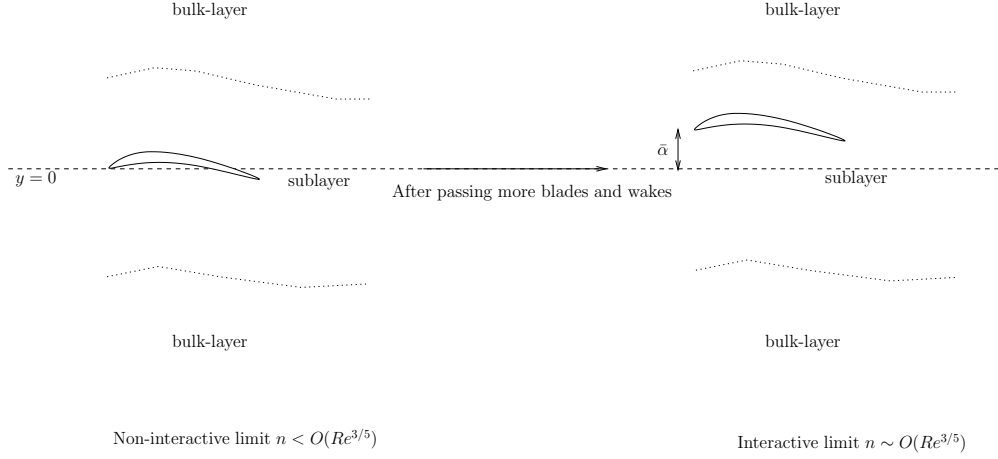


Figure 6.2: Influence of the global angle of attack $\alpha = Re^{-1}\bar{\alpha}$ on the vertical position of the blade within the sublayer on entering the interactive multi-blade limit.

where E_{\pm} are arbitrary functions of integration and are determined upon matching with the sublayer.

The main interest here lies in the sublayer problem where the influence of the global angle of attack is first experienced. Given that the global angle of attack is much smaller than the sublayer thickness, the same expansions for $(U, V, P) = (Re^{-1/5}\hat{u}, Re^{-3/5}\hat{v}, Re^{-2/5}\hat{p})$ hold to leading order yielding the same boundary-layer equations

$$\hat{u}\frac{\partial\hat{u}}{\partial x_s} + \hat{v}\frac{\partial\hat{u}}{\partial\hat{Y}} = -\frac{d\hat{p}}{dx_s} + \frac{\partial^2\hat{u}}{\partial\hat{Y}^2}, \quad (6.7)$$

$$\frac{\partial\hat{u}}{\partial x} + \frac{\partial\hat{v}}{\partial\hat{Y}} = 0, \quad (6.8)$$

which are to be solved subject to the boundary conditions

$$\hat{u} = \hat{v} = 0 \quad \text{on} \quad \hat{Y} = f_{\pm}(x_s) + \bar{\alpha}, \quad 0 < x_s \leq l, \quad (6.9)$$

$$\text{Regularity in } \hat{u}, \hat{v} \text{ and } \hat{p} \text{ in the wake,} \quad (6.10)$$

$$\hat{u} \rightarrow \pm\lambda_{\pm}(Y + b_{\pm}(x_s)) \quad \text{as} \quad \hat{Y} \rightarrow \pm\infty, \quad (6.11)$$

$$\hat{p}_+(l) = \hat{p}_-(l), \quad (6.12)$$

$$Y\text{-shift at } x_s = L, \quad (6.13)$$

$$\text{Periodicity in } \hat{u}, \hat{v} \text{ and } \hat{p} \text{ in } x_s. \quad (6.14)$$

The condition (6.9) arises due to the vertical shift of the blade in the sublayer within the interactive limit in light of (6.5). Furthermore, we find that on matching with v_1 in the bulk-layer, the functions $E_{\pm} \equiv b_{\pm}$, as before.

The free-stream problem is unchanged from the previous chapter, as the same expansions and governing equations hold for U, V, P by matching with the bulk-layer. Thus the same pressure displacement law holds

$$p_{\pm}(x_0) = \pm \frac{\lambda_{\pm}}{L} \int_0^L b'_{\pm}(x_s) \cot \left\{ \frac{\pi(x_s - x_0)}{L} \right\} dx_s, \quad (6.15)$$

and provides the final condition to complete the full interactive sublayer problem.

In summary, the full sublayer problem with a global angle of attack $\alpha = O(Re^{-1})$ is given by the interactive boundary-layer equations with boundary conditions (6.9) - (6.14) and the pressure displacement law (6.15). In comparison to the limit in Chapter 5, the sublayer problem is now subject to different no-slip and no-penetration conditions. These in turn cause different sublayer displacements b'_{\pm} and so the free-stream solution takes on a different form. The analysis in all other flow regions is unchanged from Chapter 5.

6.3 Results

In keeping with the work in the last chapter and that of Bowles & Smith (2000b), we focus on solving the condensed flow problem, where the displacement functions $b_{\pm}(x_s) = \pm c_{\pm}$. To solve the problem numerically, we first apply a Prandtl shift in the sublayer, defined by $\hat{u} = u_1$, $\hat{v} = v_1 - f'u_1$, $\hat{p} = p_1$ and where the normal sublayer coordinate Y_1 is defined by

$$\hat{Y} = Y_1 + f_{\pm}(x_s) + \bar{\alpha}. \quad (6.16)$$

This leaves the governing interactive boundary-layer equations unchanged except u_1, v_1, Y_1 replace $\hat{u}, \hat{v}, \hat{Y}$ respectively. The boundary conditions (6.12) and (6.14) are unchanged, whilst (6.9)-(6.11) become

$$u_1 = v_1 = 0 \quad \text{on} \quad Y_1 = 0, \quad 0 < x_s \leq l, \quad (6.17)$$

$$\frac{\partial u_1}{\partial Y_1} = \hat{v} = 0 \quad \text{on} \quad Y_1 = 0, \quad l < x_s \leq L, \quad (6.18)$$

$$u_1 \rightarrow \pm(Y_1 + f_{\pm}(x_s) + \bar{\alpha}) + c_{\pm} \quad \text{as } Y_1 \rightarrow \pm\infty, \quad (6.19)$$

We adopt the numerical method used to solve the sublayer problem in Chapter 5, since the governing equations are identical. However, an additional term appears in the matching condition (6.19) and so the numerical scheme is adapted to incorporate the parameter $\bar{\alpha}$. This parameter affects the solution at each x -station in finding the pressure \hat{p} and the leading edge pressure jumps. As before, the constants λ_{\pm} appearing in (6.19) are set to unity.

First, solutions for the case of a flat blade with $\bar{\alpha} = 0, -0.1, -0.25, -0.5, -0.75, -1$ are presented. Then, the same process is repeated for an angled and a thick blade with $\bar{\alpha} = 0, -0.1, -0.25, -0.5, -1$. In our computations, the trailing edge of the blade is taken to lie at $l = 1$ with the period $L = 6$. The unknown displacement constants are set as $c_+ = c_-$, in line with the work in Chapter 5.

6.3.1 Flat blade

In figure 6.3 we present the calculated streamline profiles for the values of $\bar{\alpha}$ given above. The streamlines plotted in all the figures are given by constant increments and decrements of unity from the streamline $\psi = 0$. For $\bar{\alpha} = -0.1, -0.25$ we see very little difference compared to the case $\bar{\alpha} = 0$, whilst for values $\bar{\alpha} = -0.75, -1$, it is possible to see a shift of the streamline $\psi = 0$ emanating from the trailing edge of the blade as the leading edge of the next blade is approached. As $\bar{\alpha}$ decreases to $\bar{\alpha} = -1$, a greater spacing between the streamlines is observed, indicating a reduction in the shear strength for small Y_1 .

The pressure solutions in figure 6.4 reflect the small changes in the streamlines for the values of $\bar{\alpha}$ presented. The functions \hat{p}_{\pm} are very similar for each case of $\bar{\alpha}$. As $\bar{\alpha}$ is decreased, there is an increasing pressure difference between the upper and lower surfaces indicating the generation of lift. Furthermore, as $\bar{\alpha}$ is decreased, the fall in pressure from the leading edge to the trailing edge is less within the periodic sublayer. We believe this is due to the decrease in the value of c_+ as $\bar{\alpha}$ is decreased (see table 6.1).

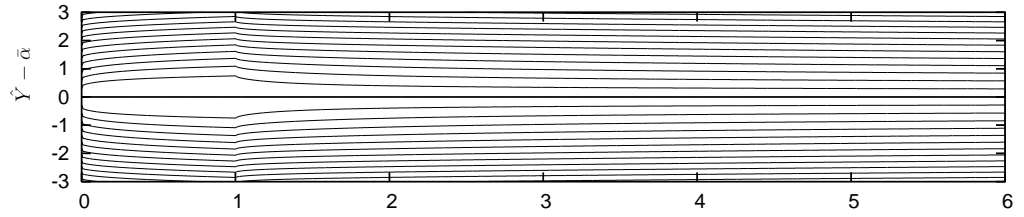
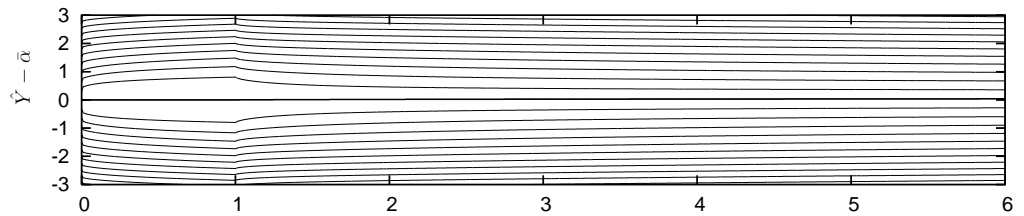
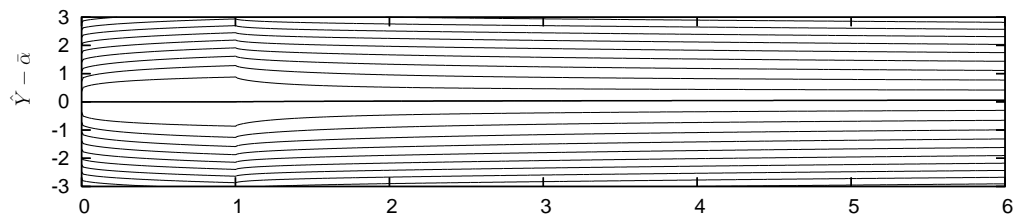
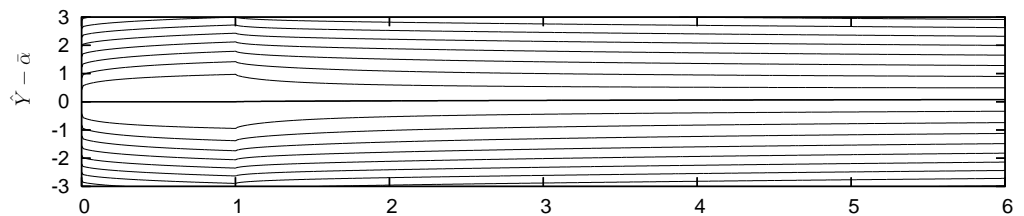
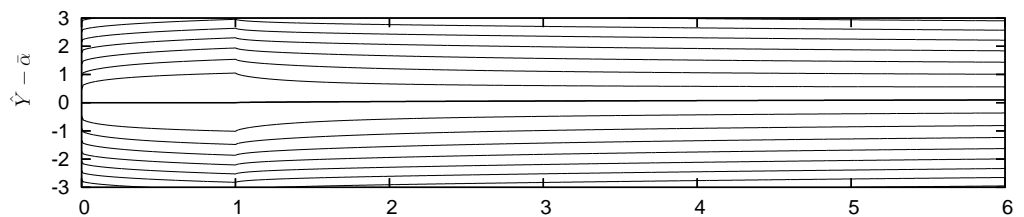
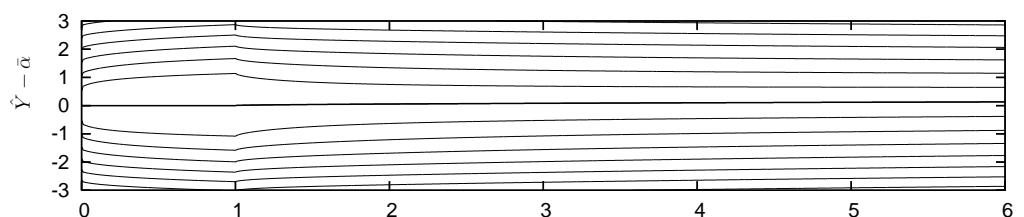
(a) $\bar{\alpha} = 0$ (b) $\bar{\alpha} = -0.1$ (c) $\bar{\alpha} = -0.25$ (d) $\bar{\alpha} = -0.5$ (e) $\bar{\alpha} = -0.75$ (f) $\bar{\alpha} = -1$

Figure 6.3: Streamline plots with the global angle of attack $\bar{\alpha}$ for the case of a flat blade.

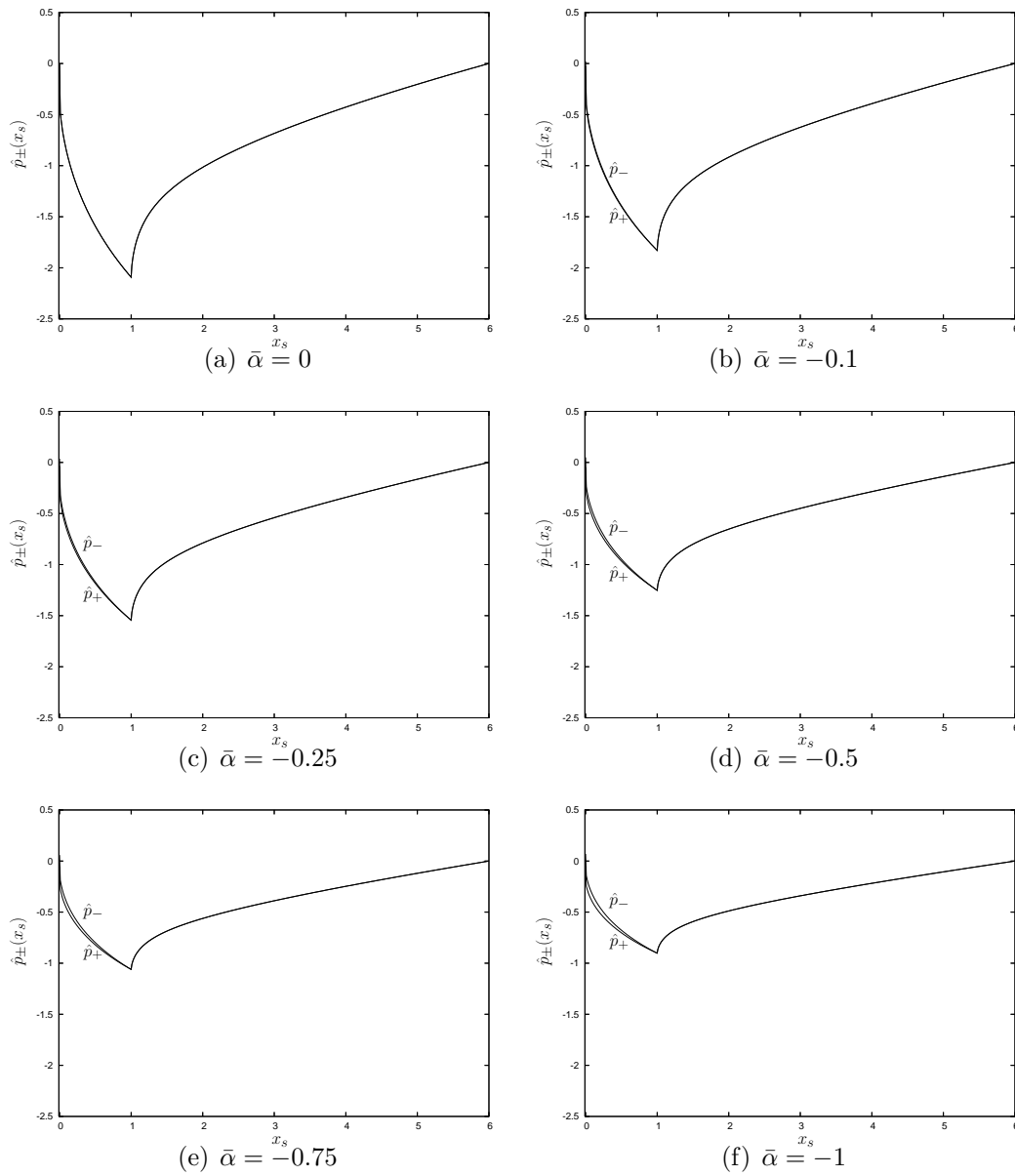


Figure 6.4: Pressure solutions for the case of a flat blade with the global angles of attack in figure 6.3.

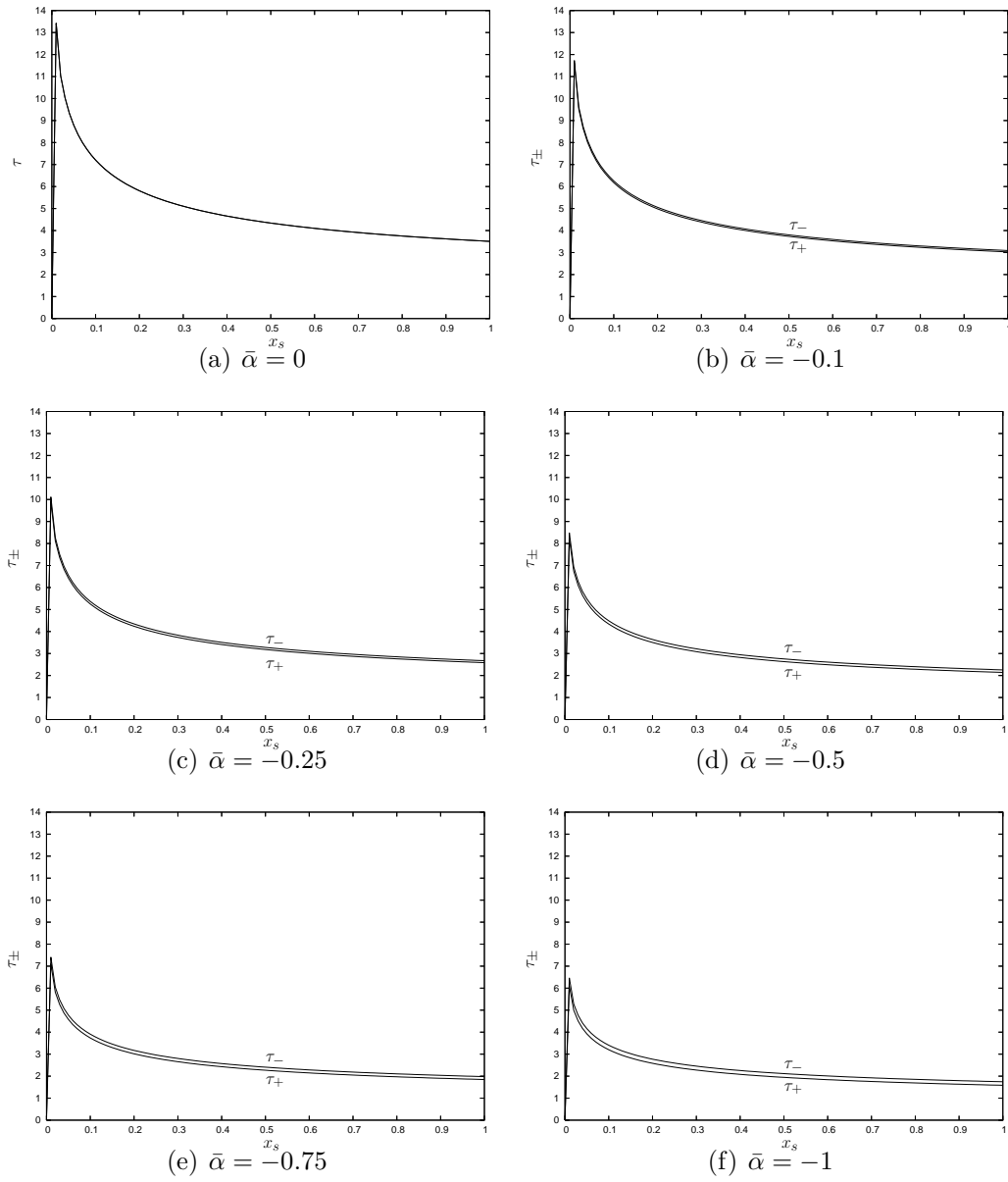


Figure 6.5: Skin frictions τ_{\pm} for the case of a flat blade with the global angles of attack in figure 6.3.

Viscous skin friction solutions are presented in figure 6.5. The skin friction takes on the same definition here as used in Chapter 5, namely through equation (5.98). For the flat blade case, the skin friction solutions are monotonically decreasing over each blade surface. There is a slight difference between profiles on the upper and lower blade surfaces when a non-zero value of the global angle of attack is included. If $\bar{\alpha} < 0$ then there is a normal component of velocity in the positive Y_1 direction through the wake. Consequently, the flow emanating from the upper and lower blade surfaces at the trailing edge of the blade is advected in the positive Y_1 direction over the wake meaning that in general, a non-symmetric velocity profile encounters the next blade. This non-symmetric velocity profile causes the differences in skin friction observed.

The leading edge pressure jumps, Y -shifts and computed values of c_{\pm} and the lift, L , are summarised in table 6.1. We see that an increase in the global angle of attack means an increase in the magnitude of the pressure jumps, as well as in the Y -shift and lift, as expected. An interesting result appears to be the decrease in the value of c_+ as $\bar{\alpha}$ is decreased and may indicate a limitation of setting $c_- = c_+$. However, in comparison to the previous chapter and Bowles & Smith (2000a,b), the main flow features of interest are captured.

$\bar{\alpha}$	$\hat{p}_+(0^+)$	$\hat{p}_-(0^+)$	c_+	Y_s	L
0	0	0	2.56	0	0
-0.1	-2.13×10^{-2}	2.15×10^{-2}	1.92	9.75×10^{-4}	1.01×10^{-2}
-0.25	-3.58×10^{-2}	3.66×10^{-2}	0.890	1.74×10^{-3}	1.76×10^{-2}
-0.5	-4.76×10^{-2}	5.01×10^{-2}	-0.503	2.51×10^{-3}	2.40×10^{-2}
-0.75	-5.41×10^{-2}	5.87×10^{-2}	-1.61	3.07×10^{-3}	2.79×10^{-2}
-1.0	-6.18×10^{-2}	6.98×10^{-2}	-2.34	3.73×10^{-3}	3.22×10^{-2}

Table 6.1: The calculated values of the leading edge pressure jumps, c_+ , the Y -shift and lift L (all to 3 s.f.) for the case of a flat blade with a global angle of attack $\bar{\alpha}$.

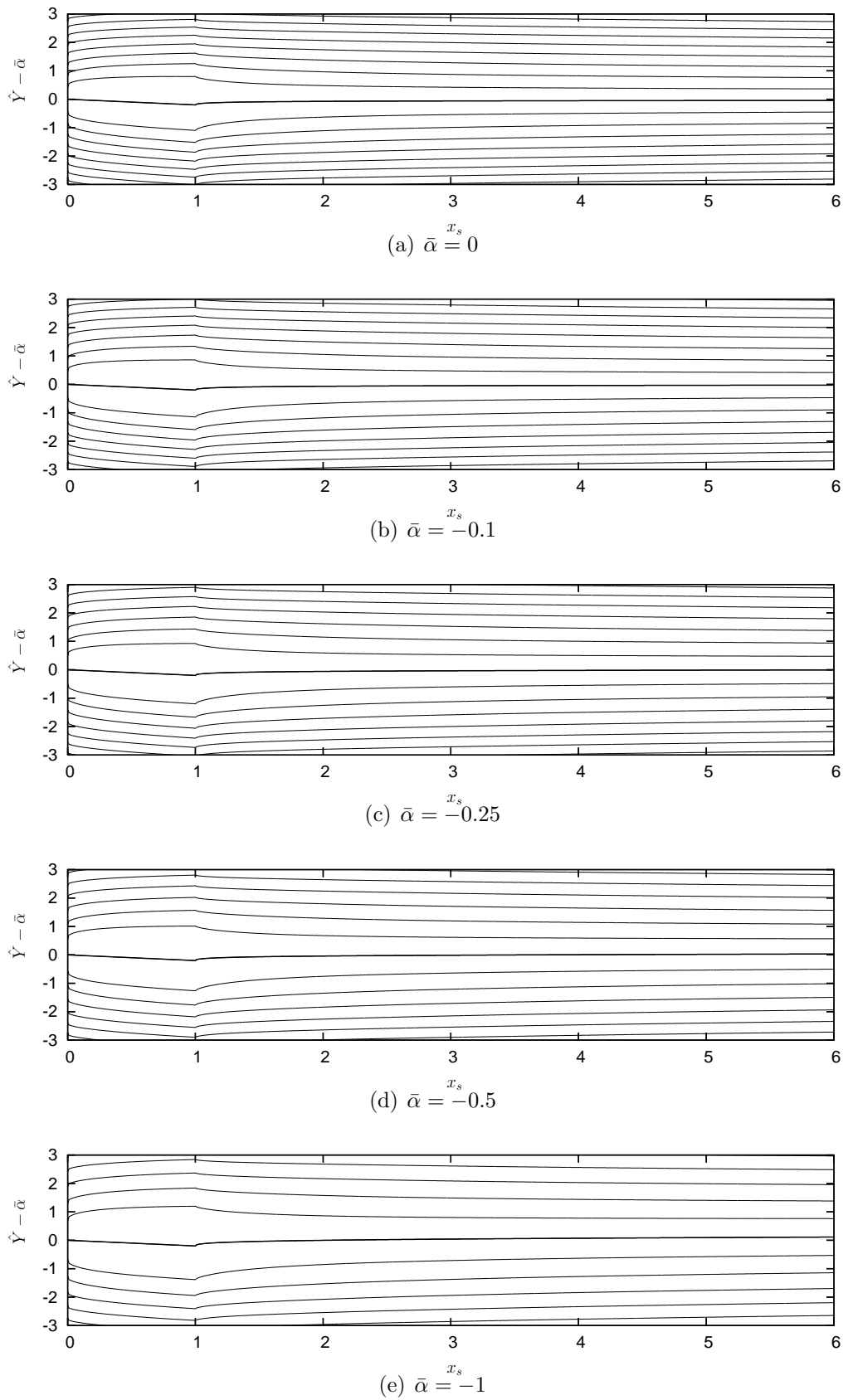


Figure 6.6: Streamline plots with the global angle of attack $\bar{\alpha}$ for the case of an angled blade given by $f_{\pm}(x_s) = -0.2x_s$.

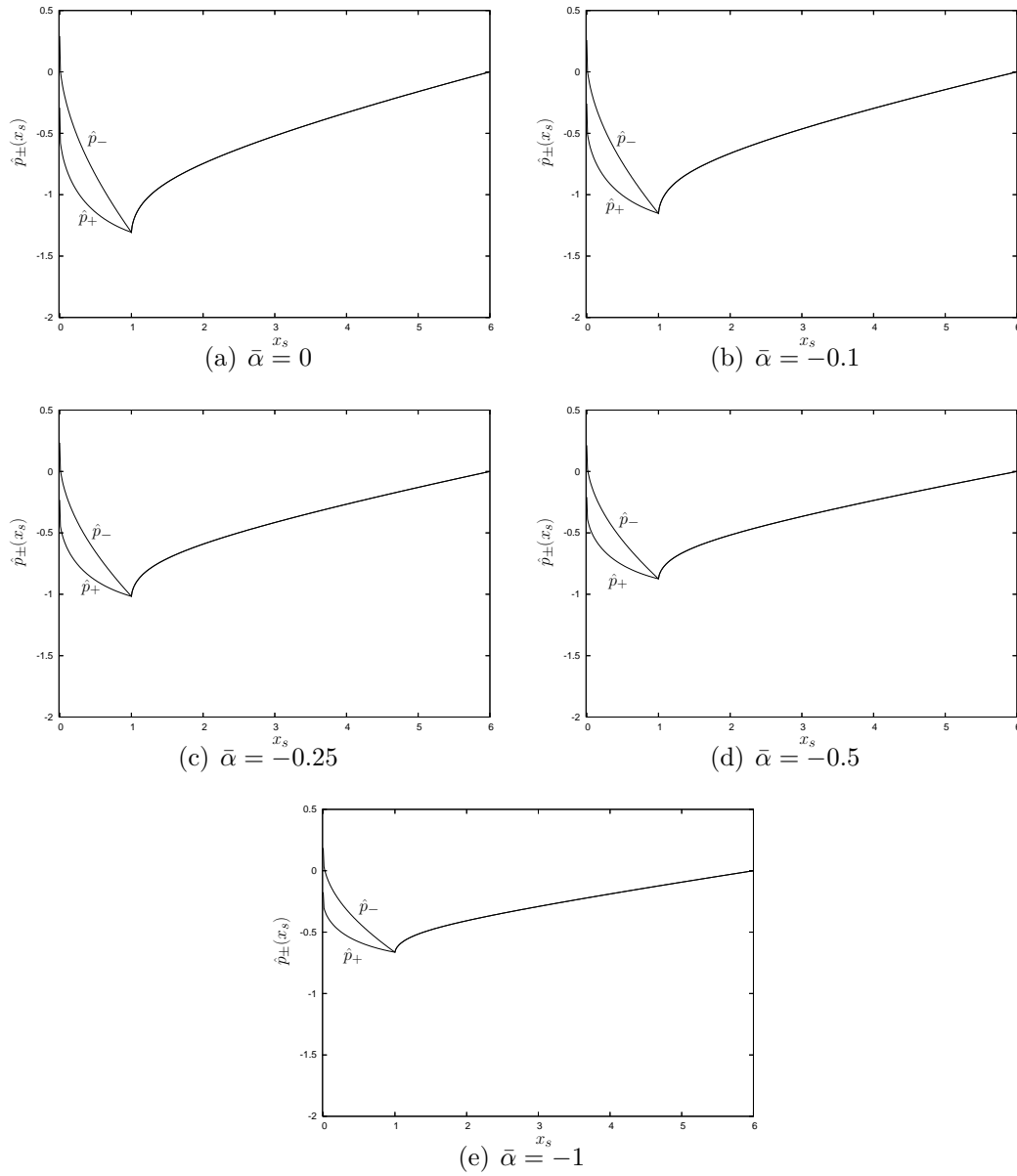


Figure 6.7: Pressure solutions for the case of the angled blade and global angles of attack in figure 6.6.

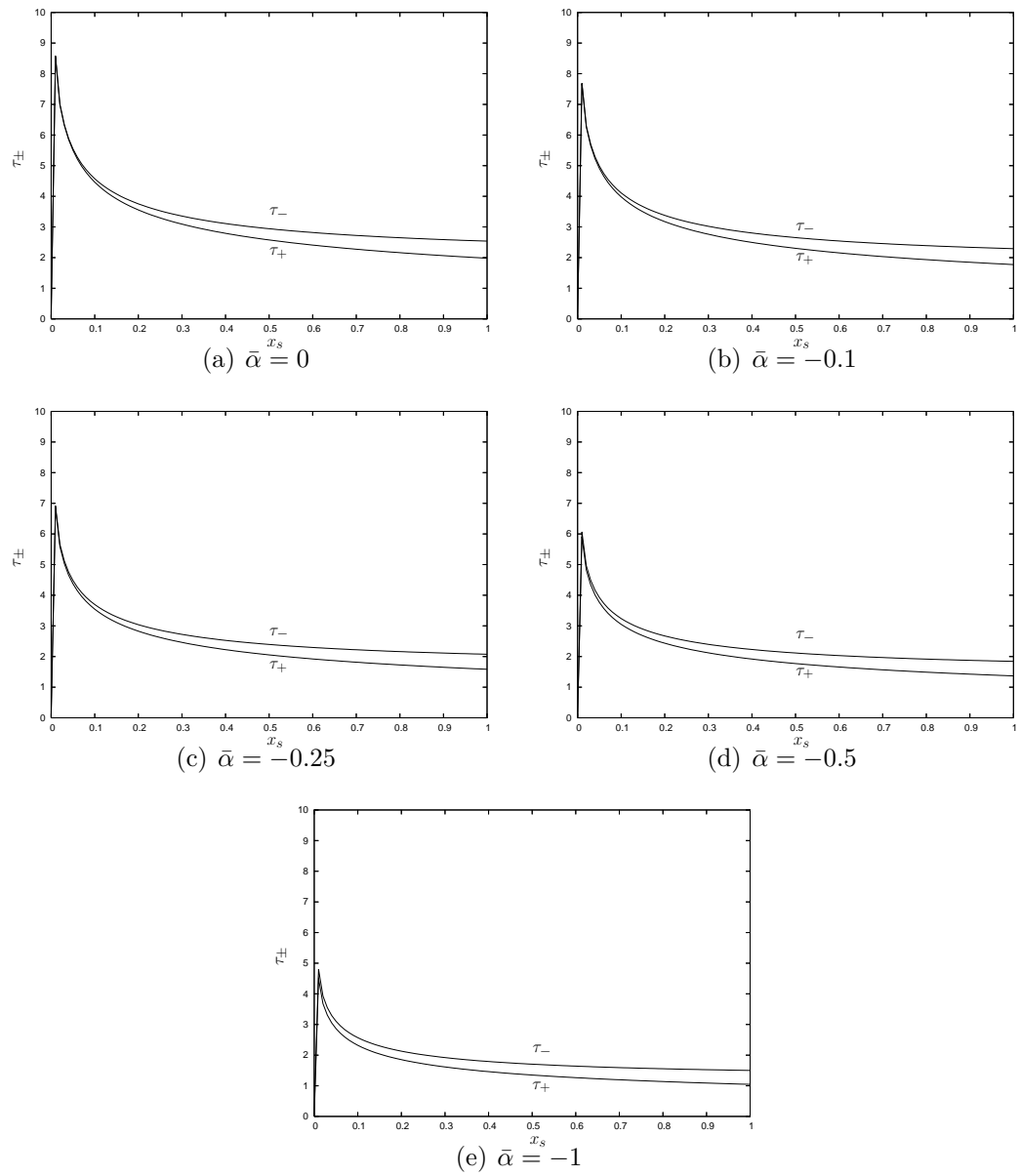


Figure 6.8: Skin friction solutions for the case of the angled blade and global angles of attack in figure 6.6.

6.3.2 Angled and thick blades

We add a local angle of attack to the blade geometry by setting

$$f_{\pm}(x_s) = \beta x_s, \quad (6.20)$$

and we take $\beta = -0.2$ in all the computations in this subsection. Figure 6.6 presents the streamlines calculated with $\bar{\alpha} = 0, -0.1, -0.25, -0.5, -1$. Many of the flow features discussed in the previous section are seen with the local angle of attack added to the problem, such as the shear strength decreasing for small Y_1 as $\bar{\alpha}$ decreases. The streamline $\psi = 0$ (seen in bold), representing the blade surface and wake centreline, encounters the next blade beneath the leading edge for $\bar{\alpha} = 0$. However, for $\bar{\alpha} = 1$, this streamline hits the next blade above the leading edge.

The pressure solutions presented in figure 6.7 comprise a large difference in the pressures \hat{p}_+ and \hat{p}_- over the blade and is caused primarily by the local angle of attack β . For the case $\bar{\alpha} = 0$, a non-symmetric problem is solved as in the previous chapter. The fall in pressure from the leading to trailing edge decreases as the global angle of attack decreases, as seen in the flat blade case.

The skin friction solutions found are monotonically decreasing functions of x_s as $\bar{\alpha}$ is decreased. There is a larger difference between τ_+ and τ_- compared to the flat blade case due to the inclusion of the local angle of attack β . The calculated values of the pressure jumps, c_+ , the Y -shift and lift for the angled blade are summarised in table 6.2.

$\bar{\alpha}$	$\hat{p}_+(0^+)$	$\hat{p}_-(0^+)$	c_+	Y_s	lift
0	-0.292	0.292	-0.136	7.32×10^{-3}	0.300
-0.1	-0.258	0.258	-1.01	6.63×10^{-3}	0.262
-0.25	-0.231	0.234	-1.80	6.09×10^{-3}	0.230
-0.5	-0.208	0.214	-2.47	5.62×10^{-3}	0.201
-1.0	-0.175	0.185	-3.61	4.94×10^{-3}	0.159

Table 6.2: The calculated values of the leading edge pressure jumps, c_+ , the Y -shift and lift L (all to 3 sf) for the case of an angled flat plate with a global angle of attack $\bar{\alpha}$.

In the final set of results presented, the functions f_{\pm} are given by

$$f_{\pm}(x_s) = \pm f_{\max} \sin^2(\pi x_s), \quad (6.21)$$

allowing thickness effects to be added to the blade. The parameter f_{\max} controls the maximum thickness of the blade and is taken to be $f_{\max} = 1.7$.

$\bar{\alpha}$	$p_+(0^+)$	$p_-(0^+)$	c_+	Y_s	L
0	0	0	0.455	0	0
-0.1	-4.51×10^{-2}	4.53×10^{-2}	-0.0473	1.13×10^{-3}	5.35×10^{-3}
-0.25	-7.37×10^{-2}	7.47×10^{-2}	-0.907	1.89×10^{-3}	1.08×10^{-2}
-0.5	-0.101	0.104	-2.24	2.71×10^{-3}	1.50×10^{-2}
-1.0	-0.143	0.151	-3.83	4.05×10^{-3}	1.84×10^{-2}

Table 6.3: The calculated values of the leading edge pressure jumps, c_+ , the Y -shift and lift L for the case of a thick blade with a global angle of attack $\bar{\alpha}$ (all to 3 s.f.).

With no global angle of attack present, the thickness of the blades causes flow reversal to occur on both the upper and lower blade surfaces. The eddies formed within the reversal close after the trailing edge is passed. As the parameter $\bar{\alpha}$ is decreased to $\bar{\alpha} = -1$ in figure 6.9, the size of the separation eddies decrease. The reduction in the size of the separation bubble is linked to the decrease in the value of the parameter c_+ as $\bar{\alpha}$ decreases. Further, the spacing of the streamlines, as with the other results in this chapter, increases as the global angle of attack decreases.

The corresponding pressure solutions in figure 6.10 show a favourable pressure gradient over the first part of the blade on both surfaces. The flow reversal reported is accompanied by an adverse pressure gradient on the backward facing sides of the blade. As the value of $\bar{\alpha}$ is decreased, a pressure difference between the upper and lower blade surfaces occurs indicating the generation of lift. The lift generated is attributed solely to the global angle of attack since the blade geometry is symmetric.

We present the skin friction solutions in figure 6.11. The skin friction increases over the first 40% of the blade, as in the thick blade cases of the previous chapter and has a local maximum around $x_s = 0.4$. There is a rapid reduction in the skin friction over the backward facing edges of the blade as the flow decelerates, leading to negative skin friction before the trailing edge

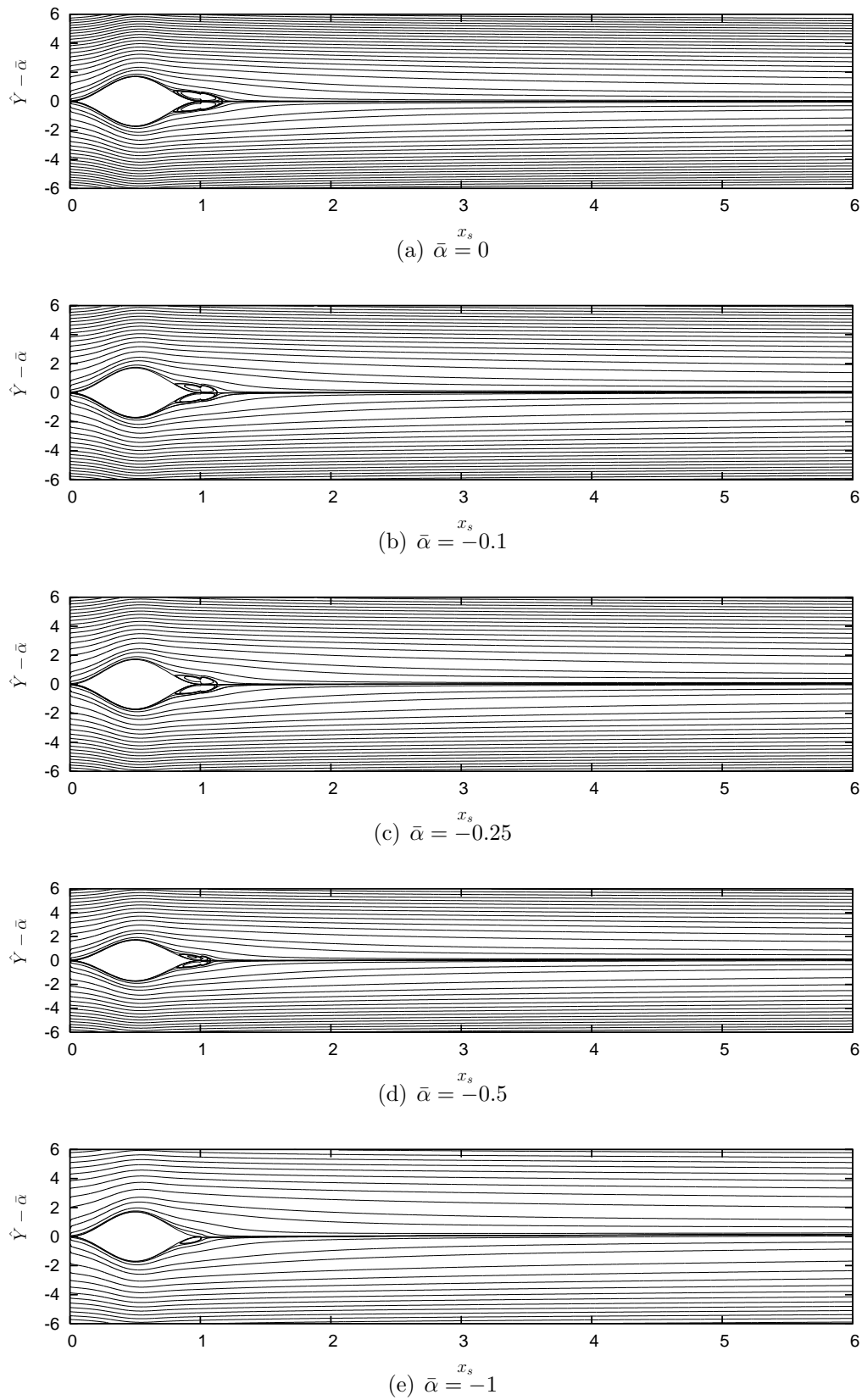


Figure 6.9: Streamline plots with the global angle of attack $\bar{\alpha}$ for the case of thick blade with $f_{\pm}(x_s) = \pm 1.7 \sin^2(\pi x_s)$.

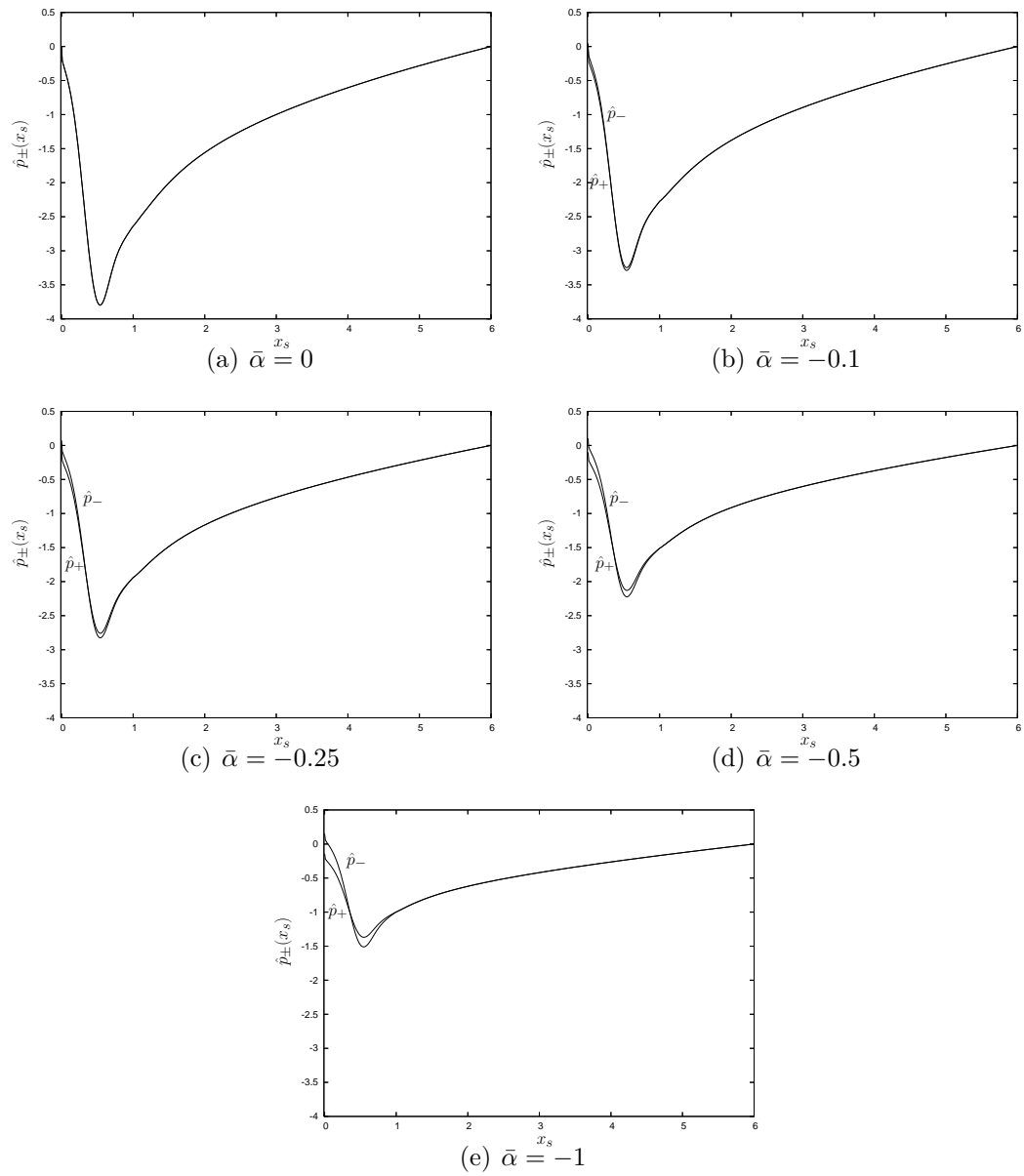


Figure 6.10: Pressure solutions for the thick blade and the global angles of attack $\bar{\alpha}$ in figure 6.9.

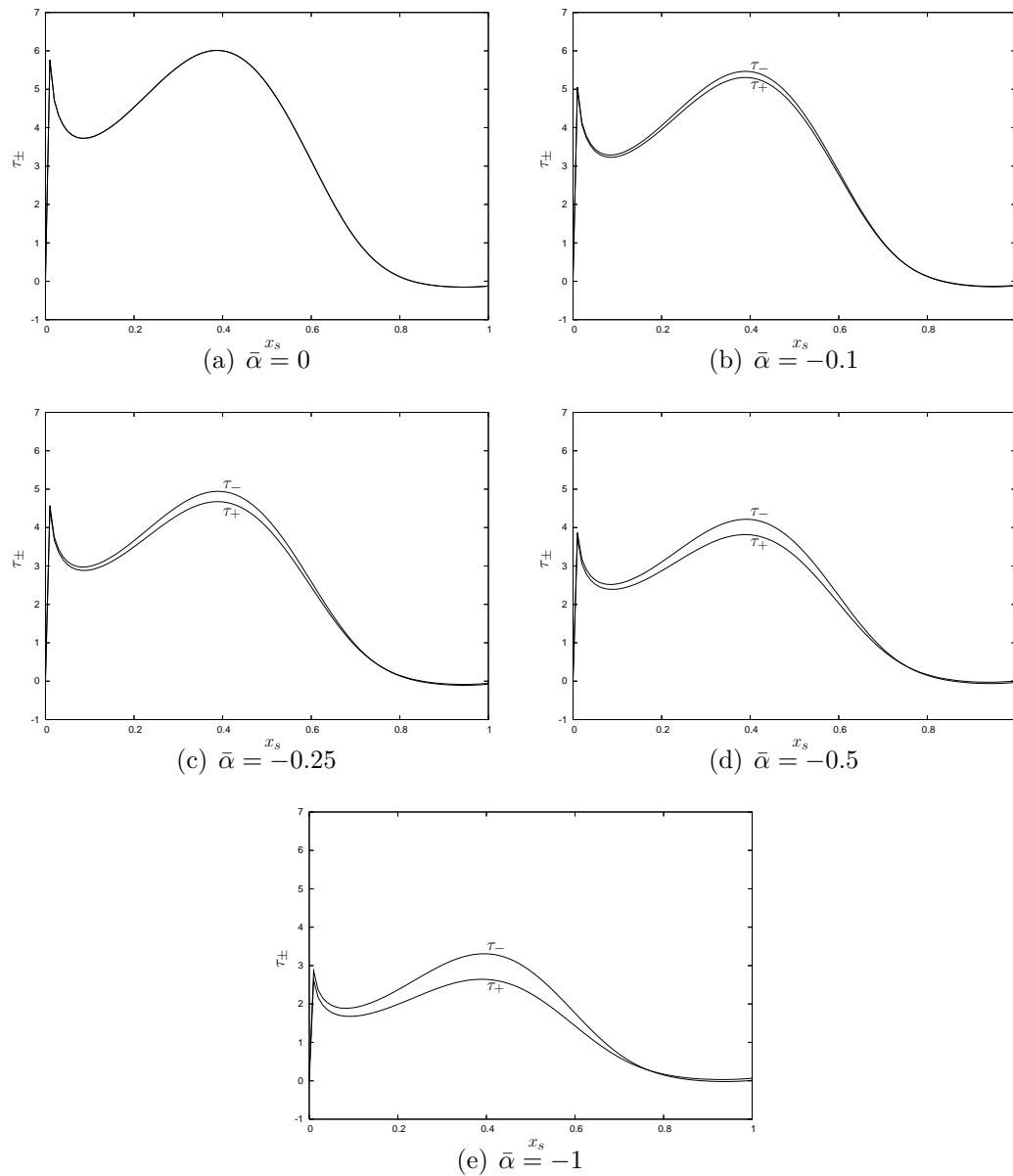


Figure 6.11: Skin friction solutions for the thick blade and the global angles of attack $\bar{\alpha}$ in figure 6.9.

in each case. The separation and reattachment x -stations are recorded in table 6.4.

$\bar{\alpha}$	x_S^+	x_R^+	x_S^-	x_R^-
0	0.79	1.18	0.79	1.18
0.1	0.80	1.15	0.80	1.15
0.25	0.81	1.14	0.80	1.14
0.5	0.83	1.08	0.82	1.08
1.0	0.89	0.97	0.83	1.00

Table 6.4: Separation and reattachment positions x_S^+ and x_R^+ on the upper blade surface and x_S^- and x_R^- on the lower blade surface for the thick blade case.

In conclusion to this chapter, we have added a global angle of attack to the periodic, interactive many-blade limit of Chapter 5 and Bowles & Smith (2000a,b). The global angle of attack $\alpha = O(Re^{-1})$ in this chapter is the smallest possible angle such that a leading order change in the sublayer formulation occurs. With the global angle of attack of this size and the very large downstream distances considered in the interactive many-blade limit, the blade is shifted within the sublayer to leading order. This caused different no-slip and no-normal flow boundary conditions. The formulation in the bulk-layer and free-stream regions is the same as before. We presented numerical solutions for flat, angled and thick blades with various values of $\bar{\alpha}$. The results report a decrease in the local shear strength of the flow for small Y_1 in the sublayer and there was a decrease in the size of the pressure drop from the leading edge to the trailing edge as $\bar{\alpha}$ decreased.

Chapter 7

The pressure interactive many-blade limit with larger global angles of attack

7.1 Analysis for larger global angles of attack

In the previous chapter, we considered the smallest global angle of attack that has any influence on this interactive many-blade structure. The purpose of this chapter is to find larger global angles of attack that still preserve the overall structure of our interactive many-blade limit. The starting point for this chapter is equation (6.2) of Chapter 6, where we derived an equation for the y position of the boundary-layer structure at distances $x = O(Re^{3/5})$ in the interactive limit as

$$y = Re^{-\frac{2}{5}} f_{\pm}(x_s) + Re^{-\kappa} \bar{\alpha} x_s + Re^{\frac{3}{5}-\kappa} \bar{\alpha}. \quad (7.1)$$

The global angle of attack $\alpha = Re^{-\kappa} \bar{\alpha}$, where $\bar{\alpha} = O(1)$ and κ is a constant to be determined.

In this chapter, we will consider the cases of $\kappa = 4/5, 3/5, 2/5$ which cause interactions to occur in the bulk-layer, the free-stream and over the short x_s scale within the sublayer respectively. In each case, we show how the interactive limit changes to incorporate these new interactions. There are two other values for κ that arise, namely $\kappa = 1/5, 0$, that are not considered in this thesis. These cases give α much larger than the sublayer, to which we

question whether the interactive limit would develop.

7.2 Formulation for $\alpha = O(Re^{-4/5})$

The case $\kappa = 4/5$ arises by considering a balance between the right-hand side of equation (7.1) and the bulk-layer thickness. The normal coordinate in the bulk-layer is given by $Y_b = O(1)$ where $y = Re^{-1/5}Y_b$. Thus on comparing this estimate for y with (7.1), we find

$$Y_b = Re^{-\frac{1}{5}}f_{\pm}(x_s) + Re^{\frac{1}{5}-\kappa}\bar{\alpha}x_s + Re^{\frac{4}{5}-\kappa}\bar{\alpha}. \quad (7.2)$$

The choice $\kappa = 4/5$, so that $\alpha = O(Re^{-4/5})$, gives the smallest global angle of attack that first affects the bulk-layer to leading order. Hence, the leading order balance of the normal bulk-layer coordinate and the global angle of attack $\alpha = Re^{-4/5}\bar{\alpha}$ for large Re is taken as

$$Y_b = \bar{\alpha}. \quad (7.3)$$

A global angle of attack of this size represents a constant normal shift by an amount $\bar{\alpha}$ in the position of the whole sublayer within the bulk-layer from $Y_b = 0$ previously to $Y_b = \bar{\alpha}$.

We adopt the same interactive many-blade limit expansions for the velocities and pressure in the bulk-layer as seen before, with $Y_b = O(1)$ the normal bulk-layer coordinate. This can be done, since the global angle of attack is much smaller than the leading order velocities in the bulk-layer and the sublayer. Hence the same governing equations hold for the leading order behaviours of u_0 and v_1 in the bulk-layer, with the matching conditions to the sublayer given by

$$u_0 = v_M = 0 \quad \text{on} \quad Y_b = \bar{\alpha}^{\pm}, \quad (7.4)$$

The original mean Blasius flow still holds as the leading order solution for U , but is Prandtl shifted from $Y_b = 0$ in the non-symmetric case of Chapter 5 to $Y_b = \bar{\alpha}$ in this chapter. The solution for v_1 remains unchanged, except that matching with the sublayer must take place as $Y_b \rightarrow \bar{\alpha}^{\pm}$.

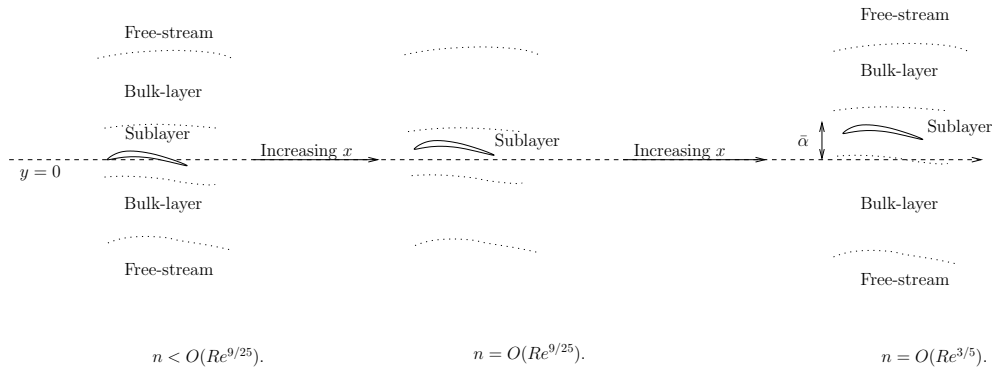


Figure 7.1: Illustration of the development of the interactive many-blade limit structure with a global angle of attack $\alpha = O(Re^{-4/5})$.

The sublayer lies at a shifted position $Y_b = \bar{\alpha}$ within the bulk-layer. Hence, the normal coordinate $\hat{Y} = O(1)$ in the sublayer is introduced, where

$$y = Re^{-1/5}\bar{\alpha} + Re^{-2/5}(\hat{Y} + f_{\pm}(x_s)) \quad (7.5)$$

gives the y position of the sublayer. On matching to the bulk-layer, the same expansions for the velocity and pressure hold, leading to the governing interactive boundary-layer equations for the sublayer. The boundary conditions for the problem are exactly those given in Chapter 5. To see why $\bar{\alpha}$ does not appear in the sublayer formulation in this instance, consider the flow before the interactive many-blade limit is approached, where the non-interactive limit of Chapter 4 holds. We can modify (7.1) to consider downstream distances for $x < O(Re^{3/5})$, and by comparing the resulting equation to the sublayer thickness, we find that the blade is shifted within the sublayer after passing a number $n = O(Re^{9/25})$ of blades (see figure 7.1). As the downstream distance increases to that of the interactive limit, the cumulative effect of passing many blades \hat{Y} means that the vertical displacement of the blade within the sublayer is large enough for the position of the whole sublayer to be shifted within the bulk-layer and when $x = O(Re^{3/5})$, $\bar{\alpha}$ drops out of the leading order problem in the sublayer. Comparing the free-stream coordinate y with equation (7.1), we find no balances with the global angle of attack terms at leading order and hence the free-stream problem is

unchanged for $\alpha = O(Re^{-4/5})$.

In summary, the new interaction featured in this section amounts to a constant shift of size $\bar{\alpha}$ of the whole sublayer within the bulk-layer. The interactive many-blade structure therefore still holds with the mean Blasius flow behaviour Prandtl shifted to $Y_b = \bar{\alpha}$ within the bulk-layer. The free-stream and sublayer problems are unchanged from Chapter 5.

7.3 Formulation for $\alpha = O(Re^{-3/5})$

We next compare the normal coordinate $y = O(1)$ with (7.1) to find that the global angle of attack that causes a leading order change to the free-stream is given by the case $\kappa = 3/5$. By substituting $\kappa = 3/5$ into (7.1), we see that a global angle of attack of this size causes a shift of the whole boundary-layer structure within the free-stream, from $y = 0$ previously to $y = \bar{\alpha}$.

The normal coordinate in the bulk-layer, Y_b , is now defined as

$$y = \bar{\alpha} + Re^{-\frac{1}{5}}Y_b, \quad (7.6)$$

and the same bulk-layer expansions are taken as before. We find that the problem in the bulk-layer is unchanged from Chapter 5 with the exception that the boundary-layer structure is shifted vertically by an amount $\bar{\alpha}$. Likewise, the normal sublayer coordinate, \hat{Y} , is given by

$$y = \bar{\alpha} + Re^{-\frac{2}{5}}\hat{Y}, \quad (7.7)$$

with the same expansions and governing boundary-layer equations at leading order. The global angle of attack parameter $\bar{\alpha}$ does not appear in the sublayer formulation at leading order and has dropped down to lower order terms.

However, we will need to adapt the formulation for the free-stream problem because of the normal shift in the boundary layer structure. Due to the small global angle of attack, the expansions used are unchanged and yield the governing Cauchy-Riemann equations for v and p at leading order. To find v and p we employ the method used in Chapter 5, using Cauchy's integral formula. We choose a field point (x_0, y_0) with $y_0 \neq \bar{\alpha}$ and define a new contour Γ^* consisting of two semi-circular contours γ_+^* and γ_-^* each made up

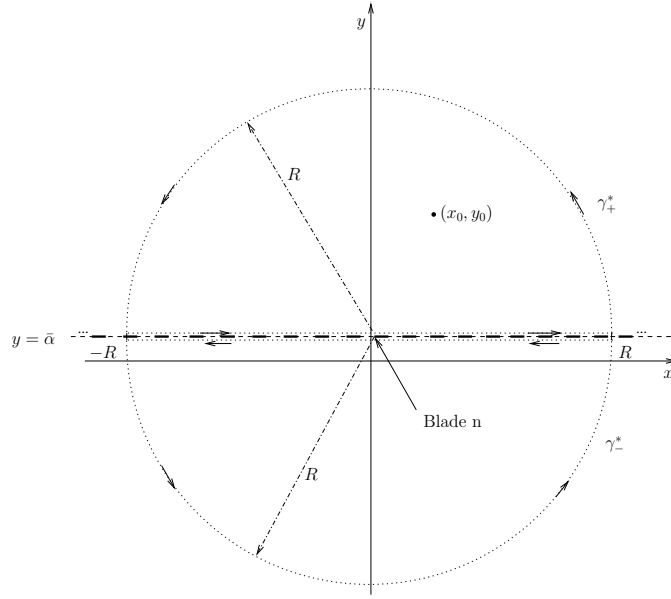


Figure 7.2: The new contour Γ^* used to solve the free-stream problem for a point (x_0, y_0) with $y_0 \neq \bar{\alpha}$.

of a semi-circle of radius R in the upper and lower half-planes respectively, and a straight line segment from $(-R, \bar{\alpha})$ to $(R, \bar{\alpha})$ (see figure 7.2). In the limit $R \rightarrow \infty$ and taking real and imaginary parts gives the pressure p and normal velocity v as

$$p(x_0, y_0) = \frac{1}{2\pi} \int_{-\infty}^{\infty} \frac{(x_s - x_0)[v](x_s) - (\bar{\alpha} - y_0)[p](x_s)}{(x_s - x_0)^2 + (\bar{\alpha} - y_0)^2} dx_s, \quad (7.8)$$

$$v(x_0, y_0) = -\frac{1}{2\pi} \int_{-\infty}^{\infty} \frac{(x_s - x_0)[p](x_s) + (\bar{\alpha} - y_0)[v](x_s)}{(x_s - x_0)^2 + (\bar{\alpha} - y_0)^2} dx_s, \quad (7.9)$$

dependent on the values of $[p](x_s) = p_+(x_s, \bar{\alpha}) - p_-(x_s, \bar{\alpha})$ and $[v](x_s) = v_+(x_s, \bar{\alpha}) - v_-(x_s, \bar{\alpha})$ across $y = \bar{\alpha}$. Since the values of v_+ and v_- across the blades and wakes are unknown (since we have that $v_{\pm} = \mp \lambda_{\pm} b'_{\pm}$, the unknown displacement gradient from the sublayer), we use Cauchy's integral formula again for the point $(x_0, \bar{\alpha})$. With the field point $(x_0, \bar{\alpha})$, the contours γ_+^* and γ_-^* are deformed slightly by including a small semi-circle of radius ϵ , centred at $(x_0, \bar{\alpha})$ (see figure 7.3). We take the real and imaginary parts of the resulting equation to yield the following relations for the pressure and

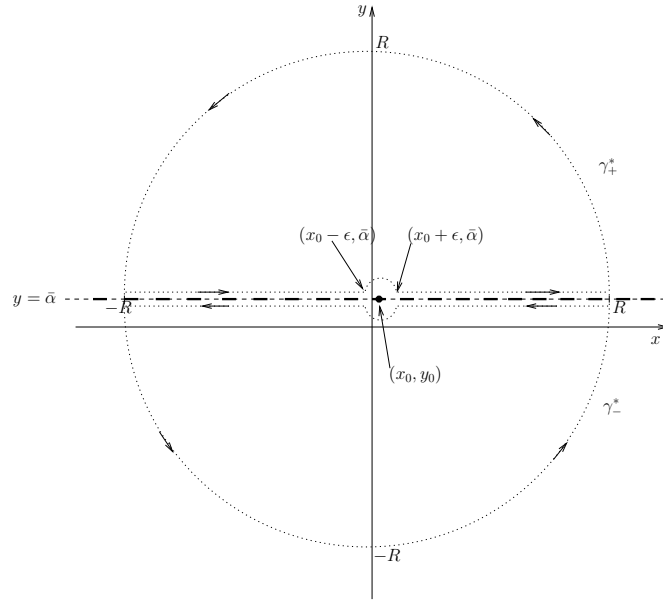


Figure 7.3: The contour Γ^* used to solve the free-stream problem for the point $(x_0, \bar{\alpha})$, with the inclusion of two other small semi-circles of radius ϵ .

velocities just above and below $y = \bar{\alpha}$

$$p_{\pm}(x_0) = -\frac{1}{\pi} \int_{-\infty}^{\infty} \frac{v_{\pm}(x_s)}{x_s - x_0} dx_s, \quad (7.10)$$

$$v_{\pm}(x_0) = \frac{1}{\pi} \int_{-\infty}^{\infty} \frac{p_{\pm}(x_s)}{x_s - x_0} dx_s. \quad (7.11)$$

We notice immediately that these relations are exactly the same as those found in the case of a general non-symmetry. The same analysis presented in Chapter 5 can be applied to these equations to reveal the same periodic pressure-displacement laws as found in Chapter 5. An alternative approach to finding the relations (7.8) - (7.11) would be to apply the transformation $y = y_* + \bar{\alpha}$ to the p - v relations in Chapter 5 and reformulate the problem for y_* .

To complete the analysis, we find the downstream distances at which the sublayer and bulk-layer first feel the effects of a global angle of attack to leading order within the non-interactive limit. With $\alpha = O(Re^{-3/5})$ and the sublayer and bulk-layer thicknesses of $O(Re^{-1/2}n^{1/6})$ and $O(Re^{-1/2}n^{1/2})$ respectively, we deduce that on passing $n = O(Re^{3/25})$ the global angle of attack appears as a shift of the blade within the sublayer at leading order. Following the same approach, after $n = O(Re^{1/5})$ blades the sublayer is

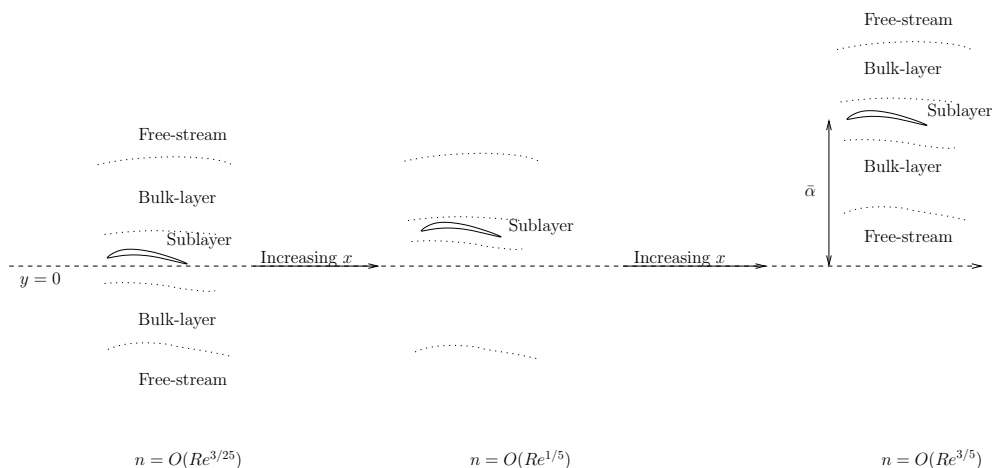


Figure 7.4: Illustration of the development of the interactive many-blade limit structure with a global angle of attack $\alpha = O(Re^{-3/5})$.

shifted within the bulk-layer (see figure 7.4). Then, when $n = O(Re^{3/5})$, as in this chapter, the whole boundary-layer is shifted within the free-stream.

In conclusion, the interaction for a global angle of attack of size $\alpha = O(Re^{-3/5})$ causes a normal shift in the whole boundary-layer structure to lie at $y = \bar{\alpha}$, with the formulation and solutions in each region largely unchanged. No sublayer solutions are presented here, since the problem is given by that of Chapter 5 to leading order.

7.4 Short scale balance in the sublayer

So far, we have described analyses for the global angle of attack being much smaller than the sublayer size. The final limit of interest arises by taking $\kappa = 2/5$ on comparing equation (7.1) with the sublayer thickness, so that there is a balance between the short scale global angle of attack term, $\bar{\alpha}x_s$ and the thickness of the sublayer. Thus in this section, we take $\alpha = Re^{-2/5}\bar{\alpha}$. At distances $x = O(Re^{3/5})$ in the free-stream, the whole boundary-layer system is shifted from $y = 0$ to $y = Re^{1/5}\bar{\alpha}$. The bulk-layer coordinate, Y_b , is given by

$$y = Re^{1/5}\bar{\alpha} + Re^{-1/5}Y_b, \quad (7.12)$$

with the same expansions holding for U, V, P with the normal coordinate Y_b . The bulk-layer solution is still governed by mean Blasius flow at leading order

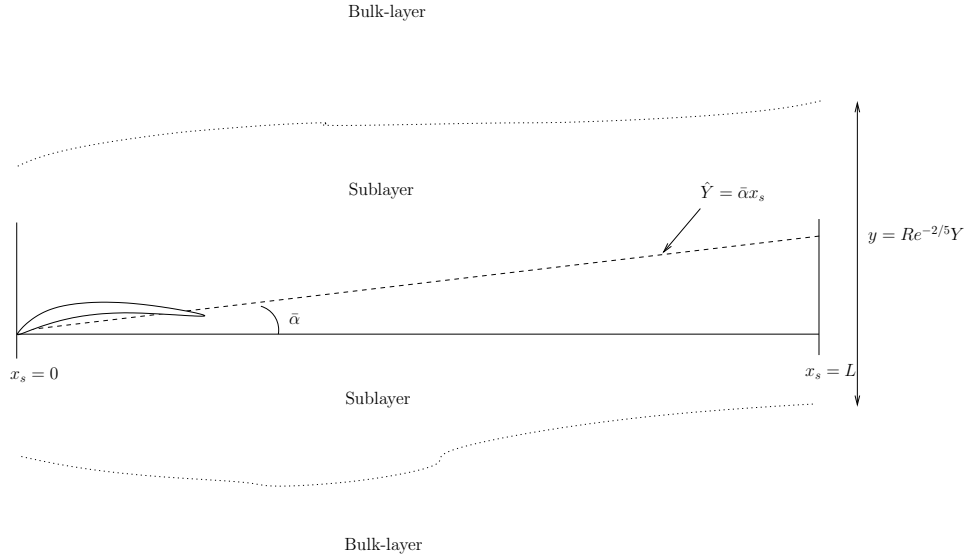


Figure 7.5: Illustration of the flow geometry within the sublayer for $\alpha = Re^{-2/5} \bar{\alpha}$.

in U , Prandtl shifted in the y direction by an amount $Re^{1/5} \bar{\alpha}$.

The normal sublayer coordinate is given by

$$y = Re^{1/5} \bar{\alpha} + Re^{-2/5} \hat{Y}, \quad (7.13)$$

and the same expansions in the velocity and pressure hold to match with the bulk-layer. Thus the leading order problem is given by the interactive boundary layer equations

$$\hat{u} \frac{\partial \hat{u}}{\partial x_s} + \hat{v} \frac{\partial \hat{u}}{\partial \hat{Y}} = -\frac{d\hat{p}}{dx_s} + \frac{\partial^2 \hat{u}}{\partial \hat{Y}^2}, \quad (7.14)$$

$$\frac{\partial \hat{u}}{\partial x_s} + \frac{\partial \hat{v}}{\partial \hat{Y}} = 0, \quad (7.15)$$

but now subject to the revised boundary conditions

$$\hat{u} = \hat{v} = 0 \quad \text{on} \quad \hat{Y} = f_{\pm}(x_s) + \bar{\alpha} x_s, \quad 0 < x_s \leq l, \quad (7.16)$$

$$\text{Regularity in } \hat{u}, \hat{v} \text{ and } \hat{p} \text{ in the wake,} \quad (7.17)$$

$$\hat{u} \rightarrow \pm(\hat{Y} + b_{\pm}(x_s)) \quad \text{as} \quad \hat{Y} \rightarrow \pm\infty, \quad (7.18)$$

$$\hat{p}_+(l) = \hat{p}_-(l), \quad (7.19)$$

$$Y\text{-shift at } x_s = L, \quad (7.20)$$

$$\text{Periodicity in } \hat{u}, \hat{v} \text{ and } \hat{p} \text{ in } x_s. \quad (7.21)$$

Here, the application of the no-slip and no-penetration flow conditions is at $\hat{Y} = f_{\pm}(x_s) + \bar{\alpha}x_s$ instead of $\hat{Y} = f_{\pm}(x_s)$ in Chapter 5. This means that the global angle of attack will directly influence the matching conditions for v_1 in the bulk-layer at leading order, not previously seen in our interactive analyses. This may be seen by first introducing the normal coordinate $\hat{Y} = Y_1 + \bar{\alpha}x_s$ and has the effect of rotating the whole sublayer to lie horizontally along the x -axis. On substitution into the boundary conditions, the $\bar{\alpha}x_s$ term in (7.16) then appears in the matching condition (7.18). Using continuity and integrating with respect to Y_1 in the far-field, gives the sublayer entrainment velocities as $\mp(b'_{\pm}(x_s) + \bar{\alpha})$ and hence on matching with the bulk-layer, we have that $E_{\pm}(x_s) = b_{\pm}(x_s) + \bar{\alpha}x_s$ and

$$v_1 = \mp(\bar{b}'_{\pm}(x_s) + \bar{\alpha})u_0. \quad (7.22)$$

Here, the global angle of attack $\bar{\alpha}$ now appears directly in the match with the bulk-layer, as yet not seen in the previous analyses.

The normal coordinate for the free stream is given by $y = Re^{1/5}\bar{\alpha} + y_*$. The same expansions for U, V, P still apply with y replaced by y_* and hence the same pressure-displacement laws can be derived as listed in equations (7.10) and (7.11). However, the influence of the global angle of attack now appears explicitly in the matching conditions with the bulk-layer through (7.22) and will directly influence the free-stream perturbation solution.

Before finding numerical solutions to the problem, we note that the angle $\alpha = O(Re^{-2/5})$ is larger than the original global angle of attack in Chapter 3, that of $O(Re^{-1/2})$. It could be argued that the interactive limit would not form if the global angle of attack is of this size, although here we assume that the interactive many-blade limit does develop. This limit may occur through a global tilt of the blade system once $x = O(Re^{3/5})$ downstream or if this model emerges as a downstream limit of the flow past many blades with $\alpha = O(Re^{-2/5})$.

To compute solutions to the sublayer problem, we apply the Prandtl shift $\hat{u} = u_1$, $\hat{v} = v_1 - (f'_{\pm}(x_s) + \bar{\alpha})u_1$ and $\hat{p} = p_1$ with the normal coordinate $\hat{Y} = Y_1 + f_{\pm}(x_s) + \bar{\alpha}x_s$. Thus, the governing sublayer equations are to be

solved with the boundary conditions

$$u_1 = v_1 = 0 \quad \text{on} \quad Y_1 = 0, \quad 0 < x_s \leq l, \quad (7.23)$$

$$\frac{\partial u_1}{\partial Y_1} = v_1 = 0 \quad \text{on} \quad Y_1 = 0, \quad l < x_s \leq L, \quad (7.24)$$

$$u_1 \rightarrow \pm(Y_1 + f_{\pm}(x_s) + \bar{\alpha}x_s) + c_{\pm} \quad \text{as} \quad Y_1 \rightarrow \pm\infty, \quad (7.25)$$

along with the conditions (7.19) - (7.21). The same numerical method as in the last two chapters is adopted to solve the sublayer problem.

7.5 Results

The pressure-interactive sublayer problem is solved for the global angles of attack $\bar{\alpha} = 0, -0.1, -0.25, -0.5$ for flat, angled and thick blades. As in Chapters 5 and 6, we solve the condensed problem, take $l = 1$ and $L = 6$ to be the trailing edge position and blade-wake period respectively and set the constants $c_+ = c_-$.

In figure 7.6, the calculated streamlines past a flat plate with a global angle of attack are presented. In comparison with the previous chapter, the streamlines show much larger deflections over all the blade and wake period for all values of $\bar{\alpha}$ used. This deflection through the wake is due to the global angle of attack term, which appears directly in the boundary conditions throughout the blade-wake period. We also see that the spacing of the streamlines increases as the parameter $\bar{\alpha}$ is decreased, as discussed in the last chapter.

The corresponding pressure and skin friction solutions are presented in figures 7.7 and 7.8 respectively. The pressure solutions show an increasing pressure difference across the upper and lower blade surfaces as $\bar{\alpha}$ is decreased, as expected. The differences between the upper and lower surface pressure and skin friction profiles are much greater compared to the previous chapter. The computed lift for each case is given in table 7.1, along with the pressure jumps, c_+ and the Y -shift.

The calculated values in table 7.1 show an interesting feature. For the current problem of a flat blade, we notice that $Y_s \approx 6\bar{\alpha} = L\bar{\alpha}$. Such a large Y -shift means that after the leading edge jumps, a nearly equal flux

has passed over the upper and lower blade surfaces and hence the pressure jumps $p_+ \approx -p_-$ is required to satisfy the Kutta trailing edge condition. We believe this is due to the assumption of c_{\pm} being equal. If the values were allowed to be unequal, this would give different far-field matching conditions for \hat{u} as the leading edge region is passed and so a different Y_s , would be needed to ensure the Kutta condition is met. This feature seemed to occur, especially for larger values of $\bar{\alpha}$ in each case presented.

$\bar{\alpha}$	$p_+(0^+)$	$p_-(0^+)$	c_+	Y_s	Lift
-0.1	-0.207	0.207	1.56	-0.560	0.212
-0.25	-0.304	0.304	-1.16	-1.49	0.312
-0.5	-0.377	0.377	-3.01	-2.99	0.391

Table 7.1: The calculated values (to 3 sf) of the leading edge pressure jumps, c_+ , the Y -shift and lift for a flat blade with a global angle of attack $\bar{\alpha}$.

In figures 7.9 - 7.11, we impose a small local angle of attack on the blade by choosing

$$f_{\pm}(x_s) = -0.2x_s. \quad (7.26)$$

In figure 7.9, similar deflections of the streamlines in the wake profile are seen as in the case of the flat blade, as well as similar behaviour in the pressure and skin friction. We see in figure 7.10, that when $\bar{\alpha} = -0.5$ a slight adverse pressure gradient occurs before the trailing edge and is due to the combination of the local and global angles of attack.

In figure 7.11, we note in the case of $\bar{\alpha} = -0.5$ that the skin friction on the lower surface becomes approximately constant before the trailing edge whilst on the upper surface, the skin friction seems to decrease linearly towards zero. This is similar to the flat blade case presented above, although in the current case with the addition of a local angle of attack this feature is emphasised. The values in table 7.1 are repeated for the angled blade case in table 7.2 and show the same characteristics as seen in the flat blade case.

In the final figures of this chapter, we take

$$f_{\pm}(x_s) = \pm f_{\max} \sin^2(\pi x_s). \quad (7.27)$$

We present solutions for $f_{\max} = 1.4$ in figures 7.12 - 7.14 and $f_{\max} = 1.8$ in figures 7.15 - 7.17. In figure 7.12, we see that for the case of $\bar{\alpha} = 0$

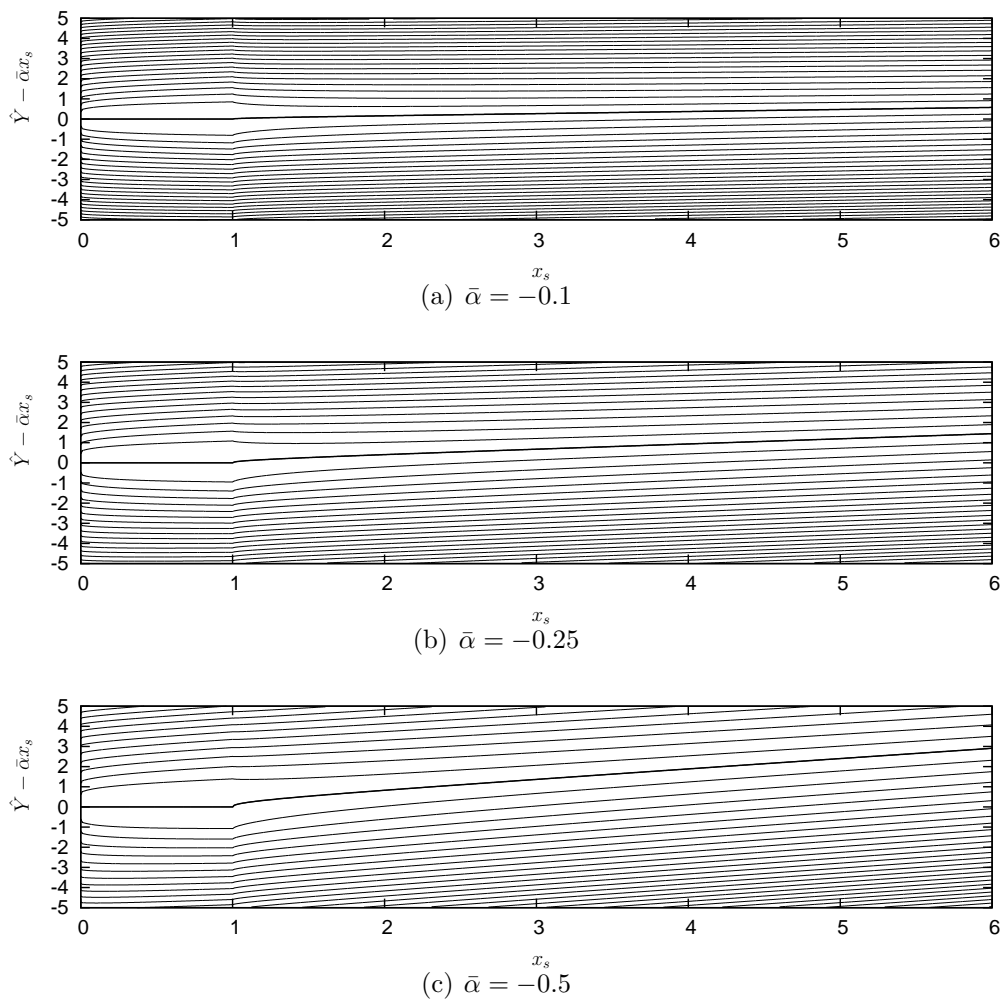


Figure 7.6: Streamline plots for a flat blade with the global angles of attack $\bar{\alpha} = -0.1, -0.25, -0.5$.

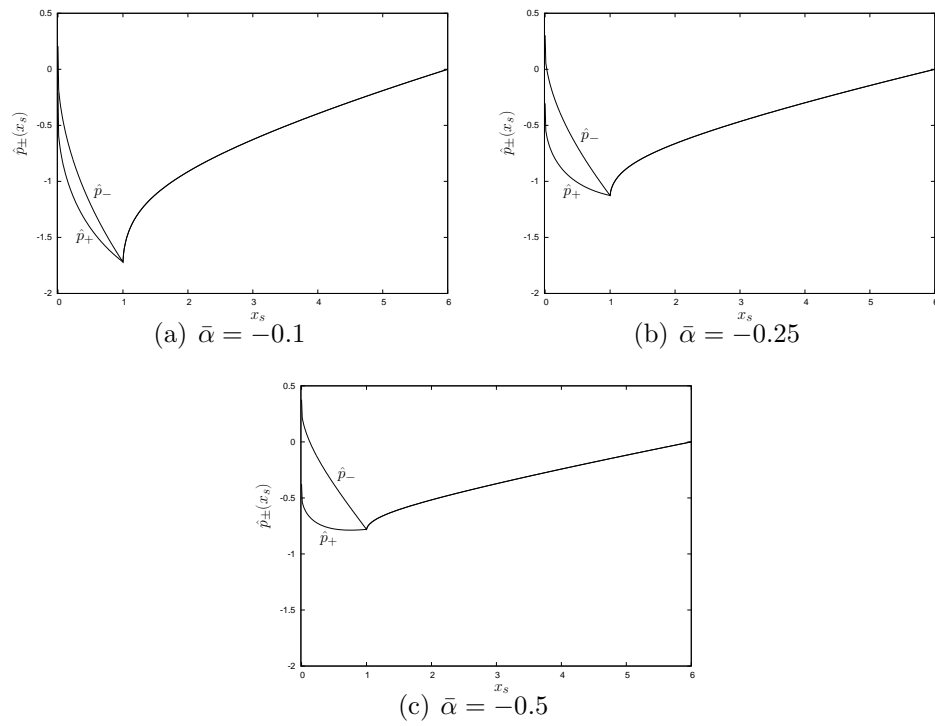


Figure 7.7: Corresponding pressure solutions for flow past a flat blade with the global angles of attack in figure 7.6.

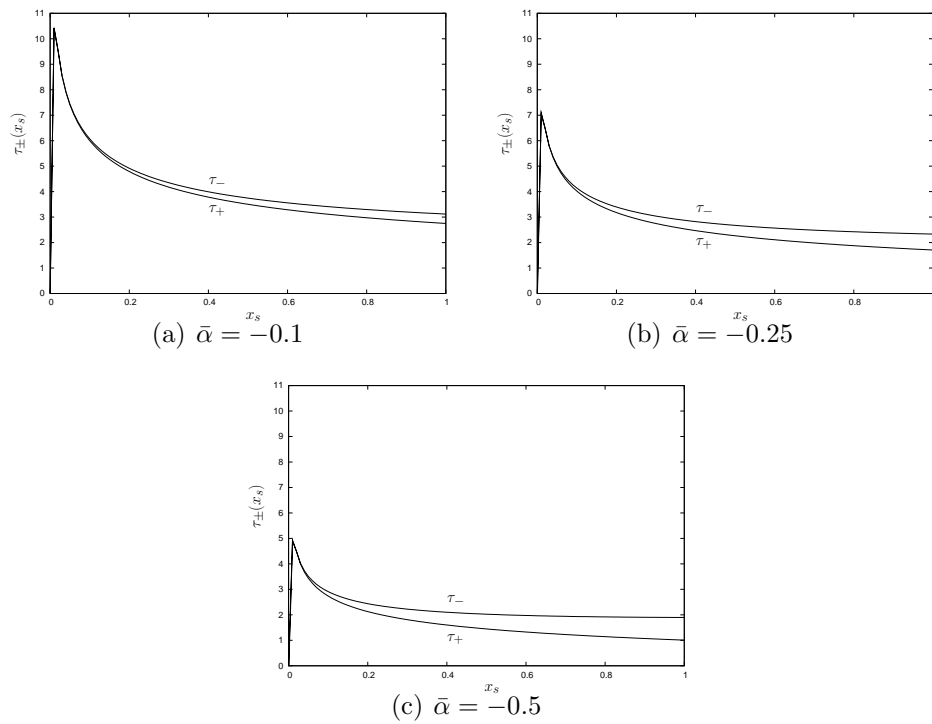


Figure 7.8: Calculated skin friction for flow past a flat blade with the global angles of attack in figure 7.6.

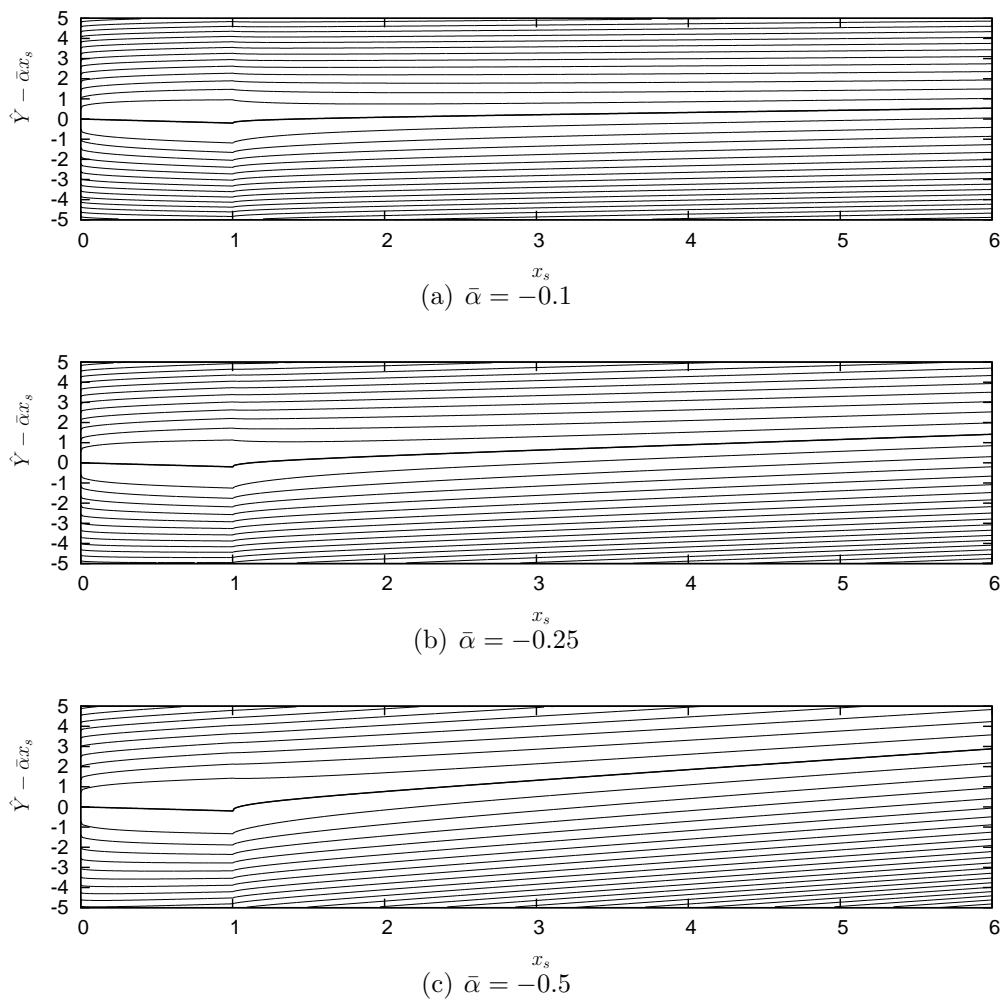


Figure 7.9: Streamline plots for an angled blade $f_{\pm}(x_s) = -0.2x_s$ with the global angles of attack $\bar{\alpha} = -0.1, -0.25, -0.5$.

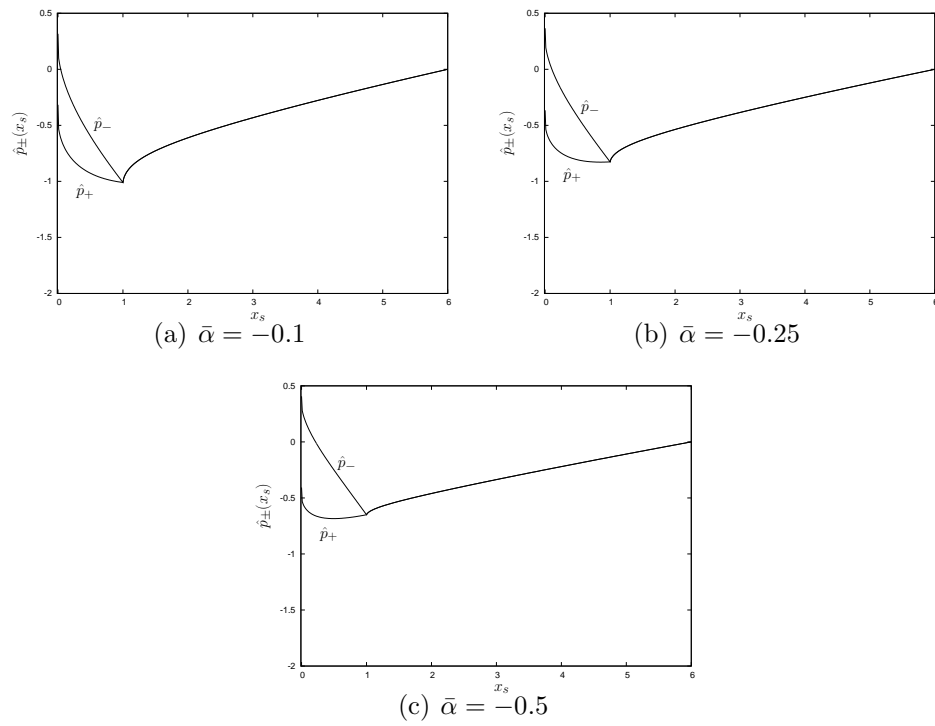


Figure 7.10: Corresponding pressure solutions for flow past an angled blade $f_{\pm}(x_s) = -0.2x_s$ with the global angles of attack in figure 7.9.

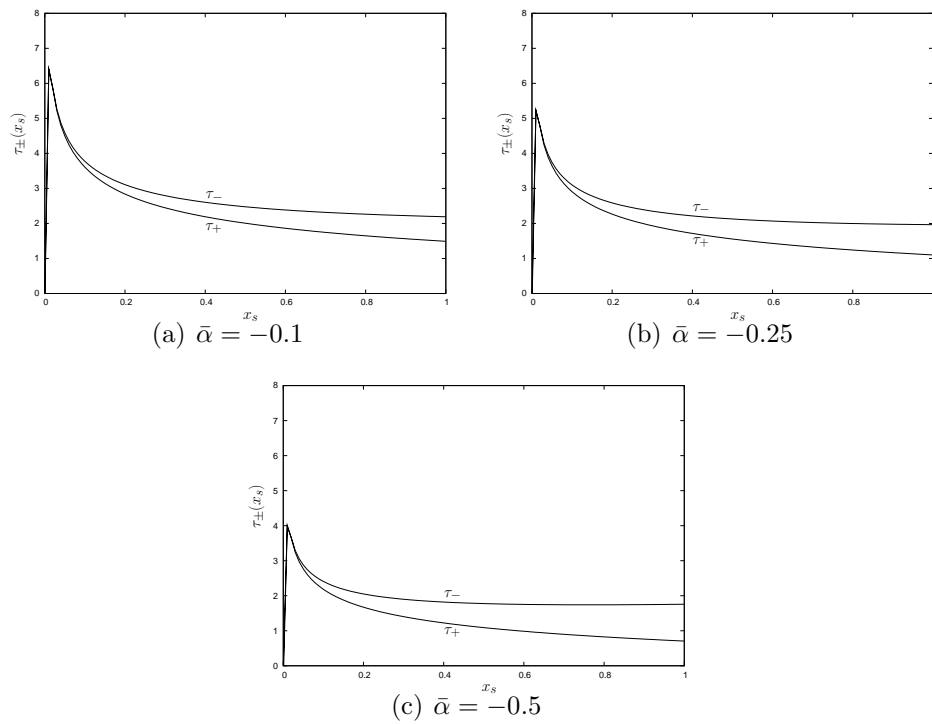


Figure 7.11: Calculated skin friction for flow past an angled blade $f_{\pm}(x_s) = -0.2x_s$ with the global angles of attack in figure 7.9.

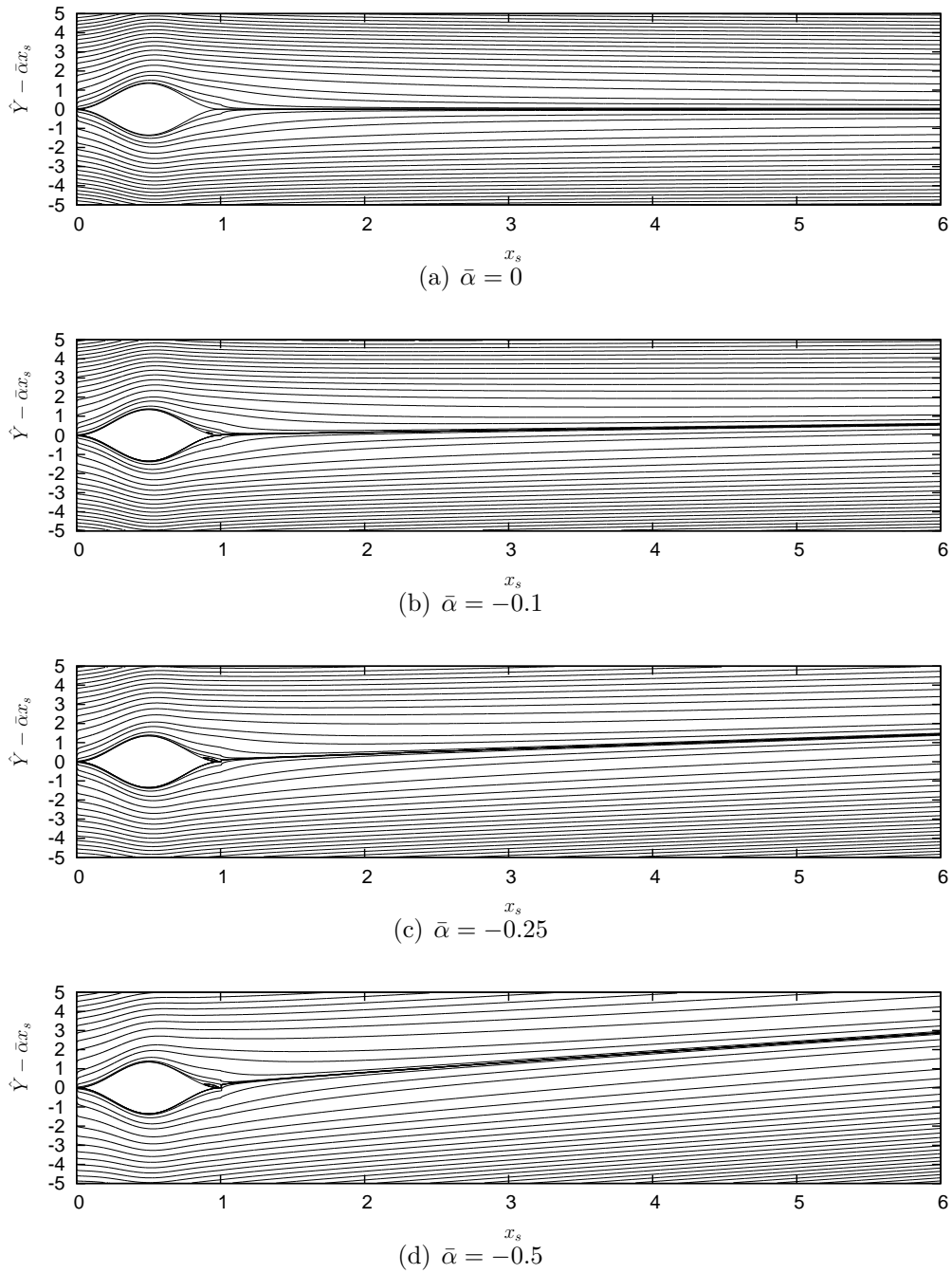


Figure 7.12: Streamline plots for a thick blade with parameter $f_{\max} = 1.4$ and the global angles of attack $\bar{\alpha} = 0, -0.1, -0.25, -0.5$.

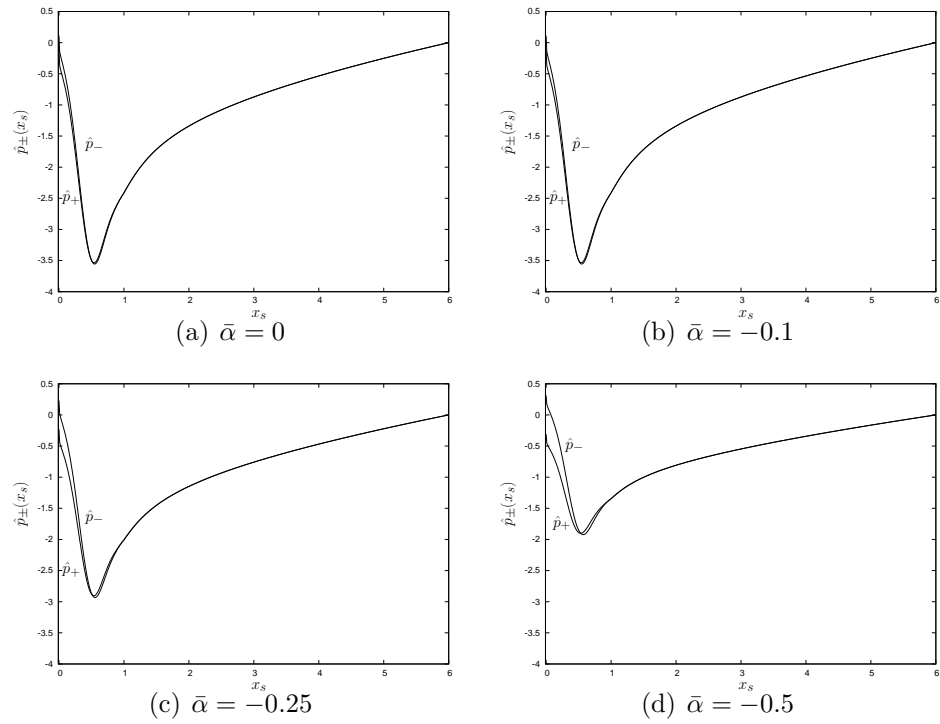


Figure 7.13: Corresponding pressures for the solutions in figure 7.12.

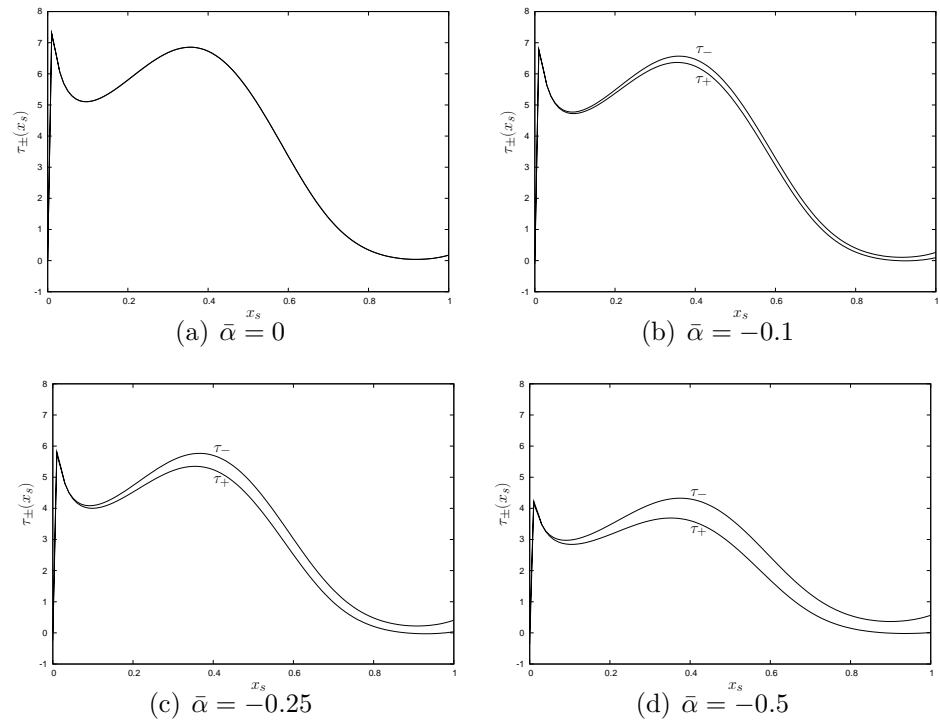


Figure 7.14: Calculated skin friction for the solutions presented in figure 7.12.

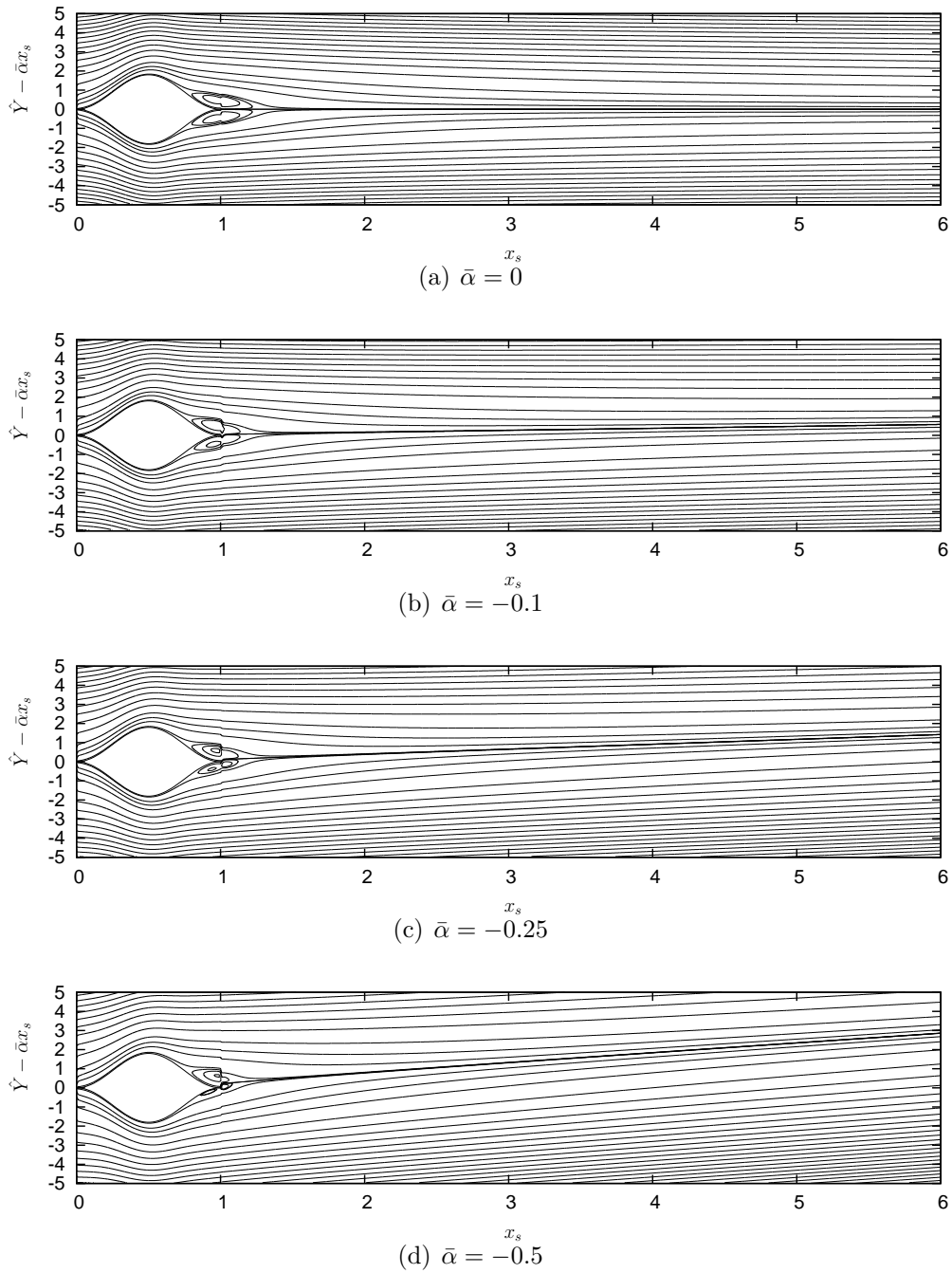


Figure 7.15: Streamline plots for a thick blade with parameter $f_{\max} = 1.8$ and the global angles of attack $\bar{\alpha} = 0, -0.1, -0.25, -0.5$.

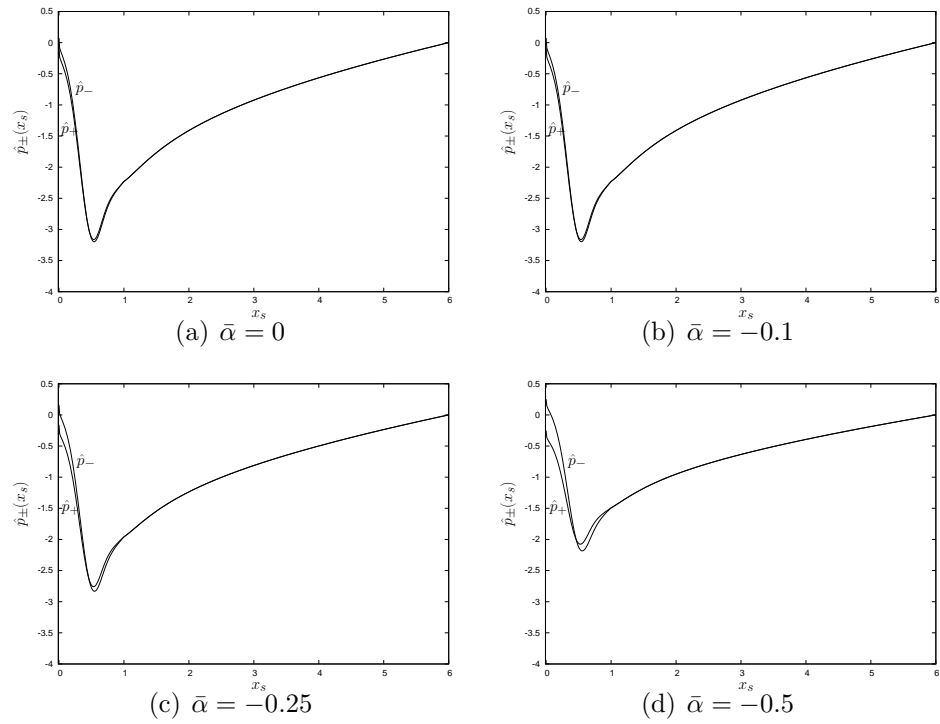


Figure 7.16: Corresponding pressures for the solutions in figure 7.15.

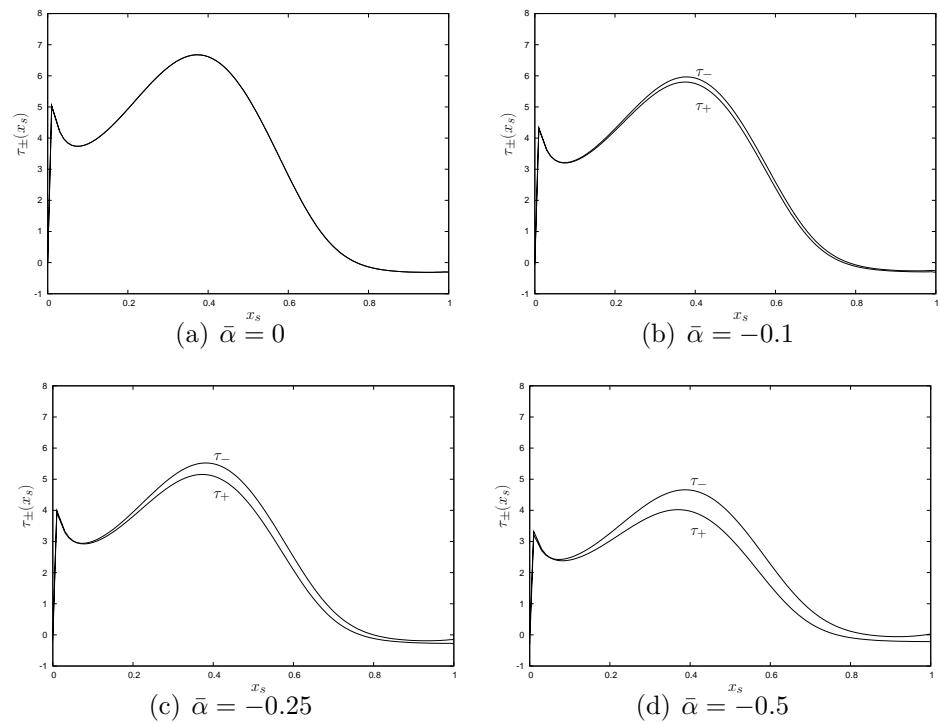


Figure 7.17: Calculated skin friction for the solutions presented in figure 7.15.

$\bar{\alpha}$	$p_+(0^+)$	$p_-(0^+)$	c_+	Y-shift	Lift
-0.1	-0.317	0.317	-1.85	-0.592	0.327
-0.25	-0.366	0.366	-2.76	-1.49	0.379
-0.5	-0.407	0.407	-3.80	-2.99	0.425

Table 7.2: The calculated values of the leading edge pressure jumps, c_+ , the Y-shift and lift (to 3 s.f.) for an angled blade $f_{\pm}(x_s) = -0.2x_s$ with a global angle of attack $\bar{\alpha}$.

there is no separation caused by the blade thickness. When $\bar{\alpha}$ is decreased, a small flow separation and subsequent reattachment is invoked on the upper surface before the trailing edge. Thus, the global angle of attack may cause separation to occur in the sublayer, even in the presence of small angles of attack.

The thickness added to the blade creates an adverse pressure gradient over the leeward facing slope of the blade in all instances in figure 7.13. We see very little pressure difference across the blade and any difference that is created is solely due to the global angle of attack. The skin friction profiles in figure 7.14, like in the previous chapter, show an increase in skin friction over the front face of the blade before a rapid deceleration of the flow on the backward facing faces. The separation is seen in these figures by the τ_+ profile falling very slightly below $\tau = 0$ before the trailing edge. On the lower surface, the skin friction increases as $\bar{\alpha}$ decreases as more flow is pressed against the under-side of the blade for negative values of $\bar{\alpha}$.

In figures 7.15 - 7.17, the parameter $f_{\max} = 1.8$. The thickness effects of the blade cause two-sided separation before the trailing edge on both sides of the blade. As the global angle of attack is decreased, the size of the eddy beneath the blade becomes smaller and less pronounced. This increase in skin friction on the lower surface is again due to the global angle of attack. For the cases of $\bar{\alpha} = -0.25, -0.5$, the flow around the trailing edge becomes very complicated.

As with the case $f_{\max} = 1.4$, the pressure solutions in figure 7.16 show an adverse pressure gradient across the last half of the blade. The skin friction profiles in figure 7.17, show very similar behaviour to the previous case, with the flow reversals toward the trailing edge being clearly seen. In the case of

$\bar{\alpha}$	$p_+(0^+)$	$p_-(0^+)$	c_+	Y_s	Lift
0	0	0	1.00	0	0
-0.1	-0.113	0.113	0.789	-0.592	0.327
-0.25	-0.229	0.229	-0.0641	-1.49	0.379
-0.5	-0.311	0.311	-2.31	-2.99	0.176

Table 7.3: The calculated values of the leading edge pressure jumps, c_+ , the Y -shift and lift (to 3 s.f.) for a thick blade with $f_{\max} = 1.4$ with a global angle of attack $\bar{\alpha}$.

$\bar{\alpha}$	$p_+(0^+)$	$p_-(0^+)$	c_+	Y_s	Lift
0	0	0	0.301	0	0
-0.1	-0.0733	0.0733	-0.257	-0.592	0.0283
-0.25	-0.160	0.160	-0.968	-1.49	0.0634
-0.5	-0.253	0.253	-2.45	-2.99	0.107

Table 7.4: The calculated values of the leading edge pressure jumps, c_+ , the Y -shift and lift (to 3 s.f.) for a thick blade with $f_{\max} = 1.8$ with a global angle of attack $\bar{\alpha}$.

$\bar{\alpha} = -0.5$, there is a slight acceleration in the flow beneath the blade just before the trailing edge and is enough to cause reattachment. The pressure jumps, values of c_+ , the Y -shift and the lift are given in tables 7.3 and 7.4 and show similar behaviour to that discussed earlier in this section.

7.6 Summary

This concludes our discussion on the interactive many-blade limit with a global angle of attack. In Chapter 5, we introduced the interactive limit as seen in Bowles & Smith (2000a,b). At large downstream distances $x = O(Re^{3/5})$ a new feature arises whereby a pressure gradient is supported throughout the sublayer, in contrast to the non-interactive limit in Chapter 4. We outlined a numerical procedure to solve the condensed sublayer problem and found solutions in a different way to Bowles & Smith (2000a,b).

In Chapter 6, we extended the interactive limit of Chapter 5 to include a global angle of attack. We sought the smallest global angle of attack that causes a leading order change to the flow within the sublayer and found this is the case when $\alpha = O(Re^{-1})$. Analysis of the problem revealed that the

global angle of attack parameter $\bar{\alpha}$ appeared within the sublayer boundary conditions, causing a constant vertical shift of the blade within the sublayer. Numerical solutions were found for the condensed case, as seen in Chapter 5 and Bowles & Smith (2000a,b) to find solutions for various values of $\bar{\alpha}$ and different blade geometries.

In this chapter, we found larger global angles of attack that preserve the overall structure of the interactive many-blade limit but cause leading order changes to the bulk-layer and free-stream. We found that an angle $\alpha = O(Re^{-4/5})$ was sufficient to cause a shift of the whole sublayer within the bulk-layer. The sublayer and free-stream problems in this case were given by those in Chapter 5, whilst the bulk-layer problem was found to be governed by a Prandtl shifted mean Blasius flow at leading order.

A leading order change to the free-stream problem occurred when $\alpha = O(Re^{-3/5})$, whereby the whole boundary-layer system was shifted to a position $y = \bar{\alpha}$ within the free-stream. The bulk-layer and sublayer solutions were unchanged from that of Chapter 5, but the analysis for the free-stream had to be adapted to allow for the change in normal position of the boundary-layer. We used Cauchy's integral formula to derive slightly different equations for v and p away from $y = \bar{\alpha}$ compared to Chapter 5. On considering a point lying on $y = \bar{\alpha}$, we found that the same pressure-displacement laws held, as derived in Chapter 5.

Finally, we considered a short scale balance between the normal sublayer coordinate and the global angle of attack, yielding $\alpha = O(Re^{-2/5})$. Although the same structure of the boundary-layer still holds, we found that the presence of $\bar{\alpha}$ now appears directly in the matching conditions for V in the bulk-layer and hence the free-stream. Numerical solutions to this problem using the same methods used in Chapters 5 and 6 were found and a discussion was given of the most interesting features of the flow, including increased pressure differences over the blades in the case of flat and angled blades and separation features in the case of thick blades.

An extension to the work would be to investigate the flow behaviour if c_{\pm} were unequal. In the numerical solutions presented throughout Chapters 5, 6 and 7, we arbitrarily took these to be equal. However, if c_+ (say) is used

to gain pressure periodicity, then c_- would be unknown, and hence another condition to determine c_- would need to be found. A possible resolution to this problem could be to simply impose a value for the constant c_- ansatz and find a value of c_+ to obtain periodicity based on a choice of c_- . Another option is to find solutions, in the same way as Bowles & Smith (2000b), where the constants c_{\pm} are fixed and the problem then becomes finding the correct local angle of attack such that a periodic solution occurs. A way to extend their method to the numerical procedure in this chapter would be to fix c_{\pm} and the local non-symmetries and find the (now unknown) value of $\bar{\alpha}$ required to obtain a periodic solution. This could be regarded as the inverse of the method used in this thesis. A further extension is to develop a stable numerical scheme to calculate solutions to the full sublayer problem including the pressure-displacement laws.

Chapter 8

Flow past vertically aligned blades within a channel

8.1 Introduction

In this chapter, we consider an array of N vertically aligned blades within a bounding horizontal channel, subject to a uniform oncoming stream. The motivation for this chapter arises in aeronautical applications, such as gas turbine and atomizer flows appearing in the combustors of jet engines and the accompanying need to reduce pollutants (see Cohen *et al.* (1972) and Lefebvre (1999)). Furthermore, in axial fan flows such as those above, there is a need to reduce noise, as mentioned in Chapter 1. Further applications are motivated in physiological flows, such as blood flow past a cerebral arteriovenous malformation (AVM). Such flows are investigated experimentally by, for example, Marks *et al.* (1992) and Diehl *et al.* (1995) by measuring velocity and volume flow rates. An AVM occurs when a large artery or vein rapidly branches into many smaller blood vessels raising health concerns of stroke. Thus, it is important to understand the flow behaviour in such applications in order to combat these problems.

Smith (2002) considers the symmetric wake flow at the trailing edges of an array of vertically aligned blades in both external and internal flow problems, as a theoretical investigation into the gas turbine flows mentioned above. An internal wake is bounded within a larger channel, whilst the external wake is open to the free-stream flow. The normal scale in y is taken to be

much smaller than the streamwise extent in x , leading to a boundary-layer formulation of the problem at leading order. For the external wake, a semi-periodic flow is specified at the start of the wake, composed of Pouseuille-like flow at the exit of each daughter channel with a Blasius solution above the uppermost blade. The periodic nature of the Pouseuille flows at the trailing edge holds for a very short distance downstream of the trailing edges, before fluid is entrained into the central parts of the wake. Then, the parabolic nature of the Pouseuille flows decay downstream to a uniform state, different from unity. In the internal wake problems, the pressure is non-zero at leading order within the wake and a new, laterally periodic flow problem is derived. It is found that a similar uniform state emerges downstream in the wake, with exponential decay of the starting periodic flow into the uniform state. Influences of a non-symmetric starting profile were also addressed. In this case, suitable boundary conditions were applied to force a periodic flow to emerge downstream. It was found that the normal flow component quickly decays to zero downstream, leading to a zero pressure gradient and a terminal form for the streamwise flow component.

Smith & Jones (2000) consider flow branchings as an application to AVM modelling. They investigate the flow close to the entry of the smaller daughter channels from the larger mother channel. The nature of the flow close to the entrances of the daughter channels is essentially inviscid, other than for the onset of a small boundary-layer close to the dividing surfaces. Solutions to the leading order problem (governed by Laplace's equation) are found subject to specified fluxes in each daughter channel. Smith & Jones (2003) extends the above work to accommodate a generalised upstream velocity profile in the mother channel. Numerical solutions to the problem are found far downstream inside each daughter for various numbers of daughter channels and approaching velocity profiles. In the non-linear formulation, it was found that non-unique solutions existed.

Three-dimensional analysis of a dividing artery is considered by Blyth & Mestel (2001), by considering an infinite straight pipe of circular cross-section, divided longitudinally by a semi-infinite flat plate. This study reconsiders the work of Smith (1977). The flow structure is divided into five

regions, an inviscid core, a base boundary-layer close to the splitter plate, a viscous wall layer and two corner regions between the dividing plate and the sides of the pipe. An asymptotic approach is adopted in each region, followed by numerical solution for the main inviscid core problem. Solutions for all values of x in the daughter channels were then found, except within the corner regions.

Other related works include Smith *et al.* (2003), Bowles *et al.* (2005) and most recently, Smith & Ellis (2010). The latter paper gives rise to another application, in the sorting of grains of rice falling down a chute. As rice descends down a chute, strong puffs of air blow bad grains of rice into a discarding container. If the grains can be sorted appropriately on the chute, then, when a bad grain of rice is detected, greater success should be achieved in removing them. The grains of rice are modelled as thin bodies that are able to move freely within a long bounding channel. The model developed allows for unsteady interactions, with a main result being the appearance of a linear instability in the solution.

Within the applications outlined above, there has been emphasis on the flow close to the daughter entrances and in the wake but not on, for example, the flow within each daughter, subject to non-symmetric dividing blade shapes and various incoming flow profiles, the determination of fluxes entering each daughter and the flow past the array of N blades as a whole. In this chapter, we consider the flow past the system of blades in its entirety and answer some of the questions posed above. We do this by formulating and solving the whole flow problem, from upstream of the blades, through all the daughter channels and in the wake. This will extend knowledge into the gas turbine and AVM modelling applications above. For the latter application, we will be able to predict theoretically the response of the fluid through an array of dividing capillaries, before they rejoin into one artery or vein downstream.

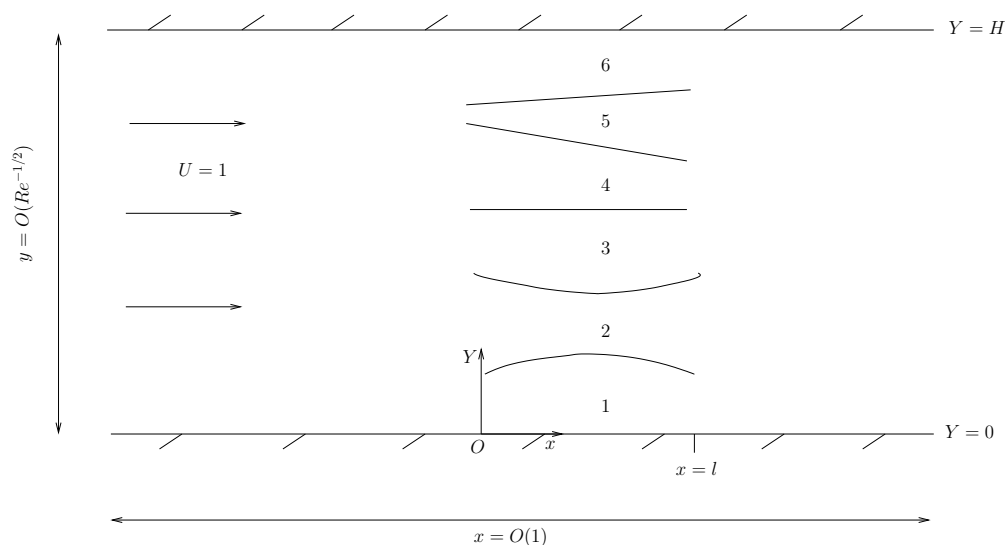


Figure 8.1: Problem illustration with $N = 5$ dividing blades in a non-symmetric configuration. The daughter channels from one to six are labelled. The coordinate of the n^{th} leading edge is taken as $(0, h_n)$.

8.2 Formulation

In our problem, N dividing blades of finite length are placed within an infinite channel, giving rise to $M = N + 1$ daughter channels. The length of the blades are taken to be $x = O(1)$. We take the bounding channel width to be $y = O(Re^{-1/2})$, and so we define a normal coordinate, $Y = O(1)$, within the mother channel where $y = Re^{-1/2}Y$. All of the leading and trailing edges of the N blades will be taken to lie at $x = 0$ and $x = l$ respectively and the flow upstream of the blades is given by $U = 1, V = 0, P = 0$.

The position of the n^{th} leading edge is taken to lie at a position $(x, Y) = (0, h_n), n = 1, \dots, N$, within a channel of width H and where the parameters $h_n > 0$ and $0 < h_i < h_j$ for $i < j$. The channel width, H , is taken such that $H > h_N$ so that all dividing blades lie within the channel. Physically, the problem is equivalent to the array of blades moving through still air within the channel. Our aim is to describe how the flow adapts as it approaches and passes through the daughter channels and in the wake of the dividing blades.

8.2.1 Expansions within the main pipe

The oncoming flow velocity $U = O(1)$ and so by continuity and the scales of the streamwise and normal coordinates, we have that $V = O(Re^{-1/2})$. Consequently, we expand the velocities and pressure in the pipe as

$$U = u(x, Y) + \dots, \quad (8.1)$$

$$V = Re^{-\frac{1}{2}}v(x, Y) + \dots, \quad (8.2)$$

$$P = p(x, Y) + \dots, \quad (8.3)$$

and substitution into the Navier-Stokes equations yields the boundary-layer equations at leading order

$$u \frac{\partial u}{\partial x} + v \frac{\partial u}{\partial Y} = -\frac{\partial p}{\partial x} + \frac{\partial^2 u}{\partial Y^2}, \quad (8.4)$$

$$0 = -\frac{\partial p}{\partial Y}, \quad (8.5)$$

$$\frac{\partial u}{\partial x} + \frac{\partial v}{\partial Y} = 0, \quad (8.6)$$

and by integrating (8.5), we obtain $p = p(x)$. The boundary conditions for the problem are given by

$$u = 1, v = 0 \quad \text{on } Y = 0 \text{ and } Y = H, \forall x \quad (8.7)$$

$$u = v = 0 \quad \text{on } Y = f_n(x), \quad n = 1, \dots, N, \quad 0 < x < l \quad (8.8)$$

representative of the no-slip and impermeable boundary conditions on the dividing blades and bounding channel walls. Here, $f_n(x)$ is a function that represents any shape or camber on the n^{th} blade. Upstream of the blades and as $x \rightarrow 0^-$, the solution is given by

$$u = 1, \quad v = 0, \quad p = 0. \quad (8.9)$$

The flow must satisfy the Kutta trailing edge condition, requiring

$$p(l) = p^*, \quad (8.10)$$

where p^* is an unknown constant. If there are N different shape functions f_n representing the N blades, then the pressures in the $M = N + 1$ daughter channels are not equal since the pressure gradient depends on the channel

geometry. Hence, the Kutta condition is not satisfied in general. This indicates that there is a leading edge discontinuity, akin to that in Chapters 2 and 5, allowing the flow velocity and pressure to jump to satisfy the Kutta condition. As flow passes through the leading edge region, the flow must jump from $u = 1, v = 0, p = 0$ upstream to $N + 1$ different starting conditions, one per daughter channel. The magnitude of the jumps is determined by the unknown p^* in equation (8.10).

8.3 Flow discontinuity region

The discontinuity region spans all the leading edges in a small neighbourhood around $x = 0$. A similar leading edge region appears in the work by Bowles & Smith (2000b) and Jones & Smith (2003), as well as earlier in this thesis in Chapters 2, 5, 6 and 7.

8.3.1 Expansions and formulation

The y coordinate is $O(Re^{-1/2})$ as the normal extent of the region must span all the leading edges and $U = O(1)$ due to the oncoming flow to the region. As in Chapter 2, we let $x \rightarrow 0$ as flow approaches the leading edges and on examining the normal momentum equation, the inertial forces balance with the pressure gradient when $x = O(Re^{-1/2})$. Thus by continuity, $V = O(1)$ in this region and the expansions take the form

$$U = \bar{u}(X, Y) + \dots, \quad (8.11)$$

$$V = \bar{v}(X, Y) + \dots, \quad (8.12)$$

$$P = \bar{p}(X, Y) + \dots, \quad (8.13)$$

as seen previously. Here, we have defined the new x coordinate in the region, $X = O(1)$, where $x = Re^{-1/2}X$. Substitution into the Navier Stokes equations yields the inviscid Euler equations at leading order. We note that within the region, all blades appear as semi-infinite dividers within an infinite channel. As in Chapter 2, thin boundary-layers are created due to the no-slip conditions occurring on each blade surface for $X > 0$. These boundary-layers are of thickness $O(Re^{-3/4})$, much thinner than the normal

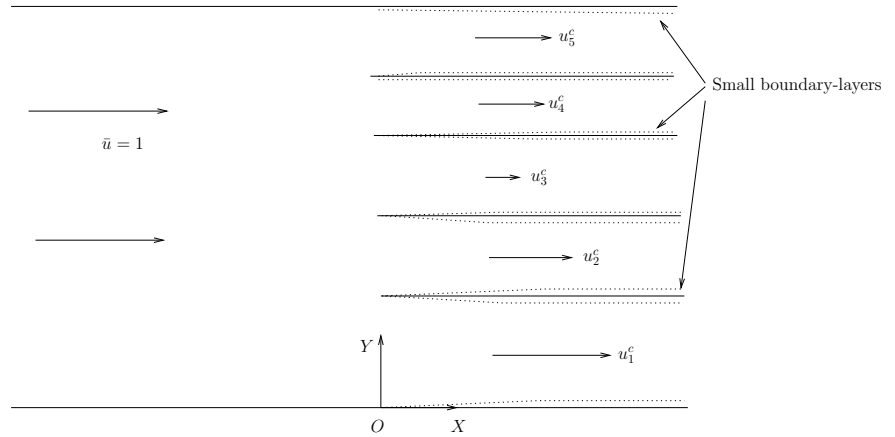


Figure 8.2: Illustration of $N = 4$ dividing blades in the discontinuity region. The flow speed jumps to u_m^c in the m^{th} channel and will be different in general for each.

scale of each daughter channel (of $O(Re^{-1/2})$) and further discussion of these boundary-layers is not given. Instead, we concern ourselves with the leading order inviscid problem past N blades.

The flow entering the leading edge region from upstream (as $X \rightarrow -\infty$) is given by the uniform flow $\bar{u} = 1, \bar{v} = 0, \bar{p} = 0$. Since the flow is inviscid to leading order, by Bernoulli's equation we have that on every streamline

$$\bar{p} + \frac{1}{2}(\bar{u}^2 + \bar{v}^2) = \frac{1}{2}, \quad (8.14)$$

throughout the region. The vorticity ω , in the region is given by

$$\omega = \frac{\partial \bar{v}}{\partial X} - \frac{\partial \bar{u}}{\partial Y}, \quad (8.15)$$

and since the approaching flow is uniform, upstream of the blades $\omega = 0$. The Cauchy-Lagrange theorem (Acheson (1990)) states that the vorticity retains the same value for all X in the region and hence $\omega = 0$ everywhere. Defining the streamfunction in the leading edge region as

$$\bar{u} = \frac{\partial \psi}{\partial Y}, \quad \bar{v} = -\frac{\partial \psi}{\partial X}, \quad (8.16)$$

and by substituting (8.16) into (8.15), the governing equation for the streamfunction is given by Laplace's equation

$$\nabla^2 \psi = 0. \quad (8.17)$$

The boundary conditions on each blade are given by $\psi = \psi_k = \text{constant}$, where ψ_k is a streamline representing the k^{th} blade surface for $X > 0$ ($0 \leq k \leq N + 1$). We define the two cases $k = 0$ and $k = N + 1$ to be the lower and upper walls of the mother channel respectively. The values of ψ_k are determined by downstream flux considerations within each daughter channel. Since the incoming flow is uniform, as $X \rightarrow \infty$ the velocities and pressure in the m^{th} daughter channel are given by

$$\bar{u}_m \rightarrow u_m^c, \quad \bar{v}_m \rightarrow 0, \quad \bar{p}_m \rightarrow p_m^c. \quad (8.18)$$

The values u_m^c and p_m^c are unknown constants at this stage, but may be fixed by $N + 1$ downstream flux constraints. As $X \rightarrow \infty$, Bernoulli's equation (8.14) says that the velocity and pressure jumps in the m^{th} daughter channel are related by

$$u_m^c = \sqrt{1 - 2p_m^c}. \quad (8.19)$$

Hence, the values of ψ_k are given by

$$\psi_k = \begin{cases} 0 & \text{for } k = 0, \forall X, \\ u_k^c(h_k - h_{k-1}) + \psi_{k-1} & \text{for } k = 1, \dots, N, X > 0, \\ H & \text{for } k = N + 1, \forall X. \end{cases} \quad (8.20)$$

To find the streamfunction ψ , we first write it in the form

$$\psi(X, Y) = Y + \Psi(X, Y), \quad (8.21)$$

and find the $O(1)$ disturbance streamfunction $\Psi(X, Y)$. By substitution, Ψ satisfies Laplace's equation and must be solved subject to

$$\Psi_k = \begin{cases} 0 & \text{for } k = 0, \forall x, \\ h_k(u_k^c - 1) - h_{k-1} + \psi_{k-1} & \text{for } k = 1, \dots, N, x > 0, \\ 0 & \text{for } k = N + 1, \forall x. \end{cases} \quad (8.22)$$

To find Ψ , we employ a conformal mapping technique. Let the Z -plane represent the leading edge region with $Z = X + iY$. We use the Schwarz-Christoffel technique (see Carrier *et al.* (1966)) to map the upper half χ -plane, with $\chi = \xi + i\zeta$, onto the leading edge geometry. The Schwarz-Christoffel transformation maps the upper half χ -plane onto a $T = 2N + 2$ sided polygon by

$$Z = f(\chi) = A^* \int \prod_{k=1}^T (\chi - \bar{\chi}_k)^{\frac{\theta_k}{\pi} - 1} d\chi + B^*, \quad (8.23)$$

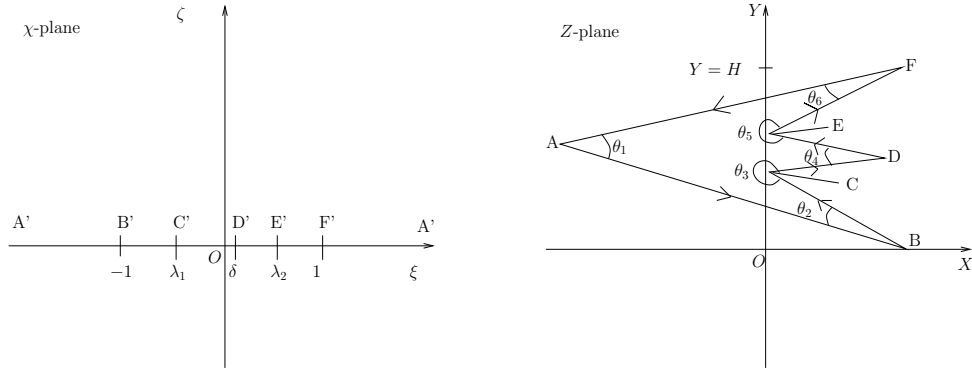


Figure 8.3: Conformal mapping of the χ -plane onto the Z -plane with $N = 2$. The labels A-F are the vertices of the polygon in the Z -plane with corresponding points A'-F' in the χ -plane. The positions λ_1, λ_2 and δ are the two leading edge points and one other downstream end points respectively, whose position in the χ -plane is unknown. The points B'-F' satisfy $-1 < \lambda_1 < \delta < \lambda_2 < 1$.

where A^* and B^* are complex constants. The values $\bar{\chi}_k$ are the positions of the vertices of the polygon in the χ -plane with θ_k the corresponding angle in the Z -plane.

8.3.2 Derivation for the case $N = 2$

As an illustration of the leading edge region solution, we find the Schwarz-Christoffel transformation for the case $N = 2$ explicitly. We first consider the leading edge geometry as a degenerate polygon (as in figure 8.3) and we take the limit

$$\theta_1, \theta_2, \theta_4, \theta_6 \rightarrow 0, \quad \theta_3, \theta_5 \rightarrow 2\pi, \quad (8.24)$$

to produce our desired leading edge geometry. We choose the upstream point A in the Z -plane to lie at $\xi = -\infty$ and furthermore, we take the downstream ends of the daughter channels $m = 1$ and $m = 3$ (points B and F) to lie at the points $(-1, 0)$ and $(1, 0)$ in the χ -plane respectively. On substitution into the transformation equation (8.23), finding partial fractions and then integrating, we have that

$$g(\chi) = B^* - A^*(a\text{Ln}(\chi + 1) + b\text{Ln}(\chi - \delta) + c\text{Ln}(\chi - 1)), \quad (8.25)$$

where Ln denotes the principal branch of the complex logarithm. The constants a, b, c are given by

$$a = \frac{(1 - \lambda_1)(\lambda_2 - 1)}{2(\delta - 1)}, \quad (8.26)$$

$$b = \frac{(\delta - \lambda_1)(\delta - \lambda_2)}{(\delta + 1)(\delta - 1)}, \quad (8.27)$$

$$c = \frac{(1 + \lambda_1)(1 + \lambda_2)}{2(\delta + 1)}. \quad (8.28)$$

We use the conditions that $f(\chi) \rightarrow \infty$ as $\chi \rightarrow -1$ and $g(\chi) \rightarrow \infty + iH$ as $\chi \rightarrow 1$ to determine values for A^* and B^* up to a real constant, B_R . The transformation then takes the form

$$g(\chi) = B_R + Hi - \frac{H}{\pi}(a\text{Ln}(\chi + 1) + b\text{Ln}(\chi - \delta) + c\text{Ln}(\chi - 1)). \quad (8.29)$$

The next task is to find the constants a, b, c . To do this, we evaluate $\Im(g)$ on each blade surface and map the intervals $(-1, \delta)$ and $(\delta, 1)$ in the χ -plane to $\Im(g) = h_1$ and $\Im(g) = h_2$ respectively. We first find that $c = (H - h_2)/H$ and then $b = (h_2 - h_1)/H$. The partial fractions in the original transformation give us that the sum $a + b + c = 1$, hence $a = h_1/H$. It is now convenient to define the channel width of the m^{th} daughter as

$$\bar{h}_m = h_m - h_{m-1}, \quad (8.30)$$

so that the conformal mapping is given by

$$g(\chi) = B_R + Hi - \frac{1}{\pi}(\bar{h}_1\text{Ln}(\chi + 1) + \bar{h}_2\text{Ln}(\chi - \delta) + \bar{h}_3\text{Ln}(\chi - 1)). \quad (8.31)$$

Finally, we must find the positions of λ_1, λ_2 and δ in the χ -plane. In the Z -plane, we require that the leading edges line-up exactly. We consider the quantity

$$|\chi + 1|^{\bar{h}_1} |\chi - \delta|^{\bar{h}_2} |\chi - 1|^{\bar{h}_3}, \quad (8.32)$$

which is the argument in the summation of the logarithms upon taking the real part of (8.31). The constant B_R is temporarily dropped. This constant will act as a horizontal shift of the leading edges within the Z -plane, so that the n^{th} leading edge has coordinates $(X, Y) = (0, h_n)$. Let

$$g_1(\lambda_1, \delta) = (\lambda_1 + 1)^{\bar{h}_1} (\delta - \lambda_1)^{\bar{h}_2} (1 - \lambda_1)^{\bar{h}_3}, \quad (8.33)$$

$$g_2(\lambda_2, \delta) = (\lambda_2 + 1)^{\bar{h}_1} (\lambda_2 - \delta)^{\bar{h}_2} (1 - \lambda_2)^{\bar{h}_3}, \quad (8.34)$$

be the X position in the Z -plane of each leading edge. By finding the maxima and minima of g_1 and g_2 , we will find the positions $\lambda_1(\delta)$ and $\lambda_2(\delta)$ which when mapped back to the Z -plane correspond to the position of each leading edge. We differentiate g_1 and g_2 with respect to λ_1 and λ_2 respectively and find that λ_1 and λ_2 are given by the solution of the quadratic equations

$$\bar{h}_1(\delta - \lambda_1)(1 - \lambda_1) - \bar{h}_2(\lambda_1 + 1)(1 - \lambda_1) - \bar{h}_3(\lambda_1 + 1)(\delta - \lambda_1) = 0, \quad (8.35)$$

$$\bar{h}_1(\lambda_2 - \delta)(1 - \lambda_2) + \bar{h}_2(\lambda_2 + 1)(1 - \lambda_2) - \bar{h}_3(\lambda_2 + 1)(\lambda_2 - \delta) = 0. \quad (8.36)$$

Once solved, we can substitute for λ_1 and λ_2 in (8.33) and (8.34), followed by subtracting (8.33) - (8.34) to reveal one equation to determine δ . Once δ is found, we can then determine λ_1 and λ_2 . The real constant B_R may be found by substituting either λ_1 or λ_2 into $\Re(g) = 0$. For example, if we choose to substitute for λ_1 , then

$$B_R = \frac{1}{\pi} \{ \bar{h}_1 \ln(\lambda_1 + 1) + \bar{h}_2 \ln(\delta - \lambda_1) + \bar{h}_3 \ln(1 - \lambda_1) \}. \quad (8.37)$$

For arbitrary values of \bar{h}_1 , \bar{h}_2 and \bar{h}_3 a numerical approach is needed to determine the value of δ . However, if all the channel widths are equal, an explicit solution for δ can be found.

8.3.3 The special case $\bar{h}_1 = \bar{h}_2 = \bar{h}_3 = \bar{h}$

In the special case of equal channel widths, we may take out a common factor \bar{h} from (8.31) and replace equations (8.33) and (8.34) by

$$g_1^*(\lambda_1, \delta) = (\lambda_1 + 1)(\delta - \lambda_1)(1 - \lambda_1), \quad (8.38)$$

$$g_2^*(\lambda_2, \delta) = (\lambda_2 + 1)(\lambda_2 - \delta)(1 - \lambda_2). \quad (8.39)$$

The equations for λ_1 and λ_2 are still given by (8.35) and (8.36), but with \bar{h}_m replaced by unity for all m . The solutions to these quadratic equations are given by

$$\lambda_1(\delta) = \frac{\delta}{3} \pm \sqrt{\frac{\delta^2 + 3}{3}}, \quad (8.40)$$

$$\lambda_2(\delta) = \frac{\delta}{3} \mp \sqrt{\frac{\delta^2 + 3}{3}}. \quad (8.41)$$

In either case, the choices for λ_1 and λ_2 are the same. We must take

$$\lambda_1(\delta) = \frac{\delta}{3} - \sqrt{\frac{\delta^2 + 3}{3}}, \quad (8.42)$$

$$\lambda_2(\delta) = \frac{\delta}{3} + \sqrt{\frac{\delta^2 + 3}{3}}, \quad (8.43)$$

to satisfy the ordering $\lambda_1 < \delta < \lambda_2$ in the χ -plane. To determine the value of δ , these equations are substituted into $g_1^* - g_2^* = 0$, which gives the equation

$$\frac{4}{3}\delta \left(\frac{\delta^2}{9} - 1 \right) = 0, \quad (8.44)$$

for δ . Hence, $\delta = 0, \pm 3$ of which only $\delta = 0$ is permissible. With $\delta = 0$, we have $\lambda_1 = -\sqrt{3}/3$, $\lambda_2 = \sqrt{3}/3$ and the conformal mapping from the upper half χ -plane to the leading edge geometry in the Z -plane is given by

$$g(\chi) = B_R + Hi - \frac{\bar{h}}{\pi} \{ \text{Ln}(\chi + 1) + \text{Ln}(\chi) + \text{Ln}(\chi - 1) \}, \quad (8.45)$$

for equal daughter channel widths. Substituting λ_2 into $\Re(g) = 0$, we find the constant B_R is given by

$$B_R = \frac{\bar{h}}{\pi} \left\{ \ln \left(\frac{\sqrt{3}}{3} + 1 \right) + \ln \left(\frac{\sqrt{3}}{3} \right) + \ln \left(1 - \frac{\sqrt{3}}{3} \right) \right\}. \quad (8.46)$$

8.3.4 Generalisation for N dividing blades

The method outlined above is extendable to the case of having N dividing flat blades using the Schwarz-Christoffel transformation. We choose the downstream ends of daughters $m = 1$ and $m = N + 1$ to lie at $\chi = -1$ and $\chi = 1$ in the χ -plane respectively. Thus, we have $N - 1$ unknown positions δ_j on the real χ -plane axis, representing the remaining $N - 1$ downstream ends of the daughter channels. Further, we will need to find the positions of the N leading edges λ_n . Applying the Schwarz-Christoffel mapping, finding the partial fractions in the integrand and then integrating, we find

$$g(\chi) = B^* - A^* \sum_{m=1}^{N+1} a_m \text{Ln}(\chi - \delta_m), \quad (8.47)$$

where A^* and B^* are constants to be determined and a_m are constant coefficients. The values of A^* and B^* are found in the same way as before, revealing very similar results. Next, the coefficients a_m may be determined

using the same recursive method as before, by first determining a_{N+1} then all subsequent a_m . The final co-efficient to be determined is a_1 and is found by the result

$$\sum_{m=1}^{N+1} a_m = 1, \quad (8.48)$$

arising from the calculation of the partial fractions in the Schwarz-Christoffel transformation. We find that

$$a_m = \frac{\bar{h}_m}{H}, \quad (8.49)$$

and hence the conformal mapping is given by

$$g(\chi) = B_R + Hi - \frac{1}{\pi} \sum_{m=1}^{N+1} \bar{h}_m \text{Ln}(\chi - \delta_m). \quad (8.50)$$

To find the values of δ_m we apply the condition that the leading edge positions, when mapped back to the Z -plane have the same real part, so they all line-up. We define N functions as the argument in the summation of the logarithms on taking the real part of (8.50), evaluated at each leading edge position λ_n as

$$g_n(\lambda_n, \delta_1, \dots, \delta_{N+1}) = \prod_{m=1}^n (\lambda_n - \delta_m)^{\bar{h}_m} \prod_{m=n+1}^{N+1} (\delta_m - \lambda_n)^{\bar{h}_m}, \quad (8.51)$$

and seek the maxima and minima of each g_n to find $\lambda_n = \lambda_n(\delta_1, \dots, \delta_{N+1})$. The maxima and minima of each g_n , are given by the roots of the polynomial

$$\sum_{k=1}^{N+1} \prod_{m=1, m \neq k}^{N+1} \bar{h}_k (\lambda_n - \delta_m), \quad (8.52)$$

and notice that by changing the value of n changes only λ_n . This means that we can choose any particular value of n and find the roots of this order N polynomial equation for a given set of δ_m values. By then substituting the n^{th} root λ_n into g_n , we determine $N - 1$ equations for the $N - 1$ unknowns $\delta_2, \dots, \delta_N$ by evaluating

$$g_n - g_{n-1} = 0, \quad \text{for } n = 2, \dots, N. \quad (8.53)$$

By solving all $N - 1$ equations above will give us the unknown values of δ_m and upon substitution of these values into (8.52) we may find the values of λ_n .

We adopt an iterative numerical approach to find the values of δ_m and λ_n . Firstly, the values of δ_m on the real χ -plane are guessed and with given channel widths \bar{h}_k , the roots of equation (8.52) are found using Newton's method for the corresponding values of λ_n . Next, a test is carried out to see if the leading edges of the blades line-up. We choose a reference blade, $n = 1$ say, and force all other leading edges to line up with the reference blade's leading edge by evaluating $|g_n - g_1|$ at λ_n for all n . If $|g_n - g_1| < 10^{-7}$ for all n , then the solution has converged and the values of λ_n and δ_m are found. If not, the values of δ_m are updated and we repeat the whole process above until convergence is achieved. Lastly, we substitute any chosen value of λ_n into $\Re(g) = 0$ to determine B_R .

8.3.5 The solution for Ψ

With a suitable conformal mapping found, we can find Ψ for general N . To recall, we must solve Laplace's equation for Ψ , subject to the boundary conditions (8.22). This gives us an $(N + 1)$ -valued Dirichlet problem for the streamfunction in the upper half plane. From the work of Mathews & Howell (2001), we can immediately write down the solution for Ψ in the upper half plane as

$$\Psi(\xi, \zeta) = \sum_{m=1}^{N+1} (\Psi_m - \Psi_{m-1}) \arctan\left(\frac{\zeta}{\xi - \delta_m}\right), \quad (8.54)$$

choosing $0 < \arctan\{\zeta/(\xi - \delta_j)\} < \pi$. With Ψ known for all values of ξ and ζ in the χ -plane, the solution is mapped back to a point in the leading edge geometry $Z = X + iY$ through the relations

$$X = B_R - \frac{1}{\pi} \sum_{m=1}^{N+1} \bar{h}_m \ln((\xi - \delta_m)^2 + \zeta^2)^{\frac{1}{2}} \quad (8.55)$$

$$Y = H - \frac{1}{\pi} \sum_{m=1}^{N+1} \bar{h}_m \arctan\left(\frac{\zeta}{\xi - \delta_m}\right), \quad (8.56)$$

and hence the total streamfunction is defined implicitly in the Z -plane as

$$\psi(X, Y) = Y + \sum_{m=1}^{N+1} (\Psi_m - \Psi_{m-1}) \arctan\left(\frac{\zeta}{\xi - \delta_m}\right). \quad (8.57)$$

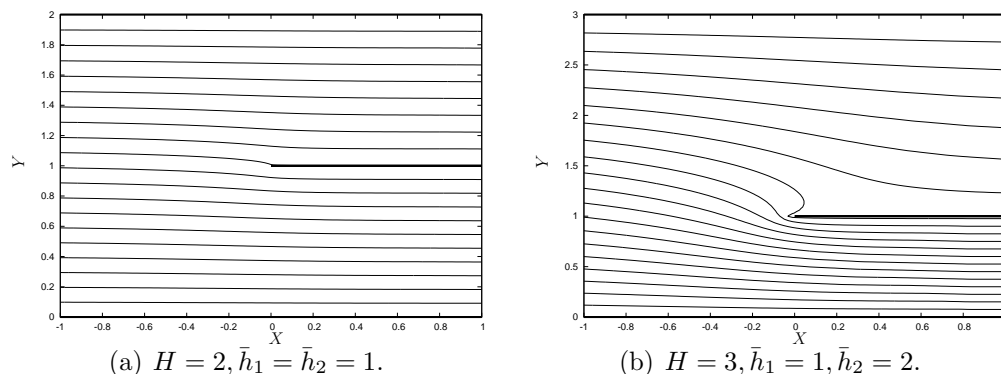


Figure 8.4: Two leading edge region solutions found for the case $N = 1$. In (a) we choose $\psi_1 = 1.1$ and (b) $\psi_1 = 2$.

8.4 Leading edge results

We now present some solutions to the leading edge problem, by choosing the downstream fluxes in each daughter channel. In the full problem, these fluxes (and hence the full flow solution) are determined by the Kutta condition. To enforce conservation of mass in the leading edge region, we choose downstream fluxes in each daughter channel, such that their sum is equal to H . We may vary the number of dividers N , the total channel width H , and the daughter channel widths \bar{h}_m .

8.4.1 The case $N = 1$

In Figure 8.4(a), we present a solution in which the main channel is split equally by one divider ($N = 1$), with near equal fluxes entering each channel. The downstream fluxes are deliberately chosen to show that when the fluxes are nearly equal, very little deflection of the streamlines occurs throughout the region. In Figure 8.4(b), the downstream flux in the bottom daughter channel 1 of width $\bar{h}_1 = 1$ is much greater than daughter channel 2, of width $\bar{h}_2 = 2$. We clearly see a much larger deflection of the incoming streamlines. In finding solutions to the $N = 1$ problem, no downstream ends need be found in the conformal mapping. We find the position of the leading edge in the χ -plane, λ , is given by

$$\lambda = -\frac{H - 2h_1}{H}, \quad (8.58)$$

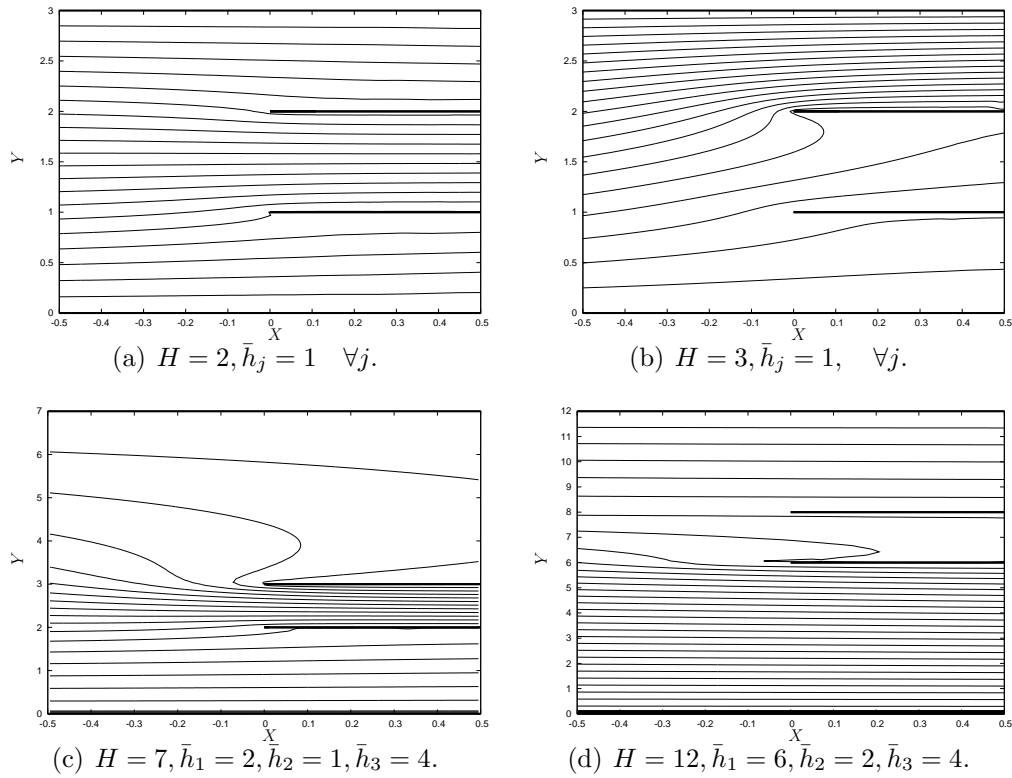


Figure 8.5: Leading edge region solutions found for the case $N = 2$. The chosen values of (ψ_1, ψ_2) are in (a) $(0.5, 2.2)$, (b) $(0.3, 0.6)$, (c) $(1, 4)$ and (d) $(8.1, 1)$.

so that, for example, in figures 8.4(a) and 8.4(b), $\lambda = 0$ and $\lambda = -1/3$ respectively.

8.4.2 The case $N = 2$

Figure 8.5 presents four leading edge solutions for various values of H and differing daughter channel widths \bar{h}_m . In figures 8.5(a) and 8.5(b), the channel widths are equal and the fluxes chosen to show similar behaviour of the streamlines as the previous subsection. Figure 8.5(b) has the greatest streamline deflection since 80% of the incoming flow is forced through the top channel. In figures 8.5(c) and 8.5(d), we choose different daughter channel widths and present solutions for two particular cases. In figure 8.5(c), we force $4/7^{\text{th}}$ s of the flow through one daughter channel whose width is only $1/7^{\text{th}}$ of the total pipe width. Flux constraints within the daughters cause some of the streamlines to reverse and enter a different channel in the leading edge region. In Figure 8.5(d) we restrict the flow that enters the

N	δ_m	λ_n
1	-	0
2	0	0.5774
3	0.4142	0.7654, 0
4	0.6180, 0	0.8507, 0.3249
5	0.7321, 0.2679	0.8966, 0.5176, 0
6	0.8019, 0.4450, 0	0.9241, 0.6395, 0.2282
7	0.8478, 0.5665, 0.1989	0.9420, 0.7210, 0.3902, 0
8	0.8794, 0.6527, 0.3473, 0	0.9542, 0.7779, 0.5077, 0.1763
9	0.9021, 0.7159, 0.4596, 0.1584	0.9629, 0.8191, 0.5951, 0.3129, 0

Table 8.1: The positive values (to 4 s.f.) of all downstream end positions δ_m and leading edge positions λ_n in the χ -plane for the case $\bar{h}_m = \bar{h}, \forall m$. The negative values of δ_m and λ_n are given by $-\delta_m$ and $-\lambda_n$ in each case.

second daughter. Most of the diverted flow inbound to the second daughter is deflected so that it passes through the first daughter. In figure 8.5(c), the trailing edge position is $\delta_2 = -0.3007$ and the leading edge positions are $\lambda_1 = -0.6334$ and $\lambda_1 = 0.08992$ and in figure 8.5(d), $\delta_2 = 0.1770$, $\lambda_1 = -0.2452$ and $\lambda_1 = 0.5594$ to four significant figures.

8.4.3 Cases of $N > 2$

For an arbitrary value of N , the first task is to find the positions of the N leading edges λ_n and $N - 1$ unknown downstream ends δ_m , in the upper half χ -plane. We tabulate the values found for equal daughter channel widths for $N \leq 9$ in table 8.1.

The leading edge flow for increasing N becomes more complicated for various downstream channel fluxes, but we observe behaviour of the streamlines similar to that in the previous subsections. Deflections of the incoming streamlines into a daughter channel (which allows more fluid to enter) are visible in figure 8.6.

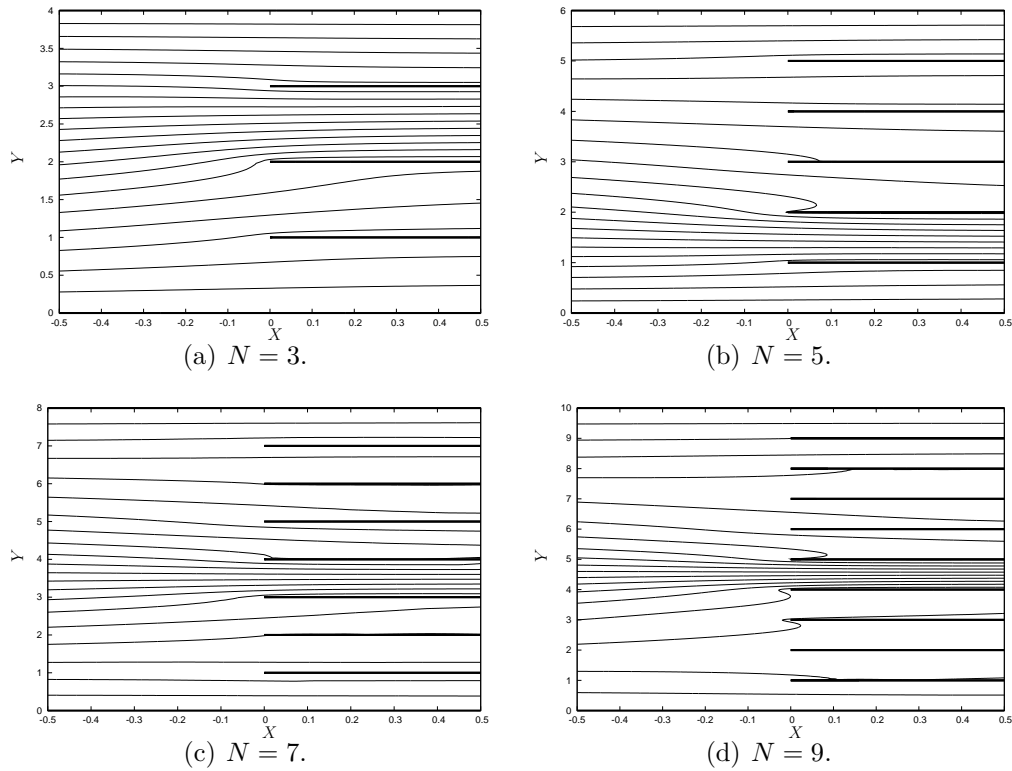


Figure 8.6: Leading edge region solutions found for cases of $N > 2$. In each case, the daughter channel widths are taken as $\bar{h}_j = 1$ and $H = N + 1$. The chosen values of (ψ_1, \dots, ψ_N) are, in (a) $(0.5, 1, 3)$, (b) $(1, 3.5, 4, 4.5, 5)$, (c) $(1, 1.5, 2, 5, 6, 6.5, 7)$ and (d) $(1, 1.2, 1.4, 1.6, 6.6, 7.4, 7.9, 8, 9)$.

8.5 Numerical Solution of the full problem

To find the solution of the full problem, we must solve the boundary-layer equations

$$u \frac{\partial u}{\partial x} + v \frac{\partial u}{\partial Y} = -\frac{dp}{dx} + \frac{\partial^2 u}{\partial Y^2}, \quad (8.59)$$

$$\frac{\partial u}{\partial x} + \frac{\partial v}{\partial Y} = 0, \quad (8.60)$$

subject to

$$u = 1, v = 0 \quad \text{on } Y = 0 \text{ and } Y = H, \forall x, \quad (8.61)$$

$$u = v = 0 \quad \text{on } Y = f_n(x), \quad n = 1, \dots, N, \quad 0 < x < l, \quad (8.62)$$

and the Kutta condition

$$p_m(l) = p^*, \quad (8.63)$$

where the unknown constant p^* is to be determined such that the total flux in all the channels is equal to H . We shall solve the equations in each channel

and wake using a finite-difference method, similar to the method used in Chapters 2-4, by solving the equations on a regularly spaced grid. To do this, a transformation is needed which maps a computational domain with flat channel walls to the real geometry of a daughter channel.

8.5.1 Transformation for each daughter channel

We choose a particular daughter channel, m , and define the functions $f = f_{m-1}, g = f_m$ to represent the lower and upper daughter channel walls, respectively. The computational domain has flat walls at $\zeta = 0$ and $\zeta = 1$ and coordinates (ξ, ζ) . If the velocity and pressure components $u = u_m(x, Y), v = v_m(x, Y)$ and $p = p_m(x)$ in the daughter channel, then we require $x = x(\xi, \zeta)$ and $y = y(\xi, \zeta)$ to map the flow solution back from our computational domain to the real daughter channel geometry.

To find the transformed boundary-layer equations to be solved in the computational domain, we need to evaluate the x and Y partial derivatives. A suitable map from the computational space to the actual daughter channel geometry is

$$x = \xi, \quad (8.64)$$

$$Y = (g(\xi) - f(\xi))\zeta + f(\xi). \quad (8.65)$$

Firstly, the derivative with respect to ζ in computational space is given by

$$\frac{\partial}{\partial \zeta} = \frac{\partial}{\partial x} \frac{\partial x}{\partial \zeta} + \frac{\partial}{\partial Y} \frac{\partial Y}{\partial \zeta}. \quad (8.66)$$

We can easily find all the partial derivatives

$$\frac{\partial x}{\partial \zeta} = 0, \quad \frac{\partial x}{\partial \xi} = 1, \quad (8.67)$$

$$\frac{\partial Y}{\partial \zeta} = g(\xi) - f(\xi) \quad \frac{\partial Y}{\partial \xi} = (g'(\xi) - f'(\xi))\zeta + f'(\xi), \quad (8.68)$$

so that by substitution and rearrangement, we have

$$\frac{\partial}{\partial Y} = \frac{1}{g(\xi) - f(\xi)} \frac{\partial}{\partial \zeta}. \quad (8.69)$$

To find the second derivative with respect to Y , (8.66) is differentiated with respect to ζ , and in a very similar way, we find

$$\frac{\partial^2}{\partial Y^2} = \frac{1}{(g(\xi) - f(\xi))^2} \frac{\partial^2}{\partial \zeta^2}. \quad (8.70)$$

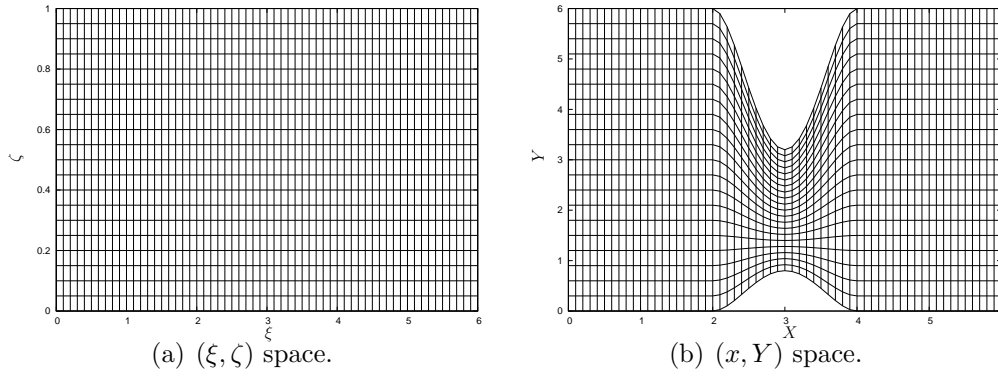


Figure 8.7: Illustration of mapping a regularly spaced grid from (a) the computational space to (b) the actual daughter channel geometry. Here, $g(x) = f(x) = 0$ except for $|x| \leq 1$, where $g(x) = 6 - 2.8(1 - x^2)^2$ and $f(x) = 0.8(1 - x^2)^2$.

We next consider the derivative with respect to ξ

$$\frac{\partial}{\partial \xi} = \frac{\partial}{\partial x} \frac{\partial x}{\partial \xi} + \frac{\partial}{\partial Y} \frac{\partial Y}{\partial \xi}, \quad (8.71)$$

and substituting for the derivatives of x_ξ and y_ξ from above

$$\frac{\partial}{\partial \xi} = \frac{\partial}{\partial x} + \frac{(g'(\xi) - f'(\xi))\zeta + f'(\xi)}{g(\xi) - f(\xi)} \frac{\partial}{\partial Y}. \quad (8.72)$$

We then substitute equation (8.66) for the Y derivative, and rearranging, we find

$$\frac{\partial}{\partial x} = \frac{\partial}{\partial \xi} - \frac{(g'(\xi) - f'(\xi))\zeta + f'(\xi)}{g(\xi) - f(\xi)} \frac{\partial}{\partial \zeta}. \quad (8.73)$$

Using the transforms of the derivatives above, in computational space the momentum equation is given by

$$u \left(\frac{\partial u}{\partial \xi} - \frac{(g'(\xi) - f'(\xi))\zeta + f'(\xi)}{g(\xi) - f(\xi)} \frac{\partial u}{\partial \zeta} \right) + \frac{1}{g(\xi) - f(\xi)} v \frac{\partial u}{\partial \zeta} = \quad (8.74)$$

$$- \frac{dp}{d\xi} + \frac{1}{(g(\xi) - f(\xi))^2} \frac{\partial^2 u}{\partial \zeta^2},$$

whilst the continuity equation is given by

$$(g(\xi) - f(\xi)) \frac{\partial u}{\partial \xi} - \{(g'(\xi) - f'(\xi))\zeta + f'(\xi)\} \frac{\partial u}{\partial \zeta} + \frac{\partial v}{\partial \zeta} = 0. \quad (8.75)$$

The boundary conditions to be solved in each channel are given by

$$u = v = 0 \quad \text{on } \zeta = 0 \text{ and } \zeta = 1, \quad (8.76)$$

except in channels 1 and $N + 1$, where we have $u = 1$ on $\zeta = 0$ and $u = 1$ on $\zeta = 1$ respectively. The starting condition in the m^{th} channel is still given by

$$u = u_m^c, \quad v = v_m^c, \quad p = p_m^c, \quad (8.77)$$

which is to be found as part of the solution. Later, we will need to find the flux in each daughter channel. In computational space, this may be evaluated at any position $\xi = \text{constant}$ through the relation

$$q = (g(\xi) - f(\xi)) \int_0^1 u(\xi, \zeta) d\zeta. \quad (8.78)$$

The boundary-layer equations do not need to be transformed within the wake, since there are flat bounding walls at $Y = 0$ and $Y = H$. We will discuss how to join the two regions later.

8.5.2 Discretisation in the daughters

The computational grid has spacings $\Delta\xi$ and $\Delta\zeta$ in the ξ and ζ directions respectively, so that the $i^{\text{th}}, j^{\text{th}}$ grid point $(\xi_i, \zeta_j) = (i\Delta\xi, j\Delta\zeta)$. Within the daughter channels, we use three-point backward differences in ξ and centred differences for all ζ derivatives. In discretised form, the momentum equation (8.74) becomes

$$\begin{aligned} w_{i-1}^j \left(\frac{3w_i^j - 4w_{i-1}^j + w_{i-2}^j}{2\Delta\xi} - K(\xi_i, \zeta_j) \frac{u_i^{j+1} - u_i^{j-1}}{2\Delta\zeta} \right) + L(\xi_i) v_{i-1}^j \frac{u_i^{j+1} - u_i^{j-1}}{2\Delta\zeta} \\ = \frac{3p_i - 4p_{i-1} + p_{i-2}}{2\Delta\xi} + L^2(\xi_i) \frac{u_i^{j+1} - 2u_i^j + u_i^{j-1}}{(\Delta\zeta)^2}, \end{aligned} \quad (8.79)$$

where the functions K and L are defined as

$$K(\xi_i, \zeta_j) = \frac{(g'(\xi_i) - f'(\xi_i))\zeta_j + f'(\xi_i)}{g(\xi_i) - f(\xi_i)}, \quad L(\xi_i) = \frac{1}{g(\xi_i) - f(\xi_i)}. \quad (8.80)$$

The discretised continuity equation is

$$\frac{1}{L(\xi_i)} \left(\frac{3w_i^j - 4w_{i-1}^j + w_{i-2}^j}{2\Delta\xi} \right) - \frac{K(\xi_i, \zeta_j)}{L(\xi_i)} \frac{u_i^{j+1} - u_i^{j-1}}{2\Delta\zeta} + \frac{v_i^{j+1} - v_i^{j-1}}{2\Delta\zeta} = 0. \quad (8.81)$$

These equations are second order accurate in both ξ and ζ and are used to find the solution at (ξ_i, ζ_j) in each daughter channel. For a particular ξ_i , the

solution for the flow between the wall and the blade is found in a similar way to Chapter 2. For a given value of p_i , equation (8.79) is rearranged into a tridiagonal system for u followed by solution using a Thomas algorithm. The normal velocity v is obtained afterwards using (8.81). The unknown value of p_i is determined by forcing the the computed values of v across the centre of the channel to be equal to within a tolerance $\epsilon_1 = 10^{-10}$. The value for p_i is updated at each x_i using a secant method until the tolerance is met. Typically, only four or five iterations of the value of p_i were needed. This procedure is used for all ξ_i in each daughter channel, except at ξ_1 . Here, the ξ derivatives, apperaring in the discretised equations (8.79) and (8.81), must be adapted to be able to solve the equations at ξ_1 . At this point only, we use first-order backward differences in ξ , followed by employing the double-stepping method of Smith & Timoshin (1996b) to ensure second order accuracy. At $\xi_0 = 0$, the starting condition in the m^{th} daughter channel is given by

$$u_0^j = u_m^c, \quad v_0^j = 0, \quad p_0 = p_m^c, \quad (8.82)$$

which arises upon matching with the leading edge region.

8.5.3 Discretisation in the wake

In the wake, the grid coordinates are given by $x_i = i\Delta x, Y_j = j\Delta Y$ and discretisation of the boundary-layer equations in the wake is achieved using the same backward differences in x and centred differences in Y as the previous subsection. The discretised momentum and continuity equations are given by (8.79) and (8.81) with $L = 1, K = 0$ and (ξ, ζ) replaced by (x, Y) respectively. The solution at a particular x_i is achieved in the same way as used in each daughter channel. The only adaptation is that the tridiagonal system for u_i^j is solved with the boundary conditions $u = 1$ on both the upper and lower channel walls.

To gain the wake starting condition, we map the emergent velocities from each daughter channel back into (x, Y) space, using cubic splines to interpolate the velocity profiles. The wake starting pressure is given by p^* . This gives the velocities and pressure at the point $x = x_0$ in the wake. We also have to

apply the double-stepping method, mentioned above, at the point $x = x_1$ in the wake to resolve the discontinuous nature of the pressure gradient as the flow exits the daughters into the wake.

8.5.4 Solution algorithm

With the solution method in each daughter channel and within the wake now described, we outline the full, iterative solution procedure.

We find the solution within the daughter channels first. Firstly, we guess a value for the unknown pressure p^* , at the trailing edge. Then, we make $N + 1$ extra guesses for the starting pressures p_m^c in each daughter channel. We can then construct the starting condition in each channel, by using the Bernoulli equation

$$u_m^c = \sqrt{1 - 2p_m^c}, \quad (8.83)$$

to find the u_m^c values. We solve each channel independently, by employing a streamwise sweep from $\xi = 0$ to $\xi = l$, finding the solution for u, v and p at each ξ by the method outlined above. When the sweep reaches $\xi = l$ in the m^{th} channel, we test to see if $p_m(l) = p^*$. If not, the pressure p_m^c and hence u_m^c are updated for this channel, using the secant method, followed by resweeping until the absolute error

$$|p_m(l) - p^*| < \epsilon_2 = 10^{-10}, \quad (8.84)$$

is satisfied. The number of iterations needed for the tolerance ϵ_2 to be met was typically eight to ten. The same procedure is repeated for all channels. Then, the flux q^* at $\xi = l$ is found using Simpson's rule on equation (8.78) and the final test

$$|q^* - H| < \epsilon_3 = 10^{-10}, \quad (8.85)$$

is carried out to ensure conservation of mass from far upstream of the blades, over the leading edge discontinuity and through all the channels. If this tolerance is not met, then the value for p^* is updated, again by the secant method, followed by repeating the whole procedure above. In all cases, no more than ten iterations were needed to determine p^* . Once all of these conditions are satisfied, the wake starting condition is constructed, followed by a sweep through the wake.

There are two possible approaches in determining the starting conditions for the daughter channels. Here, we have chosen to find the pressure jumps p_m^c iteratively so that the Kutta trailing edge condition is satisfied. Once the pressure jumps are known, the details within the leading edge region can be found retrospectively. The other method assumes values for the downstream fluxes in the daughter channels, followed by solution of the leading edge problem to obtain starting conditions for the daughter channel sweeps. Either way gives identical results.

To gain numerical accuracy in u , v and p , values of $\Delta x = \Delta Y = \Delta \xi = \Delta \zeta = 0.001$ were found to be required. To test for accuracy, the same numerical code was run for several test cases on much finer grid resolutions of $\Delta x = \Delta Y = \Delta \xi = \Delta \zeta = 0.0005$ and $\Delta x = \Delta Y = \Delta \xi = \Delta \zeta = 0.0001$. The results were identical to six significant figures.

8.6 Results

We present streamfunction and pressure solutions of the full viscous problem in the daughter channels and wake for cases of $N = 1, 2, 9$ and different blade shapes. For the case of $N = 1$ we describe features of the flow in all the daughters and through the leading edge region. For $N = 2$, we concentrate on flows through various geometries, the Kutta condition and the leading edge jumps. Finally, for $N = 9$ we look at the development and interactions of several in-parallel wakes. In all our results, we choose the trailing edge position of all the blades to be $x = 1$.

8.6.1 The case $N = 1$

We begin by presenting results for the case $N = 1$. In figure 8.8 we present streamfunctions for two symmetric configurations of the dividing blade. In each case, the streamlines undergo a rapid adjustment just after the leading edge as the flow caters for the no-slip condition on the blade surface. In figure 8.8(a), we see the streamlines become horizontal for $x > 0.1$ in each channel up to the trailing edge, indicating that $u = u(Y)$. The form of $u(Y)$ depends on the pressure gradient alone. After the trailing edge is passed, as

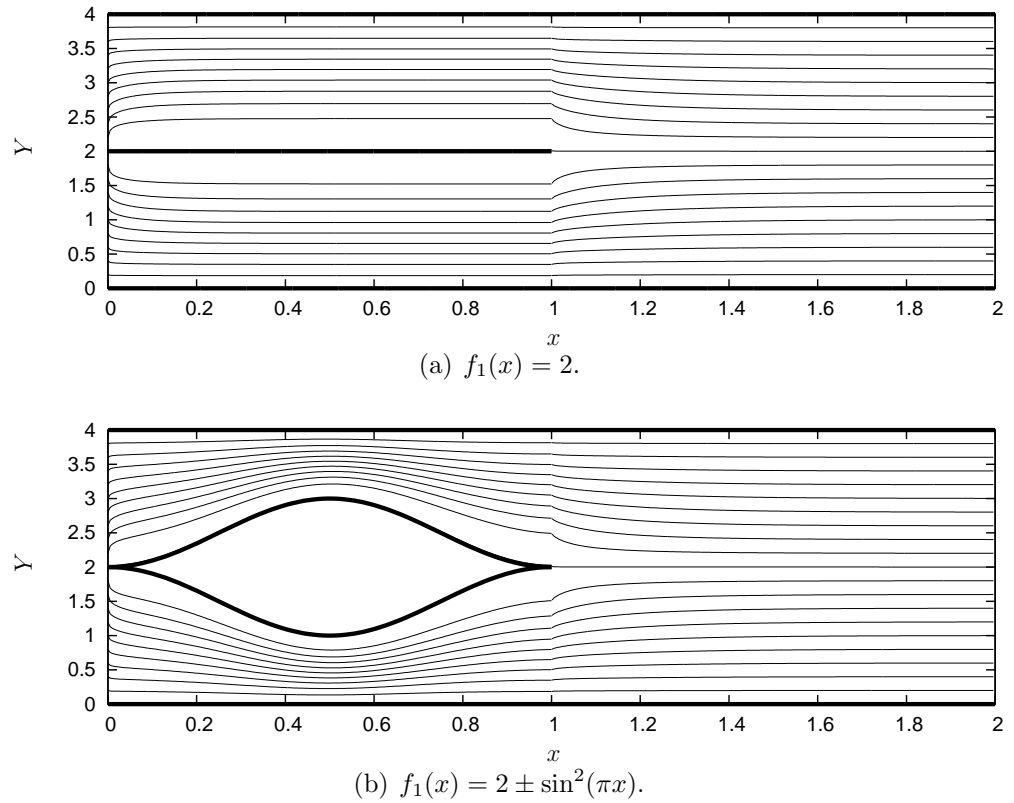


Figure 8.8: Streamfunction solutions for two symmetric configurations. The total channel width $H = 4$.

$x \rightarrow 2$, we again see $\psi_x \rightarrow 0$. This indicates that the flow is accelerating back towards a uniform profile.

The corresponding pressure solutions for each configuration are illustrated in figure 8.9. Due to the symmetry of these problems, the pressures in daughters one and two are identical. In figure 8.9(a), there is a rapid pressure variation just after the leading edge region at $x = 0$, caused by the adjustments of the flow to cater for the no-slip conditions on the daughter channel walls. Away from $x = 0$, the pressure gradient is constant to the trailing edge. There is a discontinuity in the pressure gradient at $x = 1$. As the flow enters the wake, the pressure gradient becomes large, but as $x \rightarrow 2$, $dp/dx \rightarrow 0$. In figure 8.9(b), the pressure profile shows an increasingly favourable pressure gradient within each channel, as the flow passes over the dividing blade. The flow on the leeward sides of the blade relaxes and causes a slightly adverse pressure gradient close to the trailing edge. After only a short distance in the wake, the pressure gradient approaches zero.

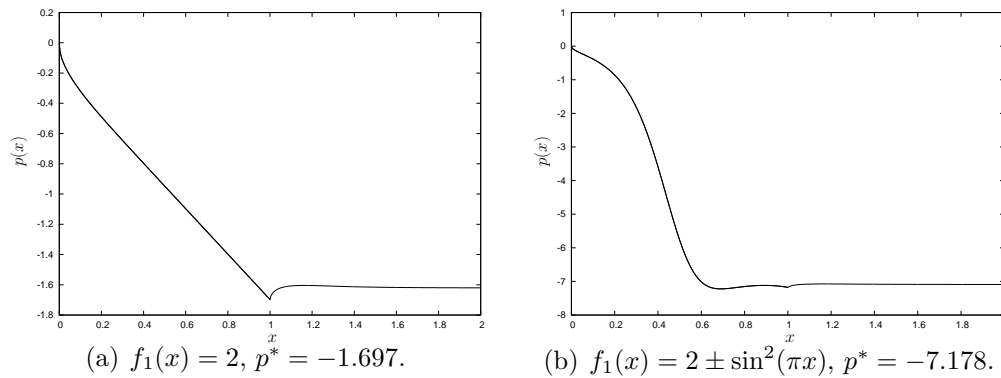


Figure 8.9: Corresponding pressure solutions for the streamfunction solutions plotted in (a) figure 8.8(a) and (b) figure 8.8(b). In each figure, the value of p^* , the pressure at the trailing edge is given to four significant figures.

A final point to note is the values of p^* at the trailing edges in each problem, the values of which are given in figures 8.9(a) and (b) to four significant figures. The symmetry of the problem and the fixed channel width forces the pressure jumps to be equal and zero at the leading edges, since the daughter channel geometries are identical and the oncoming flow is uniform. The presence of zero pressure jumps means that in the leading edge region, the streamfunction $\Psi = 0$.

In figures 8.10 and 8.11, we add non-symmetry to the blades and plot the streamfunctions in the leading edge region and for the full problem. In figure 8.10(a), the flat blade is moved to a position $Y = 1$ within the main channel. In this case, much more flow passes into the second daughter and is reflected within the plotted streamlines in the leading edge region. In figure 8.10(b), the blade has a flat bottom surface ($f_1^-(x) = 2$) with a curved top ($f_1^+(x) = 2 + 4x(x - 1)$). In this case, daughter two constricts over the first half of the channel and dilates for the second half. The maximum constriction of the channel is at $x = 0.5$, where the channel narrows to a width of unity. The streamlines within this figure show that more fluid passes into and consequently has a higher velocity through the first channel. The discontinuity in the pressure gradient at $x = 1$ causes a rapid change in the streamlines close to $x = 1$ before a slower return towards a uniform state as $x \rightarrow 2$. In figure 8.11(b), there is a large constriction in daughter 1

(or a large dilation in daughter two) towards the trailing edge. As a result, little flow enters the first daughter channel. After the solutions to these two configurations were found, we solved the full leading edge problem to establish what influence the non-symmetric blade shapes have on the flow in the leading edge region. The leading edge streamline plots agree well with the reported behaviour in the full problem, with less fluid entering the smaller channel in figure 8.11(a) and the constricted channel in 8.11(b). We then repeated the above procedure for two further cases of asymmetry in figure 8.11, to include constrictions of the main channel. Similar behaviour is seen as above, there is a rapid change in the streamlines just after the trailing edge and less fluid enters the constricted daughter channels in each case.

Pressure solutions for the configurations in figures 8.10 and 8.11 are given in figure 8.12. The shape of the pressure profiles share some similarities with the symmetric cases above. We notice that now the pressure jumps to non-zero values at $x = 0$ in each channel. For about 75% of channel one in figure 8.12(d), the pressure is adverse, but as the flow nears the trailing edge, the pressure gradient strengthens and becomes increasingly favourable. Above the blade, the flow relaxes and an adverse gradient arises over the final 40% of the blade.

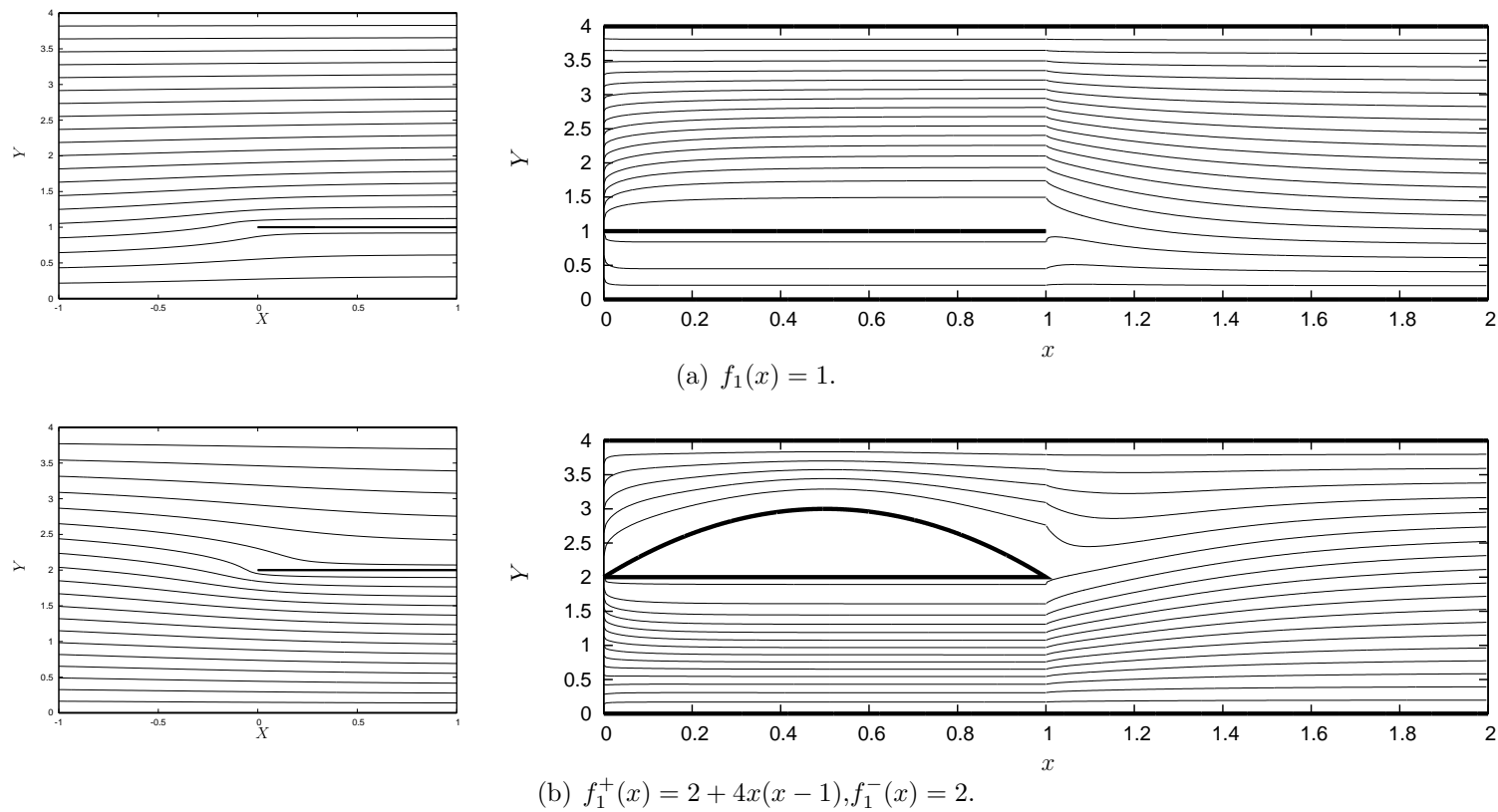


Figure 8.10: Leading edge and full problem streamfunction solutions for two non-symmetric configurations. The total channel width $H = 4$.

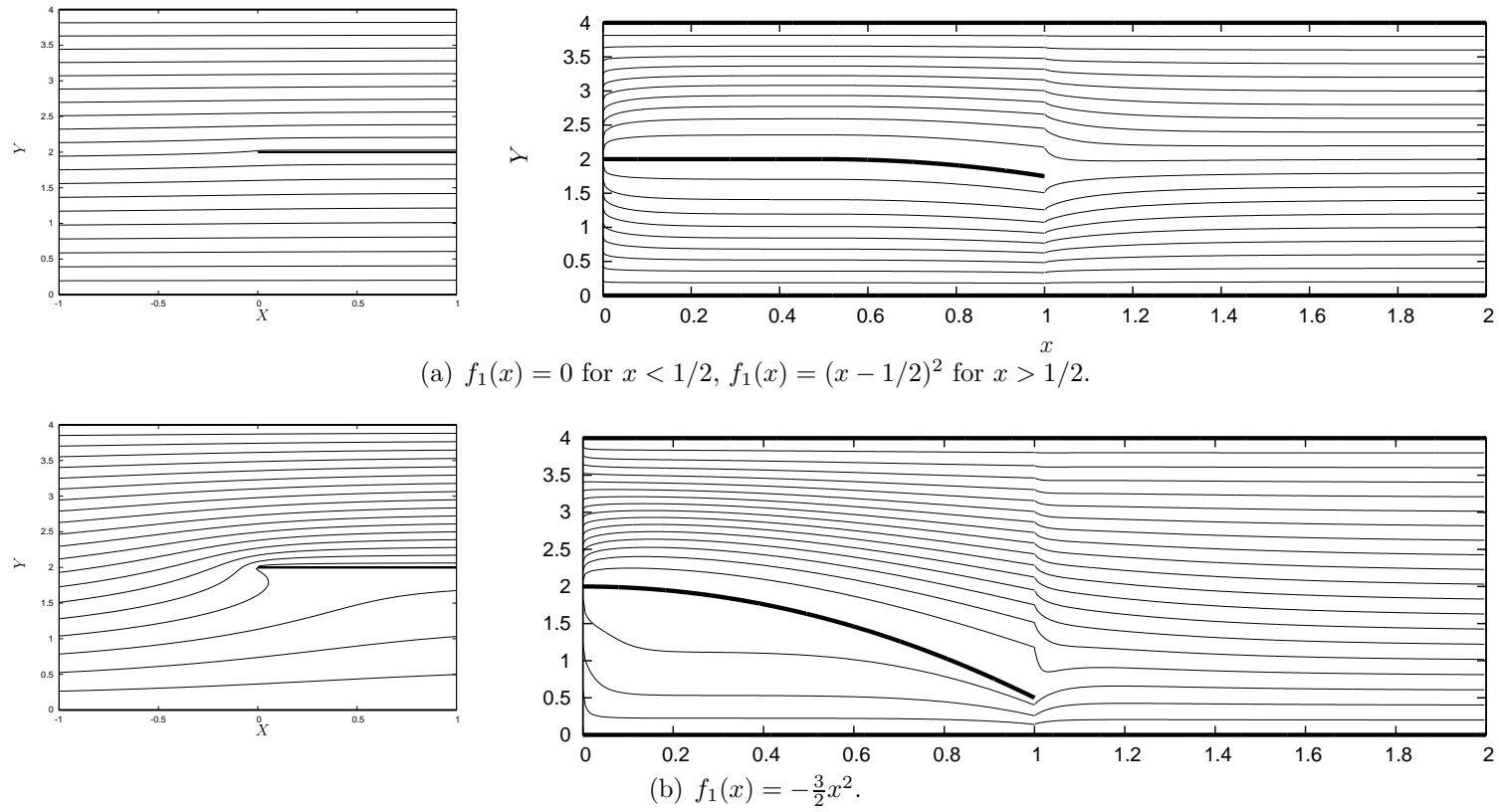


Figure 8.11: Leading edge and full problem streamfunction solutions for two cases of asymmetric blades. The total channel width $H = 4$.

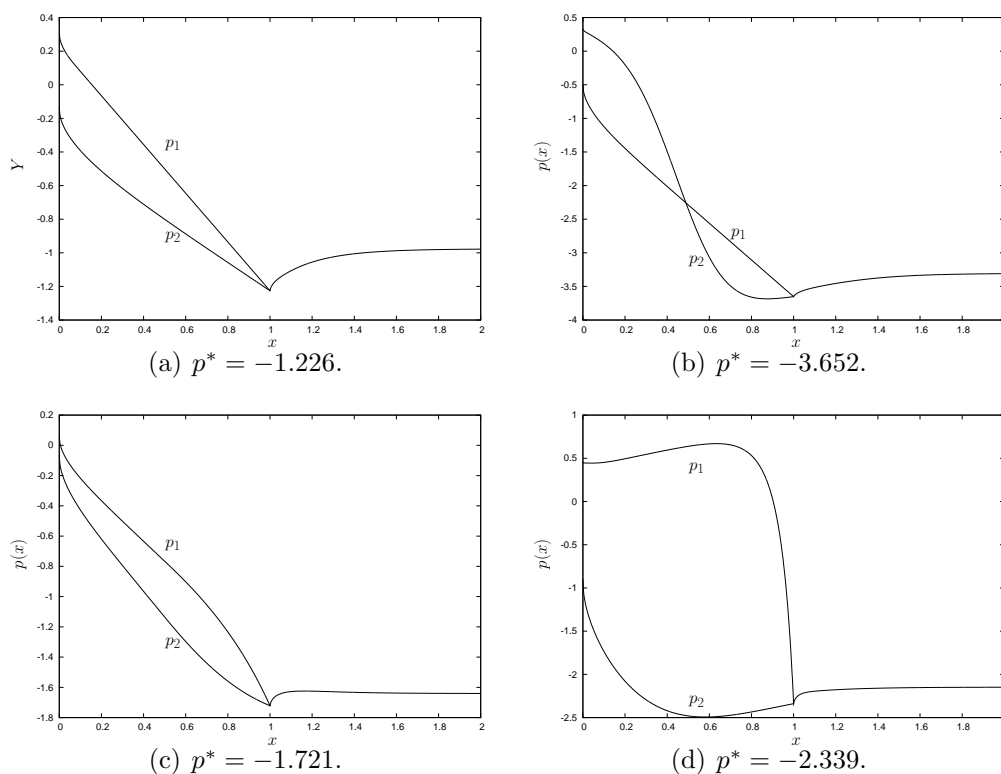


Figure 8.12: Corresponding pressure solutions for the streamfunction solutions plotted in (a) figure 8.10(a), (b) figure 8.10(b), (c) figure 8.11(a) and (d) figure 8.11(b). In each figure, the value of p^* is given to four significant figures.

8.6.2 The case $N = 2$

In this section, we introduce another dividing blade into the main channel to create three daughter channels. In figures 8.13(a)-(c), three streamfunction solutions are shown with different channel widths in the central daughter, with all dividers being flat blades. Behaviour similar to the previous cases is seen in the streamline plots. When the width of the central daughter channel is large (figure 8.13(b)), more fluid enters this channel and it flows at higher speed than in the smaller daughters one and three. When the width of the central daughter is small (figure 8.13(c)), very little flow enters this channel.

In figure 8.14, we plot the pressure for each of the solutions in figure 8.13. In figure 8.14(a), three pressure profiles are plotted, but we find that $p_1 = p_3$. This is because the channel geometries of daughters one and three

are identical. The pressure p_2 is not equal to p_1 or p_3 due to different no-slip conditions within the central channel. This theme follows through all the figures 8.14(a)-(c). We note in figure 8.14(c), that within the wake, the pressure gradient requires a longer distance in x to settle down to a constant. Since most of the flow diverts into channels one and three upstream, very little flow emerges into the wake from daughter two at $x = 1$. To accelerate the flow back towards $\bar{u} = 1$, an adverse pressure gradient is needed over a longer distance in the wake.

In figure 8.15(a), the dividing blades cause a large constriction in the central daughter at the trailing edge. We see very few streamlines within daughter channel two in this case showing that very little fluid has entered this channel upstream. We find that $p_2(0^+) = 0.4980$ in 8.17(a) and calculate that approximately 2% of the approaching flow passes through this central channel. When the central channel dilates, as seen in 8.17(b), this situation is reversed, with less fluid entering the daughters one and three. The streamfunction plotted in 8.17(c) is a non-symmetric case. Channel one constricts, channel three dilates and channel two has a constant width. Similar behaviour is seen in the constricting and dilating channels as described above.

The leading order solution in the leading edge region for the cases in figure 8.15 are given in figure 8.16. For the constricting case of blades in figure 8.16(a), very little flow enters the central channel due to the pressure jump in that channel being close to 0.5. A slight deflection of the streamlines into the central channel is seen in figure 8.16(b), due to the dilating geometry of that channel downstream. In figure 8.16(c), there is a slight deflection of the streamlines towards the top channel, again due to the dilating nature of that channel downstream.

Pressure solutions for the daughter channel geometries in figure 8.15a are plotted in figure 8.17. In figure 8.17(a), the flow within the central daughter experiences a favourable pressure gradient for 80% of the channel length. The pressure gradient strengthens rapidly over the remaining 20% as the flow approaches the trailing edge. The pressure in channels one and three also has a favourable pressure gradient, the strength of which weakens as $x \rightarrow 1$.

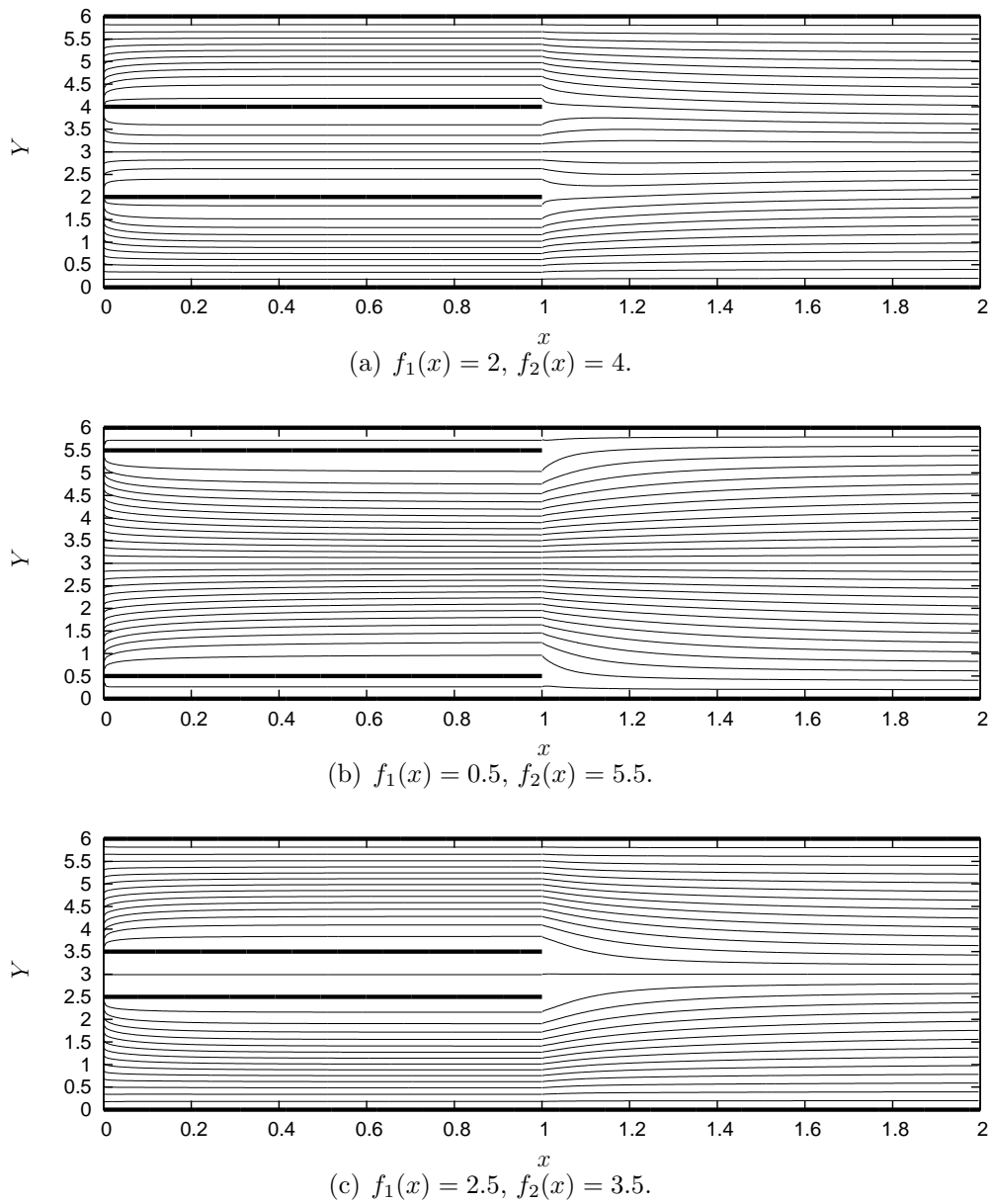


Figure 8.13: Streamfunction solutions for three symmetric configurations of $N = 2$ blades. The total channel width $H = 6$. Streamlines are plotted in increments of 0.2.

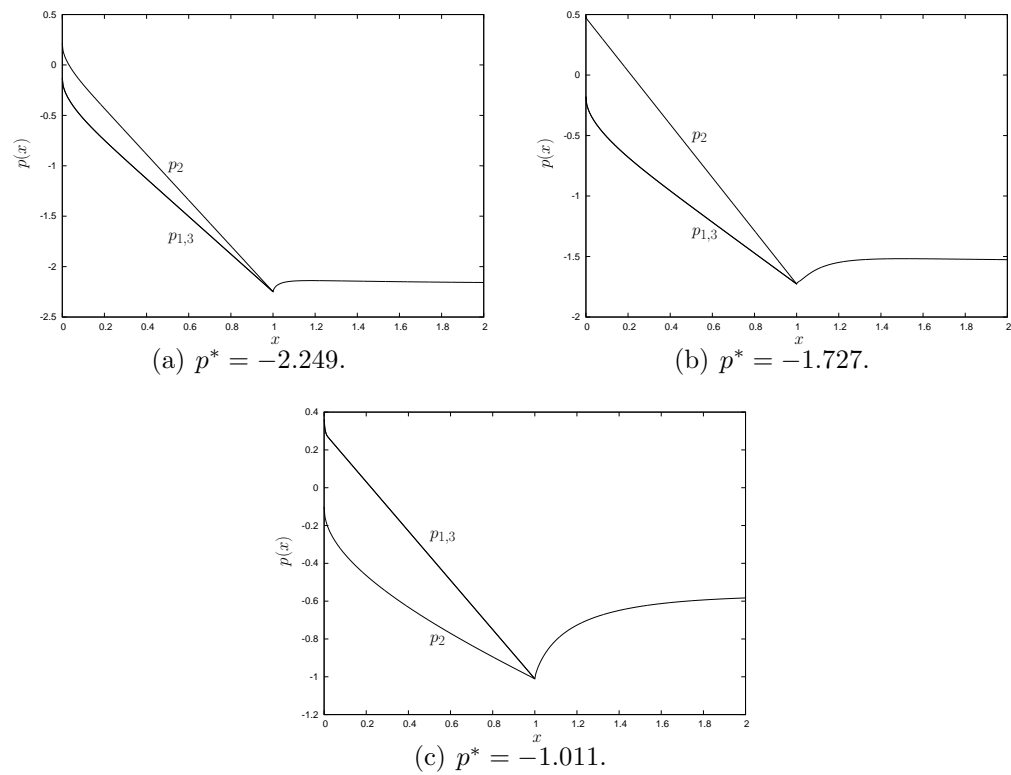


Figure 8.14: Corresponding pressure solutions for the streamfunction solutions plotted in (a) figure 8.13(a), (b) figure 8.13(b) and (c) figure 8.13(c). In each figure, the value of p^* is given to four significant figures.

This feature is reversed for a dilating central channel in figure 8.17(b), so that a strengthening favourable pressure gradient occurs in channels one and three. In the final figure, 8.17(c), we observe a strong pressure gradient in the constricting channel one and a weakening pressure gradient in the dilating channel three. However, we note that the pressure profile in channel two is similar to those seen in the cases of flat dividing blades. This is because the channel width does not vary throughout, and the blades merely guide the flow direction in this case.

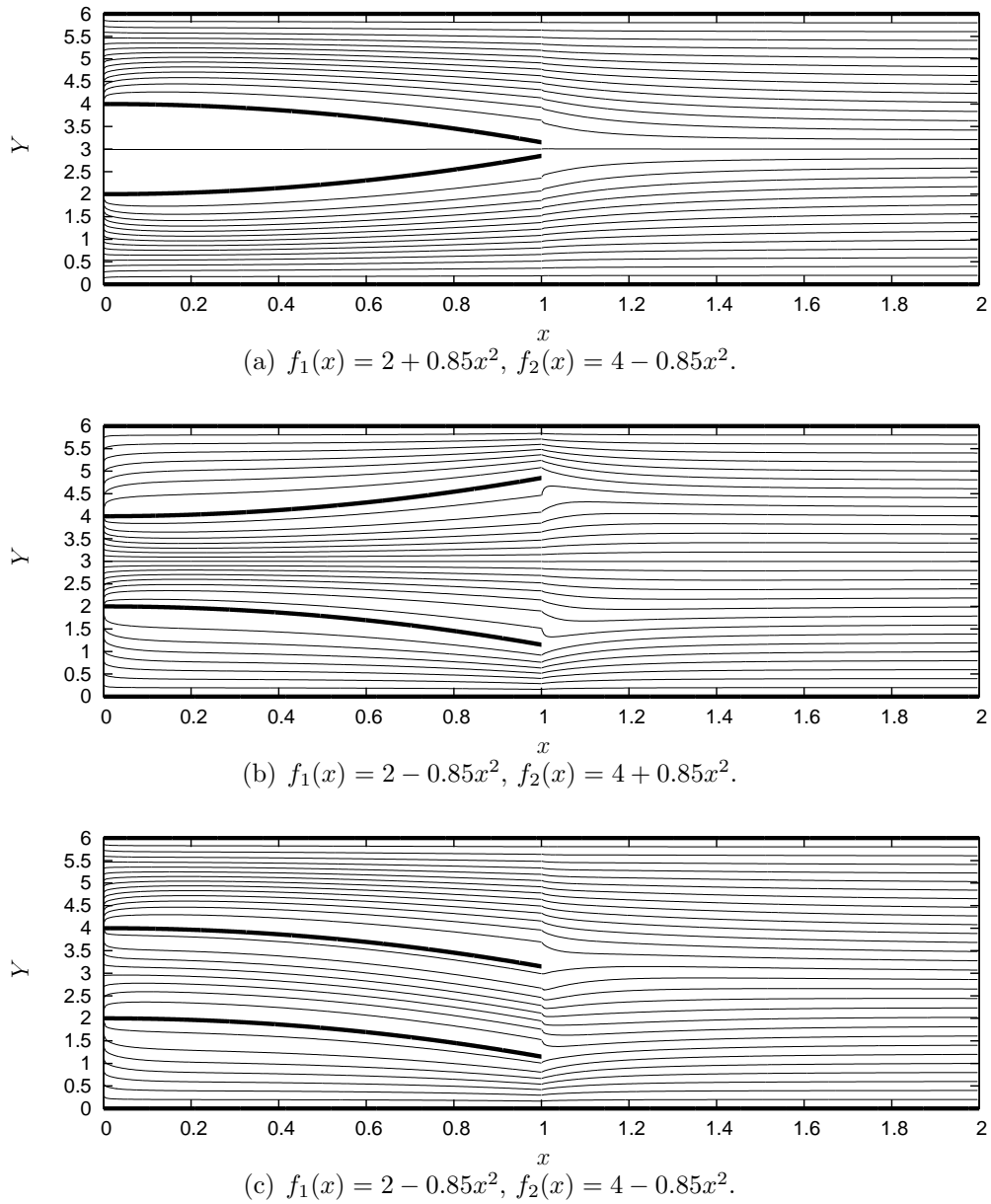
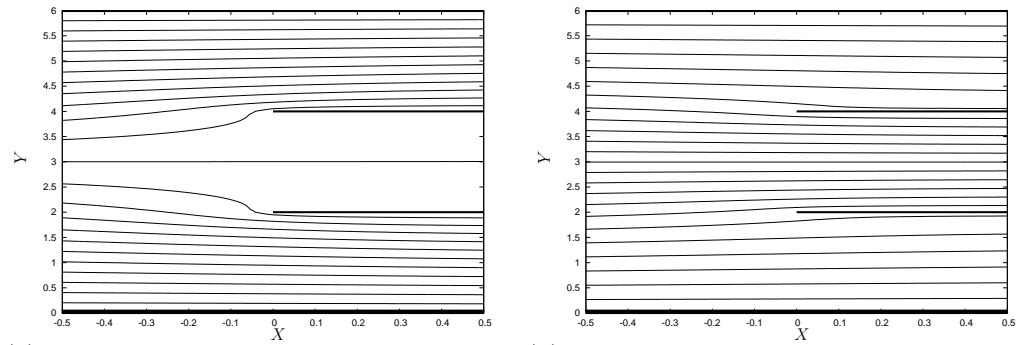
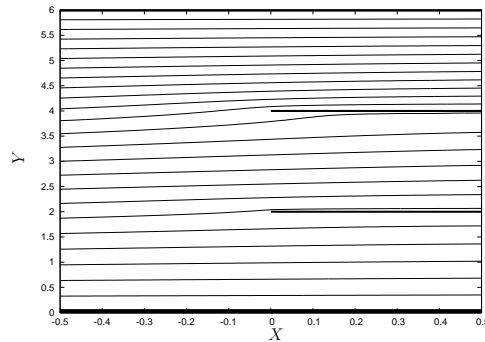


Figure 8.15: Streamfunction solutions for three other configurations of $N = 2$ blades. The total channel width is chosen as $H = 6$. Streamlines are plotted in equal increments of 0.2



(a) Leading edge solution for figure 8.15a. (b) Leading edge solution for figure 8.15b.



(c) Leading edge solution for figure 8.15c.

Figure 8.16: Calculated leading edge streamfunctions for the solutions in (a) figure 8.15(a), (b) figure 8.15(b) and (c) figure 8.15(c).

8.6.3 A case of large N

We introduce $N = 9$ dividing blades forming $M = 10$ daughter channels. In figure 8.18, we present solutions for the cases of flat blades, a general constriction and dilation of all the daughter channels and a non-symmetric configuration of blades. The corresponding pressure solutions are given in figure 8.19. The blade shapes for the constricting and dilating cases are given in table 8.2.

Similar behaviour of the flow in each daughter channel as described in previous subsections is seen. In figure 8.19(a), we see that the pressure solution for channels two to nine is identical and so the same flux enters each of these channels. Daughters one and ten have a different pressure solution, again due to the different no-slip conditions within those channels. For the constricted case in figure 8.18(b), the pressure in daughters four to eight have an increasingly favourable pressure gradient whilst daughters two and nine have a weakening pressure gradient. In the top and bottom channels,

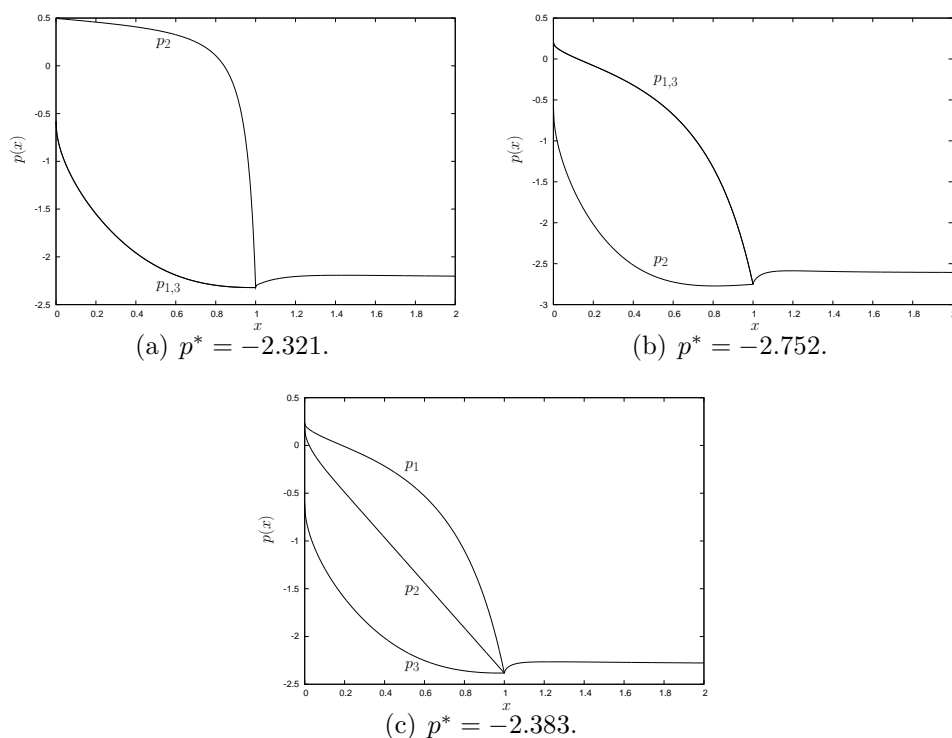


Figure 8.17: Corresponding pressure solutions for the streamfunction solutions plotted in (a) figure 8.15(a), (b) figure 8.15(b) and (c) figure 8.15(c).

the pressure gradient becomes adverse within these channels from $x = 0.4$ to $x = 1$. When the channels dilate, as in figure 8.18(c), the situation is reversed, with the favourable gradient in the now constricted channels one and ten. In the non-symmetric case, figure 8.18(d), a collection of all the behaviours is seen. All the results plotted demonstrate that the flow behaviour in each daughter channel is driven by the channel geometry and the Kutta trailing edge condition.

We consider the flow in the wake region in figures 8.20 - 8.23, and compare our results to the internal flow problem posed in Smith (2002). To recall from the introduction to this chapter, Smith (2002) poses a laterally periodic flow at the trailing edges of an array of blades under the same governing boundary layer equations as in this section. Smith (2002) reports that the periodic nature of the starting condition at the trailing edge holds for a short distance downstream of the trailing edges, before a uniform state is reached far downstream, different to unity. In figure 8.20, where the channel geometries are identical and formed by flat blades, we have a semi-periodic

f_n	Constriction	Dilation
1	$2 + 2x^2$	$2 - x^2$
2	$4 + 3x^2$	$4 - \frac{x^2}{2}$
3	$6 + 2x^2$	$6 - \frac{x^2}{4}$
4	$8 + x^2$	$8 - \frac{x^2}{8}$
5	10	10
6	$12 - x^2$	$12 + \frac{x^2}{8}$
7	$14 - 2x^2$	$14 + \frac{x^2}{4}$
8	$16 - 3x^2$	$16 + \frac{x^2}{2}$
9	$18 - 2x^2$	$18 + x^2$

Table 8.2: The blade shape functions f_n applied to the constriction and dilation cases of $N = 9$ blades in figure 8.18.

flow as the starting condition to the wake, seen in figure 8.20(a). Away from the mother channel walls and as x increases in the wake, in figure 8.20(b) we see that the periodic nature of the starting condition holds at the small downstream distances given, whilst the amplitude of the oscillations decays, in agreement with Smith (2002). Continuing further into the wake, we see in figures 8.20(c) and 8.20(d) that the central part of the wake has reached a uniform state, different to unity, again in agreement with Smith (2002). Towards the mother channel walls, the flow periodicity is broken in the starting condition due to the conditions of $u = 1$ at $Y = 0$ and $Y = H$. Thus, the features reported in the symmetric analysis of Smith (2002) do appear in our problem but do not hold completely due to the influences of the no-slip conditions at $Y = 0$ and $Y = H$. We would expect the uniform state reached within the centre of the channel to be different to that calculated by Smith (2002) due to diffusive effects into the centre of the wake as x increases. The flow emerging from daughters one and ten creates two jet-like flow velocities. These features slowly accelerate the flow within the centre of the wake back towards $u = 1$, with the maximum speed in the jet decreasing in strength as x increases. Similar jet-like behaviour occurs for the constriction and dilation cases presented above.

In figure 8.21, we consider a non-symmetric starting condition for the wake, that arising from the non-symmetric configuration of blades in figure 8.18(d). The starting condition in figure 8.21(a) has no lateral periodicity

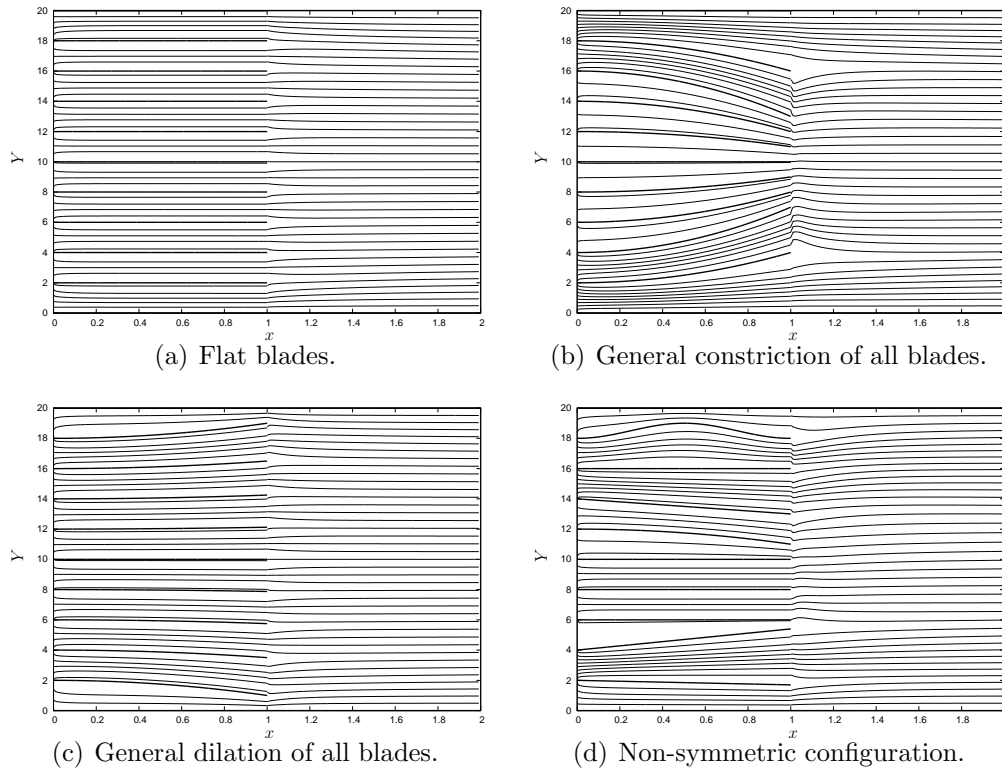


Figure 8.18: Streamfunction solutions for four configurations of $N = 9$ blades. The total channel width is chosen as $H = 20$, so that the entrance width to each daughter is 2. Streamlines are plotted in increments of 0.5.

and no periodic or uniform state emerges downstream (figures 8.21(b)-(d)). Smith (2002) discusses the influence of lateral non-symmetry within the wake but imposes a periodicity condition. Figure 8.21 shows that if the condition required for a periodic solution is not imposed, no periodic state is possible downstream for the calculated non-symmetric wake starting condition. In our problem, each component of the starting condition in the wake is allowed to interact with the wakes above and beneath it, whilst Smith (2002) imposes that the u and u_y values are equal at $y = 0$ and $y = 1$, forcing a periodic solution to emerge downstream. In figure 8.21(d), we see that the two jet-like velocities start to form far downstream, with the flow in the centre of the wake less than unity. Consulting the pressure solution in the wake in figure 8.19(d), we see that the pressure gradient is only slightly adverse in the wake as $x \rightarrow 2$ and hints that very far downstream a solution similar to 8.20(d) may be possible.

Next, we turn to computing solutions when $H = 80$ by choosing the

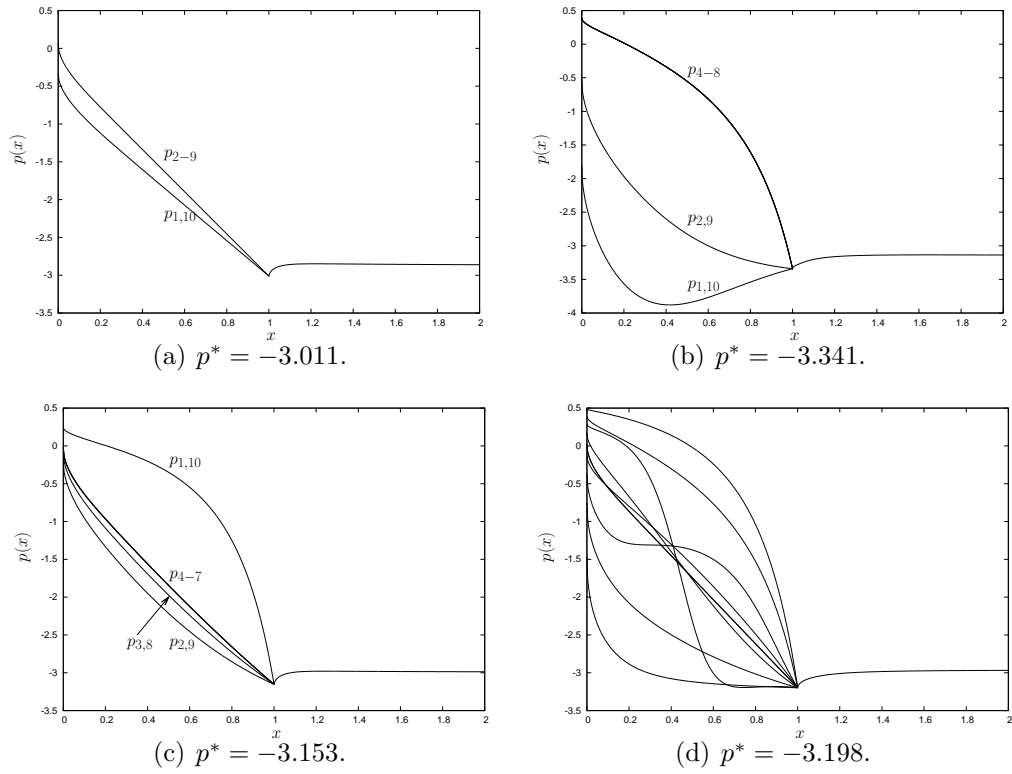


Figure 8.19: The pressure corresponding to the streamfunctions plotted in figures 8.18(a)-(d). The pressures in (d) are, in descending order of $p(0)$, $p_3, p_6, p_{10}, p_7, p_4$ and p_5, p_1, p_9, p_8, p_2 .

entrance widths to daughters one and ten as $\bar{h}_1 = \bar{h}_{10} = 32$. This is to investigate phenomena as $H \rightarrow \infty$. In figure 8.22 we present solutions for the u velocities in the wake for the flat blade and non-symmetric configurations of blades above. We first notice that much less fluid enters the array of blades, instead being diverted into the top and bottom daughter channels. Consequently, in each case similar wake starting conditions in daughters one and ten are seen. In figures 8.22(a) and 8.22(c), similar behaviour reported above occurs within the central part of the wake profiles. As x increases in the wake in figures 8.22(b) and 8.22(d) we see very similar forms of the profiles in each figure. This suggests that the effects of non-symmetric blades have little influence in the form of the velocity profile as $x \rightarrow \infty$. Figure 8.23 compares the u velocity profiles at $x = 3.5$ and $x = 3.8$. We see that there is only a very small area in the central part of the wake where any significant difference is seen.

Whilst computing results for this subsection, we found that as $H \rightarrow \infty$,

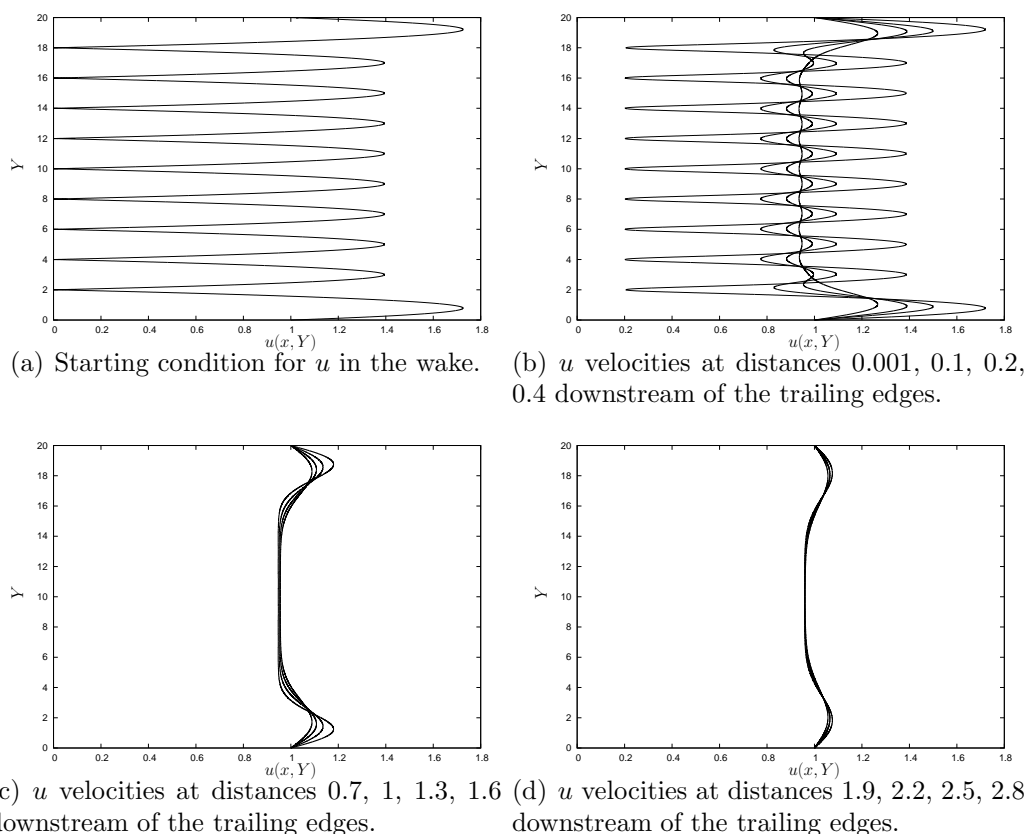


Figure 8.20: Wake velocity profiles in u of the flat configuration of blades in 8.18a.

the value of p^* at the trailing edge slowly decays to 0, proportional to $1/H$. This feature means that less flow passes into daughter channels two to nine, causing the lower flow speeds in the central part of the wake. If we let $H \rightarrow \infty$, then the configuration of blades tends to an external flow problem (i.e. no bounding channel). In the case of external flow, there will be a Blasius boundary-layer flow on the top and bottom surfaces of the dividing blades N and one. Since $p = \text{constant} = 0$ in the Blasius boundary-layer, for pressure continuity at the trailing edge we must have that $p^* = 0$.

8.7 Summary

In this chapter we have formulated and solved a problem of N dividing blades moving within a bounding channel. For a thin normal span of all the blades in comparison to the length of the blades, we found that the boundary-layer

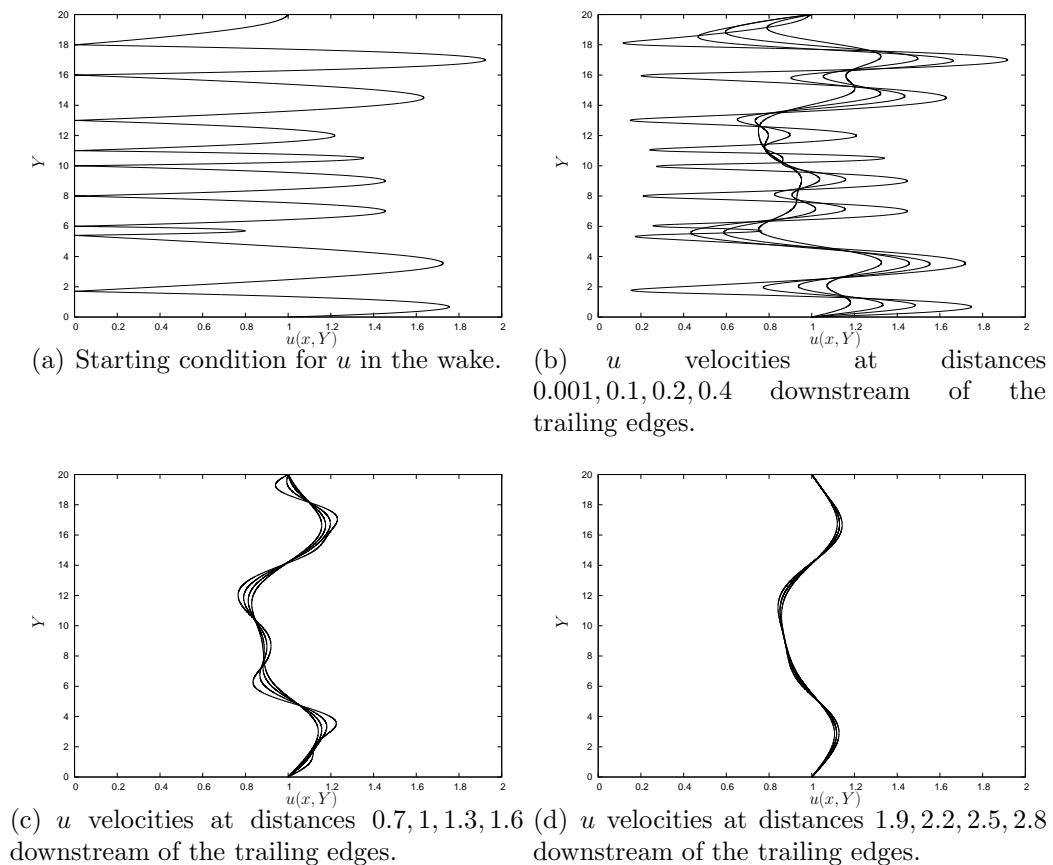


Figure 8.21: Wake velocity profiles in u of the non-symmetric configuration of blades in 8.18d.

equations held within all regions of flow, except within a very small region at the leading edges of the blades. Here, an apparent flow discontinuity occurs due to the Kutta trailing edge condition downstream. The leading order problem in this leading edge region was an inviscid one, which we were able to solve analytically for given downstream fluxes or pressure jumps.

Solutions to the full boundary layer problem were found numerically for various numbers N and profiles of dividing blades. The case $N = 1$ was studied first. When the dividing blade surface was non-symmetric, a pressure jump occurred at the leading edge to satisfy the Kutta condition. The pressure jumps were used retrospectively to find some examples of the solution in the leading edge region. We found that less fluid enters a channel that becomes constricted or is narrower than the other channel. For the $N = 2$ case, similar flow behaviour was observed as seen in the $N = 1$ case. Cases of $N = 9$ blades were then considered with respect to the wake development in

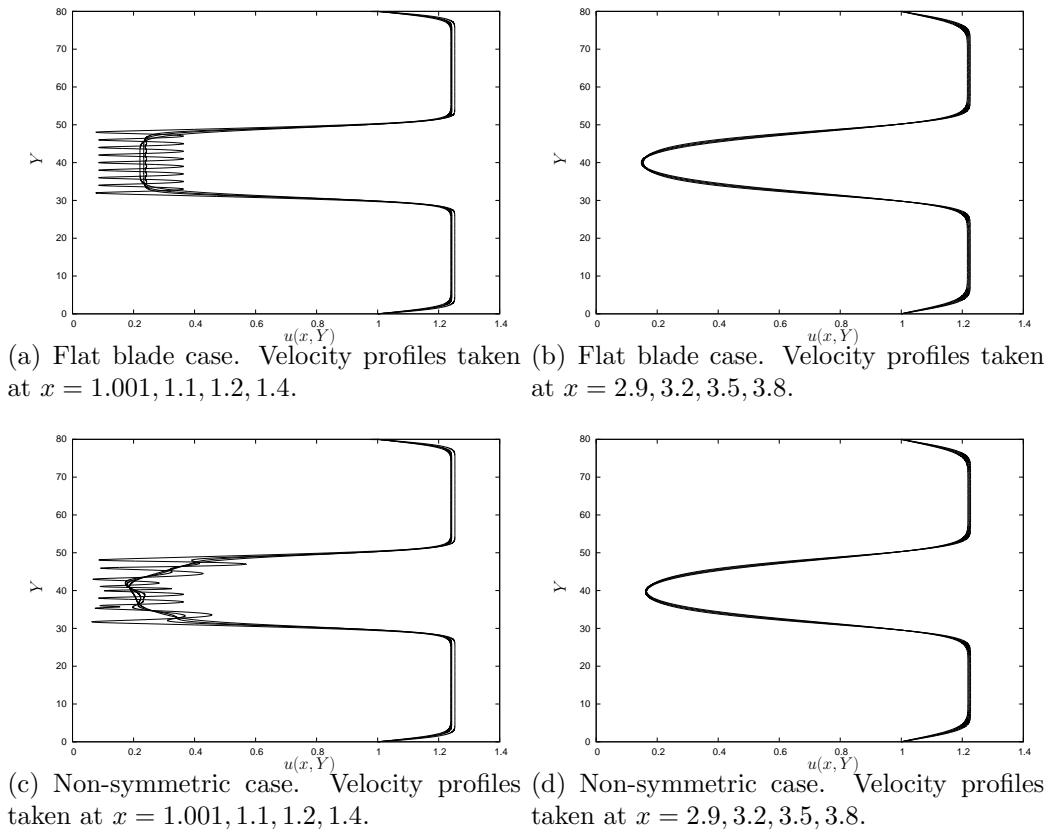


Figure 8.22: Wake velocity profiles with $H = 80$. Figures (a) and (b) are velocity profiles for the flat blade case, figures (c) and (d) for the non-symmetric configuration. The entrance widths to daughters two and nine in each of the above figures are fixed as two.

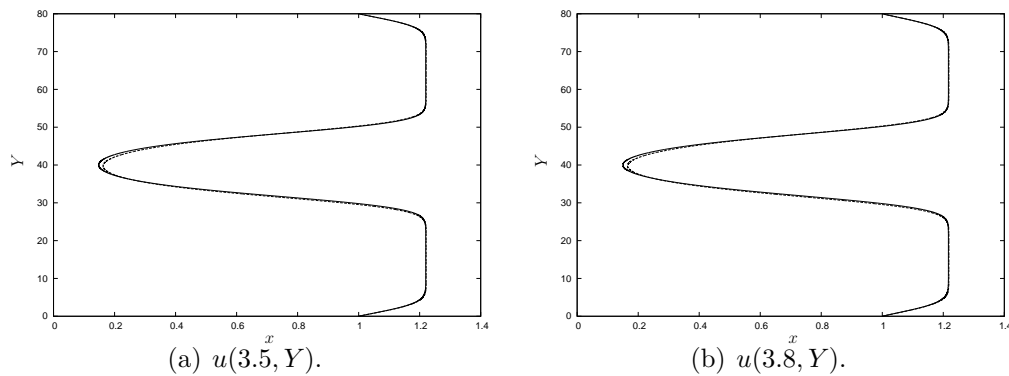


Figure 8.23: Two examples of the u velocities away at large x for the case of flat blades (solid line) and the non-symmetric configuration (dotted line).

comparison to the periodic effects reported in Smith (2002). In our problem, we found behaviour similar to that seen by Smith (2002), but with influence from the wakes of daughters one and ten causing the flow to vary in comparison to his complete theory. When we analysed features arising from the non-symmetric wake starting condition, no periodicity in Y ensued, unlike in the problem by Smith (2002). Finally, we considered the case $H \rightarrow \infty$. In our problems, results suggested that any non-symmetry in the wake starting condition has little impact on the form of the velocity far downstream, in comparison to the same wake profile gained from a symmetric starting condition.

An extension to the work in this chapter would be to change the boundary conditions on $Y = 0$ and $Y = H$ to $u = 0$, instead of $u = 1$. This means that a Pouseuille flow is a solution upstream of the blades and forms the oncoming flow to the leading edge region. The same length scales and expansions for the velocities still hold, but the leading order problem for the streamfunction now changes in that the incoming vorticity is now non-zero and is a function of Y . Thus a new scheme to determine the downstream velocities in each daughter channel is needed in this problem. Another extension is to add non-aligned leading and trailing edges into the problem. This is a worthwhile extension due to applications in AVM modelling and rice grain sorting. In this case, there would be many leading edge regions, subject to varying incoming flow profiles and numerous Kutta conditions to satisfy. This adds extra computational burden in determining the correct starting conditions for the daughter channels, but if the first extension above can be developed, then finding some solutions to this problem should be achievable.

Chapter 9

Conclusions

9.1 Summary

In this thesis we have considered high Reynolds number fluid flow past many blades in various configurations, to include features of ground effect, a global angle of attack and internal boundary-layer problems. Whilst the work conducted has been summarised as the thesis progressed, we conclude by bringing together some of the main points from each chapter and offering possible extensions.

In Chapter 2 we began by considering two-dimensional fluid flow past many blades in extreme ground effect, whereby the ground clearance of the blade was of the same size as the boundary layer thickness. This study was motivated by applications to better understanding of the flow around the front wing of a Formula One racing car. The leading order problem was governed by the boundary-layer equations with the appearance of a local leading edge region at every blade to allow the Kutta condition to be satisfied, by causing a jump in the pressure and velocity locally at the leading edge. Results showed slip-streaming effects of blades downstream through a reduction in drag and lift, for example. We found that as the ground clearance became small, these slip-streaming effects decreased over the $N = 6$ blades present within the numerical study. We considered analytically the extreme cases of very large and small ground clearances analytically. We found that for small ground clearances, the flow beneath each blade was governed primarily by a Couette flow whilst for larger ground clearances, a viscous-inviscid model,

similar to Purvis & Smith (2004) arises.

The main body of work within this thesis has been to investigate the fluid flow past a horizontally aligned array of blades at a global angle of attack. In Chapter 3, the model derived was that of a coupled viscous boundary-layer and inviscid free-stream, through unknown wake-shapes and pressure differences. Overall, we found that slip-streaming effects, like in Chapter 2, occur over all blades. The slip-streaming effects were seen immediately for smaller angles of attack, whilst for larger angles of attack we found that a near Blasius boundary layer occurred beneath the first few blades. On passing more blades, the Blasius nature of the boundary-layer beneath the blade disappeared allowing slip-streaming effects to occur.

In Chapter 4 an investigation was conducted into a periodic many-blade limit with a global angle of attack. This study was motivated by the results in Chapter 3, where an overall growth of the boundary-layer occurred with local adjustments in boundary-layer thickness over each blade and wake. A flow model was developed on the basis of this result, whereby we modelled the boundary layer in two parts, a slowly growing bulk layer and a periodic sublayer close to the blades. We found that the bulk layer was governed by a mean Blasius flow to leading order and served to pass the displacements (caused by the sublayer) to the free-stream in an inviscid manner. The sublayer was governed by the full boundary-layer equations and was found to be periodic. We computed results using this analysis and compared them to several cases in the full problem of Chapter 3 and found good qualitative agreement between the solutions.

The many-blade limit of Chapter 4 holds for all downstream distances in x until $x = O(Re^{3/5})$, where a pressure gradient appears throughout the boundary-layer. In Chapter 5, we adapted the periodic many-blade limit of Chapter 4 to include pressure interaction. The bulk-layer was still governed by mean Blasius flow to leading order, whilst the pressure interactive boundary-layer equations held in the sublayer. We found sample solutions to the sublayer problem with flat, angled and thick blades for the condensed case showing agreement with Bowles & Smith (2000a,b).

With the general, non-symmetric pressure interactive many-blade limit

outlined, we added, in Chapter 6, a global angle of attack to the analysis. We found that the sublayer is affected to leading order by a global angle of attack $\alpha = O(Re^{-1})$. An angle of attack of this size is tiny in comparison to the sublayer size, but on passing a number $n = O(Re^{3/5})$ blades, the global angle of attack caused a shift of the position of the blade within the sublayer. The change to the leading order formulation of the problem was the inclusion of a constant $\bar{\alpha}$ in the no-slip and no-normal flow boundary conditions. Various solutions were presented, and they indicated that the streamlines calculated behaved similarly for all values of the global angle of attack parameter, $\bar{\alpha}$. For some thick blade calculations, we were able to decrease the value of $\bar{\alpha}$ enough so that the global angle of attack caused flow reversal in the sublayer.

In Chapter 7, we sought larger angles of attack which brought about different leading order balances to the formulation but preserved the underlying flow structure of the interactive limit. We found that a leading order change in the bulk-layer is caused when $\alpha = O(Re^{-4/5})$, causing the mean Blasius flow to be Prandtl shifted by an amount $\bar{\alpha}$ within the bulk-layer. A leading order change was caused to the free-stream when $\alpha = O(Re^{-3/5})$, whereby the whole boundary layer was shifted within the free-stream. For these two cases, the formulations for each region remained largely unchanged from Chapter 5. We then considered a short scale balance between the global angle of attack and the sublayer coordinate. The structure of the boundary layer was seen to be much the same as before. We found numerical solutions for various blade geometries, with results showing a much greater deflection of the streamlines across the whole blade-wake period and greater pressure differences over the blade in comparison to the solutions in Chapter 6.

Finally, in Chapter 8 we considered fluid flow past many vertically aligned blades within a channel. The study was motivated by applications to atomizer flows in the combustors of jet engines and cerebral arteriovenous malformations. The model developed comprised the boundary-layer equations everywhere, with the inclusion of a leading edge discontinuity to satisfy the Kutta condition. An in-depth analysis was given to the primarily inviscid leading edge problem using complex analysis. We found that the leading edge pressure and velocity jumps are partly determined by the daughter channel

geometry in the full flow problem past all the blades. Solutions for $N = 1, 2$ and 9 blades were given for various blade geometries, and for $N = 9$ we investigated the limit $H \rightarrow \infty$. We found that the pressure jumps in daughters one and ten tended to zero as $H \rightarrow \infty$, meaning that the far downstream flow behaviour, past a now-isolated array of blades, appears to not depend on the blade geometries upstream.

9.2 Further work

Many avenues for further investigation exist in the problems of fluid flow past many blades of which the following, outlined in the thesis, are of most interest to the author.

Further study within the interactive many-blade limits of Chapters 5,6 and 7 is needed to investigate the flow response with unequal displacement constants. We found the constant c_+ to be negative in many of the calculations and further investigation into the physical relevance of a negative displacement constant needs to be understood. In this thesis, we somewhat arbitrarily took these constants to be equal and it would be interesting to see how the regime responds to unequal pressures. One constant may be used to obtain pressure periodicity, but then the other constant is unknown and another condition would be needed to find the solution. A solution to this problem would be to simply impose a value for the unknown constant and find the value of the other such that periodicity is achieved. A more technical problem is to develop a stable numerical scheme where the full, periodic pressure-displacement laws could be included within the calculations to allow a periodic solution to develop.

Another interesting extension would be to develop the extreme ground effect problem of Chapter 2 to include cambered blades, leading to the possibility of flow separation beneath the blade. It would be interesting to see if sheltering effects downstream cause a change in the separation behaviour and whether this affects the lift produced over each blade. A possible starting point from this thesis in solving the flow between the blade and the ground, is to use the transformation and numerical technique used in Chapter 8. It

is also worthwhile to find a way of solving the leading edge region in full for a general non-uniform oncoming flow, so that the wake length can be shortened within the computations. A shorter wake length would still have the same applications and allow a more general theory of the problem to be developed.

Finally, and of greatest personal interest is the adaptation of the inviscid flow problem in Chapter 3 to a three-dimensional rotary regime. A boundary-integral technique could be used to derive the governing equations for the free-stream problem, however, a difficulty arises in inverting the resulting singular integral equations without resorting to complex analysis. A first consideration may be the three-dimensional rotary flow problem for the case of infinite blade spans away from the central hub, perhaps using a panel method, to find the inviscid solution and apply the Kutta condition correctly. If the inviscid problem can be solved, then a coupled flow problem, similar to the two-dimensional one appearing in Chapter 3, could be derived. The boundary-layer formulation is given by Smith & Timoshin (1996a) and it is believed that with a suitable method to solve the three-dimensional inviscid problem, progress can be made. To then include a blade hub and finite blade spans then introduces new problems, especially with the generation of tip-vortices in the latter case. The generation of tip-vortices in the rotary framework is discussed by Smith & Timoshin (1996a) for a symmetric rotary setting and would be of much interest in the case of non-symmetry.

Bibliography

- D.J. Acheson. *Elementary Fluid Dynamics*. Oxford University Press, USA, 1990.
- V. Bertram. *Practical Ship Hydrodynamics*. Butterworth-Heinemann, 2000.
- S. Bhattacharyya and F.T. Smith. 2004. Comparisons of direct simulations and analytical predictions for multi-plate flows. *Computers and Fluids*, **33**, 257–265.
- H. Blasius. 1908. Grenzsichten in Flussigkeiten mit kleiner Reibung. *J. Math. Phys.*, **56**, 1–37.
- M.G. Blyth and A.J. Mestel. 2001. Merging flow in co-axial cylindrical pipes. *Quarterly Journal of Mechanics and Applied Mathematics*, **54**, 655.
- R.G.A. Bowles and F.T. Smith. 2000a. Interactive flow past multiple blades and wakes. *Quarterly Journal of Mechanics and Applied Mathematics*, **53**, 207–251.
- R.G.A. Bowles and F.T. Smith. 2000b. Lifting multi-blade flows with interaction. *Journal of Fluid Mechanics*, **415**, 203–226.
- R.I. Bowles, S.C.R. Dennis, R. Purvis and F.T. Smith. 2005. Multi-branching flows from one mother tube to many daughters or to a network. *Philosophical Transactions A*, **363**, 1045.
- A.R.S. Bramwell. *Helicopter Dynamics*. Wiley, 1976.
- R.E. Brown, J.G. Leishman, S.J. Newman, F.J. Perry and F.J.P.R. Consultant. Blade twist effects on rotor behaviour in the vortex ring state. In *28th European Rotorcraft Forum, Bristol, England*, 2002.

- F.X. Caradonna and M.P. Isom. 1972. Subsonic and transonic potential flow over helicopter rotor blades. *AIAA Journal*, **10**, 1606–1612.
- F.X. Caradonna and C. Tung. 1981. Experimental and analytical studies of a model helicopter rotor in hover. *NASA Technical Memorandum*, **81232**.
- G.F. Carrier, M. Krook and C.E. Pearson. *Functions of a Complex Variable: Theory and Technique*. McGraw-Hill, New York, 1966.
- T. Cebeci, H.B. Keller and P.G. Williams. 1979. Separating boundary-layer flow calculations. *Journal of Computational Physics*, **31**, 363–378.
- M.S. Chaffin and J.D. Berry. 1990. Navier-Stokes and potential theory solutions for a helicopter fuselage and comparison with experiment. *NASA TM*, **4566**.
- H. Cohen, G.F.C. Rogers and H.I.H. Saravanamuttoo. *Gas Turbine Theory*. Longman Harlow, UK, 1972.
- A.T. Conlisk. 1997. Modern helicopter aerodynamics. *Annual Reviews in Fluid Mechanics*, **29**, 515–567.
- R.R. Diehl, D. Linden, D. Lucke and P. Berlit. 1995. Phase relationship between cerebral blood flow velocity and blood pressure: a clinical test of autoregulation. *Stroke*, **26**, 1801.
- R.P. Dougherty, F.Y. Wang, E.R. Booth, M.E. Watts, N. Fenichel and R.E. D’Errico. 2004. Aircraft wake vortex measurements at Denver International Airport. *AIAA Paper*, **2880**.
- T. Gerz, F. Holzäpfel, W. Bryant, F. Köpp, M. Frech, A. Taffermer and G. Winckelmans. 2005. Research towards a wake-vortex advisory system for optimal aircraft spacing. *Comptes Rendus Physique*, **6**, 501–523.
- R. Girvin. 2009. Aircraft noise-abatement and mitigation strategies. *Journal of Air Transport Management*, **15**, 14–22.
- S. Goldstein. 1930. Concerning some solutions of the boundary-layer equations in hydrodynamics. *Proc. Camb. Phil. Soc*, **26**, 1–30.

- I.S. Gradshteyn and I.M. Ryzhik. *Tables of integrals, series, and products*. Academic Press, 1988.
- K. Gross, T. MacDonald and R. Dagenhart. 2004. Dispelling the myth of the MV-22. *Proceedings (The Naval Institute)*.
- M.M. Hafez and D. Kwak. *Numerical simulations of incompressible flows*. World Scientific Pub Co Inc, 2003.
- G.M. Hoffmann, H. Huang, S.L. Waslander and C.J. Tomlin. Quadrotor helicopter flight dynamics and control: Theory and experiment. In *Proc. of the AIAA Guidance, Navigation, and Control Conference*. Citeseer, 2007.
- D.B. Ingham, T. Tang and B.R. Morton. 1990. Steady two-dimensional flow through a row of normal flat plates. *Journal of Fluid Mechanics*, **210**, 281–302.
- M.P. Isom. *Unsteady subsonic and transonic potential flow over helicopter rotor blades*. National Aeronautics and Space Administration, 1974.
- W. Johnson. *Helicopter Theory*. Dover, UK, 1994.
- M.A. Jones. *Mechanisms in Wing-in-Ground Effect Aerodynamics*. PhD thesis, University of London, 2000.
- M.A. Jones and F.T. Smith. 2003. Fluid motion for car undertrays in ground effect. *Journal of Engineering Mathematics*, **45**, 309–334.
- J.A. Jupp and P.H. Rees. Aircraft wing and winglet arrangement, December 22 1987. US Patent 4,714,215.
- S. Kapadia and S. Roy. Detached Eddy Simulation Of Turbine Blade Cooling. In *Proc. of the 36th AIAA Thermophysics Conference*, 2003.
- H.B. Keller. 1978. Numerical methods in boundary-layer theory. *Annual Review of Fluid Mechanics*, **10**, 417–433.
- I. Kroo. 2005. Nonplanar wing concepts for increased aircraft efficiency. *VKI Lecture Series on Innovation Configurations and Advanced Concepts for Future Civil Aircraft*, pages 6–10.

- A.H. Lefebvre. *Gas Turbine Combustion*. CRC, 1999.
- M.P. Marks, N.J. Pelc, M.R. Ross and D.R. Enzmann. 1992. Determination of cerebral blood flow with a phase-contrast cine MR imaging technique: evaluation of normal subjects and patients with arteriovenous malformations. *Radiology*, **182**, 467.
- J.H. Mathews and R.W. Howell. *Complex Analysis for Mathematics and Engineering*. Jones & Bartlett Publishers, 2001.
- W.J. McCroskey. 1995. Vortex wakes of rotorcraft. *AIAA Paper*, **95**.
- A.F. Messiter. 1970. Boundary-layer flow near the trailing edge of a flat plate. *SIAM J. Appl. Math*, **18**, 241–257.
- N.I. Muskhelishvili. *Singular Integral Equations*. 1946.
- R. Natarajan, B. Fornberg and A. Acrivos. 1993. Flow past a row of flat plates at large Reynolds numbers. *Proceedings: Mathematical and Physical Sciences*, pages 211–235.
- N.C. Ovenden. 2005. A uniformly valid multiple scales solution for cut-on cut-off transition of sound in flow ducts. *Journal of Sound and Vibration*, **286**, 403–416.
- C. Polacsek, G. Desquesnes and G. Reboul. 2009. An equivalent-source model for simulating noise generation in turbofan engines. *Journal of Sound and Vibration*, **323**, 697–717.
- R. Purvis. *Rotor blades and ground effect*. PhD thesis, University of London, 2002.
- R. Purvis and F.T. Smith. 2004. Planar flow past two or more blades in ground effect. *Quarterly Journal of Mechanics and Applied Mathematics*, **57**, 137–160.
- T.A. Reyhner and I. Flugge-Lotz. 1968. The interaction of a shock wave with a laminar boundary layer. *Int. J. Non-Linear Mech*, **3**, 173–199.

- S.K. Richards, X.X. Chen, X. Huang and X. Zhang. 2007. Computation of fan noise radiation through an engine exhaust geometry with flow. *International Journal of Aeroacoustics*, **6**, 223–241.
- W. Rodi. 2006. DNS and LES of some engineering flows. *Fluid Dynamics Research*, **38**, 145–173.
- L. Rosenhead. *Laminar Boundary Layers*. Dover, New York, 1963.
- J. Seddon, S. Newman and B. Seddon. *Basic Helicopter Aerodynamics*. Blackwell, 2001.
- F.T. Smith. 1977. Steady motion through a branching tube. *Proc. R. Soc. Lond.*, **355**, 167–187.
- F.T. Smith. 1982. On the high Reynolds number theory of laminar flows. *IMA Journal of Applied Mathematics*, **28**, 207–281.
- F.T. Smith. 1983. Interacting flow theory and trailing edge separation–no stall. *Journal of Fluid Mechanics*, **131**, 219–249.
- F.T. Smith. 2002. Interference and turning of in-parallel wakes. *Quarterly Journal of Mechanics and Applied Mathematics*, **55**, 49–67.
- F.T. Smith, P.W.M. Brighton, P.S. Jackson and J.C.R. Hunt. 1981. On boundary-layer flow past two-dimensional obstacles. *Journal of Fluid Mechanics*, **113**, 123–152.
- F.T. Smith and A.S. Ellis. 2010. On interaction between falling bodies and the surrounding fluid. *Mathematika*, **56**, 140–168.
- F.T. Smith and M.A. Jones. 2000. One-to-few and one-to-many branching tube flows. *Journal of Fluid Mechanics.*, **423**, 1–31.
- F.T. Smith and M.A. Jones. 2003. AVM modelling by multi-branching tube flow: large flow rates and dual solutions. *Mathematical Medicine and Biology*, **20**, 183–204.

- F.T. Smith, N.C. Oviden, P.T. Franke and D.J. Doorly. 2003. What happens to pressure when a flow enters a side branch? *Journal of Fluid Mechanics*, **479**, 231–258.
- F.T. Smith and S.N. Timoshin. 1996a. Blade-wake interactions and rotary boundary layers. *Proceedings: Mathematical, Physical and Engineering Sciences*, **452**, 1301–1329.
- F.T. Smith and S.N. Timoshin. 1996b. Planar flows past thin multi-blade configurations. *Journal of Fluid Mechanics*, **324**, 355–377.
- K. Stewartson. 1969. On the flow near the trailing edge of a flat plate-II. *Mathematika*, **16**, 106–121.
- R. Strawn, R.C. Biswas. 1996. Numerical simulations of helicopter aerodynamics and acoustics. *Journal of Computational and Applied Mathematics*, **66**, 471–483.
- J.C. Tsao, A.P. Rothmayer and A.I. Ruban. 1997. Stability of air flow past thin liquid films on airfoils. *Computers & Fluids*, **26**, 427–452.
- K. Washizu, A. Azuma, J. Koo and T. Oka. 1966. Experiments on a model helicopter rotor operating in the vortex ring state. *Journal of Aircraft*, **3**, 225–230.
- Y.H. Yu. Rotor blade-vortex interaction noise - generating mechanisms and its control concepts. In *AHS, International Aeromechanics Specialists' Conference, 2nd - Aeromechanics Technology & Product Design for the 21st Century*, Bridgeport, CT, 1995.
- Y.H. Yu. 2000. Rotor blade-vortex interaction noise. *Progress in Aerospace Sciences*, **36**, 97–115.